

A Thesis Submitted for the Degree of PhD at the University of Warwick

Permanent WRAP URL:

<http://wrap.warwick.ac.uk/135581>

Copyright and reuse:

This thesis is made available online and is protected by original copyright.

Please scroll down to view the document itself.

Please refer to the repository record for this item for information to help you to cite it.

Our policy information is available from the repository home page.

For more information, please contact the WRAP Team at: wrap@warwick.ac.uk

FAST ATOM BOMBARDMENT MASS SPECTROMETRY OF CLUSTERS AND
ADDUCTS BASED ON URANIUM AND LANTHANIDES.

by

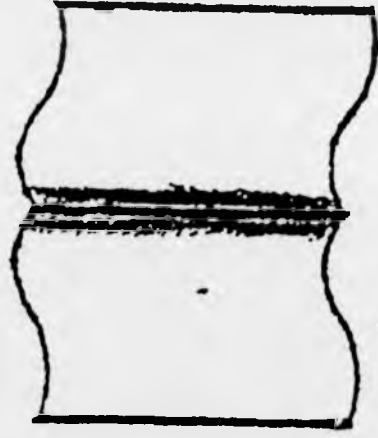
Paul A. Read

A thesis submitted to the University of Warwick in
partial fulfilment of the requirements for the degree
of Doctor of philosophy

Department of Chemistry,
University of Warwick,
Coventry CV4 7AL

1993

THIS VOLUME HAS A
VERY TIGHT BINDING



To my wife, Judith

ACKNOWLEDGEMENTS

I wish to thank Professor T.J.Kemp for guidance and encouragement throughout this work and for a research studentship.

I acknowledge the advice and support given by members of the mass spectrometry research group, especially Professors Derrick and Jennings and Mr. I.Katyal. Thanks are also due to the staff of the electronics and mechanical workshops for maintenance of and modifications to the mass spectrometers.

DECLARATION

The work described in this thesis is entirely original and my own, except where otherwise indicated.

Parts of the work contained in this thesis have been accepted for publication in the scientific literature:

JENNINGS K. R., KEMP T. J., READ P. A.,

Inorg. Chim. Acta, 1989 157 157

JENNINGS K. R., KEMP T. J., READ P. A.,

Poster presented at the 37th American Society of Mass Spectrometry Conference on Mass Spectrometry and Allied Topics, Miami Beach, May 1989

JENNINGS K. R., KEMP T. J., READ P. A.,

Poster presented at the 25th symposium of the Royal Society of Chemistry, Faraday Division, University of Warwick, December 1989

KEMP T. J., READ P. A.,

Poster presented at the 1991 Gordon Conference on the Physics and Chemistry of Matrix Isolation, Plymouth, New Hampshire, U.S.A.

KEMP T. J.,

Overview of lecture accepted for publication,

Coord. Chem. Revs. 1993

ABSTRACT

The fast atom bombardment, FAB, of salts of uranium, the lanthanides and related metals yield long, well defined series of cations of metal-oxygen clusters, $(M_xO_y)^+$ with x up to 30-40. Up to seven values of y are associated with each value of x, but in each set of clusters there is usually a well-defined ion of maximum abundance. These series consist of regular patterns of clusters whose relative stabilities and structures can be directly related to reported solid state structures, demonstrating the strong influences of solid state processes at the molecular level. Thus, direct correlations are found between these metal-oxygen clusters and the complex metal-oxide phases exhibited by the actinide and lanthanide metals.

The mass spectral and collision-induced decomposition (CID) spectral data obtained for many of these clusters feature ion abundances depending on cluster size, and a pronounced odd/even alternation, both of which are interpreted in terms of the electronic and geometrical structures of the clusters. Similar trends are also demonstrated for series based on the general formula $(U_xCL_n)^+$ with x up to 13. Conditions of sample preparation (matrix, source pressure, etc.) are described for the achievement of maximal cluster formation and fragmentation reactions. The fabrication and deployment of a 'split' FAB source is described which enables the simultaneous bombardment of two samples to yield 'mixed' clusters.

The FAB spectra of a variety of uranyl complexes containing biologically important molecules, such as peptides, demonstrate the sequential loss of the ligands. The inter-relationship between their mode of fragmentation, and the extent of ligand coordination, as well as their relative ion abundances is described.

CONTENTS

| | | |
|-----------|---|----|
| CHAPTER 1 | INTRODUCTION | 1 |
| 1.1 | Fast Atom Bombardment Mass Spectrometry | 1 |
| 1.2 | The Processes Involved in Desorption Mass Spectrometry | 2 |
| 1.3 | Gas Phase Chemistry | 4 |
| 1.4 | The Electronic Structure of the Actinide Elements | 6 |
| 1.4.1 | The Hydrolysis of the Actinide Elements | 6 |
| 1.4.2 | The Uranyl Ion (Electronic Structure) | 9 |
| 1.4.4 | The Uranyl Ion (Aqueous Chemistry) | 12 |
| 1.5 | The Uranium Oxygen System | 13 |
| 1.5.1 | The Uranium - Uranium Dioxide Region | 15 |
| 1.5.2 | The UO_2 - $\text{UO}_{2.25}$ Region | 15 |
| 1.5.3 | The $\text{UO}_{2.25}$ - U_3O_{8-x} Region | 16 |
| 1.5.4 | The U_3O_{8-x} - UO_3 Region | 18 |
| 1.6 | The Gas Phase Chemistry of Uranium | 21 |
| 1.7 | Bonding Models For Clusters | 25 |
| 1.7.1 | The Spherical Jellium Model | 25 |
| 1.7.2 | The Structured Jellium Model | 27 |
| 1.7.3 | The Linear Combination of Atomic Orbitals Model | 28 |
| 1.8 | Models For Main Group and Transition Metal Clusters | 30 |
| 1.8.1 | The Tensor Surface Harmonic Model | 30 |
| 1.8.2 | Polyhedral Skeletal Electron Pair Theory | 33 |
| 1.8.3 | The Application of PSEPT to gas Phase Transition Metal Clusters | 34 |
| 1.9 | Major Cluster Classes | 35 |
| 1.9.1 | Rare Gas Clusters | 35 |
| 1.9.2 | Ammonia Clusters | 37 |
| 1.9.3 | Methanol Clusters | 38 |

| | | |
|-------------------------------|---|-----|
| 1.9.4 | Acetone Clusters | 41 |
| 1.9.5 | Alkali Metal Clusters | 43 |
| 1.9.6 | Silver Clusters | 48 |
| 1.9.7 | Gold Clusters | 51 |
| 1.9.8 | Aluminium Clusters | 52 |
| 1.9.9 | Vanadium, Niobium and Tantalum Clusters | 59 |
| 1.9.10 | Iron Clusters | 61 |
| 1.9.11 | Cobalt Clusters | 64 |
| 1.9.12 | Nickel Clusters | 68 |
| 1.9.13 | Trends in Metal Cluster Chemistry | 73 |
| CHAPTER 2 EXPERIMENTAL | | |
| 2.1.1 | The Mass Spectrometer | 81 |
| 2.1.2 | The FAB Gun | 85 |
| 2.2 | Matrix Effects on Various aspects of FAB Spectra | 86 |
| 2.2.1 | The Matrix Compounds | 87 |
| 2.2.2 | Effect of Sample Temperature | 90 |
| 2.2.3 | Effect of Size of Probe Tip | 91 |
| 2.3 | The Effect of Source Pressure on Cluster and Adduct Formation | 93 |
| 2.4.1 | Materials | 101 |
| 2.4.2 | Preparations | 103 |
| CHAPTER 3 LANTHANIDE CLUSTERS | | |
| 3.1 | The Lanthanide Elements | 105 |
| 3.2 | The Gas Phase Chemistry of the Lanthanides | 105 |
| 3.3 | Lanthanide Oxide Systems | 107 |
| 3.3.1 | Cerium Oxide | 107 |
| 3.3.2 | Praseodymium Oxide | 108 |

| | | |
|-----------|---|-----|
| 3.3.3 | Terbium oxide | 109 |
| 3.4 | Lathanide Clusters | 112 |
| 3.4.1 | Lanthanum Clusters | 112 |
| 3.4.2 | Cerium Clusters | 121 |
| 3.4.3 | Praseodymium Clusters | 124 |
| 3.4.4 | Samarium Clusters | 130 |
| 3.4.5 | Europium Clusters | 135 |
| 3.4.6 | Terbium Clusters | 139 |
| 3.4.7 | Holmium Clusters | 141 |
| 3.5 | Discussion of Results | 144 |
| 3.5.1 | Praseodymium and Terbium Clusters | 144 |
| 3.5.2 | Lanthanum Clusters | 149 |
| 3.5.3 | Holmium Clusters | 152 |
| 3.5.4 | Cerium Clusters | 156 |
| 3.5.5 | Europium Clusters | 162 |
| 3.5.6 | Samarium Clusters | 166 |
| 3.6 | Conclusions | 171 |
| CHAPTER 4 | URANYL CLUSTERS | 180 |
| 4.1 | Uranyl Clusters | 180 |
| 4.2 | The Collision Induced Decomposition of Uranyl Clusters | 191 |
| 4.3 | Discussion of Results | 204 |
| 4.4 | Thorium Clusters | 209 |
| 4.5 | Conclusions | 211 |
| CHAPTER 5 | LIGATED CLUSTERS | 213 |
| 5.1 | Fab Spectra of Lathanide Acetates | 213 |
| 5.1.1 | Lanthanum Acetate | 213 |
| 5.1.2 | Cerium Acetate | 215 |

| | | |
|-------------------|---|-----|
| 5.1.3 | Praseodymium Acetate | 216 |
| 5.1.4 | Terbium Acetate | 218 |
| 5.1.5 | Holmium Acetate | 219 |
| 5.2 | Discussion of Results | 219 |
| 5.3 | Lanthanide Malonates | 221 |
| 5.4 | Amino Acid Complexes of the Uranyl Ion | 224 |
| 5.4.1 | Uranyl-(Glycine) Complexes | 225 |
| 5.4.2 | Uranyl-(α , β - Alanine) Complexes | 227 |
| 5.5 | Uranyl-(α , β , γ - Aminobutanoic Acid) Complexes | 230 |
| 5.5.1 | Uranyl-(α - Aminobutanoic Acid) Complexes | 231 |
| 5.5.2 | Uranyl-(β - Aminobutanoic Acid) Complexes | 232 |
| 5.5.3 | Uranyl-(γ - Aminobutanoic Acid) Complexes | 233 |
| 5.5.4 | Trends Observed in the Uranyl - (α , β , γ - Aminobutanoic Acid) Clusters Formed | 234 |
| 5.6 | Uranyl-(Serine) and (Theonine) Complexes | 236 |
| 5.7 | Summary if FAB Spectrometry for Uranyl-(Amino Acid) Complexes | 238 |
| 5.8 | The FAB Mass Spectrum of Uranium (IV) Chloride | 243 |
| CHAPTER 6 SUMMARY | | |
| 6.1 | Cluster Chemistry | 252 |
| 6.2 | Concluding Summary | 256 |
| 6.3 | Further Work | 261 |
| | REFERENCES | 263 |

FIGURES

| | | |
|-----------|--|----|
| Fig 1.4.1 | The Coordination Geometries of Isoelectric Dioxometal Ions | 10 |
| Fig 1.5.1 | The Pressure - Temperature Relationship Between UO_2 - UO_3 | 14 |
| Fig 1.5.2 | The Pressure - Temperature Phase Relationships At U_2O_5 | 17 |
| Fig 1.5.3 | The I.R Spectra of U_2O_5 Phases | 17 |
| Fig 1.9.1 | a) The Conventional TOF Spectrum of $\text{H}^+(\text{CH}_3\text{OH})_n$, Laser $\lambda=266\text{nm}$ | 39 |
| | b) The Daughter Ion TOF Spectrum of $\text{H}^+(\text{CH}_3\text{OH})_{n-1}$, Laser $\lambda=266\text{nm}$ | 39 |
| Fig 1.9.2 | The Abundance of $(\text{Na})_n$ Clusters Formed by Free Jet Expansion, Using AR Carrier Gas | 44 |
| Fig 1.9.3 | The Photoproducts from Mass Selected Na_{53}^+ , at Three Photo Energies. Competition Between Photoevaporation and Photoionisation is Clearly Observed. | 46 |
| Fig 1.9.4 | The Size Distribution of Silver Clusters | 50 |
| Fig 1.9.5 | The Size Distribution of Gold Clusters | 50 |
| Fig 1.9.6 | The Mass Spectrum of Aluminium Cluster Ions | 53 |
| Fig 1.9.7 | A Diagrammatic Representation of the Electronic Band Structure for Mercury Clusters | 75 |
| Fig 2.1.1 | The Ion Optics of the 'CONCEPT' 4 Sector | 83 |
| Fig 2.1.2 | The Flexicell - Plate and Slit arrangement | 84 |
| Fig 2.2.1 | A Schematic Representation of the change in Total Ion Yield with Increasing amounts of Matrix Compounds | 89 |
| Fig 2.2.2 | Diagrammatic Representation of the Twin-Sector Probe Tip | 93 |
| Fig 2.3.1 | Diagrammatic Representation of the Position of the Source Covers to reduce the Source Conductance, hence Allowing the Effect of Source Pressure on Cluster Formation to be Studied | 98 |
| Fig 2.3.2 | a) Gas Inlet Plate, Materials Stainless steel, all Dimensions in mm | 99 |
| | b) Source Block Cover, Material 'PEEK', all Dimensions in mm | 99 |

| | |
|---|-----|
| c) Source Lens Plate, Material Stainless steel, all Dimentions in mm | 100 |
| Fig 2.3.3 Schematic Representation of the Change in Total ion current, I, with Increasing Duration of Bombardment, T, at a Number of Buffer Gas Pressures | 101 |
| Spec 3.4.1 The Cluster Spectrum for Lanthanum, with Sulpholane Matrix | 114 |
| Fig 3.4.1 The Ranges of x and y observed for Each Successive Seriesfor Lanthanum-Oxygen Clusters, $[(LaO)_xO_y]^+$ | 117 |
| Spec 3.4.2 The CID Spectra of $(LaO)_{16}O_8^+$, $m/z = 1630$, Using Argon Collision Gas, Flexicell At 2KV, 30% Transmittance | 119 |
| Spec 3.4.3 The FAB Spectrum of Cerium Nitrate | 122 |
| Spec 3.4.4 The Mass Spectrum of Praseodymium Clusters | 125 |
| Spec 3.4.5 The High Mass Spectrum of the Praseodymium Clusters | 126 |
| Spec 3.4.6 The CID Spectrum for $[(PrO)_{10}O_5]^+$, with Argon Collision Gas, Flexicell At 2KV, 20% Transmittance | 128 |
| Tabl 3.4.1 A Comparison Between the % Natural Abundances of Samarium Isotopeses and Their Relative Intensities as Detected | 131 |
| Spec 3.4.7 The Isotopic Distribution From Mass Spectral Data | 132 |
| Fig 3.4.2 The Calculated Distribution From Isotopic Abundances. | 132 |
| Spec 3.4.8 The FAB Mass Spectrum for Samarium Nitrate. | 133 |
| Spec 3.4.9 The FAB Mass Spectrum for Europium Nitrate. | 136 |
| Spec 3.4.10 The FAB Mass Spectrum for Terbium Nitrate | 140 |
| Spec 3.4.11 The FAB Mass Spectrum for Holmium Nitrate | 142 |
| Fig 3.5.1 A Graphical Representation of the Relationship Between x and y for the Praseodymium Clusters | 145 |
| Fig 3.5.2 The Variation in Metal : Oxygen Atom Ratio with Increasing Cluster Size for Praseodymium and Terbium Clusters | 147 |
| Fig 3.5.3 The Variation in Metal : Oxygen Atom Ratio, z, with $1/x$. For Praseodymium and Terbium Clusters. | 148 |
| Fig 3.5.4 The Variation in the Number of Additional Oxygen Atoms, y, with Cluster Size, x, for the Lanthanum Clusters. | 150 |

| | | |
|------------|--|-----|
| Fig 3.5.5 | A Graphical Representation of the Variation of the La : O Ratio with x. | 151 |
| Fig 3.5.6 | The Variation in Additional Oxygen Atom Content with Cluster size for Holmium. | 153 |
| Fig 3.5.7 | A Plot of the Metal Oxygen Atom Ratio Variation With Cluster Size. | 155 |
| Fig 3.5.8 | A Graphical Representation of the Variation in Additional Oxygen Atom Contents, y, with cluster size, x. | 157 |
| Fig 3.5.9 | The Variation in Cerium : Oxygen Atom Ratio, z, with Cluster Size, x. | 159 |
| Fig 3.5.10 | The Cerium : Oxygen System, $Ce_{32}O_{y..}$ | 161 |
| Fig 3.5.11 | a) The Change in Relative Intensity with Cluster size. | 163 |
| | b) The Change in Additional Oxygen Atom Content with Increasing Cluster Size. | 163 |
| Fig 3.5.12 | A Plot of the Metal : Oxygen Atom Ratio with Cluster Size | 165 |
| Fig 3.5.13 | The Variation in the Number of Additional Oxygen Atoms with Cluster Size for Samarium Clusters | 168 |
| Fig 3.5.14 | The Variation in Metal : Oxygen Atom Ratio with Cluster Size for Samarium Clusters. | 170 |
| Fig 3.6.1 | The Potential Energy Surface for Structure S ₁ with Increasing Cluster Size | 176 |
| Fig 3.6.2 | The Variation in the Potential Energy Surfaces for Structures S ₁ and S ₂ with Increasing Cluster Size, x. | 176 |
| Spec 4.1.1 | The FAB Mass Spectrum for Aqueous Uranyl Nitrate, using Sulpholane matrix. | 181 |
| Fig 4.1.1 | The Variation in Additional Oxygen Atom Content, y, with Increasing Cluster Size, x. | 182 |
| Fig 4.1.2 | The Variation of Uranium : Oxygen Atom Ratio, z, with Cluster Size, x. | 184 |
| Fig 4.1.3 | The Variation in Uranium : Oxygen Atom Ratio, z, with Increasing Numbers of Additional Oxygen Atoms, y. | 185 |
| Fig 4.1.4 | A Graphical Representation of the Variation of the Uranium : Oxygen Atom Ratio, z, with 1/x | 186 |

| | | |
|------------|--|-----|
| Spec 4.2.1 | The CID Spectrum for $[(UO_2)_n O_6]^+$, $m/z = 2256$, Argon Collision Gas, Flexicell at 2KV and 30% Transmittance | 192 |
| Spec 4.2.2 | The CID Spectrum for $[(UO_2)_n O_5]^+$, $m/z = 1970$, Argon Collision Gas, Flexicell at 2KV and 30% Transmittance | 195 |
| Spec 4.2.3 | The CID Spectrum for $[(UO_2)_n O_4]^+$, $m/z = 1684$, Argon Collision Gas, Flexicell at 2KV and 30% Transmittance | 198 |
| Fig 4.2.1 | The CID Spectrum for $[(UO_2)_n O_y]^+$, Argon Collision Gas, Flexicell at 2KV and 30% Transmittance. These Clearly Display the Fragmentation Pattern and daughter Clusters formed and their Relative intensities. | 199 |
| Fig 4.2.2 | The Variation in Daughter Cluster Intensities with Decreasing Cluster size, x , for a Range of collision Gas Pressures | 201 |
| Fig 4.3.1 | A Graphical Representation of the Different fragment Cluster Sequences, x_n , and Their Size Relationship to the Number of additional Oxygen Atoms Present, y . | 206 |
| Fig 4.3.2 | The Variation in the Uranium : oxygen Atom ratio, z , with $1/x$, for the Fragment Clusters Formed During CID | 207 |
| Spec 4.4.1 | The Cluster Spectrum for Thorium | 210 |
| Spec 5.1.2 | FAB Spectrum of Praseodymium Acetate in Glycerol/water | 217 |
| Spec 5.4.1 | Spectrum of Uranyl-Tetraglycine Complex. | 226 |
| Spec 5.5.1 | Mass Spectrum of Uranyl-(α Aminobutanoic Acid) Complex | 231 |
| Spec 5.5.2 | Mass Spectrum of Uranyl-(β Aminobutanoic Acid) Complex | 232 |
| Spec 5.5.3 | Mass Spectrum of Uranyl-(γ Aminobutanoic Acid) Complex | 233 |
| Fig 5.7.1 | The Fragmentation Pattern Observed for the Uranyl-Glycine Species Observed in the Mass Spectra of Tetrakis(Glycine) Uranyl Nitrate | 241 |
| Fig 5.7.2 | The Relative Intensities, with Respect to $[(UO_2)]^+$, $m/z = 270$, for the Various Uranyl-(Amino Acid) Clusters Studied | 242 |
| Spec 5.8.1 | Negative ion FAB Spectrum of UCl_4 in DMSO Matrix | 244 |
| Fig 5.8.1 | Graphical Representation of the Variation in Chlorine Atom Content, n , with Cluster Size, x , for the Most Abundant Clusters in Each Series | 246 |

Fig 5.8.2 Graphical Representation of the Variation of 247
Uranium : Chlorine Atom Ratio, z , with Cluster Size, x ,
for the Most Abundant Clusters in Each Series

Fig 5.8.3 Graphical Representation of the Variation of z 249
with $1/x$, Showing the Crossover Between the two
Cluster Structures at $z = 5$

INTRODUCTION.

1.1 FAST ATOM BOMBARDMENT MASS SPECTROMETRY.

Fast atom bombardment (FAB) mass spectrometry was first described in a brief publication by two research groups from Manchester in 1981 (1)(2). These publications described a new method by which the ionization of labile and non-volatile molecules could be carried out, which were unsuitable for ionization by conventional electron impact (EI) methods.

While EI had been used for about 25 years for the analysis and characterisation of volatile organometallic and inorganic molecules, it had found limited use in the analysis of involatile or thermally labile species of high relative molecular mass (RMM) such as macromolecules, like polymers, proteins and metal cluster compounds. However the use of FAB enables the mass spectra of such molecules to be obtained at high resolution (3)(4)(5).

FAB is referred to as a soft ionizing technique in which 'fast atoms' of noble gases (argon, xenon) with energies of the order of 10 keV are fired at a viscous solution of the sample (3)(5). On impact, the beam causes the sample to undergo a process called sputtering (6) and ion formation takes place either in the sample or in its immediate vicinity. The ions formed are then accelerated and analysed in a conventional mass spectrometer.

1.2 THE PROCESSES INVOLVED IN DESORPTION MASS SPECTROMETRY

Desorption techniques such as FAB, secondary ion mass spectrometry (SIMS) and laser desorption mass spectrometry (LDMS) are all primarily based on the kinetic competition between evaporation and decomposition processes (7). Thus the higher the rate at which energy is supplied to the target molecules, the higher the level of local rapid heating, which promotes evaporation, and hence the lower the extent to which decomposition occurs. (8)

For thermally labile molecules, such as peptides, their volatility is the major limiting factor in their ability to undergo mass spectroscopic analysis. The volatility problem exists primarily because of the thermal instability of such molecules at the energies required for evaporation to take place, which is often greater than the energy needed for thermal decomposition. There are many ways of surmounting this problem; one is the use of field desorption, but most other methods involve the use of rapid heating techniques.

In FAB the time scale of this rapid heating, i.e. 10^{-12} s, is so fast compared with the diffusion coefficient of a typical liquid, i.e. $10 \text{ cm}^2 \text{ s}^{-1}$, (9) that the molecules can be considered as essentially stationary. Consequently over the time periods involved, liquids and solids can be considered to behave identically (10).

The term sputtering is used in FAB to describe the processes taking place in the sample during its bombardment by the neutral atom beam. This process may take place by two main mechanisms (10). The first of these is that of collisional cascade, in which momentum is transferred, via screened coulombic interactions, from the incoming particle to the

target molecule. The target molecule may then undergo further collisions before being sputtered from the sample surface. The primary particle will continue, leaving many recoiling molecules in its penetration track.

In the second process, linear cascade, the recoiling molecule is able to set up further, higher order, recoils in the surrounding sample. Some of these may result in the molecules acquiring sufficient energy to overcome the surface binding energy and hence for sputtering to take place.

After impact with the surface, the primary particle continues into the body of the sample, causing further collisions and transferring momentum to the respective nuclei. This may result in the formation of excited species (11). The collisional cascade resulting within the sample causes displacement, i.e. the recoiling of target molecules along the penetration path of the primary particle. As the cascade progresses, the kinetic energy transferred will decrease, resulting in elevated temperatures (12)(13), with the cascade core reaching temperatures of the order of 10^4K (7)(8)(14). This causes the formation of a high-density, supersaturated, 'hot gas' consisting of target molecules, their fragments and the excited species of these in the primary particle track. These species may then undergo ion-molecule collisions and reactions before their violent expansion into the surrounding vacuum (15)

The depth to which the 'thermal spike' of the collisional cascade reaches depends on the initial energy of the primary bombarding particle. This was shown to have a maximum useful value of approximately 15 to 20 keV, after which the number of ions recorded by

the mass spectrometer decreased (16). This may be due to the major energy-releasing collisions occurring too far below the surface for the extent of ionisation and fragmentation to be detected correctly.

1.3 GAS PHASE CHEMISTRY

FAB-MS has shown itself to be well suited to the characterization, analysis and mass spectral study of a wide range of compounds (20)(21). These include involatile, often polar, organics and bio-organics such as peptides macromolecules, enzymes and other large involatile systems as well as inorganics, organometallics and coordination compounds.

These studies have shown a variety of chemical processes to be induced by the bombardment and subsequent energy deposition. These reactions include

- 1 Sequential ligand loss.
- 2 Redox reactions, in which the central metal atom undergoes either one or a sequence of one electron reductions.
- 3 Ligand fragmentation.
- 4 The formation of matrix adducts and oligomeric species by association reactions between sample molecules themselves and matrix or solvent species.

These processes have been reported for a large number of systems and are clearly demonstrated in the FAB spectra of cyanometallic complexes of various transition metals (17)(18).

The formation of matrix adducts and oligomeric species has been widely reported for a variety of matrices and co-solvents, with Fenton

et al. reporting species containing 2 and 3 magnesium atoms to be formed in the FAB of mixed ligand complexes of magnesium (19).

These reactions have been generally viewed as the result of gas phase association reactions occurring between species present in the sample both before and after bombardment (20)(21) and may result in the formation of gas phase clusters. The formation of clusters in this way has been used in the analysis of a wide range of substances, as diverse as archaeological artifacts (22) and low temperature water-alcohol mixtures (15). The resulting clusters can take several forms, each showing different properties, with the type and mechanism by which the clusters are produced depending on various influences including both the nature of the aggregating moieties and their local environments.

This dependence is readily demonstrated by the various types of clusters formed. For example,

Van der Waals molecules which are held together by virtue of weak electrostatic forces, these clusters are of particular interest in the study of nucleation and condensation phenomena (23). Other notable classes of clusters are small covalent molecules (24), pure metallic clusters (25) and clusters formed by metal salts, of which CsI clusters are classic examples (26).

The association mechanism by which these clusters are formed, however, are not well understood although they have attracted many investigations aimed at gaining insight into the underlying processes occurring in the various desorption methods and their subsequent fragmentations.

1.4 THE ELECTRONIC STRUCTURE OF THE ACTINIDE ELEMENTS

The close proximity of the energy levels of the 7s, 6d and 5f electrons result in the actinides being able to exhibit a wide range of oxidation states, this is markedly so for the early actinide elements. This, along with their hydrolytic behaviour, leads to the mid-actinides, Protactinium to Americium, showing some of the most complex chemical behaviour of all elements.

The oxidation states of the post-curium elements decrease in number and show an increased resemblance to the lanthanides, with the adaption of 3+ as the principal oxidation state. This change in behaviour is a consequence of the actinide contraction with the latter elements corresponding to 5f, 6d inversion.

1.4.1 THE HYDROLYSIS OF THE ACTINIDE ELEMENTS.

The actinides show a richness of aqueous chemistry, due to their wide range of accessible oxidation states, and hence have a tendency to undergo hydrolysis to give oxo- and hydroxo-species. The trivalent oxidation state exists for uranium and heavier actinides in aqueous solutions and becomes increasingly stable with increasing mass. The IV oxidation state is the most important state for thorium and is one of uranium's stable states in aqueous solution. However since the aqueous actinide ions become increasingly acidic in nature with increasing

| Lanthanide series | | Actinide series | | | |
|-------------------|-------------|-----------------|-----------------|---------------------|-------------------------|
| Element atom | $M^{3+}(g)$ | Element atom | $M^{+}(g)$ | $M^{2+}(g)$ | $M^{3+}(g)$ $M^{4+}(g)$ |
| La | 5d 6s2 | Ac | 6d 7s2 | 7s | |
| Ce | 4f 5d 6s2 | Th | 6d2 7s2 | 5f 6d | 5f |
| Pr | 4f 3 6s2 | Pa | 5f2 6d 7s2 | 5f2 7s2 | 5f2 5f |
| Nd | 4f4 6s2 | U | 5f3 6d 7s2 | 5f3 7s2 | 5f3 5f2 |
| Pm | 4f5 6s2 | Np | 5f4 6d 7s2 | 5f5 7s2 | 5f4 5f3 |
| Sm | 4f6 6s2 | Pu | 5f6 7s2 | 5f6 | 5f5 5f4 |
| Eu | 4f7 6s2 | Am | 5f7 7s2 | 5f7 7s | 5f6 5f5 |
| Gd | 4f7 5d 6s2 | Cm | 5f7 6d 7s2 | 5f7 7s2 | 5f7 5f6 |
| Tb | 4f9 6s2 | Bk | 5f9 7s 2 | 5f9 7s | 5f8 5f7 |
| Dy | 4f10 6s2 | Cf | 5f10 7s2 | 5f10 7s | 5f9 5f8 |
| Ho | 4f11 6s2 | Es | 5f11 7s2 | 5f11 7s | 5f10 (5f9) |
| Er | 4f12 6s2 | Fm | 5f12 7s2 | (5f12 7s) (5f12) | (5f11) (5f10) |
| Tm | 4f13 6s2 | Md | (5f13 7s2) | (5f13 7s) (5f13) | (5f12) (5f11) |
| Yb | 4f14 6s2 | No | (5f14 7s2) | (5f14 7s) (5f14) | (5f13) (5f12) |
| Lu | 4f14 5d 6s2 | Lr | (5f14 6d 7s2 | (5f14 7s) (5f14 7s) | (5f14) (5f13) |
| | | or | | | |
| | | | 5f14 7s 2 7p) | | |
| | | Rf | (5f14 6d 2 7s2) | | (5f) |

a predicted configurations in parentheses.

charge on the central metal ions. Th^{IV} and U^{IV} are prone to hydrolysis and the formation of polymeric species.

The actinides in higher oxidation states have a tendency to form actinyl ions, with AnO_2^+ and AnO_2^{2+} corresponding to An^{V} and An^{VI} states respectively. The AnO_2^{2+} ions are formed by U, Np, Pu and Am, while AnO_2^+ by Np, Pu and Am as symmetric linear entities. The An-O bond lengths vary over a wide range of values, depending on the chemical environment provided by the coordination as well as contraction influences and the valence state of the central An^{x+} ion. The bond length for AnO_2^{2+} is notably shorter than the corresponding AnO_2^+ length due to the additional electron being accommodated in a non-bonding orbital.

| | | |
|--------------------|----------------------------------|--------|
| UO_2^+ | average bond length (solution) | 1.76 Å |
| UO_2^{2+} | average bond length (solution) | 1.70 Å |
| UO_2^{2+} | average bond length (solid) | 1.71 Å |

The actinyl ions have an acidic nature, liberating protons in aqueous solution to form hydroxo complexes, this in turn can lead to the subsequent formation of poly-nuclear species containing hydroxo- (An-OH-An) or oxo- (An-O-An) linkage. The formation of such species is pH dependant as demonstrated by the uranyl ion.

The tendency to form large polymeric species drops significantly from An^{IV} to An^{VI} , with only small higher order An^{IV} species being formed.

1.4.2 THE URANYL ION (electronic structure)

The strongly linear uranyl, UO_2^{2+} , ions exists as a single charged entity, of a unique stability that distinguishes it both from other group VI elements and actinides. The stability of the uranyl ion is a result of its valence electrons occupying bonding molecular orbitals, with the non-bonding and anti-bonding orbitals remaining empty.

The pentavalent uranium ion forms UO_2 in aqueous solution. This is highly unstable and disproportionates to UO_2^{2+} and U^{4+} . The VO_2^+ ion is only stable over a very narrow pH range near pH2, where its rate of disproportionation is negligible. The UO_2 ions instability is a consequence of the additional electron residing in an antibonding molecular orbital. (27)

The UO_2^+ ion has a bent conformation like related oxo-cations, VO_2^+ , MoO_2^{2+} , WO_2^{2+} and ThO_2 , and has an average bond length of 1.76 Å.

The UO_2^{2+} ion is always observed with a formal $5f^0$, $6d^0$ valence configuration in crystals and complexes with a trans geometry, having 4 to 6 secondary coordinations in its equatorial plane, perpendicular to its O=U=O axis. This is in marked contrast to other isoelectronic species (MoO_2^{2+} , WO_2^{2+} , VO_2^+) which have a related d^0 valence configuration, which usually occur in octahedral ligand sets.

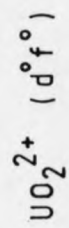
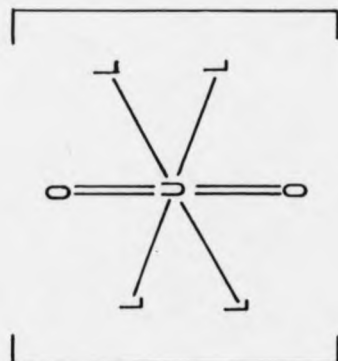
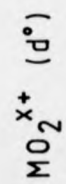
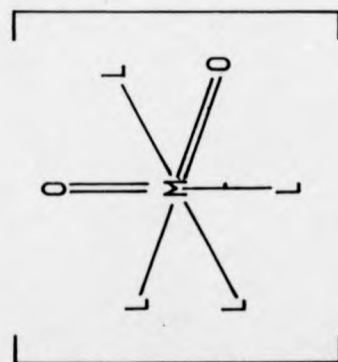


Fig 1.4.1 The Coordination Geometries of Isoelectric Dioxometal Ions

These species however, all exhibit similar properties such as short M-O bond lengths and labile coordination geometries. So the geometrical preferences of these species can be assumed to be dictated by the central metal ion, not the auxiliary ligands, although the M-O bond length is influenced by their resulting environment.

The only major differences between the species is the presence of the 5f orbitals in UO_2^{2+} . For MoO_2^{2+} a strong minimum is observed in the d, s, p potential curves in the region of $\text{O-M-O} \approx 110^\circ$, this is in agreement with crystal data.

These geometries are further stabilised by the use of 4d orbitals in π bonding with oxygen lone pairs.

For the UO_2^{2+} , although d, s, p sets are similar to the above but well defined, the 5f orbitals do not favour a bent geometry. This effect is enhanced by the influence of the inner shell unfilled 6p orbitals. Since the 6p orbitals cause the σ_{L}^+ orbital to be pushed up, increasing the $\text{O}(2p\sigma)-\text{U}(5f\sigma)$ overlap.

The position of these molecular orbitals are dependent on the external environment experienced by the central oxo-metal cation, this is clearly shown by isoelectric ThO_2 . ThO_2 is linear for shorter bond lengths, but as they increase the 5f/6d energy gap becomes greater and ThO_2 assumes a bent geometry. In the case of the UO_2^{2+} ion linearity is seen at all bond distances due to a smaller 6d/5f energy gap and the interactions with the 6p core. The effect of bond length on electronic

structure has been calculated by Tatsumi et al. using the extended Huckel theory (28)(29).

1.4.4 THE URANYL ION (aqueous chemistry)

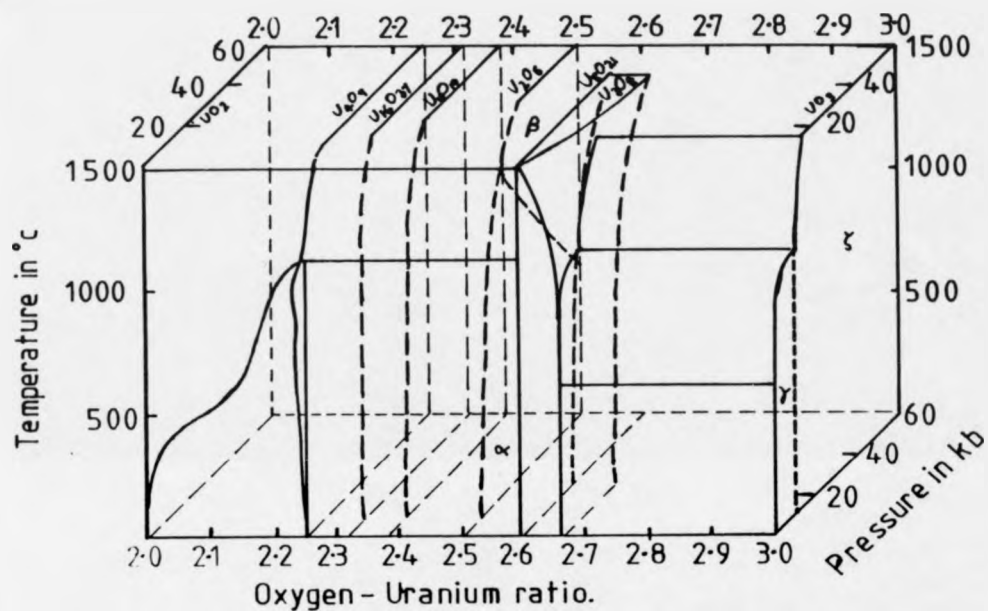
The uranyl ion (UO_2^{2+}) is very stable and is found in both solid and aqueous solutions. In aqueous solution it is seen to be acidic in nature and has a tendency to undergo hydrolysis and form polymeric species. The extent to which this hydration takes place is dependent on both uranyl concentration and the pH of the solution. This is shown by the preferential formation of the $(\text{UO}_2)_2(\text{OH})_2^{2+}$ dimer, with UO_2OH^+ being formed only in very weak uranyl solutions.

At higher pH's the trimer $(\text{UO}_2)_3(\text{OH})_6^+$ becomes predominant, with larger polymeric species being reported as the pH of the solution increases. These species are $(\text{UO}_2)_3(\text{OH})_4^{2+}$, $(\text{UO}_2)_4(\text{OH})_6^{2+}$, $(\text{UO}_2)_4(\text{OH})_7^+$, $(\text{UO}_2)_5(\text{OH})_8^{2+}$ and $(\text{UO}_2)_5(\text{OH})_9^{2+}$ being reported (30)(31).

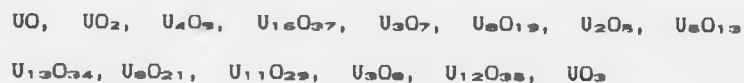
At very high pH values precipitates of hydrous oxides and hydroxides are formed. Similar behaviour is also seen for Np and Pu.

1.5 THE URANIUM-OXYGEN SYSTEM

The uranium-oxygen system is the most complex of the actinide oxide systems and one of the most complex systems known. The uranium-oxygen system contains various phases consisting of stoichiometric and non-



stoichiometric forms, with uranium : oxygen ratios being observed between 1 : 1 and 1 : 3. The simple binary oxides so far reported are in increasing U : O ratios;



in addition to the above there have also been several crystal modifications for most of these reported.

The ability to exhibit such a large range of oxides is a consequence of uranium's variability of valency and its ability to form compounds in which it simultaneously exhibits more than one valence state.

The way in which its vast array of oxides are formed are best understood by the consideration of the UO_2 fluorite structure (face centred cubic). This fluorite structure has a open nature which allows the accommodation of additional oxygen atoms in the interstitial holes. This leads to continuously increasing distortion to the original fluorite lattice

The distribution of these additional oxygen atoms can take a random form, resulting in a lattice of variable structure, stoichiometry and density. However if the oxygen atoms assume an ordered distribution then the formation of cubic, tetragonal or monoclinic superlattices based on the fluorite structure takes place. When a given number of additional oxygen atoms have been accommodated within the lattice the

stoichiometric limit is reached and at least some of these oxygen atoms become ordered in a superlattice providing a new phase. This behaviour continues via various phases until the uranium : oxygen ratio reaches approximately

1 : 2.4, when an abrupt density change occurs, with the crystal lattice adopting a lower density form. In these lower density phases the bonding is dominated by uranyl-type moieties, for at least some of the oxygen atoms present, with the uranium coordination showing the presence of two shortened co-linear bonds (32).

1.5.1 THE URANIUM - URANIUM DIOXIDE REGION

The phases in the U - UO_2 region exist at elevated temperatures mainly, with oxygen becoming increasingly soluble in uranium metal as the temperature increases up to 2425°C (33)(34). From this temperature, changes in temperature result in the stoichiometry of the solid UO_{2-x} phase decreasing so that below 300°C x is effectively zero.

1.5.2 THE UO_2 - $\text{UO}_{2.25}$ REGION

UO_2 at 25°C has a fluorite type structure, allowing oxygen vibrations in to its four surrounding interstices. As the temperature increases the motion becomes increasingly anharmonic in nature. This effectively shifts the oxygen atoms centre of vibration and leads to the formation of different types of sites for oxygen addition (35)(36).

Excess oxygen can hence be accommodated into the crystal lattice without long range deformation of the fluorite structure. This behaviour is often accompanied by increases in the valence states of some of the uranium atoms. The above continues beyond the homogeneity range and at a given temperature the $U_4O_9-\gamma$ phase is formed. In this unstable phase the cubic structure, although having larger lattice parameters, is essentially the same as for UO_{2+x} apart from the occurrence of long range ordering of the oxygen defect zones, leading to the production of a superlattice in regions (37).

1.5.3 THE $UO_{2.25} - U_3O_8-x$ REGION, (Fig. 1.5.1)

The uranium system between $U_4O_9-\gamma$, ($UO_{2.245}$), and U_3O_8 , ($UO_{2.67}$) is very complex. Hoekstra et al. provided a great deal of help to clarify the phases of this region by a series of high pressure experiments, even though such elevated pressures and temperatures can effect the stability of phases favouring denser conformations (6)(12). Hoekstra et al. proposed that the fluorite-type phases also included $U_{16}O_{37}$, ($UO_{2.31}$); U_6O_{13} , ($UO_{2.37}$); and β - and γ - U_2O_5 , ($UO_{2.5}$) as well as several U_2O_5 related higher oxides reported.

α - U_2O_5 has a predominantly uranyl type nature and is stable upto 800°C and low pressures, at higher pressures α - U_2O_5 transforms into β - U_2O_5 which has a hexagonal fluorite type configuration.

At higher pressures this again undergoes a crystal modification in to monoclinic γ - U_2O_5 . These three forms of U_2O_5 correspond to the

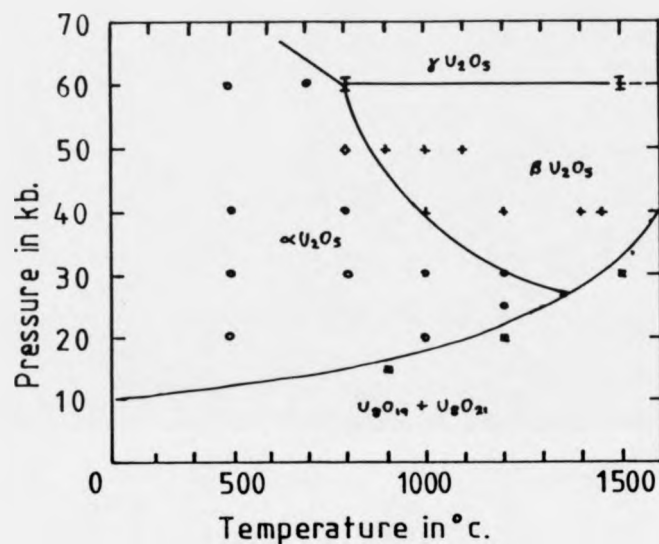


Fig 1.5.2 The Pressure - Temperature Phase Relationships At U_2O_5

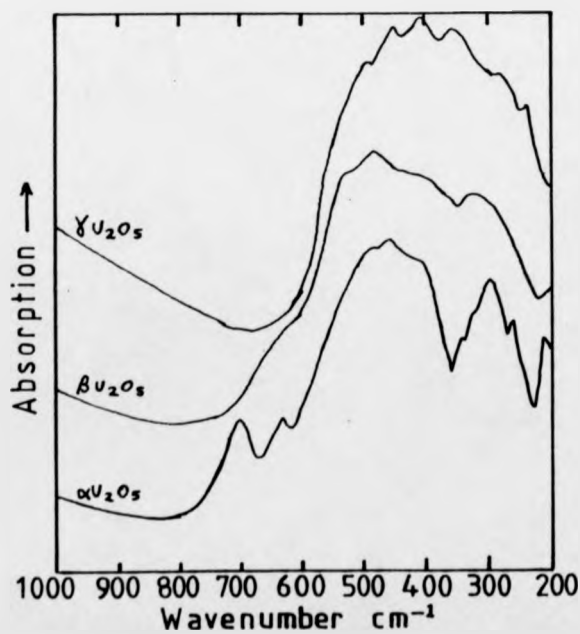


Fig 1.5.3 The I.R. Spectra of U_2O_5 Phases

uranyl / fluorite crossover region, this is shown by their i.r. spectra. These show the gradual elimination of group vibrations in the uranyl region and the assimilation of various stretching and bending modes into a single broad band of a fluorite type structure (32).

1.5.4 THE U_3O_8-x - UO_2 REGION

In this region UO_2 appears in six possible polymorphs and a seventh at high pressure. The first of these α - UO_2 is hexagonal and has a density of 7.3 g/cm^3 , which is notably less than the calculated value of 8.4 g/cm^3 . This discrepancy is due to shortened U-O bond lengths causing lattice deformation, with the i.r. spectrum showing evidence of uranyl type characteristics (39)(40). The β - and γ - UO_2 forms consist of UO_6 octahedra, sharing edges and corners, in a three dimensional network. These again show slight evidence of uranyl type bonding (41)(42).

γ - UO_2 however, formed in air at 415°C , has a cubic ReO_3 type structure containing no evidence of uranyl type bonding (43).

In the case of the high pressure form of uranium trioxide, ζ - UO_3 , which forms pentagonal bipyramidal structures, there is notable uranyl type bond formation with a colinear O-U-O axial group with a five membered puckered ring around its equatorial region. The U-O uranyl bond length is 1.83\AA , which is comparable with other known uranyl bond lengths (44).

| Compound | Symmetry | a | b | c | L ^e | Z | Density(g cm. ⁻³) |
|---|----------|------------|--------|-------|-------------------------|----|-------------------------------|
| U O ₂ | Cubic | 5.4704 | | | | 4 | 10.97 |
| U ₄ O ₉ | Cubic | 5.4441(x4) | | | | 64 | 11.31 |
| U ₁₆ O ₃₇ | Tetr. | 5.41 | | 5.49 | | | 11.37 |
| U ₃ O ₇ | Tetr. | 5.46 | | 5.40 | | | 11.35 |
| U ₈ O ₁₉ | Monocl. | 5.378 | 5.559 | 5.378 | 90.29 | | 11.42 |
| U ₂ O ₅ | Hexag. | 3.885 | | 4.082 | | | 8.65 |
| U ₈ O ₂₁ | Orth. | 6.751 | 3.176 | 8.286 | | 4 | 8.37 |
| ^α -U ₃ O ₈ | Orth. | 6.716 | 11.931 | 4.144 | | 2 | 8.43 |
| ^β -U ₃ O ₈ | Orth. | 7.05 | 11.42 | 8.29 | | 4 | 8.38 |
| U ₂₁ O ₃₅ | Orth. | 6.91 | 3.92 | 4.16 | | | 8.41 |
| ^α -UO ₃ | Hexag. | 3.971 | | 4.17 | | 1 | 8.34 |
| ^β -UO ₃ | Monocl. | 10.34 | 14.33 | 3.91 | 99.03 | 4 | 8.30 |
| ^γ -UO ₃ | Orth. | 9.71 | 9.77 | 19.92 | | 32 | 8.02 |
| ^δ -UO ₃ | Cubic | 4.16 | | | | 1 | 6.67 |
| ^ε -UO ₃ | Tricl. | 4.002 | 3.841 | 4.165 | 98.10; 90.20; 120.17 | | 8.73 |
| ^ζ -UO ₃ | Orth. | 7.511 | 5.466 | 5.224 | | 4 | 8.86 |

The crystal data for uranium oxides.

The existence of uranyl type bonding in the above lower density forms of the uranium-oxygen system, even in high pressure modifications, shows the unique stability of the uranyl configuration over a vast array of conditions. This is again shown in the uranium trioxide / water system, which contains another extensive series of phases and crystal modifications. These can on the whole be best regarded as uranyl hydroxides, for example $\text{UO}_3 \cdot \text{H}_2\text{O}$, $\text{UO}_2(\text{OH})_2$ (45).

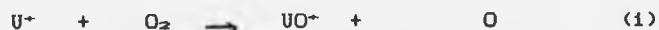
Thorium dioxide, ThO_2 , also has a fluorite structure but does not show an extensive oxide system like uranium. The actinides directly after uranium, Np and Pu, however do form large oxide systems as a consequence of the 5f / 6d valence shell crossover occurring in this region of the actinides. In addition to the above binary oxides and complexes, uranium also forms many uranates and polyuranates in which uranyl group formation predominates, with various levels of equatorial coordination (46).

1.6 THE GAS PHASE CHEMISTRY OF URANIUM

The gas phase chemistry of uranium, both in its ionic and atomic forms, has attracted interest due to its importance in the nuclear industry and other applications.

The reactions of uranium ions and atoms with O_2 , CO , N_2 , D_2 , H_2 , CD_4 , CO_2 , COS , CS_2 , H_2S and D_2O have been studied (47)(48)(49).

For oxygen the reaction is found to yield various uranium-oxygen compounds,

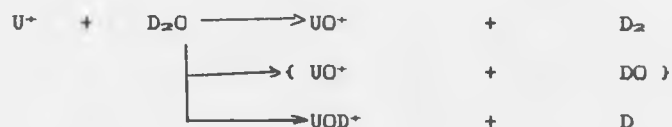


both these reactions are exothermic and reaction (1) was observed to yield small amounts of UO_2^+ which may be due to a low energy reaction pathway (50). The reactions involving D_2 , H_2 and N_2 followed the general pathway,



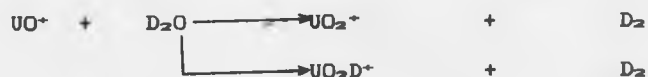
with similar results also being observed for CD_4 .

D₂O, H₂O and H₂ were also observed to react with similar character,

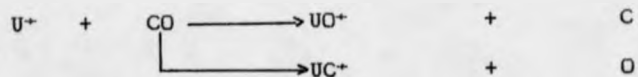


and it is suggested that these reactions proceed via an intermediate 'DU⁺OD'. Since the UO⁺ product dominates at lower energies, this pathway is preferred thermodynamically, while bond fission in UOD⁺ has a high frequency. At higher energies UOD⁺ is formed directly and its yield is found to increase.

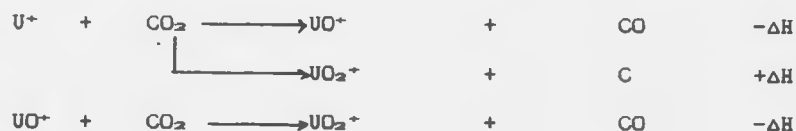
Further reactions also occur with increasing energy



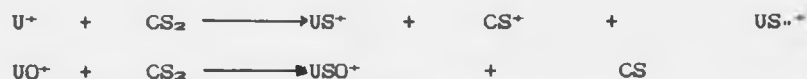
both these reactions are exothermic but the occurrence of the latter of these increases with energy. For CO the reaction is endothermic, having a notable energy threshold, resulting in,



The CO_2 reaction was found to form UO_2^+ by a single bimolecular encounter and occurs at the dissociation threshold for $\text{UO}^+ + \text{O} + \text{C}$.



While with CS_2 the exothermic reactions were found to yield



In the reactions with COS



Although the formation of US^+ is thermodynamically favoured over UO^+ due to the permanent dipole present in US^+ , the reaction proceeds by a energy dependent branching ratio. The dissociation energy for US^+ is approximately half that of UO^+ . Hence at higher energies UO^+ is preferentially formed.

The gas phase reactions of uranium clusters with different gases have also been studied. Devienne et al. investigated the reactions of

O_2 , N_2 and H_2 on the cluster formation of uranium, niobium and tantalum by high energy molecular bombardment (51). The cluster yields were seen to increase with increasing mass of the bombarding species.

In the presence of O_2 a slight decrease in the higher mass clusters was observed, for all three metals, with the latter two being observed to form a number of oxides. The reactions of N_2 with uranium formed $U_pM_q^+$ species, where $q \leq p + 1$, while niobium and tantalum only formed M_pN^+ and $M_pN_2^+$ species. In the reaction concerning H_2 and D_2 , however very few species were detected.

The CID of UO^+ and UO_2^+ , using argon collision gas, showed both species to fragment by the loss of oxygen atoms. In both cases the dissociations have thresholds in the region of that of the bond being broken. For UO_2^+ the absolute cross section is approximately twice that for UO^+ , suggesting that the dissociative collision occurs via the oxygen atoms (52).

Recently fast atom bombardment mass spectrometry has been used to form numerous uranium-oxygen clusters (53). Similar clusters have since been described by Brown et al. in the mass spectral study of metal hydroximates (54).

1.7 BONDING MODELS FOR CLUSTERS

In the early experiments it was shown that sodium clusters exhibit distinct 'Magic numbers', M_n , indicating nuclearities with high stabilities relative to adjacent clusters. These observations were rationalized by the use of the spherical Jellium model, a simple one electron model (55).

Such studies have since been extended to cover a wide range of cluster types and units, and have been used to explain a number of spectral effects and size dependent phenomena.

1.7.1 THE SPHERICAL JELLIUM MODEL

The simplest model is that proposed by Knight et al. which successfully predicted the magic number positions for alkali and related metals by associating these nuclearities with closed-shell electron counts. This model postulates that the electronic structure of free electron metal clusters may be approximately described by considering only the energies of the valence electrons, without specific information about the positions of the atomic cores. This was carried out by the use of a central field potential of the form,

$$V_0(r) = -U_0 \left\{ \exp \left(\frac{r - r_0}{\epsilon} \right) + 1 \right\}$$

where U_0 is the sum of the Fermi energy and the work function of the bulk metal and r_0 is the effective radius of the cluster sphere, assumed to be $r_0 = r_s N^{1/3}$ and r_s is the radius of a sphere containing one electron in the bulk metal and $\epsilon = 1.5$ au, with the Schrodinger equation being solved for each value of N .

This yields a series of discrete energy levels characterised by their angular momentum quantum numbers. These resulting energy levels are seen to order in the following way:

| | 1s | < 1p | < 1d | < 2s | < 1f | < 2p | < 1g | < 2d | < 3s | < 1h |
|--------------------------------|----|------|------|------|------|------|------|------|------|------|
| Number of associated electrons | 2 | 6 | 10 | 2 | 14 | 6 | 18 | 10 | 2 | 22 |
| Total number of electrons | 2 | 8 | 18 | 20 | 34 | 40 | 58 | 68 | 70 | 92 |

and are consistent with experimental magic number values.

The differences in the level orderings from that of the hydrogen-like atom are due to a number of factors, with the major of these being that the hydrogen-like potential is infinite at its origin and slowly decreases with distance ($1/r$), whereas in the Jellium model, the potential is essentially flat out to its outer spherical boundaries and is modeled as a rounded finite square well.

Although the spherical Jellium model has shown itself to be useful in explaining the positions of magic numbers, it does have many drawbacks. These include predictions of ionization energies, which are seen to be incorrect and it does not make accurate predictions of the

electronic structures of non-magic number clusters. This is a consequence of these clusters giving rise to distortions of the spherical potential, resulting in the splitting of the high degeneracy of the spherically symmetrical well.

Various extensions to the spherical Jellium model have been made in order to overcome these inaccuracies (56)(57). The most important of these involved the consideration of electron-electron interactions (58) and the removal of spherical symmetry restrictions. In the latter of these Clemenger used a perturbed harmonic oscillator model and its extensions to oblate and prolate shaped potential wells (59).

1.7.2 THE STRUCTURED JELLIUM MODEL

In this extension of the simple spherical Jellium model, the movement of an independent electron is considered in a coulombic potential, resulting from a series of point like atomic cores, of effective charge z and position x . This gives rise to a potential $V(r)$, which can be expressed using spherical harmonics (59)(61)(62),

$$V(r) = \sum_{L=0}^{\infty} \sum_{M=-L}^{+L} V_L(r, \theta, \phi)$$

where M and L are angular momentum quantum numbers.

From this it is possible to calculate the energy level structure of the resulting potential, by taking the spherical component ($L = 0$) to be the zero order potential and treating the remainder as a

perturbation. This gives the splitting patterns of the individual shells (n, l) and allows predictions as to their shape to be made.

When the spherical components are dominant, magic number shell structures are obtained. The non-spherical part of the potential however lifts the degeneracy of the shells, with the resulting splitting being dependent on the cluster shape and the effective charge on the core. The latter of these tends to decrease in importance as the cluster size increases. The extent to which splitting occurs is very strongly influenced by cluster shape, however, with prolate and oblate geometries giving rise to specific forms of distortion. The extent to which these distortions occur, and the type of geometry adopted, are dependent on the number of electrons occupying cluster orbitals. Clusters of intermediate electron numbers more favourably assume geometries that enhance their prolate/oblate character in order to increase their LUMO-HOMO gap.

1.7.3 THE LINEAR COMBINATION OF ATOMIC ORBITALS MODEL

In this model approximations for solutions of the electrostatic Schrodinger wave equation are made using spherical harmonics, relative to their radial vectors (64).

That is, for a local coordinate system, such that the 'z' axis is along a radius vector from the cluster centre, then σ orbitals (s, p_z, d_{z^2}) can be viewed as cylindrically symmetrical harmonics Y_L^M by setting the coefficient of each atomic orbital equal to the value of Y_L^M

at the core positions. The resulting symmetry adopted cluster orbitals, L_n^* , provide a framework by which the closed shell requirements and structural aspects of ligated clusters may be described.

For clusters where bonding is only due to 's' orbitals both the LCAO approach and the Jellium model give the same energy level pattern. For example, the Jellium model and LCAO model give identical conclusions for alkali metal clusters, with shell closure occurring at 2, 8, and 20 electrons. These correspond to spherical topologies, being more stable than their neighbours, and would be expected to have higher ionization energies and pseudospherical close packed structures of high symmetry (65).

The level of symmetry adopted by a cluster is dependent on its nuclearity 'n' and in turn influences its stability, with non-symmetrical structures leading to splitting of the energy levels and an inherent instability.

This is demonstrated by neutral sodium clusters, which exhibit magic numbers at $M_n = 2, 8, 20, 40, 58, \dots$ but not at 18, 34, 68, \dots which also correspond to closed shell configurations for the Jellium model. This is due to the higher symmetry of the former, with similar phenomena being reported for silver, gold and copper clusters (66).

The influence of symmetry on stability can be considered according to molecular orbital theory as explained above and is supported by ab-initio and Huckel theory calculations. (67)

1.8 MODELS FOR MAIN GROUP TRANSITION METAL CLUSTERS.

Clusters from main group elements and transition metals have long been known to show strong relationships between structure and the number of skeletal electrons present. This correlation is clearly expressed by boranes and carboranes. (60) (68) (69) (70)

1.8.1 THE TENSOR SURFACE HARMONIC MODEL.

The Jellium model is seen to fail when the electronic structure of the cluster can no longer be regarded as a perturbation of a spherical shell model, that is, the contribution from the non-spherical part of the potential is large. This has been seen to be the case for large effective nuclear charges, nuclearities or for shells with large angular momenta.

So the Jellium model can be expected to fail for clusters containing large numbers of valence electrons per atom, especially for small clusters of these atoms.

Hence, with certain exceptions the Jellium model can be expected to fail for p-block elements and the transition metals.

The reasons for this was highlighted by the LCAO approach and are overcome in the TENSOR SURFACE HARMONIC theory (TSH) described by Stone, which considers the contributions from σ , π , and δ orbitals. (64) (71) (72)

The tensor surface harmonic theory demonstrates the basic differences in the electronic structures of the main group and transition metal clusters from those of free electron metals, with approximate linear combinations of atomic orbitals being formed using the eigen functions for the particle on a sphere problem (ie spherical harmonics) and tensor surface harmonics.

In the TSH model the cluster is treated as a sphere, with angular momentum quantum numbers L and M, as in an atom, and also classified by parity.

Each cluster atom is classified by its basis functions into σ , π and δ orbitals, having 0, 1 and 2 nodal planes respectively, each containing a radius vector from the cluster centre.

Cluster orbitals are formed from the σ basis function by using the values of spherical harmonics evaluated at the cluster vertices as expansion coefficients. Hence the cluster orbital is a linear combination of the form:

$$\psi_{LM}^{\sigma} = \sum_i Y_{LM}(\theta_i, \phi_i) \sigma_i$$

where (θ_i, ϕ_i) are the spherical coordinates of cluster atom i. ψ_{LM}^{σ} sets with $L=0, 1, 2, \dots$ are denoted by $S^{\sigma}, P^{\sigma}, D^{\sigma}, \dots$, while a whole set is denoted by L^{σ} . For real clusters these denote symmetry

classifications. Molecular orbitals expressed by ψ_{LM} are not seen to undergo strong mixing.

For π orbitals, p_x and p_y orbitals are seen to be tangential to the spherical surface and hence their magnitude and direction (θ , ϕ) to the wave function can be described as to sets of vector surface harmonics, V_{LM} and \overline{V}_{LM} . These vector sets are always at right angles to each other

$$\begin{aligned} V_{LM} &= \Delta Y_{LM} \\ \overline{V}_{LM} &= \mathbf{r} \times V_{LM} = \mathbf{r} \times \Delta Y_{LM} \end{aligned}$$

Therefore, for each value of Y_{LM} , two vector functions can be obtained. V_{LM} is a polar vector surface harmonic and is given by the gradient of the spherical harmonic while \overline{V}_{LM} is an axial vector surface harmonic and is the cross product of the position vector and V_{LM} . The direction and magnitude of V_{LM} at the cluster atom i is used to give the magnitude and direction of a π orbital contribution to a π type cluster orbital ψ_{LM} with the same parity as Y_{LM} . While \overline{V}_{LM} yields a cluster orbital $\overline{\psi}_{LM}$ of the opposite parity to the parent.

However there are no s cluster orbitals, $L = 0$, since Y_{00} is constant, but P^+/P^- and D^+/D^- cluster pairs do exist and are generally denoted by L^+ and \overline{L}^+ . These sets show a pairing relationship, with each being obtainable from the other via 90° rotations about their radius vectors. This pairing operation also seems to convert bonding interactions into antibonding ones, with L^+ and \overline{L}^+ orbitals describing

these respectively. The bonding sets usually consist of L^+ , with combinations of L^+ and the strongly bonding S^+ orbitals.

V_{LM} and $\overline{V_{LM}}$ are parity related with V_{LM} being bonding and $\overline{V_{LM}}$ antibonding. This parity relationship means that under inversion of these bonding/ antibonding orbitals there are limits to which mixing can take place.

The L^+ and L^- orbitals of the same L and M values can mix with each other but not $\overline{L^-}$. For most main group clusters L^+ will be antibonding for all orbitals except S^+ . L^+ and L^- orbitals can undergo mixing to produce one bonding and one antibonding contribution, resulting in changes in the energy level ordering among the bonding orbitals. (20)

In transition metal cluster bonding contributions for σ , π and δ atomic orbitals must be considered. These are handled by the use of the second order derivatives of V_{LM} , giving two polar vectors of the same parity, and one axial vector of opposite parity. These are parity related.

1.8.2 POLYHEDRAL SKELETAL ELECTRON PAIR THEORY, (PSEPT).

This is a combination of TSH, the associated electron counting rules and the use of the isobal analogy as well as orbital calculations.

This theory relates the number of electron pairs involved in skeletal bonding to the polyhedral geometry, and is characterised by three basic rules.

- i) Main group and transition metal ring compounds have a total of $6n$ and $16n$ valence electrons respectively.
- ii) Main group and transition metals in three connected cluster compounds have $5n$ and $15n$ valence electrons respectively.
- iii) If a transition metal atom occupying a vertex position is replaced by a main group atom, then the characteristic number of valence electrons is reduced by 10.

1.8.3 THE APPLICATION OF PSEPT TO GAS PHASE TRANSITION METAL CLUSTERS.

PSEPT was developed to account for the observed structures of condensed phase, ligated clusters, with transition metal clusters of this type being predominately closed shell, diamagnetic species, with their narrow band of d-orbitals being completely filled.

Base transition metal clusters are generally open shell and have partially filled d-bonds. This results in a subtle interaction between coulombic repulsion and exchange forces making an accurate description of the electronic structure often unobtainable (73)(74).

One area in which PSEPT has shown itself to have important applications is that of ligated gas phase clustering, as shown by its role in the description of the electronic structure of a variety of transition metal carbonyls (75) (76) (77).

1.9 MAJOR CLUSTER CLASSES

1.9.1 RARE GAS CLUSTERS.

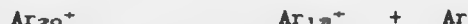
Rare gas clusters were the first atomic clusters to be produced by, neat, free-jet expansions and as a consequence of the relative ease by which they can be formed they have been subjected to a vast array of experimental and theoretical investigations. These investigations have encompassed the precise measurement of cluster growth patterns (78), the determination of thermodynamic cross sections (79) and scattering fragmentation studies (80).

In 1981 Echt et al. reported the presence of a magic number pattern that in the cluster spectrum of $(\text{Xe})_n^+$ coincided exactly with the numbers predicted by the icosohedral spheres described by McKay (81). It was also noted that the ratios of neighbouring peaks remain approximately constant and clearly denote the stability of the neutral cluster. Despite minor differences among the Ar, Kr and Xe series, similar sequences of magic numbers are clearly displayed (82).

| | | | | | | |
|--------------------|----|-------|-----|-----|-----|-----|
| Shell number | 1 | 2 | 3 | 4 | 5 | 6 |
| Icosohedral number | 13 | 55 | 147 | 309 | 561 | 923 |
| Ne | 14 | 55/56 | | | | |
| Ar | 14 | | 148 | 309 | 561 | 923 |
| Kr | 13 | | 147 | 309 | 561 | 923 |
| Xe | 13 | 55 | 147 | 309 | 561 | 923 |

The presence of these predominant magic numbers, the associated spectral fine structure and their agreement with similar structures in the spectra of a number of van der Waals cluster series is a very important source of information about the electronic and geometrical structures of such clusters.

Studies on the decay patterns of these clusters have provided a sensitive probe by which to study their dynamic and structural characteristics. In many cases the results of such studies reflect the development of shell structures, with an unstable cluster undergoing dissociation to attain a more stable atom combination, that often coincides with complete shell icosahedra. Unimolecular dissociation studies on argon clusters carried out by Stace et al. and Mark et al. (82)(83) showed



to produce a very intense fragment ion. It was suggested that the Ar_{19}^+ cluster consisted of a Ar_2^+ dimer enclosed within a seventeen argon atom icosahedra shell. Similar results were also reported with clusters undergoing fragmentation by the sequential loss of two neutral argon atoms (85).

This is further supported by studies of a number of higher nuclearity clusters and computer models. Simulations using Lennard-Jones clusters have shown icosahedral packing to be of the lowest energy, particularly for smaller clusters, and after the completion of

the first icosahedral shell the construction of the next outershell is localised as opposed to the sequential addition to all faces symmetrically (86).

Studies have also been carried out, using quantum mechanical computations, on the energy levels and wavefunctions of small rare gas clusters (87).

1.9.2 AMMONIA CLUSTERS

Studies carried out on ammonia cluster ions show them to undergo a variety of ion-molecular reactions upon ionization. In the cluster spectra ions cluster to exhibit smoothly diminishing intensities with protonated pentamer being the only strongly reproducible magic number observed.

The ammonia clusters show evidence of dissociation and extensive cluster reorientation following ionization, for example, the protonated monomer is seen to lose up to six monomer units of which at least two are lost as a result of direct unimolecular evaporative dissociation. This is true for all ammonia clusters, with the protonated pentamer exhibiting an abnormally high intensity (88).

The intra-cluster ion-molecular reaction that leads to the formation of the stable ammonium (NH_4^+) cation, with the prompt ejection of NH_2 , results in the heating of the cluster and evaporative dissociation. In addition to the large energy of proton transfer reaction a small

amount of excess energy will also be generated during cluster relaxation and reorientation about the newly formed ion (89).

Fragmentation studies have shown the binding energies of the resultant cluster ions to decrease with increasing cluster size, with abnormally high values being displayed by the $\text{NH}_4^+(\text{NH}_3)_4$ species. A similar local maximum is also seen for the $\text{NH}_4^+(\text{NH}_3)_{11}$ cluster (90)(91).

The enhanced stability of the $\text{NH}_4^+(\text{NH}_3)_4$ pentamer is due to four ammonia monomers coordinating onto the hydrogens of the central ammonium ion, constituting a closed solvation ring around the central $(\text{NH}_4)^+$ ion. So the enhanced stability observed is a result of the cluster ion's structure and not that of the neutral.

1.9.3 METHANOL CLUSTERS

Upon ionization methanol clusters undergo ion-molecule reactions leading to the production of protonated clusters. These subsequently undergo proton transfer reactions followed by a number of evaporative dissociations. The rates of these dissociations decrease with time after the ionization event and increase with cluster size. This is in agreement with the behaviour of ammonia clusters. The proton transfer reactions display size dependant reactivities, with only the resulting cluster ion being observed (92).



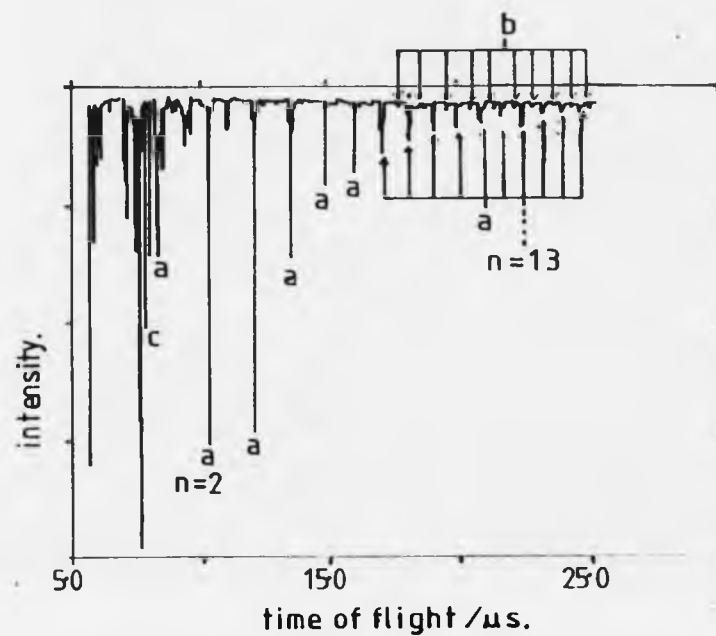
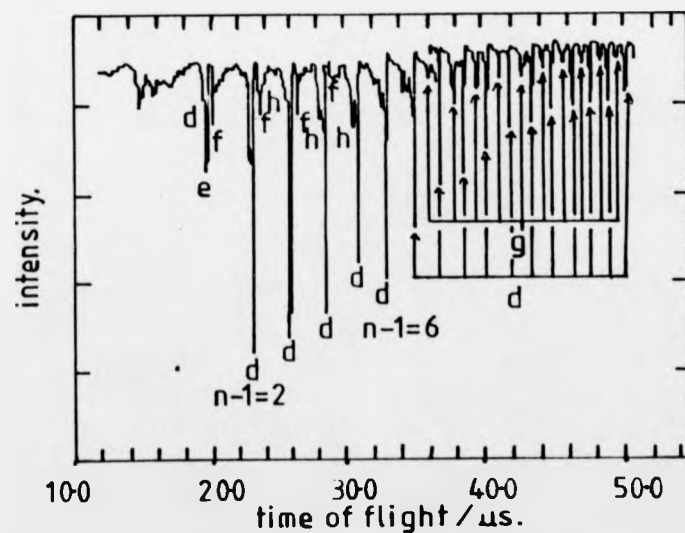


Fig 1.9.1 a) The Conventional TOF Spectrum of $H^+(CH_3OH)_N$,
Laser $\lambda=266nm$



b) The Daughter Ion TOF Spectrum of $H^+(CH_3OH)_{N-1}$,
Laser $\lambda=266nm$

The protonated trimer $H^+(CH_3OH)_3$, a, shows a increased intensity in agreement with structural calculations.

Methanol cluster ions, $H^+(CH_3OH)_n$ also undergo several other intra-cluster reactions, whose rates are dependant on cluster size (93).

This is clearly demonstrated by the reaction resulting in the formation of the $H^+(H_2O)(CH_3OH)_n$, b, cluster series, that only appear at $n \geq 7$. This sequence of clusters is envisaged to be formed by the reaction,



Fragmentation studies of these clusters show the presence of several series of daughter ions. The main series of these corresponds to the loss of neutral monomer units, with the loss of up to five monomers being lost from the protonated octamer.

Another important reaction involves the loss of water from the protonated dimer,



This reaction requires an induction time, due to rearrangement, and is not observed for higher order clusters (94)(95). This is due to the competition between several reaction pathways. In larger clusters, H_2O^+

is more strongly solvated and the loss of the protonated dimethyl ether, $(\text{CH}_3)_2\text{OH}^+$, occurs more readily and leads to the production of $\text{H}^+(\text{H}_2\text{O})(\text{CH}_3\text{OH})_n$. The rates of $(\text{CH}_3)_2\text{O}$ elimination increases with cluster size, as a result of solvation effects and has been reported for other alcohols (96)(97)(98).

1.9.4 ACETONE CLUSTERS

Tzeng et al. have carried out a comprehensive study of the reactions of acetone clusters (99). The major cluster ions observed are,

| | |
|--|--------------|
| $[(\text{CH}_3)_2\text{CO}]_m\text{H}^+$ | $m = 1 - 5$ |
| $[(\text{CH}_3)_2\text{CO}]_m\text{CH}_3^+$ | $m = 1 - 10$ |
| $[(\text{CH}_3)_2\text{CO}]_m\text{C}_2\text{H}_5\text{O}^+$ | $m = 1 - 17$ |

The nature of these clusters was shown to be due to monomer fragmentation during ionization, followed by the loss of one acetone unit by unimolecular decomposition.

Many other ion-molecule reactions have been reported (100)(101). These reactions are similar to those of ammonia and methanol clusters and show the importance of solvent molecules on such reactions.

METAL CLUSTERS

Numerous investigations into the physical and chemical properties of metallic clusters have been carried out. These have shown metallic clusters to display a vast array of types, with their stability depending on such properties as their electronic and geometrical structures as well as internal energy requirements.

Clusters of simple metals, eg. the alkali metals, can be clearly described by single-electron models, while more complex models are needed for heavier metals and transition metals. In the latter case transitions from van der Waals-type clusters to metallic binding, via covalent bonding, have been observed (102).

The aim of this section is to outline those trends occurring in cluster structures and reactivities within groups and periods as well as describing the chemistry of the major transition-metal clusters.

1.9.5 ALKALI METAL CLUSTERS

Alkali metals are often considered as simple prototype metals due to their single free 's' electrons and their ready description by the free electron model. Thus on cluster formation the valence electrons become readily delocalized and exhibit the properties of a Fermi electron gas.

The neutral cluster spectra of various alkali metals, $(Am)_n^+$, have been reported and all exhibit similar basic characteristics. These are (i) 'shell like' intensity distributions, with the intensities decreasing with cluster size, and (ii) size-dependent reactivities. The 'steps' in the spectral intensities are observed to change with cluster charge and occur for cationic clusters when the cluster size n_s corresponds to the number of valence electrons needed to bring about shell closure, with $n_s = 2, 8, 20, 40, 58, 92, \dots$ (55)

The alkali metal clusters also exhibit strong even/odd alternation, with the even clusters being seen to display greater intensities than those of neighbouring odd clusters. This is a consequence of the even clusters corresponding to electron pairing and hence filling of subshells.

This effect is further enhanced by the decay pathways shown by these two types of cluster. Even clusters only undergo dissociation via one dissociative pathway involves the evaporation of a single monomer unit, while odd clusters present two competing dissociation pathways. (103)

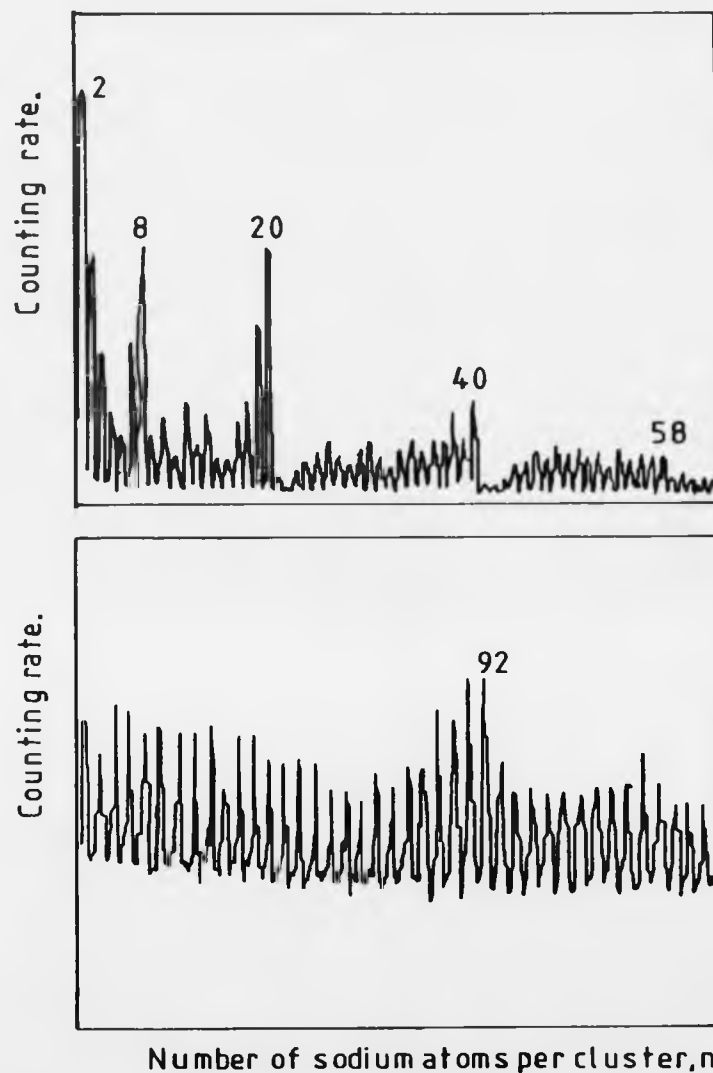
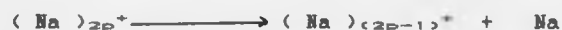
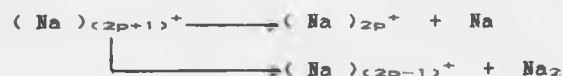


Fig 1.9.2 The Abundance of $(Na)_n$ Clusters Formed by Free Jet Expansion, Using AR Carrier Gas

Even cluster,



Odd clusters,



of which are (i) the loss of neutral monomer units and (ii) the dissociation of neutral dimers. The rates of these two pathways are size-dependent, with small clusters preferentially undergoing dimer loss. This loss of neutral dimer leads to greater reduction of the spectral intensities of odd clusters, and enhanced even/odd alternation.

As cluster size increases however the rate of dissociation of the monomer increases until it becomes the dominant pathway for all the larger clusters. Monomer loss is also seen to be energy dependent and laser studies have shown rates to increase with increasing energy input to the cluster. Brechignac et al. have shown these effects can be interpreted in terms of cluster binding energy for the monopositive cluster (103)(104). When plotted against cluster size, these are seen to be higher for odd clusters and also show peaks at $n = 9$ and $n = 21$ corresponding to the enhanced stabilities of these species. These clusters reflect shell-closing electron configurations of $ns = 8$ and 20 electrons. This is more pronounced for $(Na)_n^+$ than $(K)_n^+$ due to its smaller radius and hence deeper potential well. The ionization energies mimic the cluster binding energies and are also seen to decrease with increasing cluster size. This is also displayed by the cohesive energies of small clusters which show greater relative increases upon

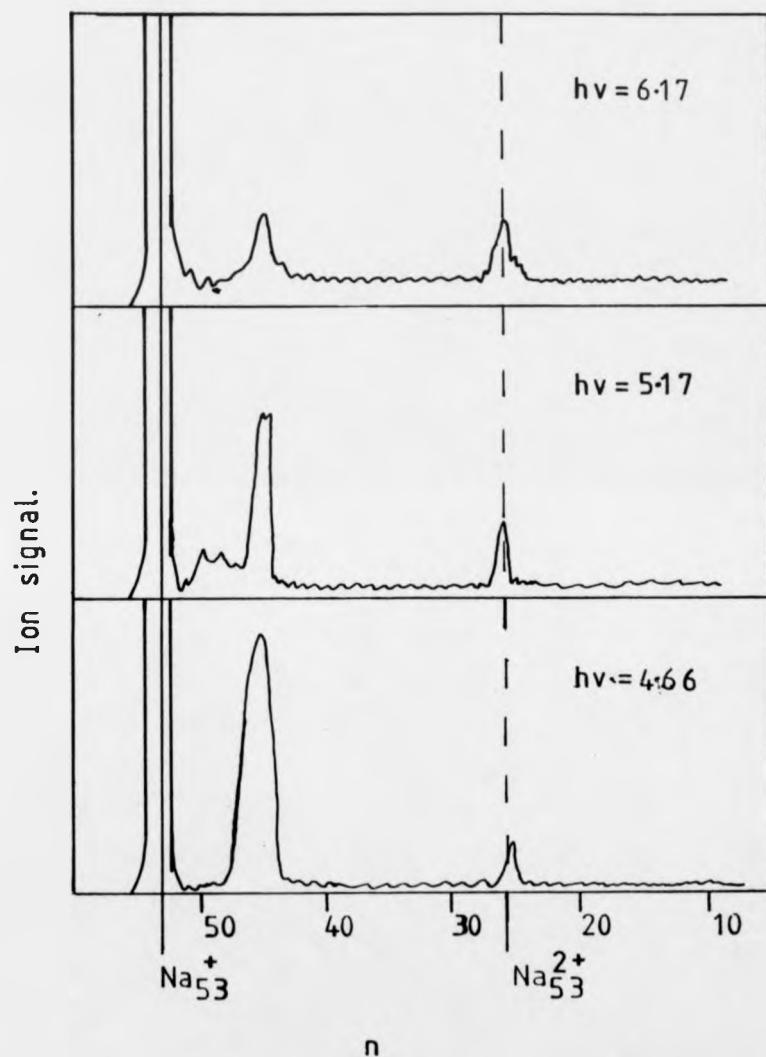
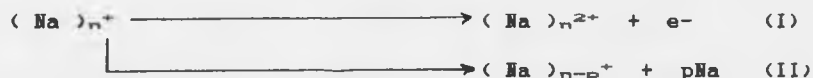


Fig 1.9.3 The Photoproducts from Mass Selected Na_{53}^{+} , at Three Photo Energies. Competition Between Photoevaporation and Photoionisation is Clearly Observed.

the loss of neutral units, due to the extensive charge redistribution required in addition to the energetics of bond breaking.

Another striking example of the size-dependence of cluster reactivity is shown by multiply-charged sodium clusters. Laser-induced ionization of $(\text{Na})_n^+$ clusters to produce $(\text{Na})_n^{2+}$ (I), shows a size threshold, n_c , below this photodissociation takes place (II).



For reaction (I) the input energy causes photoionization and the ejected electron is emitted with most of the excess energy, while in reaction (II) the input energy does not exceed the ionization threshold of the cluster and photo-induced dissociation takes place. The process leading to the formation of doubly-charged clusters (I) only occurs at $n_c \geq 19$ and is also seen to lead to the production of triply-charged clusters for very large clusters ($n_c \geq 70$). The doubly-charged clusters are found to undergo unimolecular dissociation by the loss of neutral monomer units,



1.9.6 SILVER CLUSTERS

Silver clusters show similar behaviour to that of the alkali metals. In their spectra, the intensity is seen to decrease with increasing cluster size and marked odd/even alternation is apparent (105), with odd clusters being the more intense species for both positive and negative clusters. In addition to these phenomena a number of anomalous discontinuities are observed in the cluster intensities. The position of these marked drops in cluster intensity are seen to differ by two mass units between negative and positive clusters. Thus abnormalities are observed at $n^- = 1, 7, 17, 19, 33, 39, 57, 91, 137$ and 197 for negative clusters $(Ag)_n^-$, while for positive clusters $(Ag)_n^+$ they are seen to occur when $n^+ = 3, 9, 19, 21, 35, 41, 59, 93, 139$ and 199 . (106)(107)

The positions of these 'steps' are related to the number of valence electrons contained within the cluster with $n^- = n_s - 1$ and $n^+ = n_s + 1$, where n_s is the number of valence electrons required to bring about electronic shell closure. The resulting values of n_s are equal to the magic numbers displayed by the alkali metal clusters (108), hence their size distributions reflects those of neutral clusters.

The presence of such phenomena demonstrates that a 'one-electron shell model' can be used to explain the stabilities of those metals in which 's' valence electrons are bound in a spherically symmetrical potential well.

The presence of odd/even alternation can be explained in terms of electron pairing, with odd clusters always containing paired electrons. This is supported by ionization energies and electron affinity studies (109). This odd/even alternation is most pronounced for smaller clusters, that is $n^- \leq 30$, $n^+ \leq 40$. The spectral stabilities of the odd-numbered clusters are also demonstrated by their dominance of fragmentation spectra with the loss of neutral dimers being essentially the only fragmentation pathway observed (110)(111).

Multiply-charged silver clusters, $(Ag)_n^{2+}$, also show odd clusters to be preferentially formed, for $n \geq 19$. Smaller doubly-charged clusters however, are not observed since the coulombic repulsive energy would exceed their binding energies and hence lead to coulombic explosion (112)(113).

Silver clusters also show a series of interesting ion-molecule reactions involving other species. Brocker et al. (114) carried out laser desorption of AgO, which produced Ag^+ , Ag_2^+ and $(Ag_2O)^+$, with cluster enhancement being observed on the reduction of the laser power. When the AgO was mixed with ZnO, an extended cluster series corresponding to $(Ag)_n^+$ and $[(Ag)_nO]^+$ was detected. These species showed strong odd/even alternation and no zinc species were observed, suggesting that Zn or Zn^+ may be acting as a third body to stabilize the silver clusters or reduce the incident laser power.

The reactions of various silver species with organic species, such as C1 - C3 alkanes, C2 - C6 alkenes, C1 - C3 alcohols, ferrocene and

Fig 1.9.4 The Size Distribution of Silver Clusters

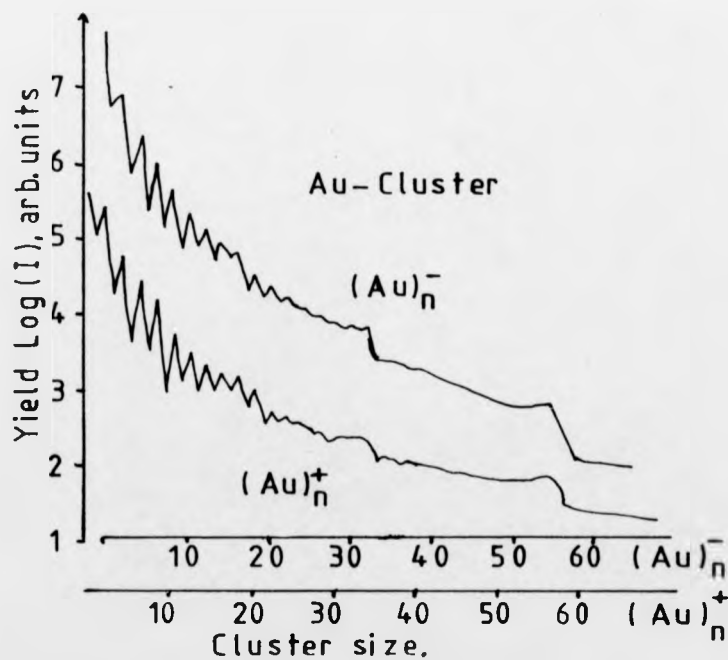
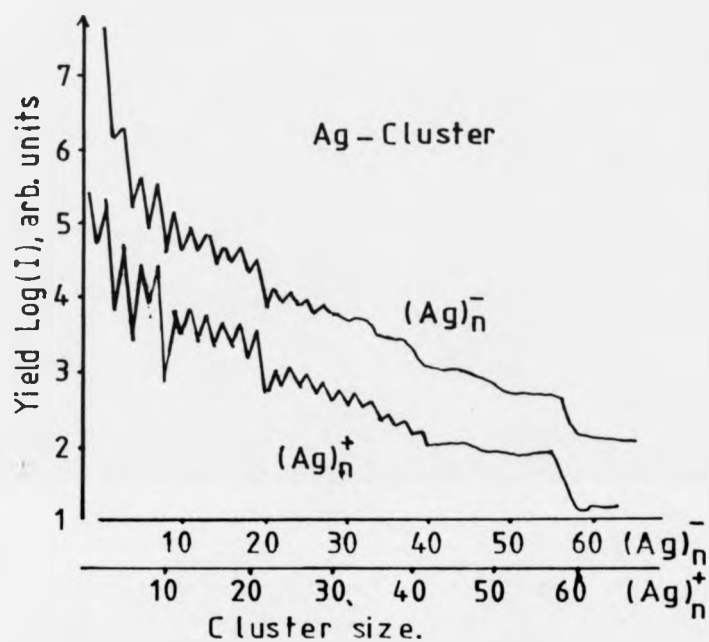


Fig 1.9.5 The Size Distribution of Gold Clusters

glycerol (115) have also been studied and involve such processes as charge exchange, reduction and dehydration. Sec-butylamine is also found to undergo deamination. In addition to these studies the reactions of silver supported on a graphite matrix has also been investigated leading to the exclusive production of only odd clusters, of the form $[Ag_nC_x]^+$, where x is even (116).

1.9.7 GOLD CLUSTERS

Gold clusters, $(Au)_n^+$, display the same basic properties as the silver clusters, with their cluster spectrum showing the presence of odd/even alternation as well as magic numbers.

The positions of these are,

$$n = 3, 9, 19, 21, 35, 59, 93, 139,$$

$$n = 17, 33, 57, 91, 137,$$

with a number of shell closure configurations not being seen to lead to enhanced stabilities (106)(107). This behaviour is due to the high level of delocalization of the 6s valence electrons in gold and these clusters are able to be described by the single electron model.

Similar results have been reported by Beuhler and Friedman who studied the effects of projectile ion mass and velocity on cluster yields. In this work $H^+(H_2O)$ projectile clusters were impacted onto gold foils, and the cluster yields were not seen to increase with

projectile mass or velocity, but however the clusters were seen to have increased kinetic energies (116).

1.9.8 ALUMINIUM CLUSTERS

Aluminium is almost a free electron metal, and is trivalent in almost all its known compounds. However many of these compounds are borderline between ionic and covalent.

Meiwees-Broer et al. investigated the metastable dissociations of mass selected aluminium clusters, $(Al)_n^+$, $n \leq 23$, with metastable decomposition being observed for clusters $n \geq 7$, with the dominant dissociation pathways leading to the loss of single neutral monomer units (Al) . For $n \geq 15$ the loss pattern is seen to favour the sequential loss of two Al monomers (117).

However in CID studies on $(Al)_n^+$, $n = 3-26$, the major dissociation product was Al^+ and Al_{n-1}^+ for larger clusters. In the region of aluminium cluster magic number species the dissociation pathways of neighbouring clusters were seen to change in order to preferentially yield these magic number clusters (118). For example :-

| Parent Cluster | | Dissociation Pathway | Productions | |
|----------------|-------------|----------------------|-------------|-------------|
| Al_6^+ | Al_{15}^+ | $(Al)_{n-1}^+$ | Al_7^+ | Al_{14}^+ |
| Al_9^+ | Al_{16}^+ | $(Al)_{n-2}^+$ | Al_7^+ | Al_{14}^+ |
| Al_{10}^+ | Al_{17}^+ | $(Al)_{n-3}^+$ | Al_7^+ | Al_{14}^+ |

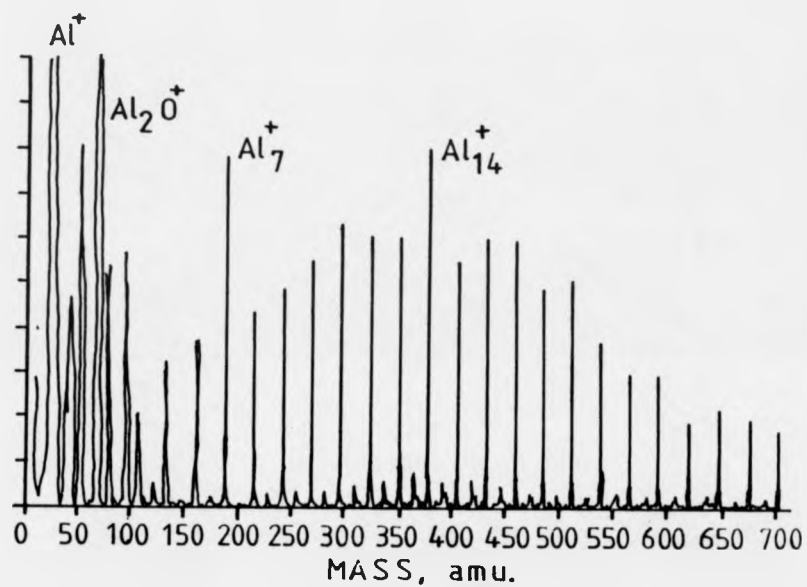


Fig 1.9.6 The Mass Spectrum of Aluminium Cluster Ions

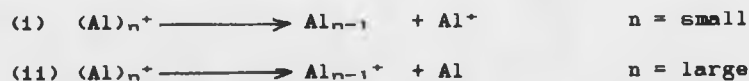
The products of these multiple dissociations yield clusters of nuclearities $n = 7$ and 14 , which are proposed magic numbers for aluminium clusters. These clusters are also seen to be at the positions of sharp drops in cluster ionization potentials and decreased dissociation energies leading to their enhanced stabilities. This is also demonstrated by their collisional cross sections which show very small values at $n = 7$ and $13 / 14$.

The position of these magic numbers are also confirmed by Jellium model calculations, which show peaks at:

$$\begin{array}{ll} n = 7, 13, 19, 23, 31 \\ \text{no. of } e^- = 21, 39, 57, 69, 93 & \text{for neutral aluminium clusters.} \end{array}$$

Hence the Al_7^+ (2s) and Al_{14}^+ (2p) species correspond to closed shell electronic configurations containing 20 and 40 valence electrons respectively, with weak evidence also being displayed for a shell closure at Al_{23}^+ with 68, (2d), valence electrons.

The difference in dissociation pathways between small (i) and large (ii) clusters,



is caused by energetic influences and is reflected in the relative ionization potentials of Al and Al_{n-1} . For small clusters, their

ionization potential is greater than that of the atom and hence Al^+ is the major product, while for larger clusters Al_{n-1} has a lower ionization potential than that of the Al atom and so retains the positive charge.

The crossover between these two dissociation regimes is seen to occur at $(\text{Al})_n^+$ and hence this must correspond to the position where the ionization potential of the cluster (Al_{n-1}) drops below that of the neutral aluminium atom, before decreasing to that of the bulk values.

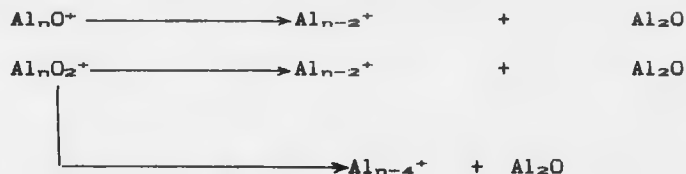
Another unusual phenomenon observed in the ionization potential of small $(\text{Al})_n^+$ clusters, $n \approx 1$ to 4, is an initial increase in their values, this is a consequence of the high 3p character of the aluminium valence orbitals. This results in small aluminium clusters having deeper Fermi levels than those of most other metals (119).

Similar investigations carried out on boron clusters, B_n^+ ($n = 3 - 8$), show the primary fragmentation pathway to involve the formation of B^+ . However the dissociation energies for B_n^+ were found to be approximately three times greater than those of the corresponding Al_n^+ clusters. B_8^+ was found to be of a notably higher intensity in both the cluster spectrum and the CID spectra of B_n^+ .

The ion-molecule reactions of Al_n^+

The chemisorption of oxygen onto Al_n^+ gives rise to a series of mixed aluminium - oxygen clusters of the form $(\text{Al}_n\text{O}_m)^+$, where $n = 3 - 26$, $m = 1, 2$. These were studied by Jarrold and Bower (120).

In addition they also investigated the collision induced decomposition of these clusters, with CID being seen to cause the preferential loss of neutral Al_2O units,



This loss of Al_2O units was seen to be the dominant fragmentation pathway for all clusters except Al_nO_2^+ , $n = 3, 14$, where the major product was seen to be Al^+ . The dominance of the major of these fragmentation pathways is probably due to the very strong bonding in Al_2O .

These CID results were also used to approximate the interaction energies between Al_n^+ and oxygen. These large interaction energies were seen to be similar over a range of cluster sizes and suggests that the oxygen atoms are multiple bonded to a number of aluminium atoms around its chemisorption site. Similar conclusions were also reported by Pallmioni et al. (121).

The collision cross-sections of $Al_nO_2^+$ show the presence of minima at $Al_9O_2^+$ and $Al_{15}O_2^+$, suggesting that these species have enhanced stabilities. Jarrauld (118) suggested that those species correspond to closed shell structures in which each oxygen atom involves two valence electrons from the cluster.

$$\begin{array}{lcl} \text{So} & Al_{15}O_2^+ & = 40 \text{ valence electrons} \\ & Al_9O_2^+ & = 22 \text{ valence electrons} \end{array}$$

The reactions of oxygen and aluminium clusters are seen to be dependent on collision energy and exhibit energy dependent threshold barriers. These thresholds are seen to increase between $n = 3$ and 7 and the drop for $n = 8$ (122)(123). The major product of these reactions arise from cluster fragmentation, with very little oxygen incorporation being observed. For $n = 3$ to 6, Al_2O^+ is seen to be the dominant product, while Al_{n-5}^+ is the major product when $n > 6$, changing to Al_{n-4}^+ for $n > 13$ except for Al_{19}^+ which undergoes the loss of five aluminium atoms to give the magic number cluster Al_{14}^+ . The Al_{n-4}^+ reaction pathway is thought to be a consequence of Al_2O formation,



with Al_{n-5}^+ and Al^+ arising from subsequent fragmentations. The lack of further fragmentations for $n > 13$ clusters, may be due to either the excess energy being lost via the numerous internal degrees of freedom present, or as a consequence of the rate of dissociation of the newly formed highly energetic Al_2O moiety. If this is sufficiently large it

may not allow enough time for the excess energy to be transferred to the parent cluster.

The reaction of Al_n^+ with D_2 has also been studied, with the investigations showing the existence of significant kinetic energy thresholds for these reactions (124). The main products observed, at 3 eV collision energy, were Al_nD^+ , $Al_{n-1}D^+$, Al_{n-2}^+ and for smaller clusters Al^+ . For larger clusters ($n > 7$) the chemisorption of D_2 onto the clusters was seen and may result from their increased numbers of internal degrees of freedom allowing the faster dissipation of excess energy.

The thresholds for these reactions show notable odd / even alternation as well as abnormally high values for $n = 13$ and 23 , which are proposed magic number clusters.

The anionic clusters of aluminium, Al_n^- , display many of the spectral characteristics seen for Al_n^+ , including pronounced odd / even alternation, and magic numbers. The positions of the magic number clusters are seen to be particularly inert and to correspond to close shell electronic and geometric structures.

1.9.9 VANADIUM, NIOBIUM AND TANTALUM CLUSTERS

The cluster spectra and reactions of these metals have been extensively studied and show that while there are many similarities between niobium and tantalum, they differ in character from those of vanadium clusters. In this section the aim is to discuss the differences that become apparent on descending a group.

Vanadium clusters have only been subjected to limited studies, which have shown vanadium-oxygen bonds in clusters to be stronger than vanadium-vanadium bonds (125). Vanadium, $(V)_n^+$, and vanadium-oxygen, $(V)_nO^+$ clusters have been reported to react with ethene in a similar way, with dehydrogenation being the major process taking place, apart from V_3^+ which promotes C - C bond cleavage (126). Dehydrogenation is also found to occur with cyclohexene to produce vanadium-benzene complexes (127).

Both pure vanadium clusters and those containing impurities, for example V_nO and V_nC , were observed to react with D_2 by pseudo first order kinetics. The presence of the impurity atom was found to alter significantly the reactivities of the vanadium clusters, with the induced change being characteristic of the impurity atom present. The presence of carbon in V_nC dramatically reduces its reactivity towards D_2 but in V_nO the opposite effect is observed, while for V_nO , $n = 5$ and 9 , the reactivities are comparable with those of the corresponding V_n clusters.

The reactivities of V_n and Nb_n towards D_2 show size dependence, with evidence for the presence of structural isomers with Nb_9 , Nb_{11} and Nb_{12} (128). The two different structural forms, in the case of Nb_9 and Nb_{12} , showed one form to be highly reactive towards D_2 compared with the other, and similar evidence was observed for the reactions with N_2 .

For V_n , $3 \leq n \leq 32$, no evidence of isomerism was found from the reactions with D_2 or N_2 . A wide range of reactivities was observed for $n < 15$, with a dominant peak being found at V_6 as well as the presence of pronounced odd/even alternation. At $n > 20$ the reactivities exhibited a more regular increase. Niobium clusters however showed marked biexponential depletion rates at $n = 9, 11$ and 12 , indicating the presence of isomeric forms (5). The chemisorption rates for Ta_n , $n < 30$, displayed odd/even alternation for $3 \leq n \leq 27$, with the intermediate regions constituting troughs. Ta_{12} showed evidence of isomerism. For their reactions with N_2 , tantalum clusters were observed to be intermediate in behaviour between the low size-dependence of V_n and the highly size selective niobium clusters.

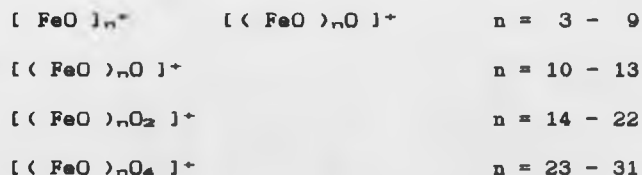
The presence of cluster impurities in the above reactions results in significant impurity characteristic effects, similar in nature to those demonstrated for D_2 . These effects were notably reduced with increasing values of 'n' as the influence of the impurity atoms on structural and electronic geometries becomes less pronounced. For Ta_n and Ta_nO the reactivity patterns converge at $n \approx 13$. The effects of charge on reaction rates were only found to produce minor changes in the reactivities of niobium clusters, for $n < 28$. Nb_9 , Nb_{12} and Nb_{12}^+ were

observed to clearly display isomeric forms. In the case of Nb_{12}^- it is suggested that isomeric forms may exist, but that either their reactivities towards D_2 may be too similar to enable their differentiation by their reactions or that the negative charge results in the preferential formation of only one isomer. The reactivities for all clusters regardless of charge state were seen to be temperature dependent, with their properties converging as cluster size increases, due to the high density of states leading to the charge being smeared out (129)

The reactions of vanadium, niobium and tantalum clusters with ethane show a simple monotonic increase in reactivity with cluster size, combined with a general decrease as the group is descended.

1.9.10 IRON CLUSTERS

The reaction of $(\text{Fe})_n^+$ with molecular oxygen yields a number of characteristic size-dependent cluster series, with the extent to which oxygen is accommodated within the product cluster being seen to increase with cluster size (130).



Similar results have also been reported by Whetten et al. who studied the reactions of neutral iron clusters towards H_2S and methane using collisionally cooled and uncooled clusters (131). In these investigations they showed the level of oxygen chemisorption for cooled clusters also to be dependent on the pressure of oxygen present. Thus for low O_2 pressures the reaction is :



while at high pressures, the reaction is :



For experiments involving uncooled Fe_n clusters both products for the low-pressure reaction were observed in approximately equal intensities, suggesting a form of plasma-bound co-condensation reaction to occur in the latter case.

The reaction with H_2S showed evidence of dissociative adsorption, in which H_2S undergoes loss of hydrogen atoms. These reactions were shown to be exothermic and very similar in nature to those of O_2 . In the case of methane no reaction was observed, regardless of the pressure used.

The reactions of both neutral and monopositive iron clusters were found to be similar in character, with many size-dependent phenomena being enhanced for the charged clusters, suggesting the presence of an activation barrier. This in turn suggests that the reaction proceeds by activated chemisorption (132). These clusters also show a strong correlation between their reactivities and ionization potentials (133).

This relationship between cluster reactivity and ionization potential is a result of most dissociative chemisorptions involving some degree of electron donation from the cluster into the antibonding orbitals of the molecule to be adsorbed. Thus the smaller the ionization potential of the cluster, the greater the ease with which this electron transfer can take place (134).

For $(Fe)_n$ and $(Fe)_n^+$, their reactivity patterns show similar distributions for $n \geq 20$, with a sharp increase in the region of $n = 23$ and a subsequent leveling-off being observed. However for $n < 20$ their reactivity patterns are substantially different. $(Fe)_n^+$ shows a sudden sharp peak in the region of $n = 4 - 6$, of similar reactivity to clusters in the $n \geq 20$ region, while for clusters with $n = 9 - 14$ the reactivity is suppressed relative to their neighbours. This is in marked contrast to the neutral clusters which display a broad peak, $n = 8 - 15$, which has a maximum at $n = 10$.

The positive charge also shifts the sudden onset of reactivity to lower n values, being observed at $n \approx 19$, while both types of cluster show the presence of a kinetic isotope effect. The above effects and size-dependent reactivities are a consequence of changes in the position and geometry of the clusters' Fermi level.

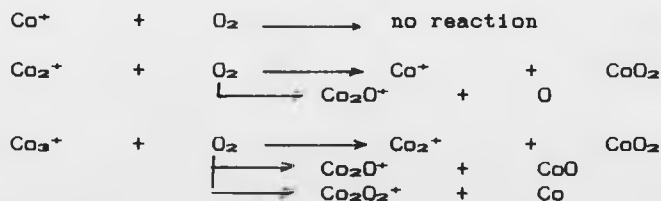
$(Fe)_n$ has also been found to display highly size dependent reactivities towards D_2 , similar in character and format to their reactions with H_2 , while their reactions with CO were found to show a simple monotonic increase in rate with cluster size. However they were

seen to be relatively inert towards N_2 , only undergoing weak interactions with $(Fe)_n$ to form $(Fe)_nN_2$.

1.9.11 COBALT CLUSTERS

These clusters have been widely studied and have been produced by both laser vapourization (135) and fast atom bombardment, FAB (136). The former of these methods of generation has usually involved the laser vapourization of cobalt carbonyl compounds followed by CID and the mass selection of the resulting cobalt clusters. The reactions of the resulting $(Co)_n^+$ species have been studied with various gas phase species.

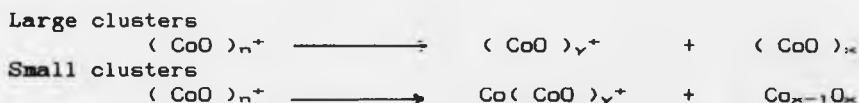
The reaction of $(Co)_n^+$ with O_2 gives rise to a number of cluster series, with the dominant series being dependent on the initial cluster size. For example (137):



The major series produced can be described by the general formulae

| | |
|-------------------|----------------------------|
| $[Co_nO_{n-1}]^+$ | oxygen-deficient clusters |
| $[Co_nO_n]^+$ | oxygen-equivalent clusters |
| $[Co_nO_{n+1}]^+$ | oxygen-rich clusters |

The CID of these clusters shows the oxygen-equivalent species to undergo fragmentation involving the loss of $(CoO)_x$ units to form the charged $(CoO)_y^+$ species for larger clusters; smaller clusters however were found to fragment to form oxygen-deficient clusters in addition to the pathway given above.



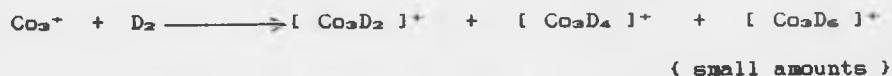
Oxygen-deficient species however are observed to fragment to form charged oxygen-equivalent clusters.



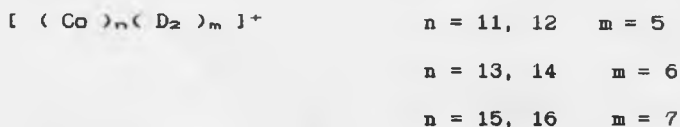
It has been proposed that the CoO cluster units are ionic in character, so in smaller clusters the additional cobalt atom stabilizes the positive charge (138).

The reactions of pure cobalt clusters are also observed to exhibit size-dependent reactivities with a variety of species; this is most

evident in their reactions with D_2 . Neither the clusters with $n = 1$ or 2 react with D_2 , while Co_3 is highly reactive as regards the chemisorption of several D_2 molecules.



The clusters $n = 4 - 9$ are also found to react with D_2 , but at a lower rate than with $n = 3$, but the clusters $n = 9 - 16$ are observed to be highly reactive towards D_2 forming clusters of the form;



This suggests that a dramatic change occurs at $n = 10$ in cluster reactivity, with the clusters $n = 10 - 16$ being assumed to be D_2 -saturated and the binding being due to dissociative chemisorption; for reactions involving H_2 , species with $n = 3, 5$ and $n > 10$ were found to be highly reactive via dissociative chemisorption, while all other clusters were almost unreactive.

Reactions involving N_2 show a similar pattern to those of D_2 and H_2 , but the rapid change in chemical reactivity was observed only to occur at $n = 18 - 20$ (135).

The reactions of cobalt clusters and mixed metal-cobalt clusters have been investigated with a number of organic species. Unlike Co^+ , Co_2^+ is found to be unreactive towards alkanes, as well as ethene, propene, isobutene and butadiene, but reacts via dehydrogenation with larger clusters. Similar results were also reported by Jacobson et al. for CoFe^+ , which was generated by sequential ligand displacement reactions from $\text{Fe}(\text{CO})_5$ (139). CoFe^+ , on reaction with benzene, forms $\text{CoFe}(\text{C}_6\text{H}_6)_2^+$ which on collisional activation produces $\text{Co}(\text{C}_6\text{H}_6)_2^+$ and $\text{CoFe}(\text{C}_6\text{H}_6)^+$. The trinuclear species Co_2Fe^+ was observed to react differently towards alkanes by undergoing C - H bond activation. The reaction of Co_2Fe^+ with cyclohexane to produce benzene was found to occur by thermal-dehydrogenation (140). Both Co_3^+ and Co_2Fe^+ were observed to abstract sequentially three oxygen atoms from ethylene oxide molecules, whereas the dimers (Co_2^+ , CoFe^+ , Fe_2^+) were found only to extract two oxygen atoms. Similar work has also been performed by Freas et al. on cobalt-copper clusters (138)(141)(142).

Freas et al. have also reported the reactions of Co_2CO and found it to be significantly different from that of Co^+ , CoCO^+ and Co_2^+ . They suggested that this is a result of the CO ligand leading to polarization of the Co - Co bond and hence the increased reactivity being a consequence of the increased positive charge on the unbound Co atom (143).

Investigations of the reactivities of cobalt-oxygen clusters towards organic species have also been carried out (136). In their reactions with isobutane, the resulting species involve the addition of

a single isobutane unit, with the cluster reactivities displaying a dependence on the oxygen content of the cluster as well as its size. CID studies showed the oxygen-deficient clusters to undergo dehydrogenation to form $[Co_nO_{n-1}(C_4H_4)]^+$, while the oxygen-equivalent species fragment by the loss of a neutral isobutane unit.

These differences in reactivity have been attributed to structural differences, in which oxygen-deficient clusters have cobalt atoms occupying terminal sites and hence are more accessible to reaction (136). Similar effects are also observed to occur at surface defects in crystals.

1.9.12 NICKEL CLUSTERS

These were first reported by Fayet and Woste, and were found to show an exponential decay in their intensities with increasing cluster size (144). In addition to this monotonic decrease, the spectral intensities did not exhibit any structural information, such as magic numbers or odd/even alternation effects. Laser induced dissociation studies also yielded limited information, with the sequential loss of single neutral nickel atoms being observed upon the absorption of each photon (145).

The reactivities of nickel clusters, towards D_2 were observed to show a mild monotonic increase with cluster size (146). The reactions of $(Ni)_n^+$ clusters with CO results in the production of

$[(Ni)_n(CO)_k]^+$ and small amounts of $[(Ni)_{n-1}(CO)_k]^+$ and $[(Ni)_n C(CO)_m]^+$. The pressure dependence of these reactions suggests that the major product is formed by a series of third-body association reactions, with the value of k increasing with CO pressure until saturation occurs. For $(Ni)_4^+$ this was observed at $k = 10$ and for $(NiO)_3^+$ at $k = 22$. These results are in keeping with the electron counting rules predicted by PSEPT (75).

However the reaction of $(Ni)_n^+$ with C_4H_{10} displays a size-dependant character. For small clusters the reaction results in dehydrogenation involving the loss of two hydrogen molecules.



For $n = 6 - 10$, more extensive dehydrogenation takes place, with the dominant product resulting from the loss of three hydrogen molecules to give $[(Ni)_n C_4H_4]^+$. In the case of atomic nickel however the reaction involves the cleavage of a C - C bond. Hence C - C bond cleavage is reduced with increasing cluster size in favour of dehydrogenation, the extent of which also increases with cluster size. These reactions were found to be dependent on the internal energies, of the cluster with collisional cooling resulting in enhanced dehydrogenation (147).

The results of above reactions, while showing the presence of size-dependent reactivities towards different species, do not yield any structural information. However Parks et al. reported the chemisorption

of ammonia and water over a large range of n values to display a number of very important structural influences (148).

For NH_3 , the extent of reaction is observed to be pressure-dependent until saturation occurs, then under saturation conditions the cluster reactivities were found to display marked minima at 'n' values that correspond to the magic numbers displayed by rare gas clusters. The existence of these minima suggests that nickel clusters exist in three dimensional networks, of icosahedral geometry.



The resulting species display a range of m values for each n value, which decreases as n increases as a consequence of decreasing bond strength and the increasing importance of equilibrium effects. Plots of m', the average value of m, against n show similar distributions regardless of the ammonia pressure used; these were seen to display pronounced minima at n = 55, 71, 83, 92, 101, 116 and 147 as well as a plateau region at n = 50 - 120. Each of these minima correspond to m' = 12 suggesting the presence of strong structural influences upon reactivity.

Seaburg et al. suggested that the binding of ammonia onto cluster surfaces occurred via the nitrogen atom, with $\text{N}(\sigma) \rightarrow \text{Ni}(\text{d})$ donation as well as electrostatic attraction between the ammonia dipole and the surface being maximised (149). This was shown to be so when ammonia binds onto a metal atom as opposed to a multiatom site and is strongly

supported by the similarities between adsorption minima and the magic numbers exhibited by rare gas clusters, since these correspond to shell closures of Mackay icosahedral structures which have twelve apical atoms.

For $(Ni)_n^+$, the apical atoms will be six-coordinate, while face atoms are eight-coordinate, hence favouring apical coordination.

These plots of m' against n also show the presence of three distinct regions.

For $n = 4 - 48$, the structures adopted by the clusters are strongly influenced by the extent of ammonia adsorption, since the adsorption energy is a significant fraction of the total cluster energy. When $n < 7$ the ammonia uptake is observed to occur in approximately a 1:1 ratio, while for $n \geq 7$ a plateau region appears that extends up to $n = 19$. $n = 7$ corresponds to a pentagonal bipyramidal structure, while $n = 19$ shows a m' value of twelve and a possible double-icosahedral structure. Similar behaviour was also noted for $n = 23, 26, 29, 32$, etc.. Evidence was also found that the take up of ammonia also induces structural changes at certain n values, with the level of conversion depending on the ammonia pressure. These structural changes may also bring about the decomposition of ammonia after its absorption, observed for $n \geq 20$. This behaviour is marked for $n = 7$ which induces the loss of between one and three hydrogen molecules from ammonia molecules.

For $n = 49 - 147$ a number of minima are observed, each of which corresponds to the absorption of twelve ammonia molecules, supporting

the theory of absorption on apical sites. The clusters featuring $Mn + 1$ metal atoms uniformly display an additional absorption site for a single ammonia molecule. This suggests that clusters in this region are strongly icosohedral in structure, although under certain conditions isomeric structures may occur.

For $n = 116 - 160$, at room temperature the adsorption pattern of ammonia is inconsistent with an icosohedral structure, with no m' minima being observed at $n = 147$. However as the reaction temperature is increased the presence of icosohedral-type absorption is observed, with a strong minimum for $n = 147$ at 82°C . This suggests that nickel clusters in this region can exist in a series of energy-dependent structures and may mark a change over the region with bulk-metal structural influences starting to play a more significant role.

The reaction of nickel clusters with water leads to the production of $[(Ni)_n H_2O]^+$ as the dominant species, with the intensity distribution showing a similar character to that for ammonia, with the presence of strong absorption peaks at $n = 36$ and 39 , with various plateau regions also being present. These variations in reactivity reflect shifts in the equilibrium for the reaction



and suggests that equilibrium effects are more important in these reactions than for ammonia. The resulting minima for water are observed for clusters containing one additional nickel atom than for ammonia.

Hence water undergoes stronger binding to clusters containing a single metal ion outside its closed shell or subshell, that is the binding takes place onto a nickel atom with the least possible M - M coordination. The above reactions show nickel clusters to exist in three-dimensional frameworks, based on icosahedral geometries. These structures are adopted in order to minimise energies in small clusters and are found to dominate the reactivities of mid-range clusters. However for larger clusters bulk influences and the adoption of other low-energy structures cause isomerization and temperature dependence of their reactivities.

1.9.13 TRENDS IN METAL CLUSTER CHEMISTRY

The foregoing discussion shows cluster properties to be characteristic of the metal from which they are formed, with significant size dependences being observed in most cases.

Metals containing delocalized valence electrons are found to be described by jellium-type electron models, for example tensor harmonic theory and polyhedral skeletal electron-pair theory. This type of cluster encompasses such metals as the alkali metals, aluminium, silver and gold, and becomes increasingly applicable along the series of transition metals.

The importance of electronic structure to the stability of these clusters is observed to strongly influence their reactions and heterocluster properties. Martin et al. reported the properties of Na,

Cs, Ca and Ba oxide clusters (150). The group I metal, sodium and caesium, oxide clusters showed the presence of strong decreases in cluster intensity after electron shell closures. In the case of caesium these clusters followed the general formulae $[Cs_{2n+Z}O_n]^+$, where $Z = 8, 18, 34, 58, \dots$, i.e. the same electron counts as for the jellium model (each oxygen atom is assumed to involve two cluster electrons in its bonding). Calcium clusters however were observed to form ionic 'rock salt'-type lattice structures, while barium clusters show a tendency to adopt icosahedral structures.

This competition between geometrical and electronic influences on the cluster properties continues for transition metals, with certain metals showing distinct changes between bonding modes with increasing cluster size (102)(151). This transition is clearly demonstrated by mercury clusters. Small clusters, i.e. $n \leq 13$, show van der Waals bonding changing to covalent in the region of $30 \leq n \leq 70$ and then undergo a sudden transition to metallic character at $n \geq 100$. In the small clusters, as for atomic mercury which is isoelectronic with helium, the s/p energy gap is so large that sp hybridization is not energetically favourable and hence electronic influences only play a small role in their bonding (152). As the cluster size increases, however, the valence band broadens allowing sp hybridization and confers an increasing covalent nature to the bonding present. On further increases in cluster size, i.e. $n \approx 70$, the s-p splitting becomes so small that a transition to metallic bonding occurs. In this region, $90 \leq n \leq 100$, the mean nearest neighbour distance for the atoms in the cluster is found to suddenly and rapidly decrease. This results from a

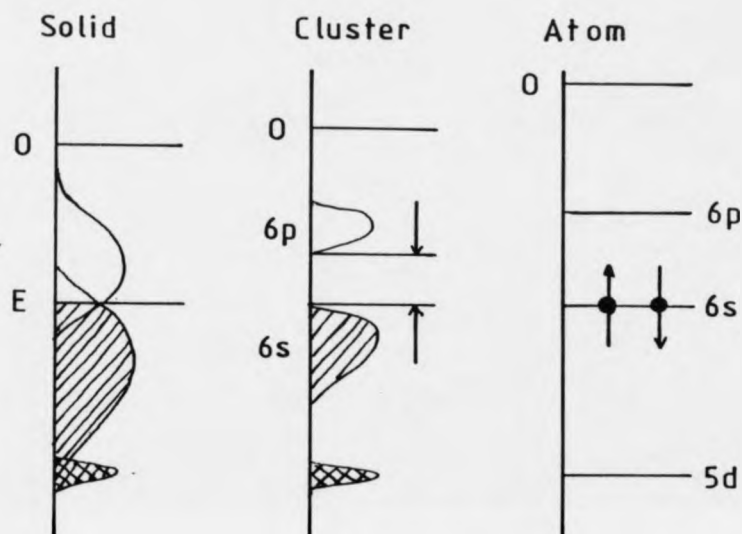


Fig 1.9.7 A Diagrammatic Representation of the Electronic Band Structure for Mercury Clusters

The Hg atom has a $6s^2$ closed electronic shell, with the atomic lines broadening into 'bands' for the clusters. The band gap $\Delta(n)$ decreases as a function of the cluster size. The two bands overlap in the solid, giving mercury a metallic character. For large Δ the binding is of the Van der Waals type, for intermediately sized Δ the binding is covalent in character, with the binding becoming increasingly metallic as Δ becomes negligible.

increase in bandwidth and decrease in the 6s - 6p energy gap as the cluster size traverses this region. Hence a rapid electronic transition takes place, accompanied by a sudden shrinkage in interatomic distances (102)(153). Similar behaviour is also observed for beryllium clusters which undergo the initial van der Waals-to-covalent transition at $n \approx 4$ (151), while $(\text{Zn})_2^+$ is reported to be covalent in character (154)(155).

These changes in bonding regime and geometry dictate the reactivities and stabilities of cluster species. Small clusters have near-atomic behaviour, since the minimizing of the surface energy is the dominant requirement for stability due to the large fraction of surface atoms. The properties of larger clusters gradually converge towards those of the bulk material as cluster size increases.

In rare gas clusters, atom - atom interaction potentials are relatively short range and cluster stability is directly related to cluster geometry, with clusters trying to maximise the number of their atom - atom bonds. This results in icosohedral packing. The stability of alkali and alkaline earth metal clusters however is dominated by their electronic shell structure with geometrical distortions enhancing their HOMO - LUMO energy gap.

This dependence of the structure and stability of smaller cluster on their electronic structure is demonstrated by vanadium which exhibits strong odd/even alternation and size-dependant reactivity changes in its smaller clusters; however these effects decrease with increasing cluster

size. Similar effects are also observed for vanadium clusters containing impurity atoms, such as O and C. In this case the influence of the impurity atom is observed to decrease as the cluster size increases, and at $n \approx 20$ their effects are insignificant. For intermediate-size clusters, the ability to exist in a number of geometric and electronic isomers acts to stabilize the clusters. This reduces the dominance of electronic considerations. As the cluster size increases further, structural considerations gain in importance as near-bulk properties are approached (148)(156)(157).

Changes in cluster binding, in addition to occurring almost linearly with size, also occur across periods. Cobalt clusters for the most part exhibit icosohedral structures, with the detailed dependence of structure on cluster size being complex, while no such behaviour is found for iron. Nickel clusters, however, show definite icosohedral structures, with their reactions with ammonia clearly displaying the magic numbers known for rare gas clusters. This trend towards icosohedral structures at the right hand side of the first transition series is a consequence of the decreased spatial extent and the increased filling of the 'd' orbitals. If the bonding in nickel clusters is predominantly from the electrons in the spherically symmetrical 's' orbitals, then it may not be surprising to find the same structures as for clusters of the spherically symmetrical rare gas atoms (148).

Cluster binding energies are also observed to result in similar trends being displayed in cluster reactivities across a transition

series. The early transition metal ions show, in their atomic form, a marked tendency to undergo C-H bond activation and dehydrogenation reactions (158), while the later transition metals are selective towards C-C bond activation and alkyl elimination reactions (159)(160). Like V^+ vanadium clusters undergo dehydrogenation reactions with ethene, with the exception of V_3^+ . Chromium clusters however are unreactive apart from Cr_2^+ , while manganese is unreactive in all but its atomic form. Clusters of the later transition metals readily undergo dehydrogenation, with smaller nickel clusters also undergoing dealkylation reactions as does copper which also forms various complexes (147). Hence as cluster size increases, dehydrogenation becomes more favourable for all transition metals, with C-C bond cleavage being confined to the post-nickel metals.

The later metals in the first transition series correspond to the idealized single electron model and show icosahedral tendencies. This behaviour is also demonstrated as their respective groups are descended, in addition to enhanced reactivities. This is shown by the nickel group: nickel undergoes dehydrogenation with butene while platinum clusters are capable of causing the dehydrogenation of benzene. However for complete filling of the 'd' levels, covalent behaviour is observed, as shown for zinc and smaller mercury clusters.

As regards the post-transition metals, group IIIA shows similar reactivities and spectral phenomena (161), while groups IVA and VA show increasingly covalent tendencies. Lead clusters are observed to bind four ammonia molecules, of which the first two bond predominantly

covalently while the third and fourth bond mainly by electrostatic interactions. Similar behaviour is found for methanol and methylamine and has been attributed to $6s/6p$ hybridization.

The increasing 'p' nature of the clusters leads to the formation of three-dimensional framework structures of the types demonstrated by carbon, silicon and antimony. These clusters are observed to exhibit clear preferences in forming certain cluster units and fragment by fission or the sequential loss of larger units as opposed to the monatomic dissociations more commonly observed (117).

In the case of antimony clusters, which are built from Sb_4 units, the mass spectra are dominated by peaks corresponding to $(Sb_4)_n^+$ clusters and evaporative dissociation is observed to occur via the loss of Sb_4 units. The stability of the Sb_4 moiety has been confirmed by ionization potentials and binding energies, which are well below those for antimony atoms in the bulk metal (162)(163).

Hence the properties of many clusters can be described by their electronic structures, with their corresponding band gaps being one of the dominant factors in determining the geometry adopted. These can be described as;

a) Monovalent metals, which as a consequence of their dominant high 's' electron delocalization can be described by shell models. This applies to the later transition metals due to the increased contribution of the s orbitals.

b) Divalent metals, in which a transition from van der Waals to metallic structures is observed, as clearly demonstrated by mercury.

c) Small trivalent metals, The properties of small trivalent metal clusters, $n < 10$, are dominated by p-bonding, while in larger clusters the valence electrons become delocalized and shell models apply.

d) Late post-transition metals, in which the bonding is predominantly p-bonding, with electron counting rules of the form described by Wade applying (164). This is represented by antimony clusters

EXPERIMENTAL

2.1.1 THE MASS SPECTROMETERS

This work described in this thesis was carried out using a modified MS-50 double-focusing instrument and a 'Concept' four-sector instrument (Kratos Analytical Instruments). Both of these instruments utilise forward-geometry mass spectrometers and are fitted with a DS-90 data system. The bombarding atom beams were produced using a radially mounted Ion Tech Ltd. Saddle-field fast atom bombardment gas gun (FAB-11-NF). The 'Concept' four-sector mass spectrometer consists of two horizontally-opposed forward-geometry mass spectrometers connected via a collision cell, termed the flexicell, in which ion-molecule reactions can be carried out. (Fig 2.1.1)

The flexicell consists of a series of slit plates, two post acceleration detectors, collectors and a collision cell, fig. 2.1.2 , and is situated between the resolving slit of the first mass spectrometer, MS1, and the source slit of the second mass spectrometer, MS2. The first of these sets of slits is the input lens which can be used to focus the ion beam emerging from the resolving slits of MS1 onto a number of points enabling the operation indicated;

- 1) PAD1, when MS1 is used under normal operating conditions.

2) To focus the ion beam onto a region within the collision cell, where it may undergo ion-molecule reactions with the collision gas.

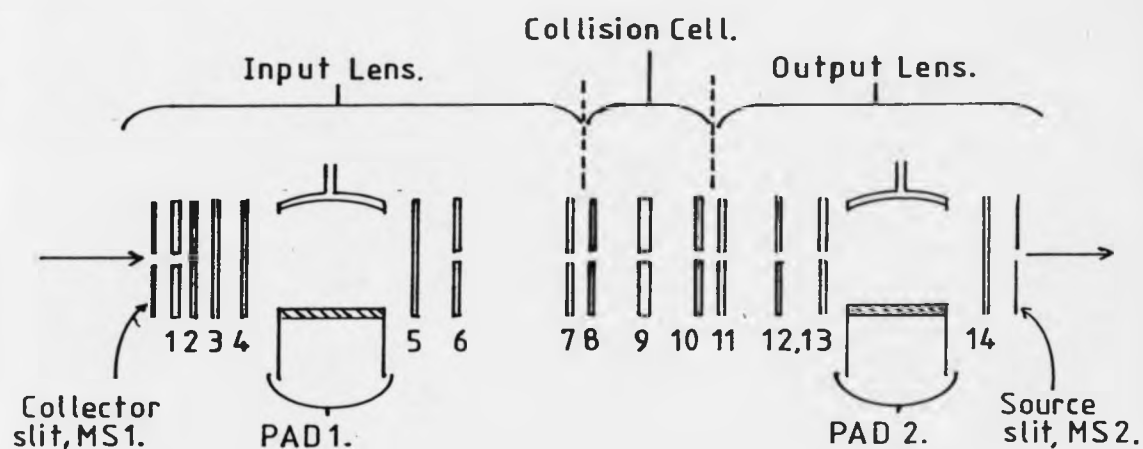
The second major component is the collision cell, which consists essentially of a metal box containing input and output slits, on opposite sides. The collision cell may be maintained at earth potential or at a positive potential of up to 8kV, this potential being applied in order to reduce the energy of collisions between the incident ion beam and the collision gas and/or to accelerate the post-collision ions out of the cell towards the output lens and MS2.

The final major component is the output lens which consists of a number of slits which focus the post-collision ion beam onto the source slit of MS2. PAD2 allows the intensity of the ion beam emerging from the collision cell to be monitored before entering MS2.

By setting up the 'concept' 4-sector spectrometer in MS1/MS2 mode the collision cell enables collision-induced dissociation experiments to be carried out. In this kind of experiment ions emerging from the source are mass analysed by MS1 to produce an intense ion beam of a given mass, parent ion, and are focused into the collision cell.

In the collision cell the ion beam undergoes collisions, with the essentially stationary collision gas, at a specified energy. The resulting ions, both parent and daughter ions, then pass via the output lens into MS2 which is operated as a standard double-focusing mass

Fig 2.1.2 The Flexicell - Plate and Slit arrangement



- | | | |
|----|---|---------------------------|
| 1 | Y | Deflection 1. |
| 2 | Z | Deflection 1. |
| 3 | Z | Focus 1. |
| 4 | | Earth |
| 5 | Z | Deflection 2. |
| 6 | Y | Focus 1. |
| 7 | Y | Focus 2 / Y Deflection 2. |
| 8 | | Cell guard. |
| 9 | | Collision cell. |
| 10 | | Cell guard. |
| 11 | Y | Focus 3 / Y Deflection 3. |
| 12 | Y | Focus 4. |
| 13 | Y | Deflection 4. |
| 14 | Z | Deflection 3. |

spectrometer. The resulting spectrum shows the parent ion, mass selected by MS1, and its daughter fragment ions.

By varying the collision cell potential and the collision gas pressure, the energy and number of collisions taking place may be varied.

2.1.2 THE FAB GUN

The sample for both instruments were introduced into the ion source on a axially-mounted FAB probe fitted with either a copper or stainless steel tip. Here the sample underwent bombardment by a beam of highly energetic atoms produced by the FAB gun . This bombardment took place at a grazing angle of 15° to 20° , in order to produce maximum secondary ion yield in a forward direction (7)(8).

The ions formed were then accelerated at 8 kV and focused into a narrow beam before entering the mass spectrometer. The major factors affecting the rate at which equilibrium is reached following ionization can be summarised.

1) Ion-molecule reactions may proceed between the newly ionized moiety and a neighbouring species. This reaction may result in various third-body reactions

2) The energy content of a cluster increases as the neutral species rearrangements to accommodate a newly-formed charge; this may lead to extensive evaporation dissociation as the cluster cools.

3) Kinetic energy release measurements have shown that clusters of neighbouring x-values have comparable internal energies.

4) The rates of unimolecular dissociation decrease with time after the ionization event. This is because of the energy distribution of a cluster population, with the number of clusters having energies in excess of their dissociation threshold decreasing on cooling (165).

2.2 THE EFFECTS OF MATRICES ON VARIOUS ASPECTS OF THE FAB SPECTRUM

The FAB spectra obtained for various sample compounds have been studied with a range of matrix compounds and co-solvents. These have taken the forms of solutions or mulls, and have enabled the production of large numbers of spectral ions over prolonged periods of time. However, the choice of matrix and sample conditions have been found to influence the type and relative intensities of the species observed in the final spectrum. Hence the chemical properties of a given matrix and/or co-solvent may result in unrepresentative fragmentation patterns. Matrix peaks may also dominate or obscure vital spectral information by overlap or other misleading phenomena.

Since the nature of the matrix and/or co-solvent is so important, a number of investigations have been carried out into the effects of various matrix compounds and co-solvents (53). In this study the effects of the physical constraints of the sample have been studied for a range of matrix compounds.

2.2.1 THE MATRIX COMPOUNDS

Investigations were carried out into the effects of various matrix compounds on the observed FAB spectra for a number of compounds, in addition to their effects on cluster formation. In the latter study the spectra obtained during the use of matrix compounds were directly compared with those obtained for a single crystal of uranyl nitrate and the near identical spectra obtained by the use of continuous flow FAB-MS for aqueous uranyl nitrate.

Samples containing dimethylsulphoxide and related matrices were found to be dominated by matrix peaks and matrix adduct species, often making spectral interpretation unreliable, if not impossible. The spectral species were also observed in many cases to be non-reproducible and hence the use of these matrix compounds was assumed unjustifiable.

Glycerol and nitrobenzyl alcohol, being the most widely used FAB matrices, were found to give rise to largely reproducible FAB spectra over a range of cluster sizes. Adduct formation was in many cases significant and favoured the production of lower mass cluster species. However the use of glycerol, thioglycerol and nitrobenzyl alcohol was

useful, by allowing the comparison of the spectral species observed in the FAB spectra of a number of ligated metal complexes.

The use of sulpholane as a matrix compound was found to be unexpectedly useful in the study of both the fragmentation patterns of metal complexes and cluster formation. The spectra obtained closely resembled those obtained for pure complexes and compounds. Sulpholane was found to promote cluster formation without the formation of matrix adducts and to give rise to stable intense ion beams over extended periods of time when dry, although when allowed to absorb large amounts of atmospheric water, beam intensities could be prone to instability. Uranyl compounds were also found to be directly soluble in sulpholane.

Over the range of matrix compounds studied their chemical character was found to significantly affect ion yields, their relative distributions and abundances as well as influencing, in some cases, the species present. Matrix compounds were found to act in a similar way to reagent gases in chemical ionization, CI-MS, by either enhancing or suppressing the yields of species, this was most notable for the processes leading to cluster formation. So the choice of matrix can directly affect the relative abundances of species by favouring a particular fragmentation pattern or reaction pathway. In order to safeguard against this, in the present study, the spectra described have been reproduced on several occasions and are the result of the computer averaging of many mass spectra. In addition the spectra obtained for several matrix compounds have been compared in order to guard against the effects of a single matrix compound.

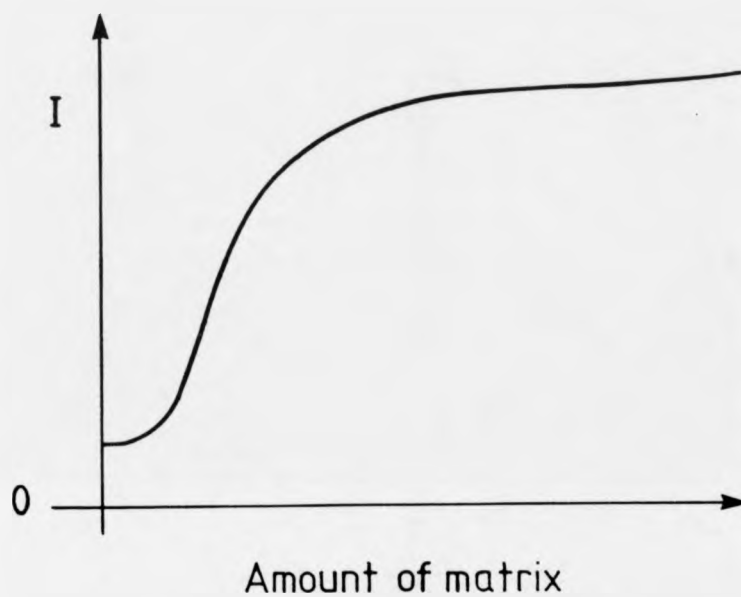


Fig 2.2.1 A Schematic Representation of the change in Total Ion Yield with Increasing amounts of Matrix Compounds

2.2.2 THE EFFECT OF SAMPLE TEMPERATURE

The effect of sample temperature during bombardment was investigated, this was carried out by assuming frozen samples to undergo uniform heating during bombardment. Hence the duration of bombardment can be assumed to be a measure of the relative temperatures experienced by samples.

The effect of the sample undergoing heating in this manner was to influence the total ion yields. These were observed to rapidly increase during the early stages of bombardment, heating, before gradually decreasing. The period for which a sample produced near optimum ion yields was found to be prolonged by applying secondary cooling to the probe tip. Hence the ion yields were found to be temperature dependent. In addition, the period of bombardment required before optimum ion yields are produced is seen to vary between matrices. This suggests that ion yields are dependent on the relative rates of matrix removal. If the rate of matrix sputtering is considered to be constant then the temperature of the sample will strongly influence the evaporation of matrix which may be expected to increase with sample temperature. Sample temperature was not observed to be as significant for samples containing no matrix. Hence the effective lifetime of a given sample and the stability of the total ion yields can be enhanced by careful manipulation of the sample temperature during bombardment.

2.2.3 THE EFFECT OF PROBE TIP SIZE

The cluster spectra for the uranyl and selected oxo-lanthanide ions were recorded using a range of probe tip diameters in order to investigate the relationship between probe tip sizes and their relative ion yields.

| Probe tip diameter | Cross sectional area | Ratio of areas |
|----------------------|----------------------|----------------|
| (mm ⁻¹) | (mm ⁻²) | |
| 2.5 | 4.91 | 1 |
| 3.5 | 9.62 | 2 |
| 5 | 19.63 | 4 |

For a given sample size minimal changes were observed in ion yields on increasing the cross sectional area of the probe tip in the absence of a matrix compound. However, on the addition of set amounts of matrix dramatic increases in ion yields were observed with increasing probe tip size, with the 5 mm diameter probe tip producing approximately ten times that for the 2.5 mm probe tip.

For a fixed probe tip size the increase in ion yields were found to increase rapidly on the addition of small amounts of matrix. However the relative increase was observed to decline when excess matrix was present, thus showing signs of matrix saturation (Fig. 2.2.1). This is similar to the behaviour displayed by ion yields with increasing sample concentration, with the position of the onset of saturation being influenced by the addition of co-solvents.

Hence, if a sample of fixed size is assumed to form a uniform layer, then the total ion yield observed is found to be dependent on the amount of matrix present. This increase in ion yield is found to be due to an increase in the relative intensities of the higher mass clusters. This behaviour is most notable when sulpholane matrix is present. In addition the effective lifetime of a fixed sample size was found to be dependent on the matrix present, with samples being rejuvenated when recharged with fresh matrix. This shows that the total ion yield and extent of cluster formation is directly related to the type and amount of matrix present and less dependent on cluster size.

The behaviour described above gives rise to the question of why the choice of matrix, its relative abundance and the size of the probe tip should influence the relative intensities of the clusters produced so strongly. This was investigated by the use of a number of probe tips which had the same cross sectional areas as above, but however split to give two equal semicircular sectors. These were charged separately with matrix and pure sample, with care being taken to avoid cross contamination. The tip was then subjected to FAB in the usual manner. After bombardment one of these sectors was cleaned before reintroduction into the mass spectrometer to allow the analysis of the remaining loaded probe tip sector for traces of contamination. A series of similar experiments were repeated with several matrix compounds.

The resulting spectra displayed evidence of the formation of oxo-metal clusters and the associated matrix adducts similar in character to those observed using a single sector probe tip. This behaviour was most

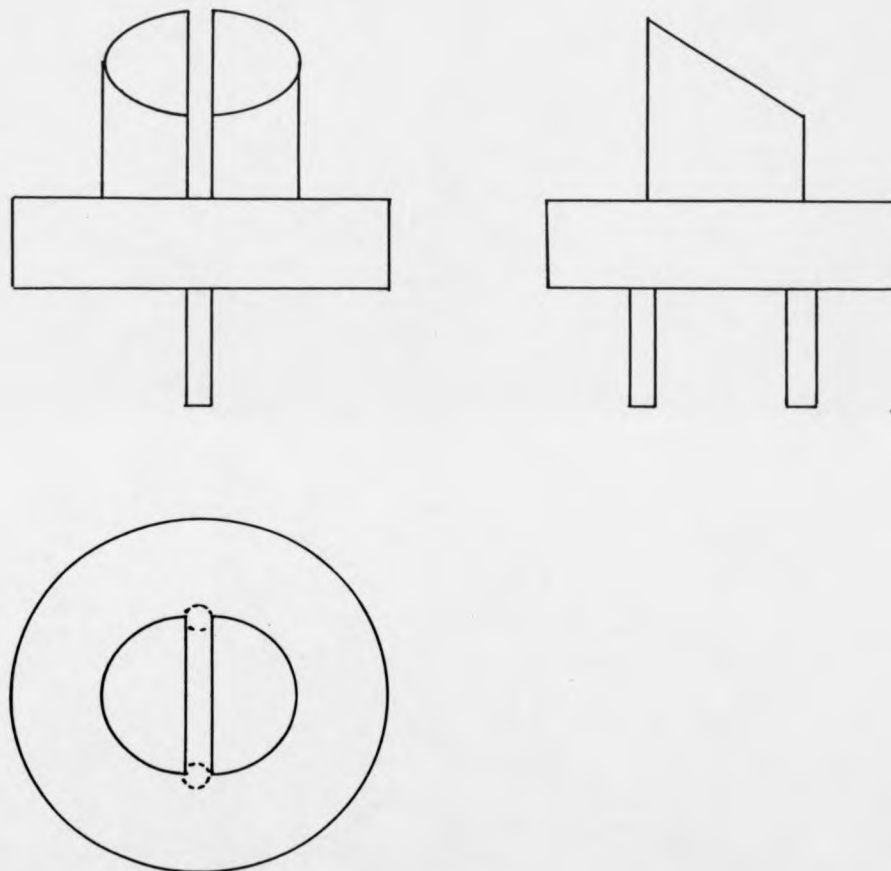
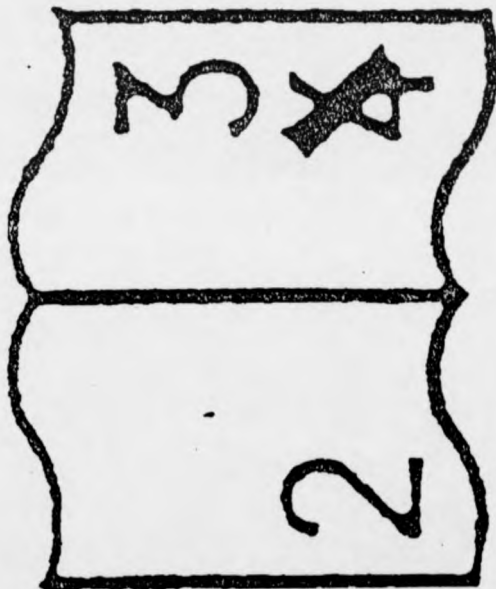


Fig 2.2.2 Diagrammatic Representation of the Twin-Sector Probe Tip

PAGINATION ERROR



94.

notable for dimethyl sulphoxide and glycerol, and shows the presence of matrix induced reactions. However, very little evidence was observed to suggest that these adducts were formed by cross contamination between the probe tip sectors. The strong similarities in the FAB spectra produced to those resulting from the use of a standard probe tip suggesting that matrix induced adduct formation and cluster formation must be taking place in the gas phase above the probe tip.

2.3 THE EFFECT OF SOURCE PRESSURE ON CLUSTER AND ADDUCT FORMATION

A series of investigations were carried out to explore the effect of increasing the gas pressure in the source during FAB, samples containing a range of matrices. During these experiments the source block was fitted with covers to reduce the source conductance, while additional buffer gases were introduced into the source using the standard Kratos CI gas inlet system (Fig. 2.3.1).

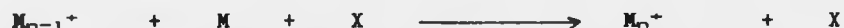
The effect of increasing the source pressure is best examined by considering its effects on various aspects of the resulting spectrum. For samples containing no matrix, various pressures of argon gas were introduced as a buffer gas into the source during bombardment. For low argon pressures no notable effects on the distribution of clusters in the resulting spectrum was observed, although the total ion current showed a slight decrease with extended bombardment times.

As the buffer gas pressure was increased, in a stepwise manner, the total ion current was found to increase slowly with increasing source pressure. This behaviour continued until a critical pressure was reached after which a rapid increase in total ion current was observed for small increments in pressure. At very high pressures evidence of a gradual decrease in total ion currents was observed, reflecting source saturation (Fig. 2.3.3).

Similarly, the presence of increasing buffer gas pressures in the source is found to influence the relative intensities of the cluster

species observed in the resulting spectrum. At very low buffer gas pressures and in the absence of a matrix compound a slight increase in the relative intensity in the cluster spectrum is observed. However, as the pressure increases the relative intensity of the higher mass clusters are observed to decrease rapidly. At higher buffer gas pressures evidence of fine structure in the distribution of the spectral intensities is observed, with possible odd/even alternation and enhanced spectral intensities for $x = 3$ being observed in the uranyl cluster spectrum. For samples containing a matrix compound or co-solvent, at low buffer gas pressures an increase in the relative intensities of the adducts formed is observed. However as the buffer gas pressure increases the number of observed adducts decrease, with no adducts being detected at high buffer gas pressures.

This suggests that the buffer gas may act so as to stabilise the formation of the higher mass cluster at very low pressures, possibly by a third-body assisted association reaction,



with the excess exothermic energy being removed by the buffer gas. However on further increasing the buffer gas pressure the increased number of collisions increase the possibility of clusters undergoing collision induced dissociations or collisions resulting in the production of charged species. This is displayed in the increased relative intensities of the lower mass clusters and the corresponding increase in total ion currents observed.

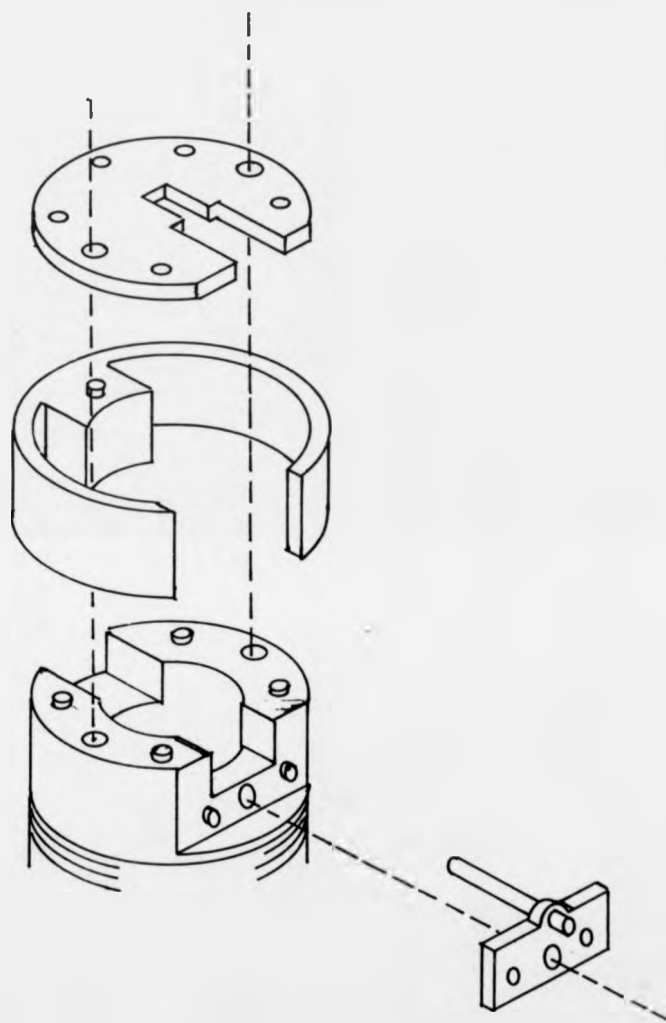
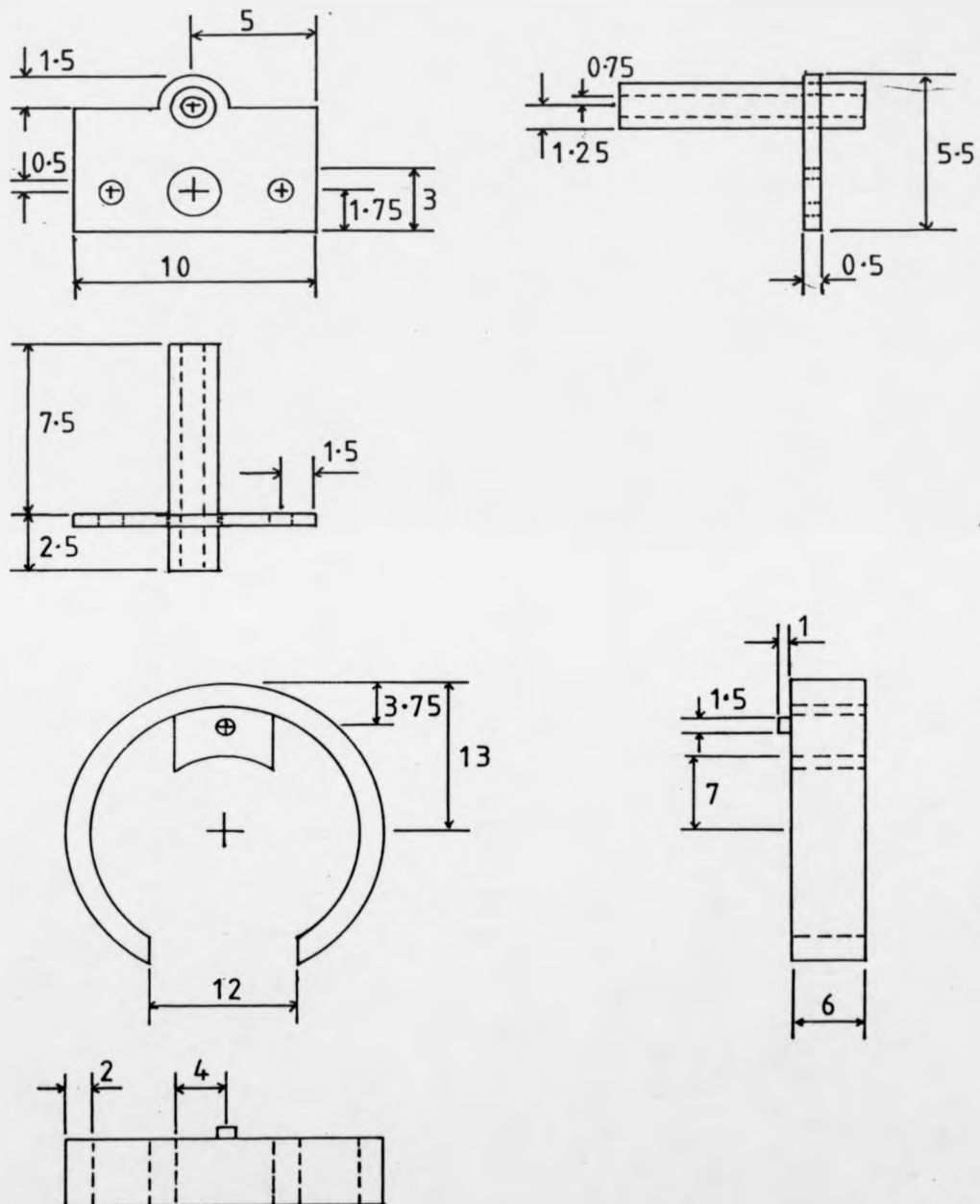
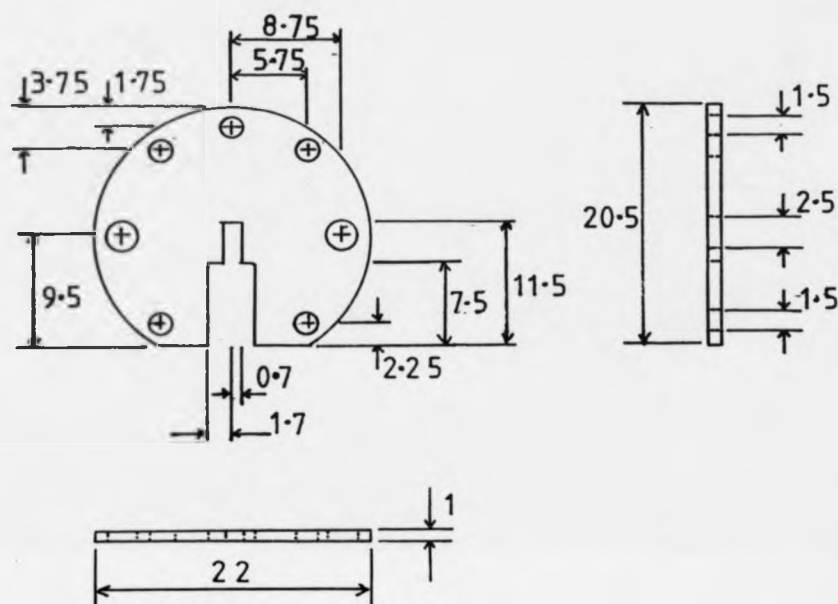


Fig 2.3.1 Diagrammatic Representation of the Position of the Source Covers to reduce the Source Conductance, hence Allowing the Effect of Source Pressure on Cluster Formation to be Studied

Fig 2.3.2 a) Gas Inlet Plate, Materials Stainless steel, all Dimensions in mm



b) Source Block Cover, Material 'PBEK', all Dimensions in mm



c) Source Lens Plate, Material Stainless steel,
all Dimensions in mm

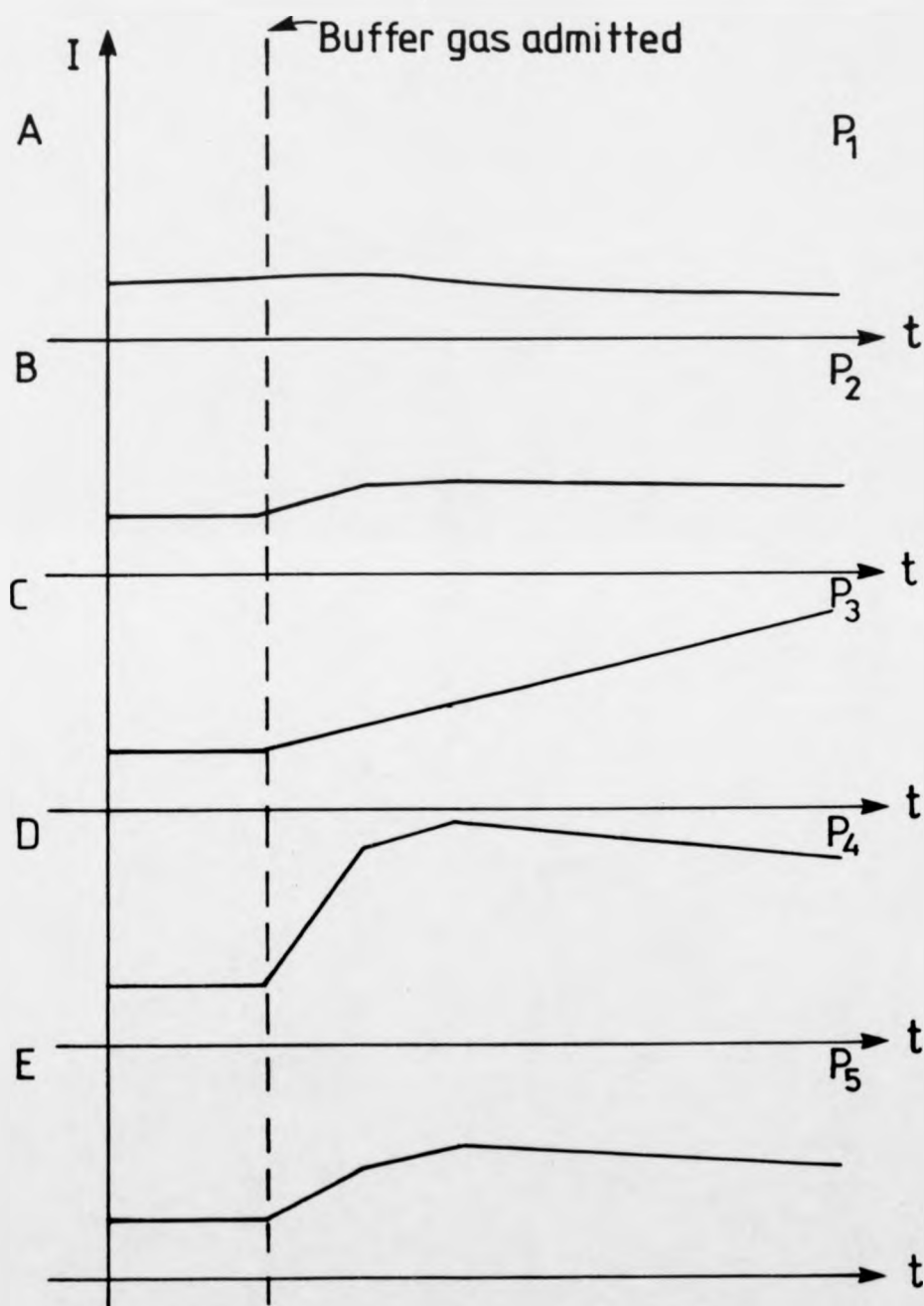


Fig 2.3.3 Schematic Representation of the Change in Total ion current, I , with Increasing Duration of Bombardment, t , at a Number of Buffer Gas Pressures

$$P_1 < P_2 < P_3 < P_4 < P_5$$

2.4.1 MATERIALS

All chemicals used were of standard laboratory grade.

| | |
|----------------------------|---------|
| Uranyl nitrate hexahydrate | Fisons |
| Uranyl acetate dihydrate | B. D. H |
| Uranium trioxide | B. D. H |
| Thorium nitrate | B. D. H |
| Lanthanum nitrate | B. D. H |
| Cerium nitrate | Aldrich |
| Praseodymium nitrate | Aldrich |
| Samarium nitrate | Aldrich |
| Europium nitrate | Aldrich |
| Terbium nitrate | Aldrich |
| Holmium nitrate | Aldrich |
| Lanthanum acetate | B. D. H |
| Cerium acetate | Strem |
| Praseodymium acetate | Aldrich |
| Europium acetate | Aldrich |
| Holmium acetate | Strem |
| Glycine | Fisons |
| L-Alanine | Aldrich |
| L-Valine | Sigma |
| L-Serine | Sigma |

| | |
|------------------------------|----------|
| L-Lysine | Sigma |
| L-Proline | Sigma |
| L-Glutamine | Sigma |
| L-Glutamic acid | B. D. H. |
| L-Tryptophan | B. D. H. |
| Cysteine | Sigma |
| Threonine | Aldrich |
| β -Alanine | Aldrich |
| α -Aminobutanoic acid | Sigma |
| β -Aminobutanoic acid | Sigma |
| γ -Aminobutanoic acid | Sigma |
| Hexachloropropene | Aldrich |
| Sulpholane | B. D. H. |

2.4.2 PREPARATIONS

a) THE PREPARATION OF THE AMINO ACID COMPLEXES OF DIOXOURANIUM(VI)

These were prepared by a standard method, in which uranyl nitrate hexahydrate was added to an aqueous solution of the ligand, in a 4 : 1 mole ratio (53). The resulting solution was then allowed to evaporate in a dark environment.

The resulting complexes for the amino acids took the form of bright yellow oils, apart from those corresponding to L-proline and L-tryptophane which formed yellow-brown oils (possibly due to their aromatic nature).

b) THE PREPARATION OF LANTHANIDE MALONATES

A standard method was used whereby a given mass of lanthanide nitrate was dissolved in a minimum volume of distilled water, to this malonic acid was added (in a 1 : 4 mole ratio respectively). The resulting cloudy solution was evaporated and cooled until a white crystalline solid formed

c) THE PREPARATION OF URANIUM(IV)CHLORIDE, UCl_4 (53)

Uranium tetrachloride was prepared by the reaction of uranium trioxide with hexachloro-propene as a chlorinating agent, giving a final product of high purity and yield.

This was carried out by refluxing uranium trioxide (2.5g) with 25 cm of hexachloropropene in a three-necked flask, under a nitrogen atmosphere, for six hours. The reaction mixture was heated slowly at first until the vigorous initial reaction had subsided, during which the temperature was kept below 373 K. The temperature was then allowed to increase slowly until a steady reflux occurred. At this point a red-brown solid, UCl_3 , was observed at the base of the flask; this was then observed to yield green UCl_4 as the reflux continued. The resulting solid was filtered under a nitrogen atmosphere, washed with dry CCl_4 and dried under high vacuum. The resulting UCl_4 was then sealed in an evacuated tube, due to its hygroscopic nature.

The compounds and complexes formed by the above reactions were analysed using a combination of infra red and UV/visible spectroscopy.

3.1 THE LANTHANIDE ELEMENTS

The lanthanide elements are the fourteen elements directly following lanthanum, La, and corresponding to the partial filling of the 4f orbitals. The bonding undertaken by these elements usually does not involve the 4f orbitals which leads to the lanthanides showing a predominant +3 oxidation state and hence displaying similar chemical characteristics to lanthanum.

The major feature of the lanthanide series is the progressive decrease in the atomic and ionic radii across the series. This is commonly referred to as the lanthanide contraction and is a consequence of the increasing effective nuclear charge experienced by each 4f electron due to imperfect shielding of the electron by the subshells. Although this leads to a regular reduction in metal radius, europium and ytterbium show significant deviations. This is a consequence of europium and ytterbium preferentially forming Ln^{2+} ions as opposed to the Ln^{3+} ions formed by other lanthanides; cerium exhibits a similar but opposite deviation with the formation of the Ce^{4+} ion. The stabilities of these additional oxidation states is due to the enhanced stabilities of their filled and half-filled 4f orbitals.

Another consequence of the lanthanide contraction is the similarity in chemical behaviour between the lanthanides and the alkali / alkaline earth metals. Ce^{4+} is the only stable tetravalent lanthanide ion in solution and solid compounds, although less stable Pr^{4+} and Tb^{4+} can be

formed. Divalent europium, ytterbium, samarium and neodymium can be formed, with Eu^{2+} being by far the most stable as a consequence of its $4f^7$ electron configuration. In europium and ytterbium two electrons enter the conduction band resulting in larger cores and notably lower binding energies. Sm^{2+} and Nd^{2+} can be viewed as trivalent ions with an extra electron forming a conduction band.

The similarities between the different lanthanide ions is clearly demonstrated by their oxide systems. For a trivalent lanthanide Ln_2O_3 is clearly the most stable oxide formed, existing in the following, three possible forms.

A-Type; This form is strongly favoured by the lighter lanthanides and consists of LnO_7 units which approximate to a capped octahedral geometry.

B-Type; This also consists of LnO_7 units, but of three types, two being capped trigonal prisms and one an octahedron. This type is favoured by the middle lanthanides.

C-Type; This is strongly related to the fluorite structure but with one quarter of the anions removed, thereby reducing the metal coordination from 8 to 6, and is favoured by middle and heavy lanthanides. The Ln_2O_3 series are strongly basic, with the lighter members resembling the oxides of group IIA, and insoluble in water.

Cerium, praseodymium and terbium however tend to form the higher oxides CeO_2 , Pr_2O_3 and Tb_4O_7 respectively. The dioxides of these metals have a fluorite structure, forming a related series of nonstoichiometric phases between $\text{LnO}_{1.5}$ and LnO_2 . The lanthanide-oxygen systems for these metals show close similarities.

3.2 THE GAS PHASE CHEMISTRY OF THE LANTHANIDES.

The gas phase chemistry reported for the lanthanide metals is very limited, with lanthanide clusters first being reported by Selbin et al. REFS. They reported clusters formed by fast atom bombardment containing up to nine metal atoms for certain lanthanides, and the collision-induced dissociation spectra for ytterbium oxide clusters. The latter, were found to fragment giving the YbO_4^+ species as the dominant daughter ion. The cluster spectrum of europium has since been described, with clusters containing nine metal atoms being detected (53). Similar work carried out by Daolio et al. using secondary ion mass spectrometry suggested the formation of polynuclear species (167).

3.3 LANTHANIDE OXIDE SYSTEMS

3.3.1 CERIUM OXIDE

The compounds of the cerium-oxygen system lie between $\text{CeO}_{1.5}$ and CeO_2 , corresponding to a number of phases with each successive phase being stable over a wide range of cerium : oxygen ratios. At $\text{CeO}_{1.5}$, a

single A-type hexagonal phase is formed with a second C-type phase, δ , being present at $\text{CeO}_{1.636}$. In the region of $\text{CeO}_{1.704}$ a third rhombohedral phase, δ , is formed; in general the δ phase becomes the stable form at increasing temperatures. At $\text{CeO}_{1.72}$ a second rhombohedral phase, γ is formed, which in turn gives rise to a third rhombohedral phase, β , at $\text{CeO}_{1.712}$. However in the region of $\text{CeO}_{1.947}$, the final α phase is formed with a face-centred cubic structure (168).

3.3.2 PRASEODYMIUM OXIDE

Studies on the praseodymium-oxygen system have shown the existence of a number of phases, each displaying differences in their structural arrangements (170)(171)(172). In the composition range Pr_2O_3 to Pr_6O_{11} a large number of complex phases exist. These belong to the series $\text{Pr}_n\text{O}_{2n-2}$ and denote the change between body-centred cubic and face-centred cubic oxide structures, with the number of oxide phases present depending on temperature and pressure.

At high temperatures the oxide system contains the lowest number of phases; these are

| Composition range | Structure | Phase |
|---|-----------|----------|
| $\text{PrO}_{1.6}$ - $\text{PrO}_{1.6}$ | A-Type | α |
| $\text{PrO}_{1.6}$ - $\text{PrO}_{1.7}$ | C-Type | σ |
| $\text{PrO}_{1.72}$ - PrO_2 | FCC | α |

As the temperature decreases additional phases are formed, with the rhombohedral λ phase developing in the region of $\text{PrO}_{1.715}$ and the triclinic β phase, based on the fluorite cell, developing at $\text{PrO}_{1.83}$. As temperatures are further reduced, other phases develop. The first of these is the rhombohedral ζ phase at $\text{PrO}_{1.777}$ while the non-stoichiometric region $\text{PrO}_{1.8}$ to $\text{PrO}_{1.83}$ develops into the two phases ϵ and δ respectively, each having a fluorite-type structure.

These intermediate phases formed at lower temperatures mark the ordered changeover region between body-centred cubic and face-centred cubic structures and demonstrates disorder-to-order transitions, with the C-type sesquioxide λ being formed at higher temperatures. This phase has a fluorite structure with approximately 25% of its anion sites vacant and ordered.

3.3.3 TERBIUM OXIDE

The terbium-oxygen system shows the presence of a number of phases between $\text{TbO}_{1.8}$ and TbO_2 , marking the changeover between body-centred cubic and face-centred cubic structures.

At $\text{TbO}_{1.8}$ the major phase, σ , has a body-centred cubic structure, C type, which gradually absorbs oxygen to form a second rhombohedral phase, δ , in the region of $\text{TbO}_{1.71}$. This in turn gives rise to a complex third phase, γ , which has either a pseudotriclinic or pseudorhombohedral structure at $\text{TbO}_{1.81}$. On further addition of oxygen,

the rhombohedral β phase is formed at $\text{TbO}_{1.88}$, while above this the final face-centred cubic α phase is formed (173)(174).

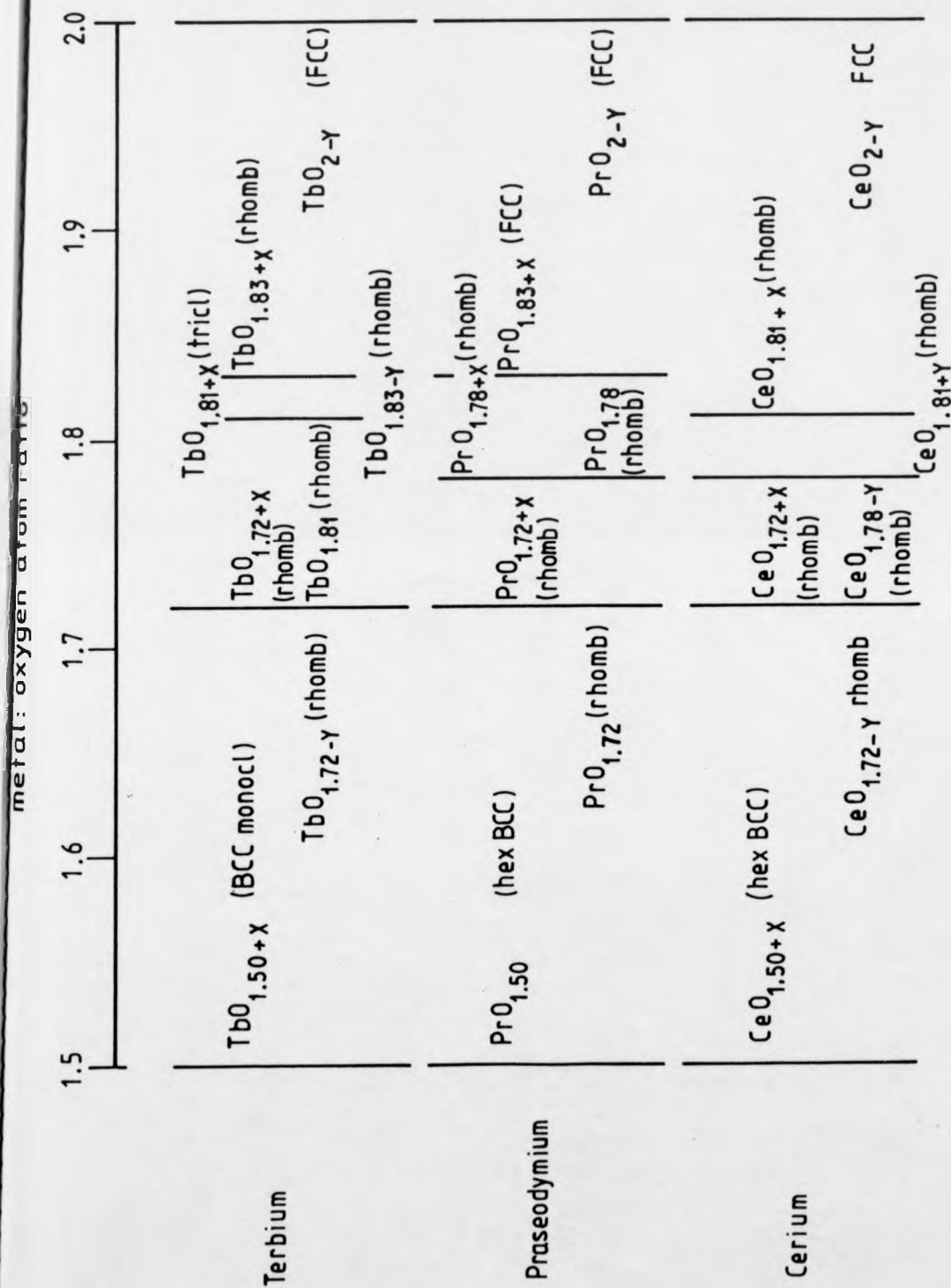
From the above discussion of the oxygen phase systems of cerium, praseodymium and terbium, many similarities can be observed;

1. $\text{LnO}_{1.718}$ appears to mark a change from body-centred cubic to rhombohedral structures for all systems, with the praseodymium and terbium phases being iso-structural.

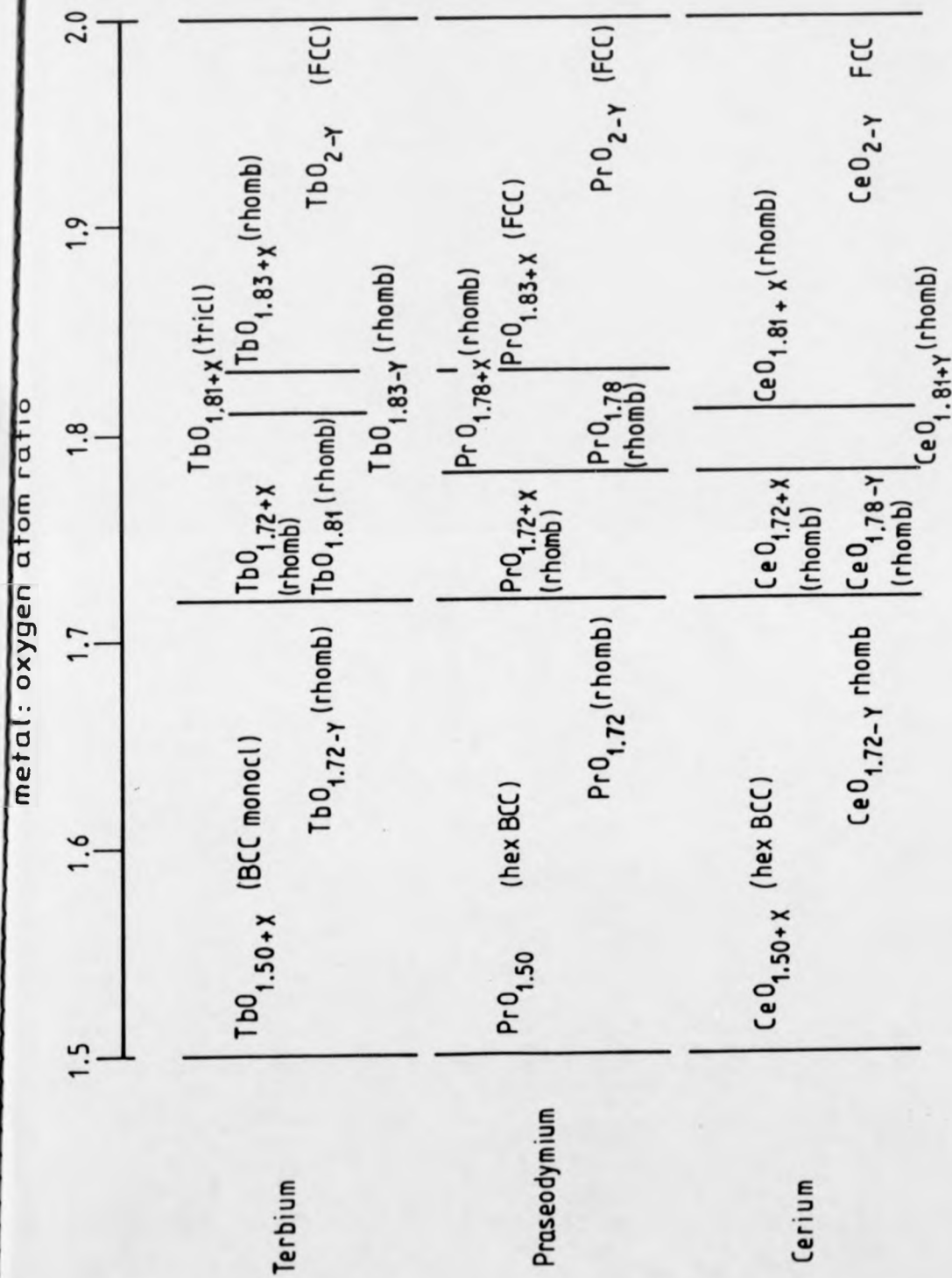
11. At $\text{LnO}_{1.78}$ rhombohedral γ phases are formed for cerium and terbium.

111. At $\text{LnO}_{1.88}$, praseodymium is face-centred cubic in structure while terbium and cerium are predominantly rhombohedral.

These points demonstrate that while all three systems are generally similar, the phases formed by terbium and cerium are very closely related. This might be expected since they each have a single unpaired 4f electron, unlike praseodymium. The oxide system for the divalent lanthanides show a small number of phases to be formed between $\text{LnO}_{1.0}$ and $\text{LnO}_{1.8}$ with europium favouring the formation of $\text{EuO}_{1.88}$.



Oxide systems for terbium, praseodymium and cerium.



Oxide systems for terbium, praseodymium and cerium.

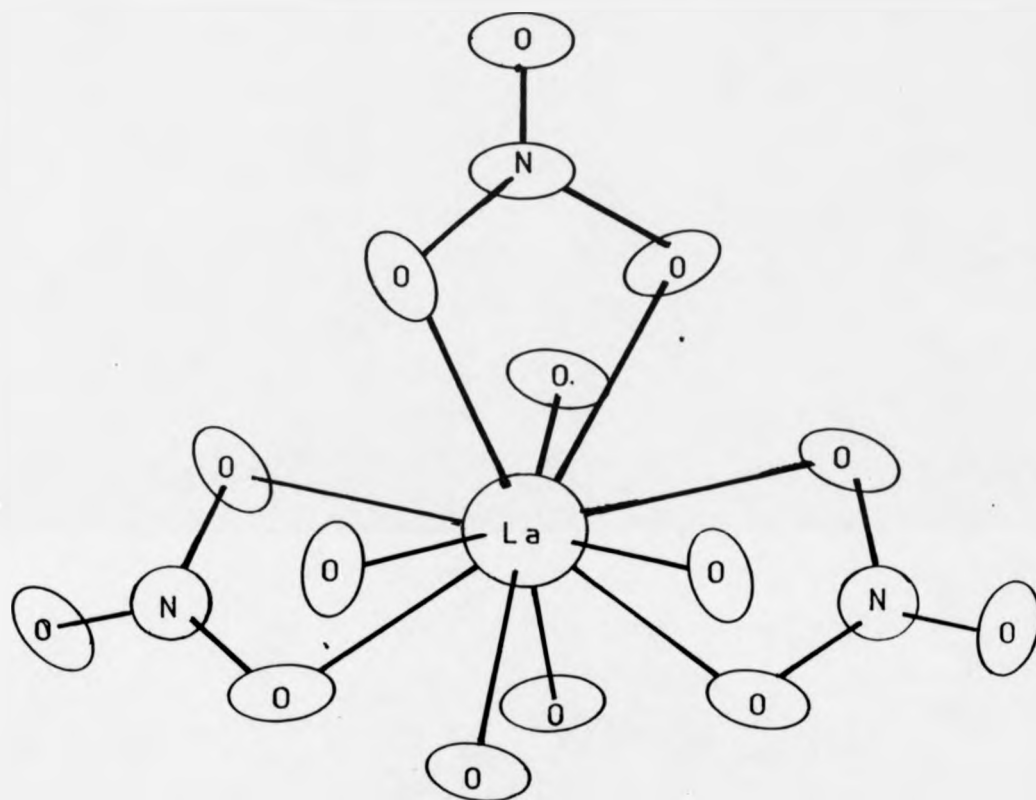
3.4 LANTHANIDE CLUSTERS

3.4.1 LANTHANUM CLUSTERS

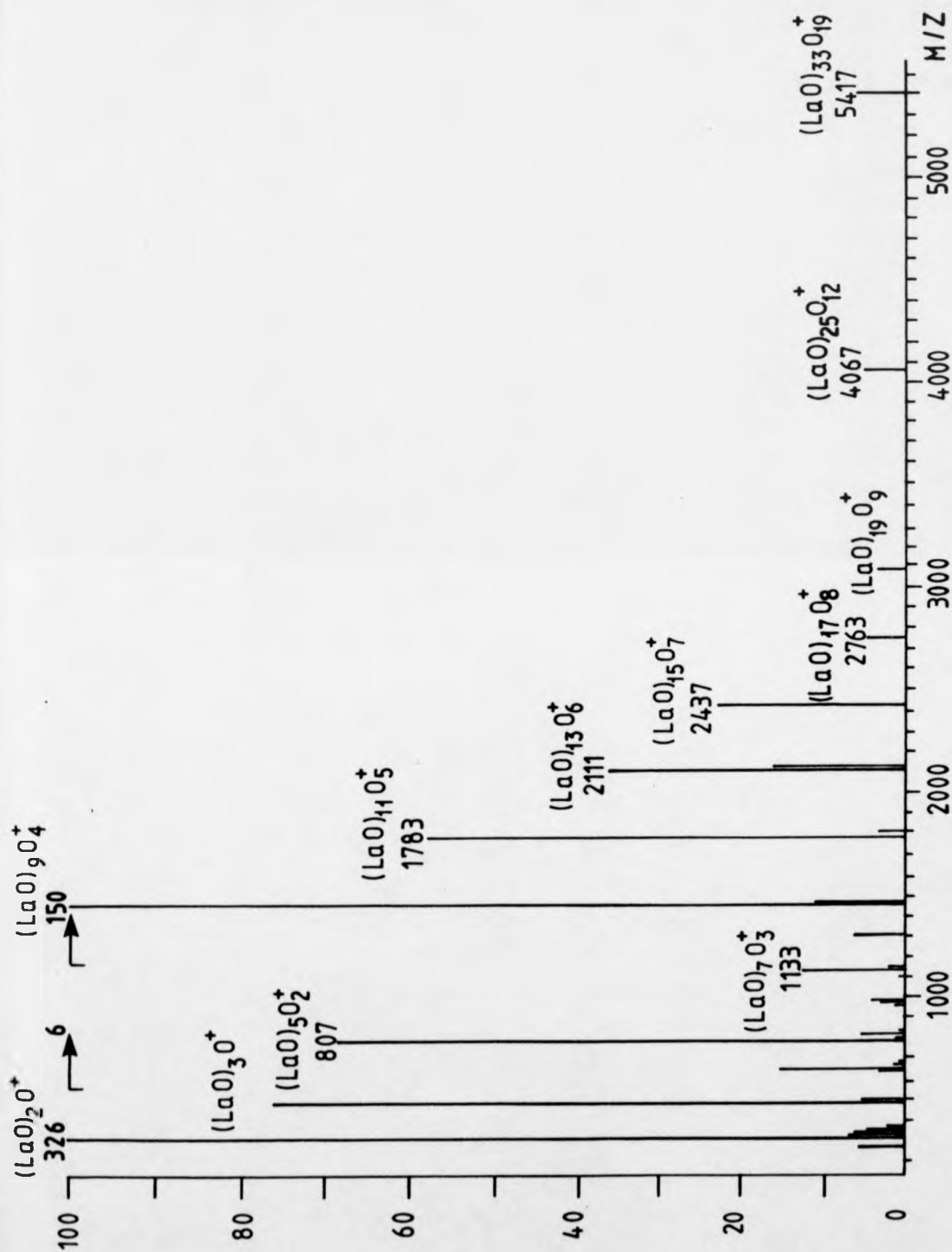
The F.A.B. spectra of lanthanum salts exhibit a series of cluster peaks that correspond to the general formula $[(LaO)_x O_y]^+$ as first reported by Selbin et al. (1966). These clusters show an exponential decrease in intensity with increasing number of lanthanum atoms, x .

In this work the lanthanum cluster spectrum derived from lanthanum nitrate (Spec. 3.4.1) is dominated by the mono-lanthanum series, $x = 1$, with the series showing $(LaO)^+$ to be the most abundant species present with a range of y values from 1 to 5 additional oxygen atoms.

In the di- and tri-lanthanum series the cluster species containing one additional oxygen atom, $y = 1$, was the most abundant, while the spectrum with $y = 2$ dominates in the sequences, $x = 4$ and $x = 5$. This intensity pattern continues with the most abundant species in each consecutive odd series being separated by a mass difference corresponding to the neutral $(LaO)_2O$ unit for smaller clusters up to the series $x = 9$. For the poly-lanthanum clusters following the $x = 9$ series however, the existence of the even-series clusters beyond $x = 9$ is limited and shows a distinct decrease in intensity relative to the odd cluster series, finally disappearing at $x = 12$. This clearly demonstrates even clusters to exhibit lower stabilities than the odd clusters in this region. The dominant species in each odd series are



The structure of $[\text{La}(\text{NO}_3)_3(\text{H}_2\text{O})_5]$.



Spec 3.4.1 The Cluster Spectrum for Lanthanum, with Sulpholane Matrix

again separated by a mass equivalent to $(\text{La O})_2 \text{O}$. This behaviour continues up to $x = 25$.

After $x = 25$ the next reproducible species observed is $[(\text{La O})_{27} \text{O}_{15}]^+$, $m/z = 4423$, which implies the addition of $(\text{La O})_2 \text{O}_3$ to the most abundant species in the $x = 25$ series.

No reproducible peaks attributable to $x = 29$ and 31 species have been detected. However $[(\text{La O})_{33} \text{O}_{19}]^+$, $m/z = 5417$, was observed at a higher intensity than the $x = 27$ species.

The nature of the cluster species observed over various mass ranges, sample conditions and matrices gives rise to clear trends which may infer size-dependent stabilities and structural effects. As the cluster sizes increase, their intensities are found to decrease in an exponential character, with marked odd/even alternation clearly evident. However some of these size-dependent effects were found to be dependent on the matrix present, with the presence of a matrix being observed to increase the degree of formation of higher-order cluster species. This may be due to the matrix participating in third-body association reactions, with the matrix being preferentially dissociated from the resulting clusters, during their subsequent structural rearrangement and fragmentation; thus no higher-order clusters are detected containing matrix molecules.

Even-numbered clusters generally have an $x : y$ ratio of 0.5, with their intensities decreasing with increasing cluster size so that they rapidly become undetectable above $x = 9$.

Odd clusters however demonstrate quite different behaviour which gives rise to a number of distinct regions as the cluster size increases (Fig. 3.4.1). The first of these regions shows $x : y$ to increase from 1 to 9 and is characterised by the steady addition of $(\text{LaO})_2\text{O}$ units between successive members of the odd-cluster series. The next series, $x = 9$ to 25, is characterised by the separation of the observed clusters by masses corresponding to $(\text{LaO})_2\text{O}$ units and a $x : y$ ratio of 0.44 to 0.48 as the stepwise incorporation of additional oxygen atoms continues. However between $x = 25$ and 27, the addition of $(\text{LaO})_2\text{O}_3$ leads to a sudden increase in the $x : y$ ratio from 0.48 for $x = 25$ to 0.55 for $x = 27$. This abrupt increase in the $x : y$ ratio which is consistent with the coordination of a larger lanthanum-oxygen moiety, may signify a sudden change in configuration or structural arrangement. The $x = 27$ species were also noted to have markedly lower intensities than the preceding cluster series, while the series in the region of $x = 28$ to 33 were detected only with difficulty. This sudden drop in intensity and the absence of later members of the series would suggest that an abrupt drop in cluster stability occurs at $x = 25$, while the repeated detection of the $x = 33$ species, $[(\text{LaO})_{33}\text{O}_{19}]^+$, $m/z = 5417$, implies the species to exhibit an enhanced stability relative to the preceding clusters, and may denote the attainment of an inherently more stable structural arrangement.

| Range in X | Range in Y | Increase in Y | Unit added |
|------------|------------|---------------|-----------------------------------|
| 1 - 9 | 1 | 0,1 | (LaO) |
| 9 - 25 | 2 | 1 | (LaO) ₂ O |
| 25 - 27 | 2 | 3 | (LaO) ₂ O ₃ |
| 27 - 33 | 6 | 4 | (LaO) ₆ O ₄ |

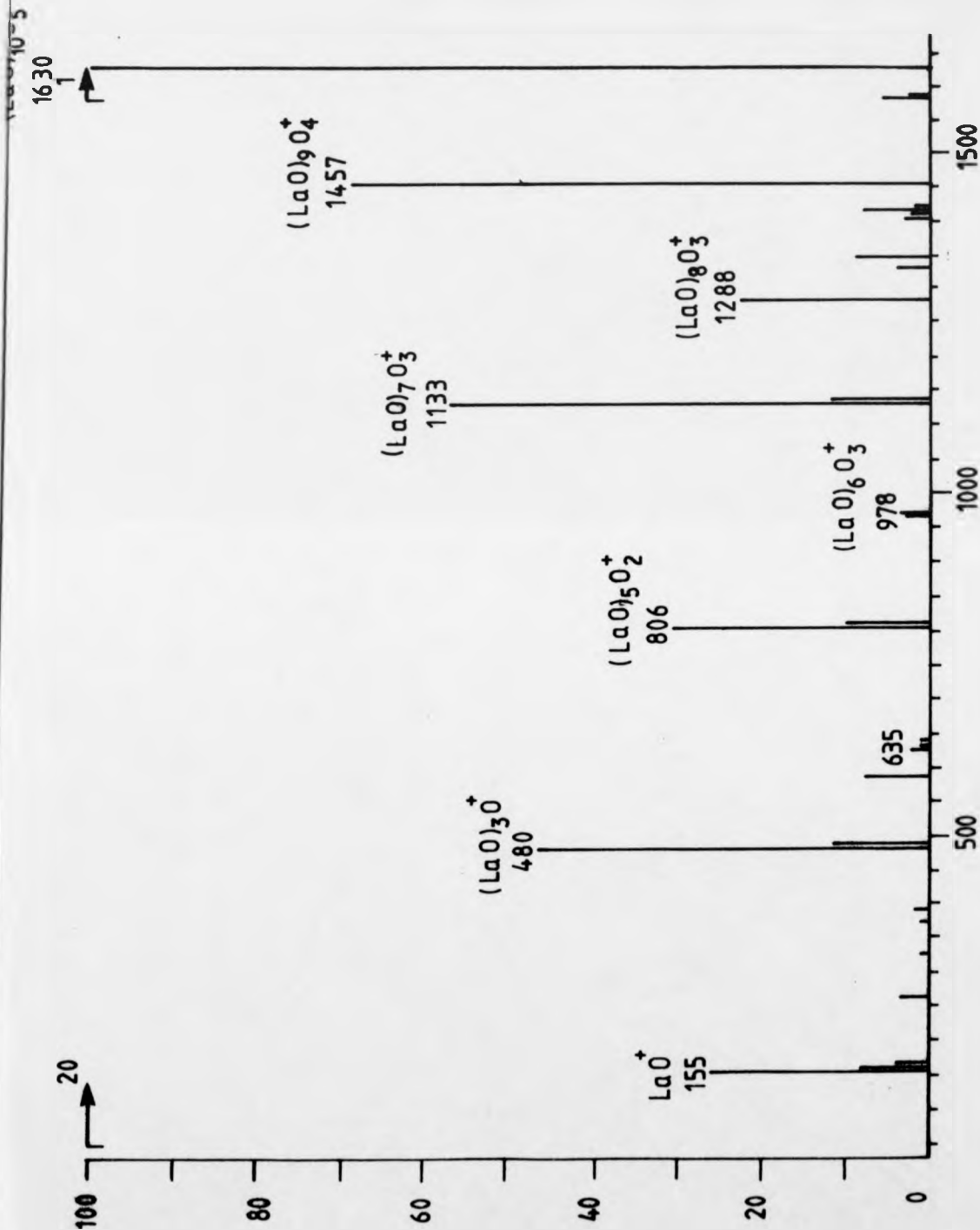
Fig 3.4.1 The Ranges of x and y observed for Each Successive Series for Lanthanum-Oxygen Clusters, $[(\text{LaO})_x\text{O}_y]^+$

An additional series of clusters was repeatedly detected at lower intensities than the lanthanum-oxygen clusters described above. These lower-intensity species were detected over the region $x = 9$ to 18 and followed the same general formulae as the above clusters, but have an $x : y$ ratio of approximately 0.125. The relative intensity of these species was very low and showed the usual exponential decay.

The collision-induced dissociation (CID) of a number of lanthanum-oxygen clusters was carried out using argon and xenon over a range of collision gas pressures, with the flexicell being maintained at a potential of 2 kV.

The CID spectra all displayed the same basic fragmentation patterns. In most cases only odd cluster species were observed, with the even species being of low intensity if detected at all. These were separated by 336 amu, indicating that fragmentation takes place via the sequential loss of $(\text{La O})_2 \text{O}$ units between each successive odd daughter cluster. However the fact that the presence of even clusters depends on the collision gas pressure may suggest that the fragmentation occurs via the sequential loss of two neutral moieties between odd-cluster series as opposed to the loss of a single unit.

Further investigations have suggested that the fragmentation takes place via the initial loss of a $(\text{La O}) \text{O}$ unit from the odd cluster followed by the spontaneous loss of (La O) from the resulting even cluster. This is illustrated for $[(\text{La O})_{10} \text{O}_2]^+$, which is found to

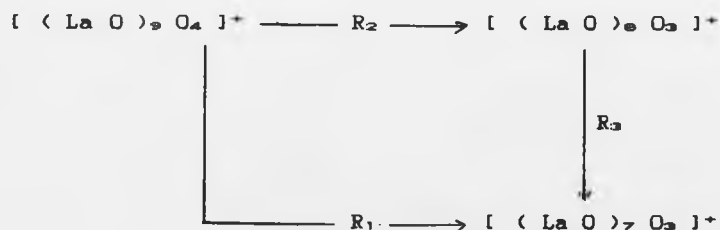


Spec 3.4.2 The CID Spectra of $(\text{LaO})_{10}\text{O}_e^{+}$, $m/z = 1630$, Using Argon Collision Gas, Flexicell At 2KV, 30% Transmittance

follow the fragmentation path shown in Fig. 3.4.2 at 20 % transmission using argon as the collision gas (Spec. 3.4.2).

Thus the fragmentation of the lanthanum-oxygen clusters may occur via two possible dissociation pathways. At low collision gas pressures the sequential loss occurs of $(\text{La O})_2 \text{O}$ moieties from each successive odd daughter-cluster. Under the multiple-collision regime occurring at higher pressures, the lower-energy pathway involving the formation of an intermediate even cluster plays a more significant role, with the energetically-labile even cluster undergoing collisional stabilization. For example;

Fig. 3.4.2



At low collisional gas pressures R_1 is equal to R_2 , since the resulting even clusters are formed with energies above their dissociation thresholds. However at higher pressures R_3 decreases as $[(\text{La O})_8 \text{O}_3]^+$ becomes increasingly collisionally stabilized.

The CID data combined with those from the high mass spectra of the lanthanum-oxygen clusters show odd clusters to be of higher stability

than their neighbouring even clusters throughout the mass range studied. This is clearly demonstrated by the CID spectra. In addition the mass spectral data also suggest that 'magic-number' clusters of enhanced stability exist at $x = 9, 25$ and 33 .

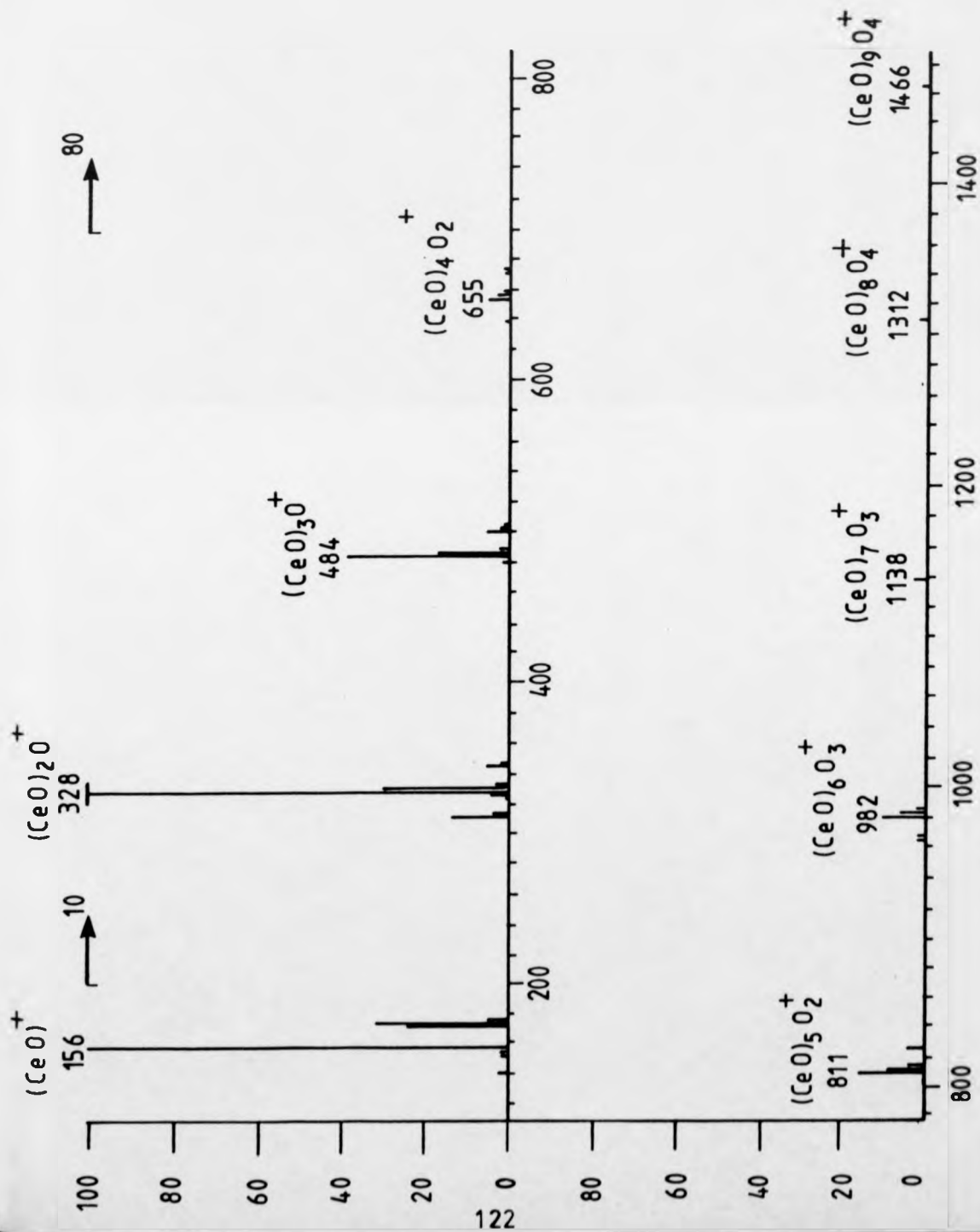
3.4.2 CERIUM CLUSTERS

The clusters formed by cerium were found to fit the general formula $[(\text{Ce O})_x \text{O}_y]^+$, with all the clusters observed existing as mono-positive ions.

The spectra studied showed the presence of both odd and even cluster species, with the intensities of both decaying in a similar exponential manner and with each series of a given x value containing a number of clusters corresponding to a range of y values. This range of y values was found to decrease with increasing cluster size as measured by x .

The mono-cerium series, $x = 1$, displayed y values between 0 and 6, with Ce O^+ ($m/z = 156$) being the dominant species observed, regardless of the nature or conditions of the matrix.

For the di- and tri-cerium clusters, the species containing one additional oxygen atom was found to be the most abundant, that is $m/z = 328$ and 484 respectively, while the $x = 4$ and 5 series showed clusters featuring $y = 2$ to be dominant. The y values increased further to $y = 3$ for the series with $x = 6$.



Spec 3.4.3 The FAB Spectrum of Cerium Nitrate

However the $x = 7$ series showed the cluster species $[(\text{Ce O})_7 \text{O}_3]^+$, $m/z = 1140$, and $[(\text{Ce O})_7 \text{O}_4]^+$, $m/z = 1172$, to be of higher intensity than the other clusters of the series. Similar behaviour was also displayed by the $x = 8$ series with the $y = 3$ and $6/7$ species showing higher relative intensities. The $x = 9$ cluster series showed a wide range of y values, i.e. with $y = 0$ to 9 , with the $y = 8$ species being the dominant, and the $y = 4$ species also showing enhanced intensities.

This pattern of behaviour continues for the $x = 10$ to 14 cluster series, with the more abundant clusters of each series steadily becoming more oxygenated as x increases. At $x = 15$ however a further series of less oxygenated clusters was observed, with intense peaks being observed corresponding to $y = 2/3$, 7 and $13/14$. For clusters of higher x value than $x = 15$, these three series were found to continue, gradually increasing in oxygen content, y , with successive values of x . Evidence of slight odd/even alternation was also found.

The cluster intensity pattern became non-reproducible after $x = 21$, apart from the $x = 26$ species $[(\text{Ce O})_{26} \text{O}_{10}]^+$ and $[(\text{Ce O})_{26} \text{O}_{11}]^+$

A graphical representation of the y values of the most intense species from each sequence against their corresponding x values, Fig. 3.5.8, shows the existence of a simple linear relationship between x and y , similar to that shown by lanthanum clusters, for x up to

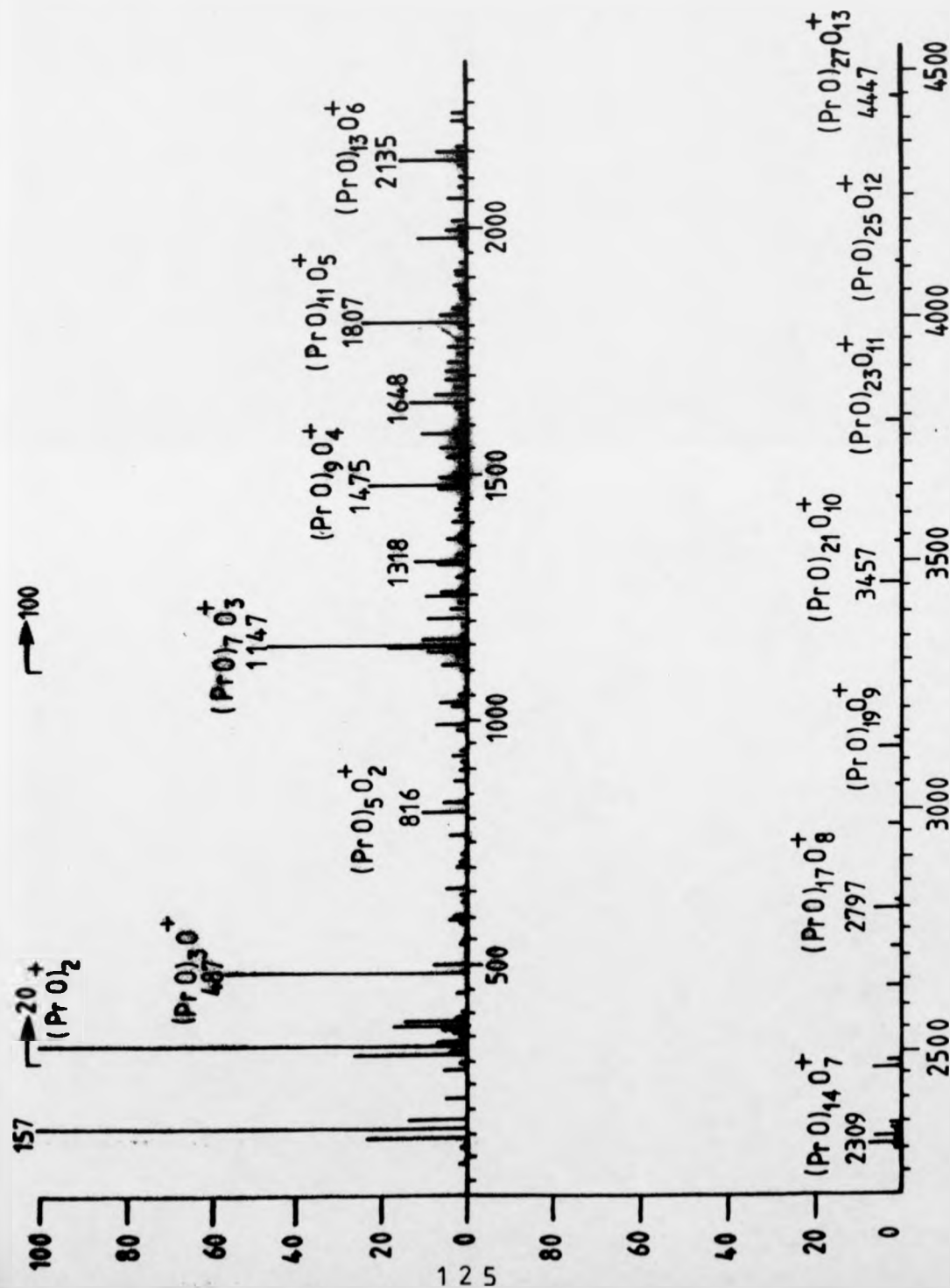
approximately 15. After $x = 15$ this regular distribution splits to produce four near-parallel sequences of cluster series.

3.4.4 PRASEODYMIUM CLUSTERS

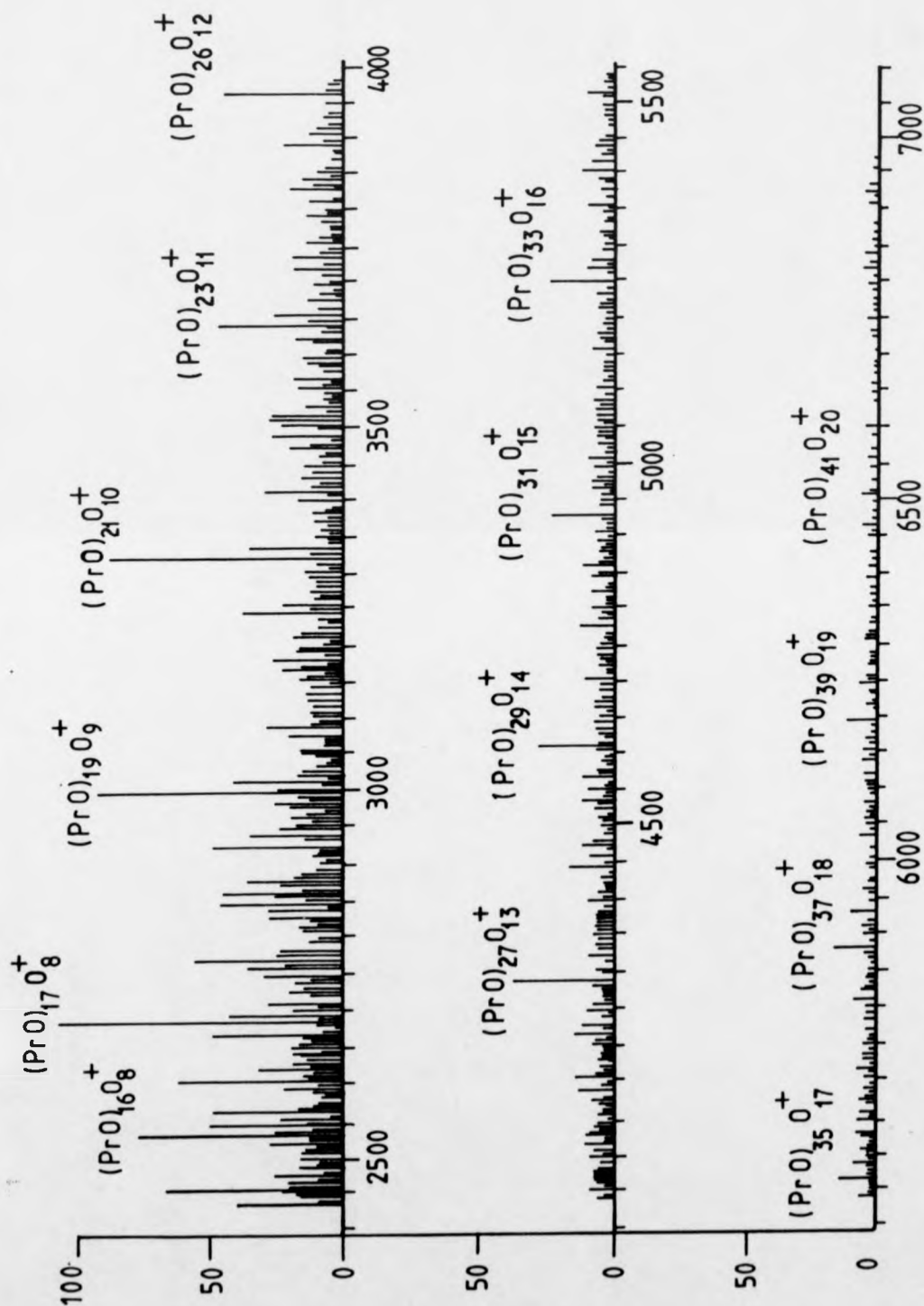
In low-mass studies of the effects of different matrices and co-solvents on the cluster formation and spectral intensities of praseodymium clusters, the $(\text{Pr O})^+$ ion, $m/z = 157$, was found to be the most abundant ion in all cases, with $(\text{Pr O})\text{O}_4^+$ also being found prominent for all matrices.

The spectra for higher-order cluster series show similar trends with different matrices, but the intensities of each cluster ion present are strongly dependent on the nature of the matrix and co-solvent present. Generally matrices containing dimethyl sulphoxide (DMSO) produced higher cluster yields while glycerol suppressed cluster formation. However the major problem with the use of samples containing DMSO-based matrices is one of spectral domination by matrix ions and adducts, resulting in the masking of much spectral information. The presence of sulpholane as a matrix, however, not only promoted cluster ion formation but also gave spectra almost free of matrix peaks and adducts.

Experiments carried out concerning the amount of matrix needed to provide reproducible spectral peaks of adequate lifetime also demonstrated sulpholane to be ideally suited, with samples being



Spec 3.4.4 The Mass Spectrum of Praseodymium Clusters



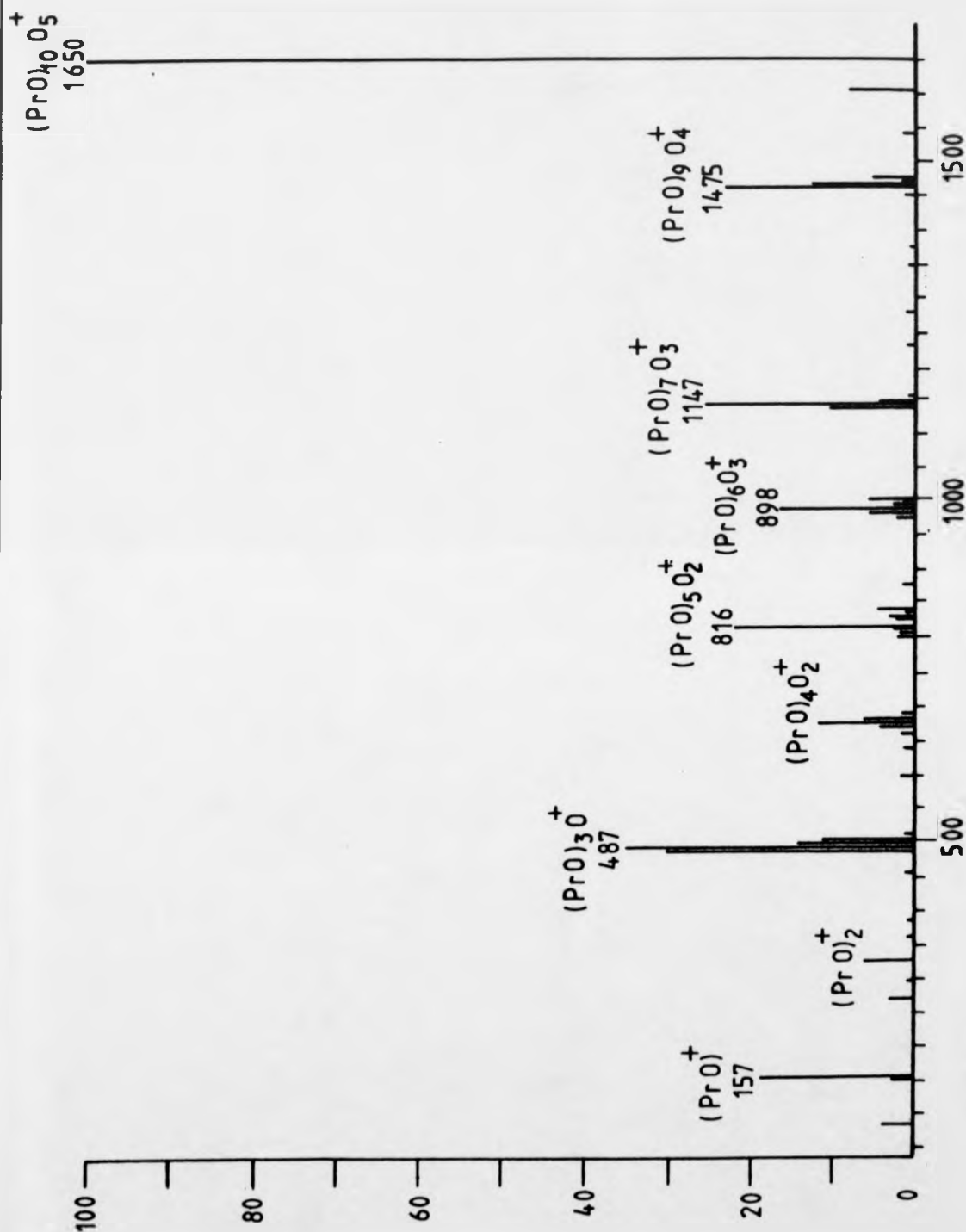
Spec 3.4.5 The High Mass Spectrum of the Praseodymium Clusters

rejuvenated by the subsequent addition of further sulpholane. The addition of dilute nitric acid to the sample in many cases increased the ion yields of the lower-mass clusters and enhanced their stabilities.

The cluster spectrum for praseodymium shows marked odd/even alternation, from the $x = 3$ series onward, with even clusters consistently being between 30% and 50% ^{of} the intensity of neighbouring odd clusters of the same y value. However discrepancies are observed for the clusters $[(\text{Pr O})_{22} \text{O}_{11}]^+$ and $[(\text{Pr O})_{23} \text{O}_{11}]^+$, and $[(\text{Pr O})_{34} \text{O}_{17}]^+$ and $[(\text{Pr O})_{35} \text{O}_{17}]^+$, which feature abrupt drops in the relative intensities of the corresponding odd clusters.

In addition to this odd/even alternation, a plot of the number of 'additional' oxygen atoms present, y , against the number of praseodymium atoms present, x , in $[(\text{Pr O})_x \text{O}_y]^+$ gives a straight line of gradient approximately 0.5. This shows that one additional oxygen atom is incorporated for every two (Pr O) units; this can clearly be seen from the species detected, with each successive even cluster being accompanied by the addition of one extra oxygen atom. The data suggest the formation of odd clusters to be relatively favoured compared with even clusters, with the even clusters requiring additional oxygen atoms in order to stabilize their structures.

The CID spectra show the fragmentation to result preferentially in odd clusters, with the fragment ions displaying notable odd/even alternation. At low collision gas pressures the fragmentation only yielded odd clusters, but as the collision gas pressure was increased



Spec 3.4.6 The CID Spectrum for $(\text{PrO})_{10}\text{O}_2^+$, with Argon
Collision Gas, Flexicell At 2KV, 20% Transmittance

even clusters were also detected. Under multiple-collision conditions the fragmentation pattern clearly demonstrated odd daughter-clusters to dissociate by the loss of neutral (PrO) units while even clusters lost neutral (PrO) O moieties, Spec. 3.4.6.

Thus CID studies show even clusters to need additional oxygen atoms to stabilize their structures. The effect of increasing collision-gas pressure on the observed dissociation patterns suggests that similar fragmentation reactions to those shown by lanthanum clusters are taking place. These involve the presence of two possible dissociation pathways in which even clusters undergo collisional stabilization under multiple-collision conditions. In addition the enhanced stability of the odd clusters gives an explanation for the marked odd/even alternation observed in the cluster spectrum.

3.4.4 SAMARIUM CLUSTERS

Samarium exists as a series of seven natural isotopes, the mass of the most abundant being 151.9 amu at 26.63%. The isotopic splitting pattern was studied for each successive cluster series and recorded using a number of matrices. For all matrices, substantial amounts of adduct formation took place. Sulpholane was found to yield the most stable and reproducible splitting pattern, which showed a direct relationship in intensity to the natural abundances (table 3.4.1).

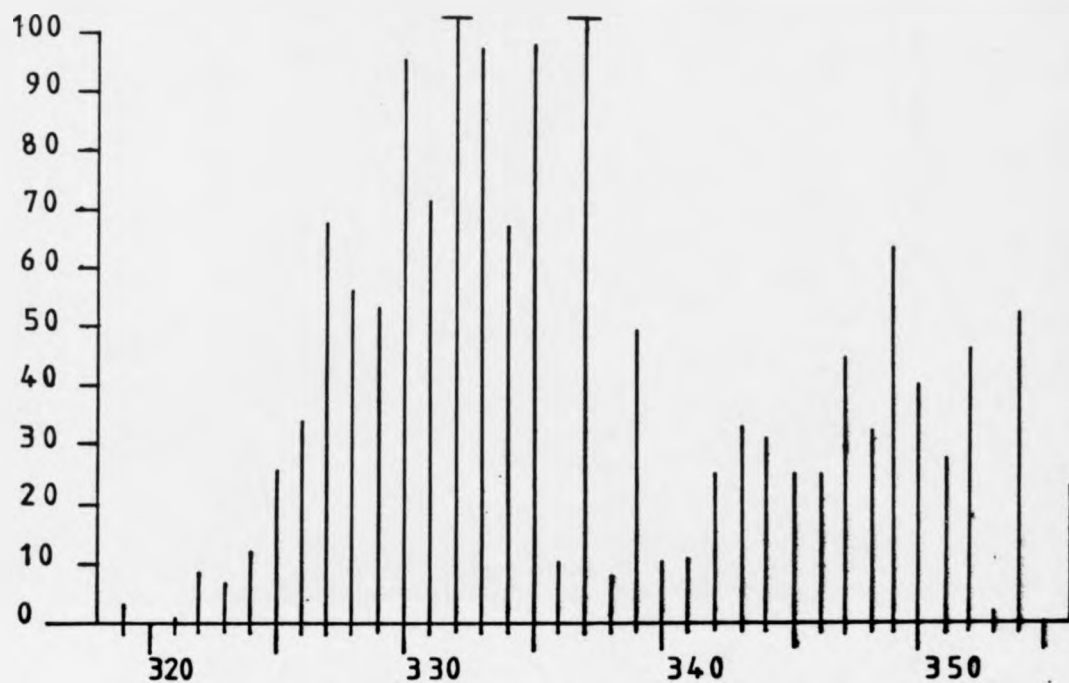
Similar behaviour was also found for the $(\text{Sm O})_2^+$ and $(\text{Sm O})_2\text{O}^+$ clusters, the distribution patterns of which overlap, with the mass spectra recorded showing close similarities to those calculated from isotope abundances assuming the statistical mixing of isotopes (spec. 3.4.7). This shows cluster formation to be independent of the isotopes present, with the 'average' detected samarium peak approaching the value of the relative atomic mass as the cluster size increases.

The mass spectra, apart from showing substantial amounts of matrix adduct formation, also yielded a number of samarium-oxygen cluster series. These clusters followed the general formula $[(\text{Sm O})_x\text{O}]^+$, with clusters up to $x = 23$ being recorded (spec. 3.4.8).

The mass spectrum was dominated by $(\text{Sm O})^+$, $m/z = 167$. The other clusters showed an exponential decay in intensity which was interrupted by the $x = 9$ series, which displayed a uncommonly high relative intensity, in addition, a step in intensity was observed at $x = 15$.

| Isotope | % Nat. abundance | % Int. reference |
|---------|------------------|------------------|
| 143.9 | 3.16 | 3.59 |
| 146.9 | 15.07 | 16.18 |
| 147.9 | 11.27 | 12.18 |
| 148.9 | 13.84 | 14.48 |
| 149.9 | 7.47 | 7.83 |
| 151.9 | 26.63 | 25.21 |
| 153.9 | 22.53 | 20.40 |

Tabl 3.4.1 A Comparison Between the % Natural Abundances of Samarium Isotopes and Their Relative Intensities as Detected



Spec 3.4.7 The Isotopic Distribution From Mass Spectral Data

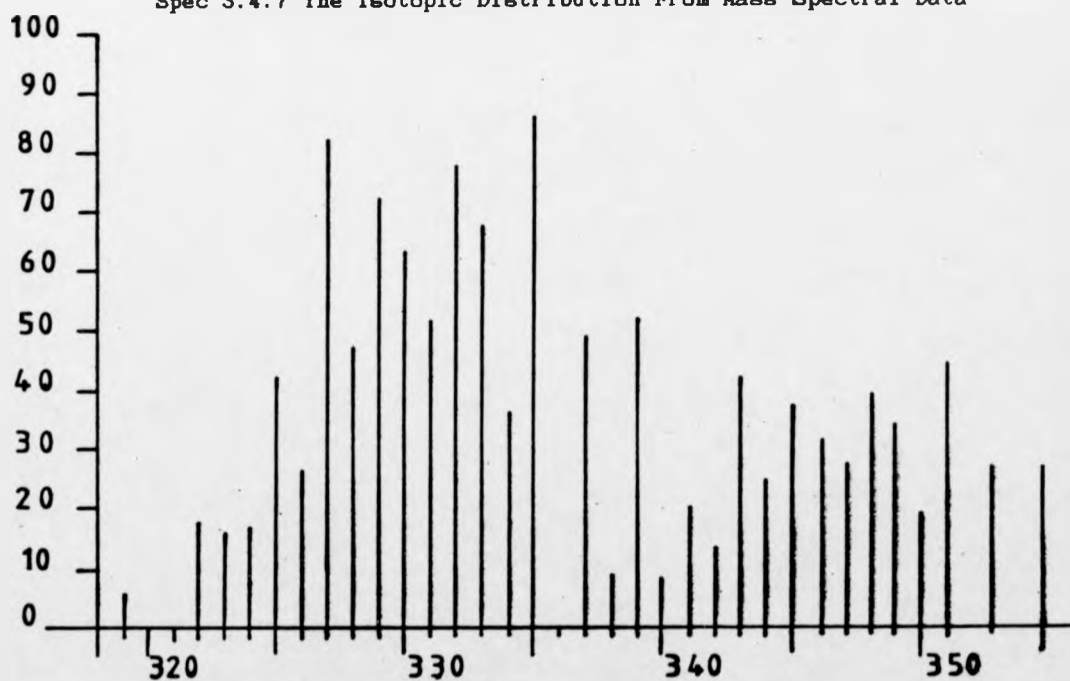
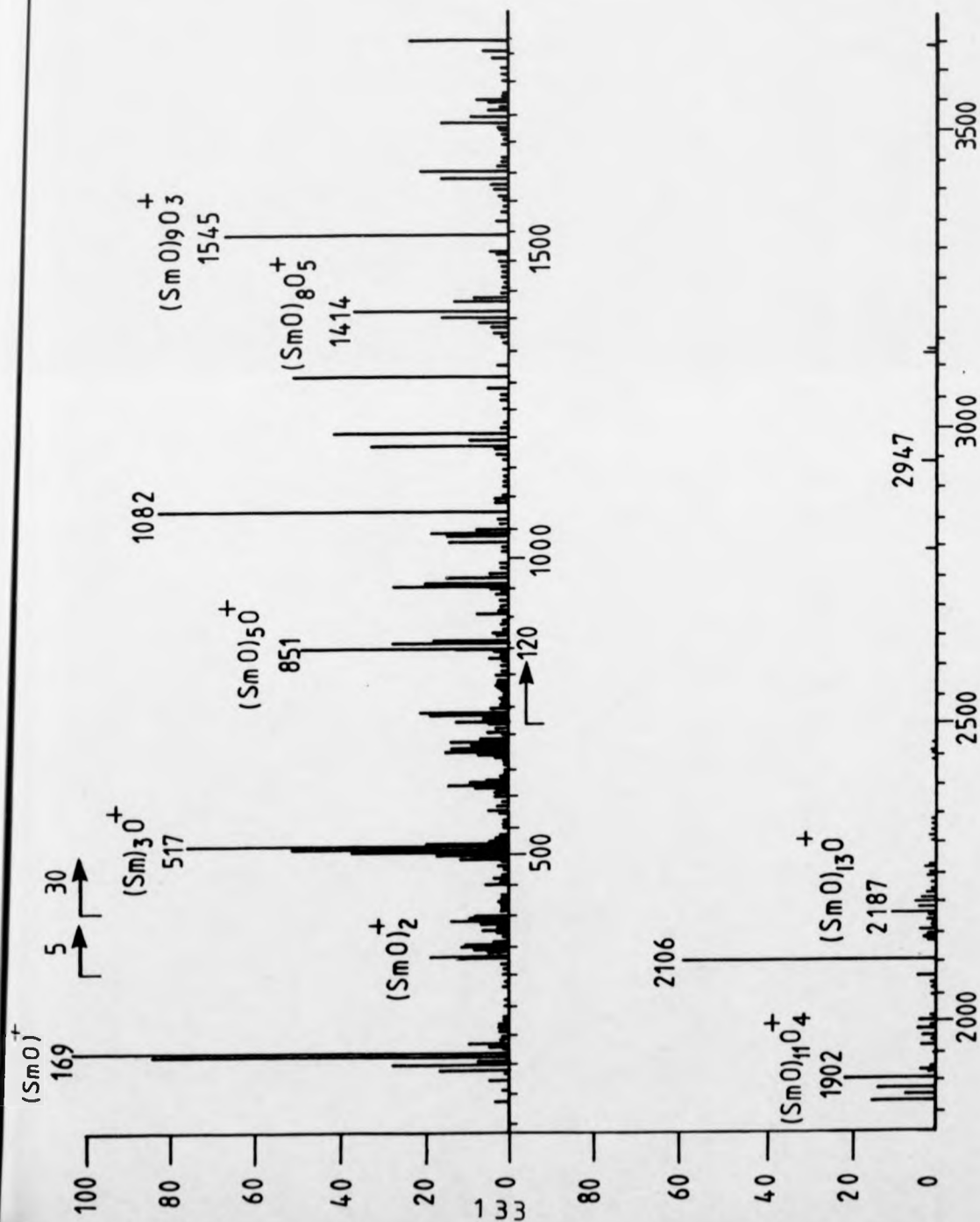


Fig 3.4.2 The Calculated Distribution From Isotopic Abundances.



Spec 3.4.8 The FAB Mass Spectrum for Samarium Nitrate.

These abrupt intensity changes may mark structural changes or the positions of magic numbers. Striking odd/even alternation is also present, with the odd x-value species displaying enhanced intensities and the data suggesting that the extra oxygen atoms are accommodated by even clusters in a similar manner to that demonstrated by praseodymium clusters.

3.4.5 EUROPIUM CLUSTERS

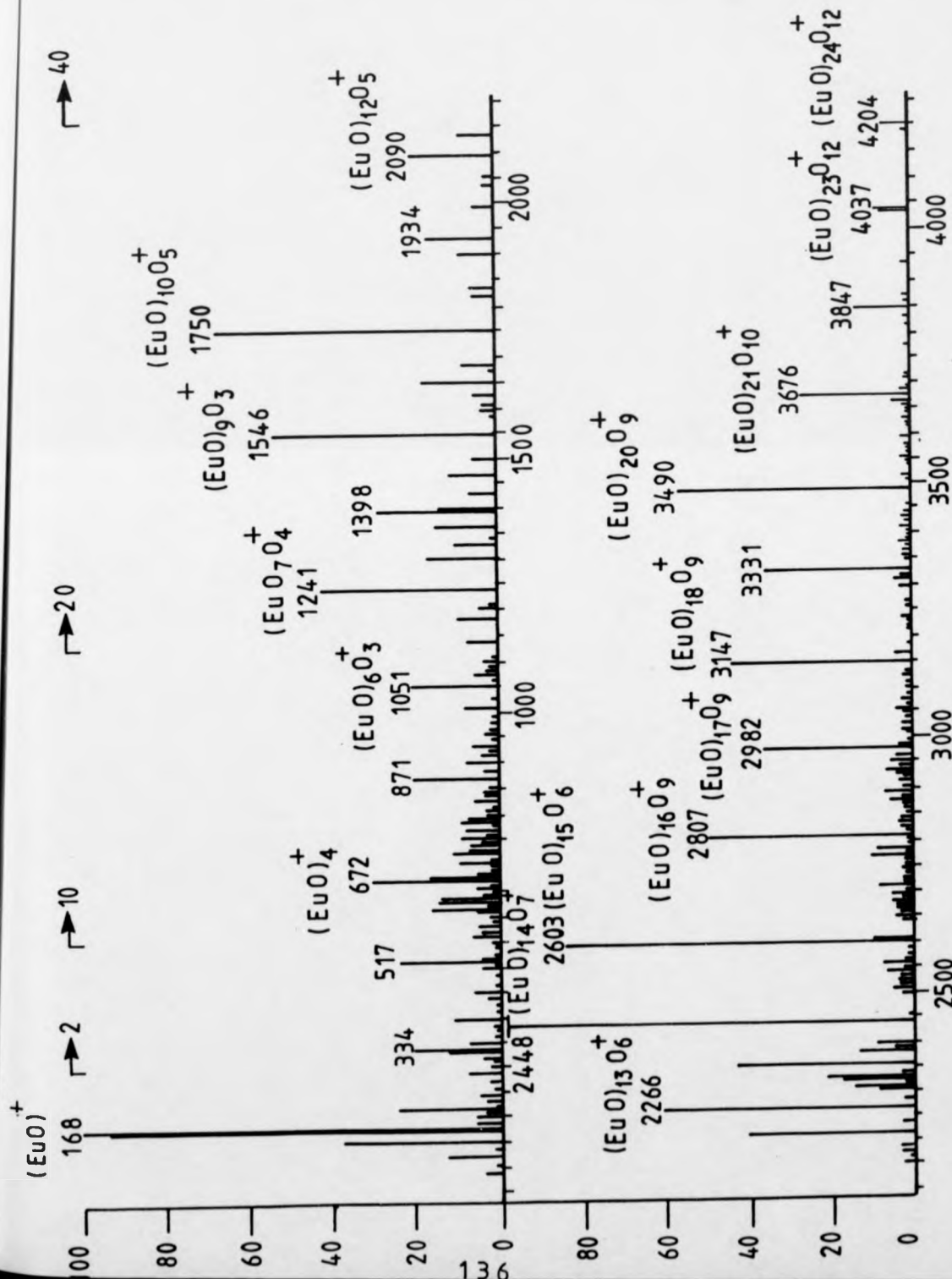
Atomic europium has one electron occupying each of its 4f subshells, leading to many differences in its chemistry from that of the other lanthanides, and also an extensive photochemistry. Europium exists as two natural isotopes, of nearly equal natural abundance, which can be clearly distinguished in lower mass clusters and show relative intensities near to those expected from their abundances.

| | % Natural abundance | % Internal Reference |
|-------------------|---------------------|----------------------|
| ^{151}Eu | 47.82 | 48.2 |
| ^{152}Eu | 52.19 | 51.7 |

For higher mass clusters however, the isotopic distribution becomes disperse and statistical mixing leads to europium being best described by its relative atomic mass.

The mass spectra of europium salts were studied using a range of matrices, and showed the same basic cluster distribution pattern with the clusters being described by the general formula $[(\text{Eu O})_x \text{O}_y]^+$, (spec. 3.4.9).

The monoeuropium cluster series was, like the mass spectrum, dominated by the $(\text{Eu O})^+$ ion. The $[(\text{Eu O}) \text{O}_4]^+$ species was also found to display an increased relative intensity in the presence of a sulpholane matrix. The bieuropium series showed the $y = 0$ peak to be the most intense, while the trieuropium series displayed a range of y



Spec 3.4.9 The FAB Mass Spectrum for Europium Nitrate.

values from -3 to +1 with the most intense species being the $y = 0/1$. The $x = 4$ series showed a similar range in y with the dominant species being observed at $y = 0$. For $x = 5$ a range of y values from 0 to 2 was observed with 1 and 2 being found to be the most intense, while the $x = 6$ series was dominated by the $y = 3$ species. This increase in the number of additional oxygen atoms present in the most abundant species of each subsequent x series was found to continue slowly. However this increase is non-uniform with the dominant peaks for the $x = 4, 9, 12, 15$ and 20 series being observed to occur for clusters containing one less additional oxygen atom than the overall trend. These abnormalities occur however in the region of abnormal spectral intensities, with an abrupt decreases in spectral intensity being observed at $x = 3, 10, 15, 20$. In the region $x = 10$ to 20 there is also evidence of even/odd alternation.

The behaviour exhibited by the europium- oxygen clusters has no parallel in the cluster chemistry shown by the other lanthanides and may be a result of the electronic structure of europium.

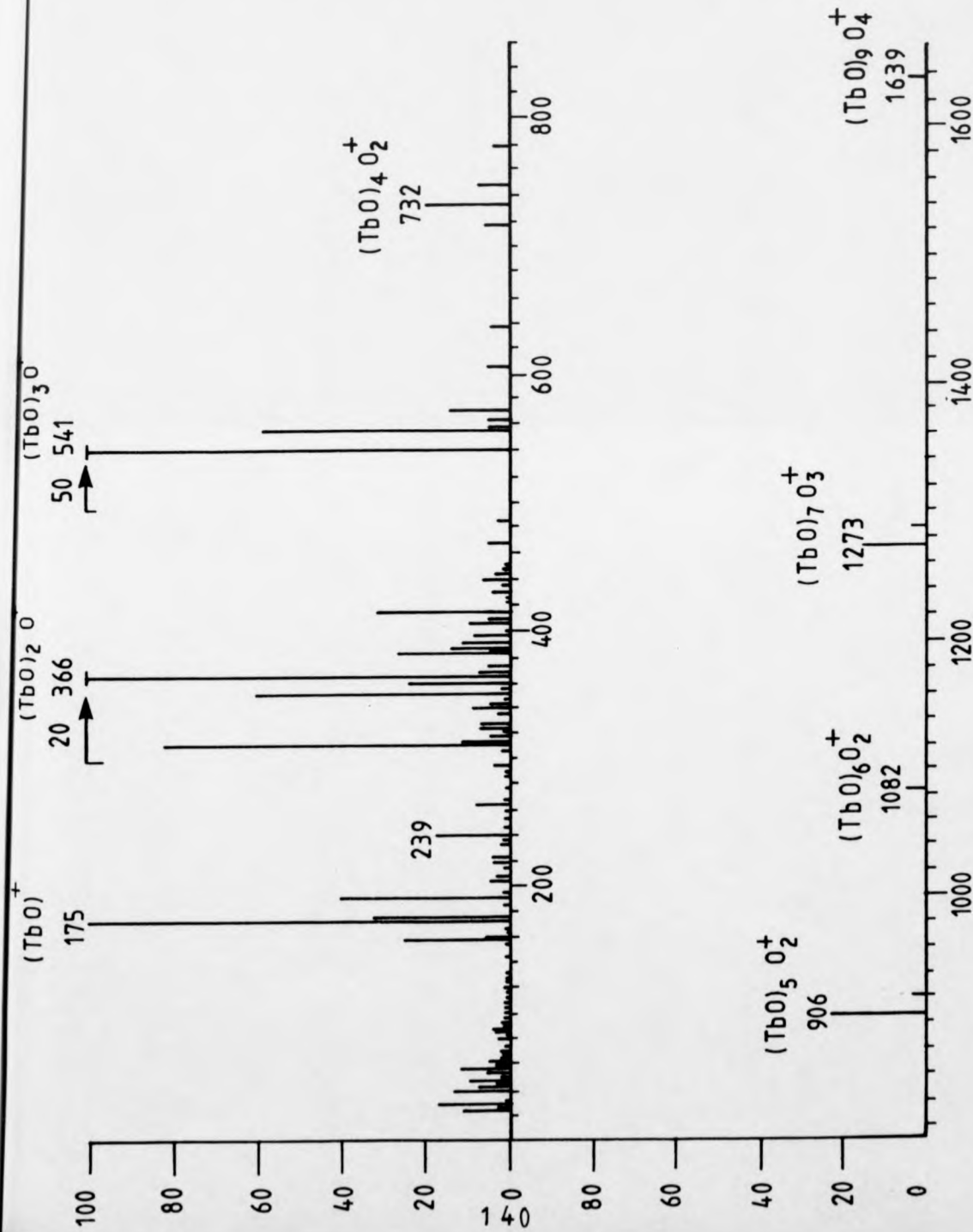
The CID spectra for europium were difficult to reproduce, with the incident beam intensities proving to be stable only over a narrow range of sample conditions of temperature and matrix content. The fragment clusters generally showed low relative intensities, with the range of y values present in each cluster series increasing with increasing collision gas pressure. Higher collision gas pressures were found to produce cluster series with lower y values.

The CID spectra studied displayed fragmentation patterns that differed significantly from those found for lanthanum and praseodymium clusters, with the levels of additional oxygen atoms being reduced rapidly with each successive fragmentation. This usually occurred by the loss of neutral $(\text{Eu O})\text{O}$ units from both odd and even clusters to form cluster species of the type $(\text{Eu O})_n^+$. Generally odd clusters showed a larger range of y values for fragment clusters with $[(\text{Eu O})_n \text{O}_2]^+$, and $[(\text{Eu O})_n \text{O}]^+$ is often found to be present, suggesting an enhanced stability for these species.

3.4.6 TERBIUM CLUSTERS

Terbium clusters were very readily formed under all matrix conditions. The spectrum shows the cluster intensities to decrease rapidly and exponentially with increasing cluster size (spec. 3.4.10). The clusters adhere to the general formula $(\text{Tb O})_x \text{O}_y$ 1^+ and display marked odd/even alternation.

A plot of y against x shows each successive even cluster usually to accommodate one additional oxygen atom, with the rate of take-up of additional oxygen atoms being found to be similar to that shown by praseodymium clusters.



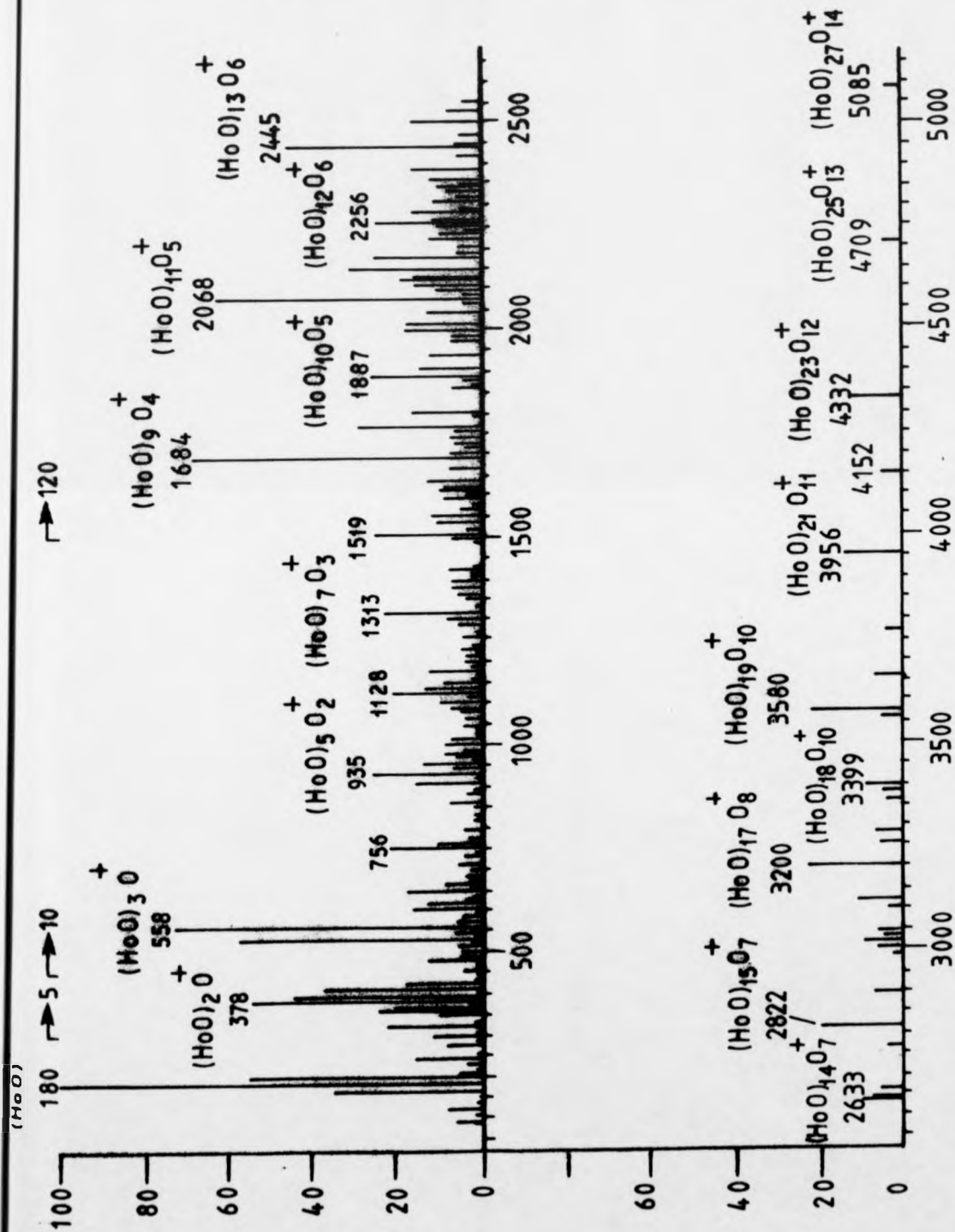
Spec 3.4.10 The FAB Mass Spectrum for Terblum Nitrate

3.4.7 HOLMIUM CLUSTERS

The mass spectrum for holmium nitrate shows the presence of a series of clusters of general formula $[(\text{HoO})_x \text{O}_y]^+$ extending to very high masses. These clusters show a slow, exponential-type decay in their intensities as well as definite odd/even alteration, with the intensities of the even cluster peaks being generally between 30% to 50% of the preceding odd clusters (spec. 3.4.11).

Each cluster series shows only a limited range of y values, with each successive even- x cluster being observed to accommodate one additional oxygen atom. This is clearly demonstrated in their spectra. Thus the rate of addition of additional oxygens to these clusters is equal to that found for lanthanum. However this uniform sequence displays an abnormality with the coordination of three additional oxygen atoms occurring between $x = 19$ and 23; furthermore the intensity of the even-series clusters drops suddenly after the slightly-increased intensity of the $[(\text{HoO})_{22} \text{O}_{12}]^+$ species. This suggests that the $x = 21$ series may be of higher relative stability, reducing the rate at which the $x = 22$ series clusters undergoes dissociation or fragmentation. Hence the increased number of additional oxygen atoms present may confer stability on the higher-mass clusters.

The rate at which y uniformly increases with respect to x after $x = 21$ is seen to be the same as before this step, with the most abundant species of each odd-cluster series observed containing one extra 'additional' oxygen atom.



Spec 3.4.11 The FAB Mass Spectrum for Holmium Nitrate

The CID spectra for holmium clusters showed the clusters to undergo the sequential loss of $(\text{HoO})_2\text{O}$ units between odd clusters, with even clusters being observed at higher collision gas pressures in a similar way to that displayed by lanthanum and praseodymium.

3.5

DISCUSSION OF RESULTS

3.5.1 PRASEODYMIUM AND TERBIUM CLUSTERS

The cluster spectra and CID spectra for praseodymium and terbium clusters are very similar and show what would seem to be ideal behaviour for lanthanide oxide clusters, with the most intense clusters detected in these spectra, over a range of matrix conditions, featuring identical for values x and y .

For both metals, a plot of the number of additional oxygen atoms present, y , against the number of metal atoms in the cluster, x , gives linear relationships described by the equations

$$Y = 0.5X - 0.5 \quad \text{Eqn. 3.1}$$

for the more intense odd clusters and

$$Y = 0.5X \quad \text{Eqn. 3.2}$$

for the even clusters (Fig. 3.5.1). These equations clearly demonstrate that even clusters incorporate additional oxygen atoms rather than odd clusters. The equation for even clusters also shows the ratio of metal-to-oxygen atoms present in the cluster, z , to be equal to $z = 1.5$ and hence correspond to the formation of Ln_2O_3 . This is also demonstrated by a plot of z against x , in which even clusters are found

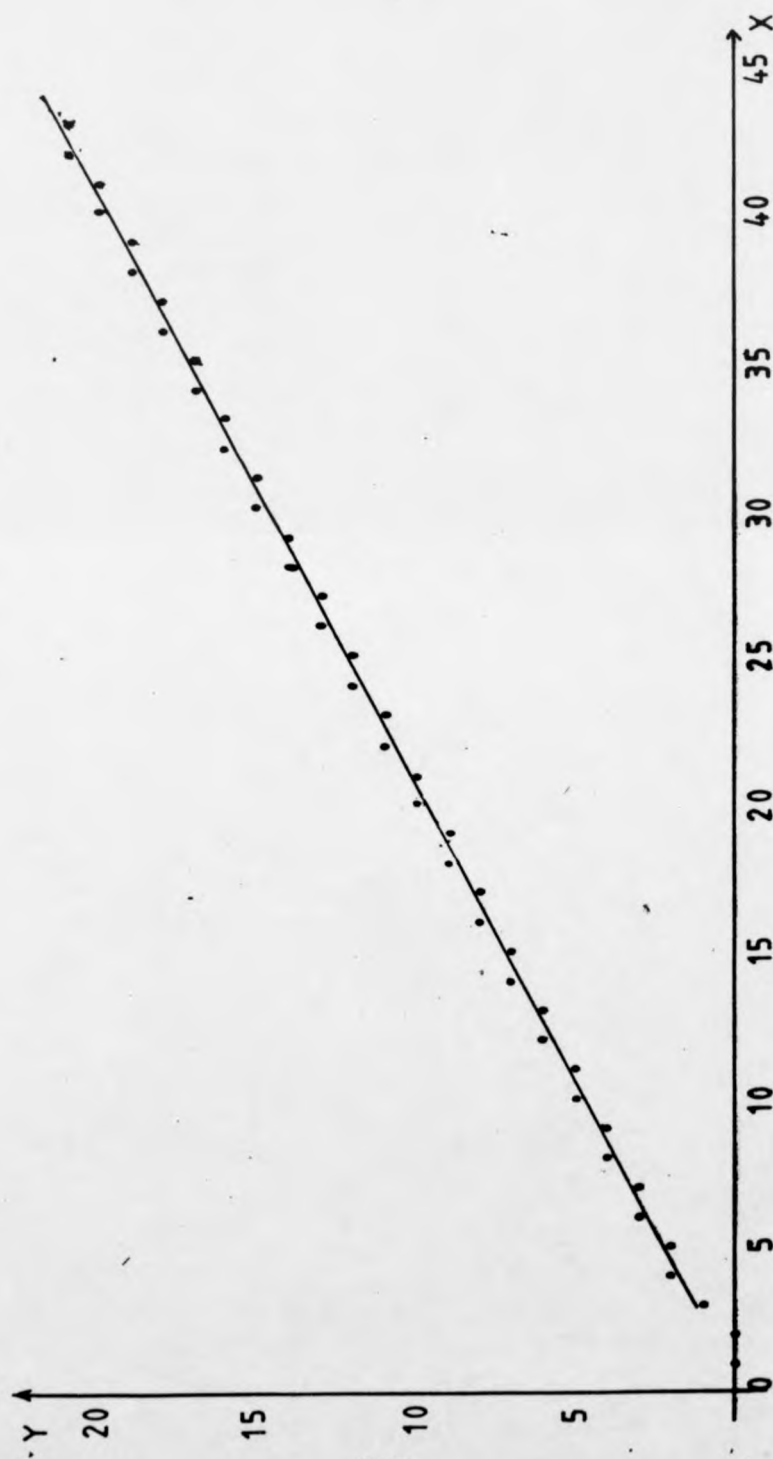


Fig 3.5.1 A Graphical Representation of the Relationship Between x and y for the Praseodymium Clusters

to display a constant value of $z = 1.5$, independent of the number of metal atoms present, (Fig. 3.5.2) While odd clusters are observed to display a nonlinear relationship, with the z values being seen to tend towards $z = 1.5$ at $x = \infty$. In a plot of z against $1/x$, however, odd clusters are observed to show a linear increase with cluster size and make an intercept with the y axis at $z = 1.5$ when $x = \infty$, while even clusters display a constant $z = 1.5$ value, (Fig. 3.5.3). This relationship between the z values for odd clusters and their respective x values can be described by the equation

$$z = -0.5/x + 1.5 \quad \text{Eqn. 3.3}$$

Hence the data shows both praseodymium and terbium to form clusters which have a tendency to form atomic combinations similar to that of the stable lanthanide oxide, Ln_2O_3 .

In the case of even clusters, species corresponding to this formula are readily formed for $x \geq 2$. However in the case of their neighbouring odd clusters, which are of higher intensity, the z ratio only reaches $z = 1.5$ at large values of x . This suggests that the structures and stoichiometries adopted by these clusters relate directly to the dominant Ln_2O_3 phase from very low x values, with the more stable structures being formed by the odd x value clusters.

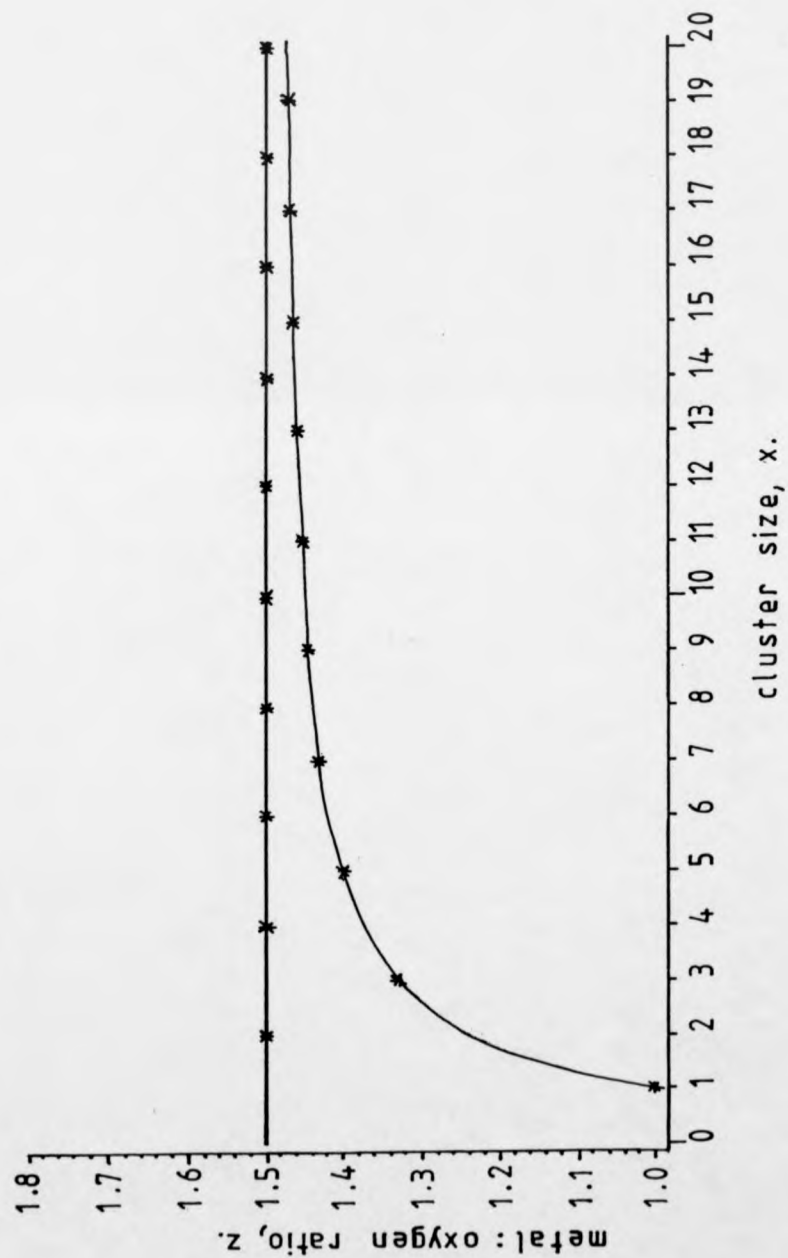


Fig 3.5.2 The Variation in Metal : Oxygen Atom Ratio with Increasing Cluster Size for Praseodymium and Terbium Clusters

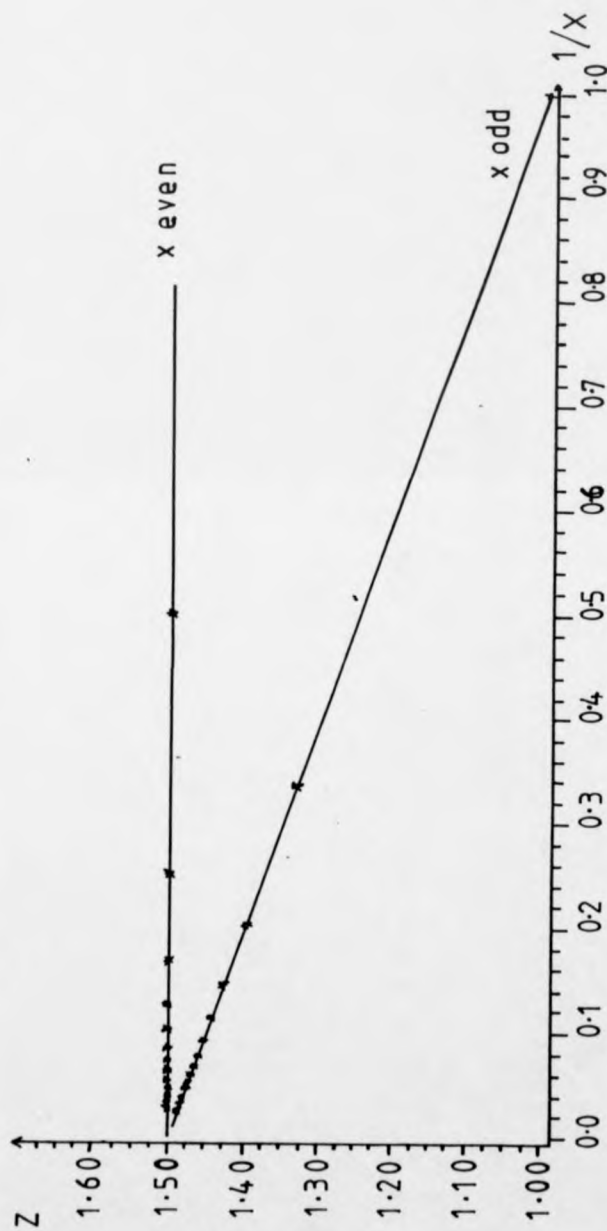


Fig 3.5.3 The Variation in Metal : Oxygen Atom Ratio, z , with $1/x$.
For Praseodymium and Terbium Clusters.

3.5.2 LANTHANUM CLUSTERS

The clusters formed by lanthanum showed a pattern of oxygen uptake roughly similar to praseodymium- and terbium-oxygen clusters, however a discontinuity in the oxygen content of the clusters occurs in the region of $x = 10$. This can be clearly observed in a plot of additional oxygen content y of the most intense species from each cluster series against their respective x values. Here the linear plots can be described by the equation

$$Y = 0.5X - 0.5 \quad \text{for odd clusters} \quad \text{Eqn. 3.4}$$

$$Y = 0.5X \quad \text{for even clusters} \quad \text{Eqn. 3.5}$$

However in the region of $x = 8$, $y = 4$, a sudden increase in the oxygen content of the clusters occurs up to $x = 10$, $y = 6$, followed by a plateau region over which y remains constant. This plateau region extends to $x = 12$, with larger clusters again being described by the above equations. This behaviour does not extend beyond $x = 25$ after which no regular pattern is readily observed.

A graph of the lanthanum : oxygen atom ratio, z , against $1/x$ gives rise to two linear plots. For the even clusters the z values are observed to display a constant value of $z = 1.5$, which is independent of cluster size (Fig. 3.5.5). Odd clusters however are seen to show a gradual increase in z with increasing size, the relationship between z and x being described by the equation

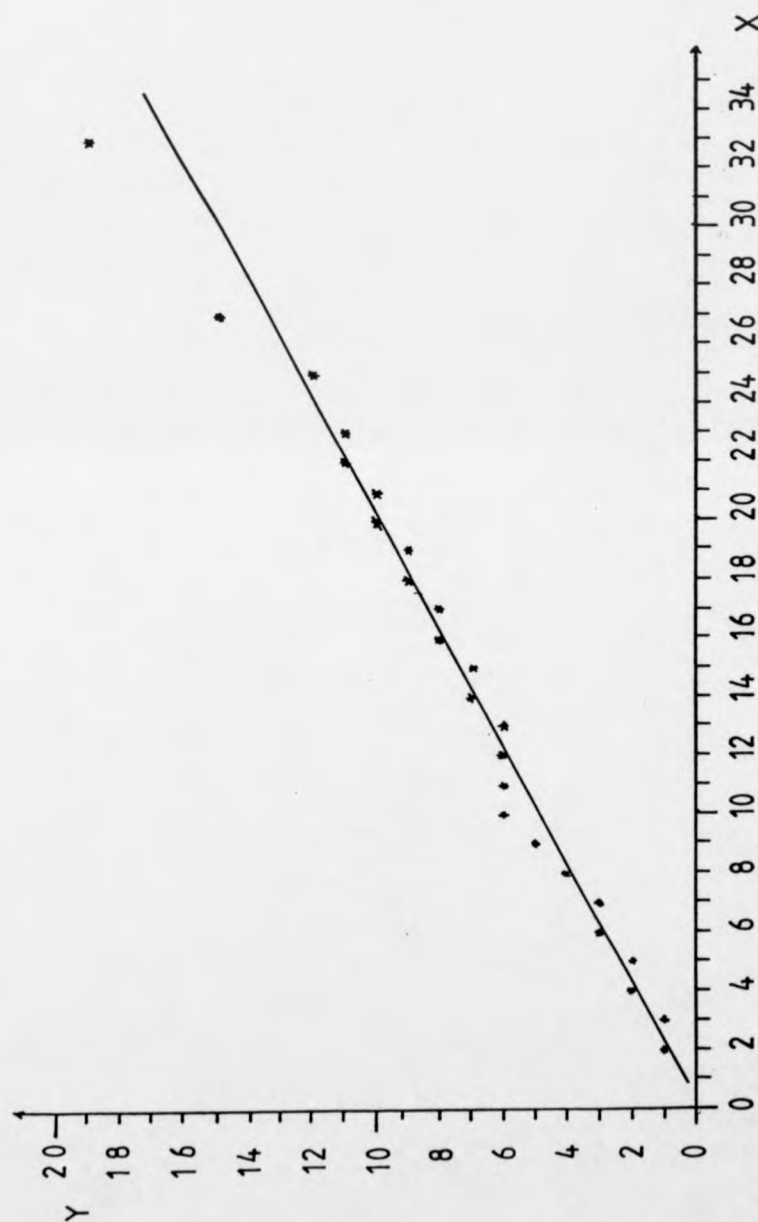


Fig 3.5.4 The Variation in the Number of Additional Oxygen Atoms, y , with Cluster Size, x , for the Lanthanum Clusters.

| Species | La:O | Species | La:O | Species | La:O |
|---------------------------------|-------|----------------------------------|-------|-----------------------------------|-------|
| LaO | 1.000 | LaO ₁₀ O ₆ | 1.600 | LaO ₁₉ O ₉ | 1.473 |
| LaO ₂ O | 1.500 | LaO ₁₁ O ₆ | 1.543 | LaO ₂₀ O ₁₀ | 1.500 |
| LaO ₃ O | 1.330 | LaO ₁₂ O ₆ | 1.500 | LaO ₂₁ O ₁₀ | 1.476 |
| LaO ₄ O ₂ | 1.500 | LaO ₁₃ O ₆ | 1.461 | LaO ₂₂ O ₁₁ | 1.500 |
| LaO ₅ O ₂ | 1.400 | LaO ₁₄ O ₇ | 1.500 | LaO ₂₃ O ₁₁ | 1.478 |
| LaO ₆ O ₃ | 1.500 | LaO ₁₅ O ₇ | 1.466 | LaO ₂₅ O ₁₂ | 1.480 |
| LaO ₇ O ₃ | 1.428 | LaO ₁₆ O ₈ | 1.500 | LaO ₂₇ O ₁₅ | 1.550 |
| LaO ₈ O ₄ | 1.500 | LaO ₁₇ O ₈ | 1.470 | LaO ₃₃ O ₁₉ | 1.575 |
| LaO ₉ O ₅ | 1.555 | LaO ₁₈ O ₉ | 1.500 | | |

The most intense clusters from each series.

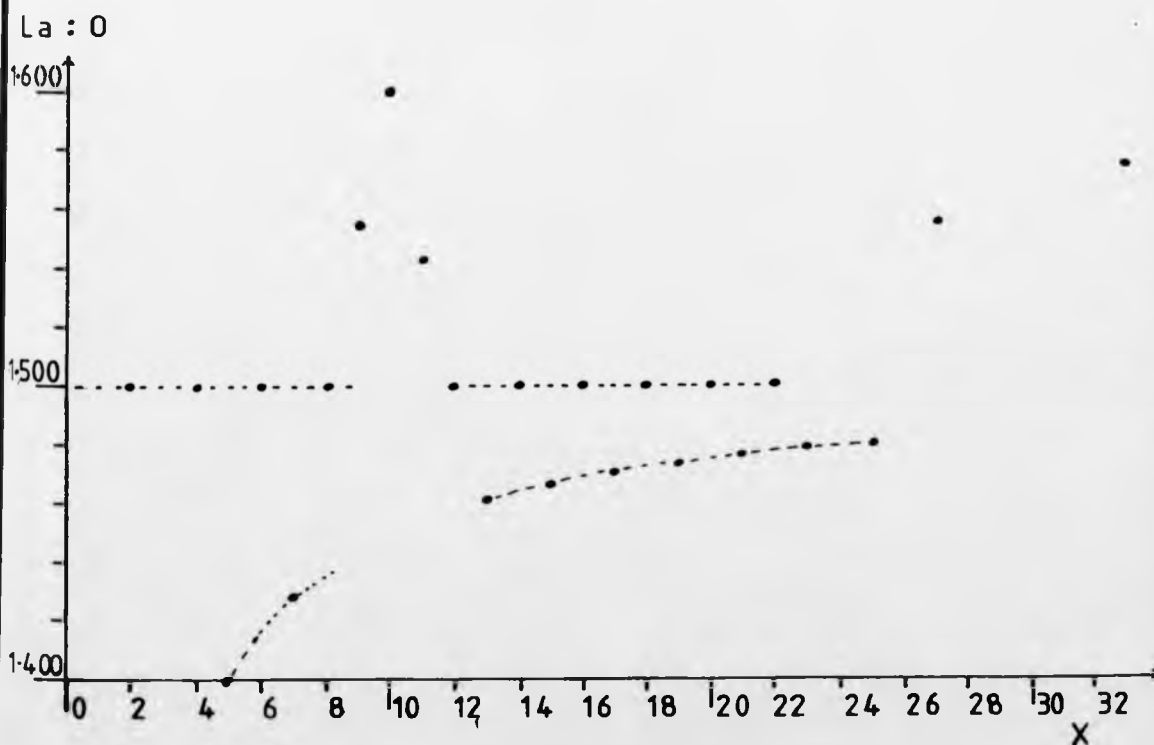


Fig 3.5.5 A Graphical Representation of the Variation of the La : O Ratio with x.

$$z = -0.5/x + 1.5 \quad \text{Eqn. 3.6}$$

when $x \leq 7$ and $x \geq 13$. In the region $8 \leq x \leq 12$ a sharp peak is observed to occur, centred on $x = 10$, the lower x -value edge of which can be extrapolated to $z \approx 2$ at $x = \infty$, i.e.

$$z = -4.0/x + 2 \quad \text{Eqn. 3.7}$$

This may denote the formation of a structural arrangement of higher stability and/or the possible existence of structural isomers. Although no direct significance could be given to the anomalous $x = 33$ species, the increased additional oxygen content of the $x = 27$ peak is likely to be due to the $x = 25$ cluster having a structurally stable arrangement.

3.5.3 HOLMIUM CLUSTERS

The oxygen content of holmium clusters shows an abrupt increase in the region of $x = 20$ holmium atoms. The presence of this step can be clearly observed in a graphical plot of y against x , (Fig. 3.5.6). This shows two linear plots of equal gradient on either side of the $x = 20$ step; the clusters with $x < 20$ can be described by the equation

$$Y = 0.5X - 0.5 \quad \text{Eqn. 3.8}$$

while clusters with $x \geq 20$ are described by the equation

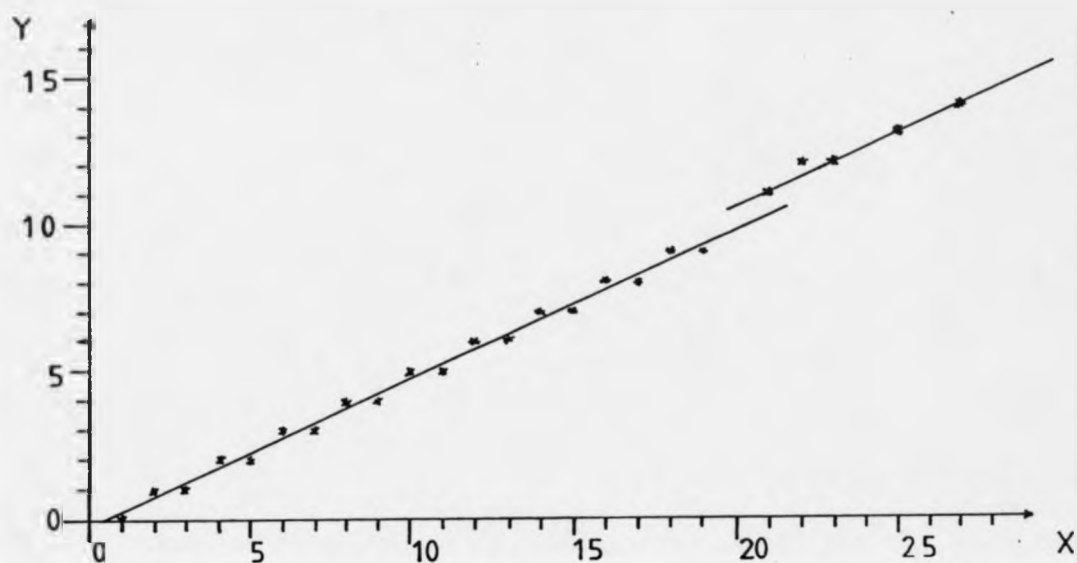


Fig 3.5.6 The Variation in Additional Oxygen Atom Content with Cluster size for Holmium.

$$Y = 0.5X + 0.5 \quad \text{Eqn. 3.9}$$

These correspond to $\text{Ho}_{32}\text{O}_{47.5}$ and $\text{Ho}_{32}\text{O}_{48.5}$ respectively.

The existence of these is further demonstrated by a plot of the Ho : O ratio, z , against $1/x$, Fig. 3.5.7. This gives rise to three lines all converging at $z = 1.5$ as $x \rightarrow \infty$. The plot for the even clusters shows a constant $z = 1.5$ value and stops abruptly at $x = 18$. For odd clusters with $x \leq 19$, the cluster metal : oxygen atom ratio, z , is found to gradually increase in a similar manner to that displayed by praseodymium and terbium, however at $x \geq 21$ the metal : oxygen atom ratio, z , is observed to undergo a sudden increase before slowly decreasing in value, tending towards $z = 1.5$ as the cluster size increases. The linear plots obtained for the odd clusters can be expressed by the equations

$$z = -0.5/x + 1.5, \quad x \leq 19 \quad \text{Eqn. 3.10}$$

$$z = 0.47/x + 1.5, \quad x \geq 21 \quad \text{Eqn. 3.11}$$

which represent $\text{Ho}_{32}\text{O}_{47.5}$ and $\text{Ho}_{32}\text{O}_{48.5}$ respectively.

That all these three plots tend to $z = 1.5$ at high values of x demonstrates the dominant trend to form the stoichiometry Ln_2O_3 . The abrupt increase in the cluster metal : oxygen atom ratio in the region of $x = 20$ and the abnormally high spectral intensity of $x = 21$ cluster series suggest $x = 21$ clusters have enhanced stabilities relative to

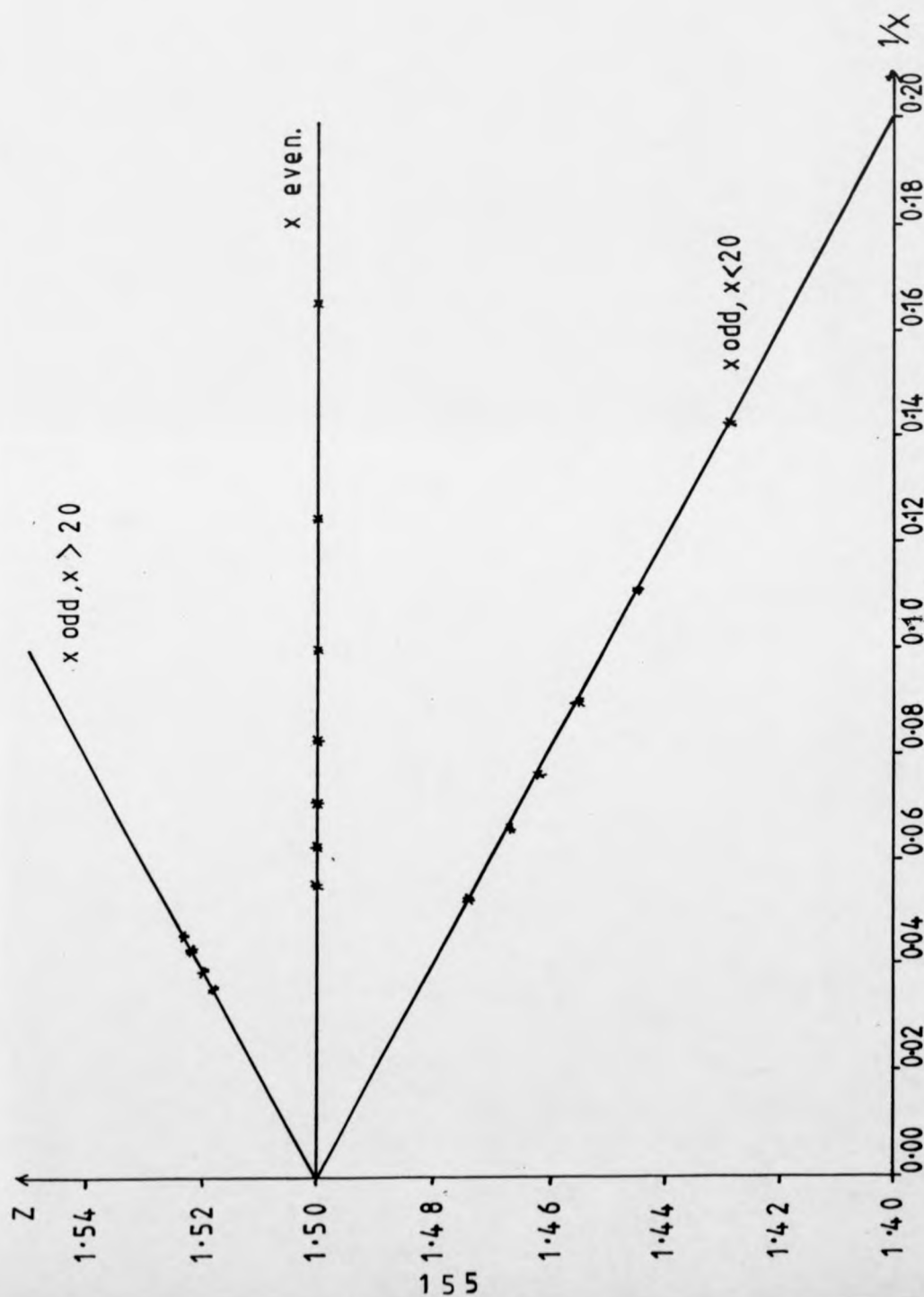


Fig 3.5.7 A Plot of the Metal Oxygen Atom Ratio Variation With Cluster Size.

neighbouring cluster series, with the additional oxygen atoms being accommodated to allow the clusters to adopt more stable structural arrangements. This may mark the completion of a structural shell, with additional units only being added in the form of HO_2O_3 , hence x remains odd.

3.5.4 CERIUM CLUSTERS

In the case of cerium, the cluster spectrum shows the species present to become significantly different from those observed for the other lanthanide metals with increasing cluster size. This is clearly demonstrated by a plot of y against x for cerium clusters, Fig. 3.5.8. In this plot two principal regions are observed; in the first, $x \leq 7$, the clusters are seen to strongly resemble those observed for the other lanthanide metals. These clusters correspond to line 1 and can be described by the linear equation

$$\text{Line 1} \quad Y = 0.5X + 0.25 \quad \text{Eqn. 3.12}$$

In the second principal region, $x \geq 8$, the dominant species are found to give rise to a series of linear relationships at successively higher x values. These plots are all of equal gradient and hence intercept the x axis at increasingly higher x values. These plots can be described by the linear equations

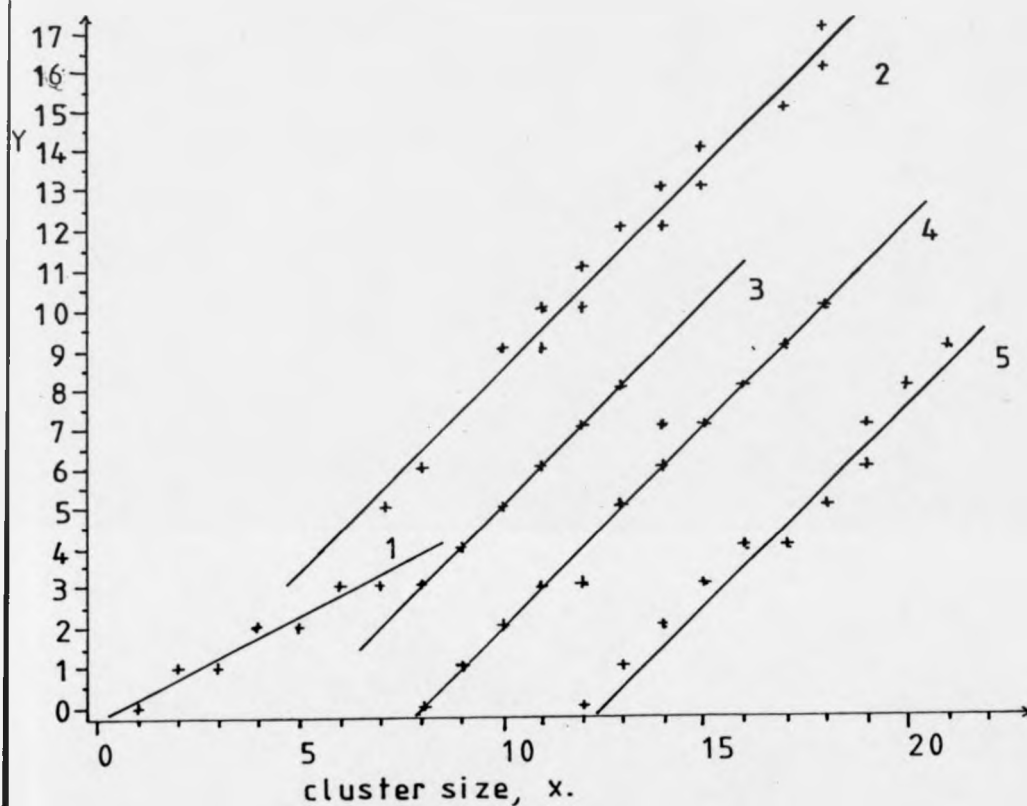


Fig 3.5.8 A Graphical Representation of the Variation in Additional Oxygen Atom Contents, y , with cluster size, x .

| | | | | | | |
|--------|-----|-----|-----|-----|------|-----------|
| Line 2 | Y | $=$ | x | $-$ | 1 | Eqn. 3.13 |
| Line 3 | Y | $=$ | x | $-$ | 5 | Eqn. 3.14 |
| Line 4 | Y | $=$ | x | $-$ | 8 | Eqn. 3.15 |
| Line 5 | Y | $=$ | x | $-$ | 12 | Eqn. 3.16 |

The equal gradients of the multiple plots of the latter region suggests that they are strongly related, while corresponding to different structural forms.

Similar behaviour is also found in plots of the cerium : oxygen atom ratio, z , against $1/x$ for these clusters, (Fig. 3.5.9). These plots again show the presence of two distinct regions. The first of these regions represents the smaller clusters containing up to seven cerium atoms in which even x -clusters display a constant $z = 1.5$ value, while the z values for odd clusters show a slow increase with increasing x value so that $z \rightarrow 1.5$ when $x \rightarrow \infty$. The relationship between the metal : oxygen atom ratio and cluster size can be described by the equation

| | | | | | | |
|--------|-----|-----|----------|-----|-------|-----------|
| Line 1 | Z | $=$ | $-0.5/x$ | $+$ | 1.5 | Eqn. 3.17 |
|--------|-----|-----|----------|-----|-------|-----------|

This indicates that small cerium-oxide clusters prefer a Ln_2O_3 stoichiometry, as shown by other lanthanide oxides.

In the second region, when $x \geq 8$, the linear plots are found to converge at $z = 2$ when $x \rightarrow \infty$. These plots may denote the existence of a number of related stable clusters, with the relationship between their

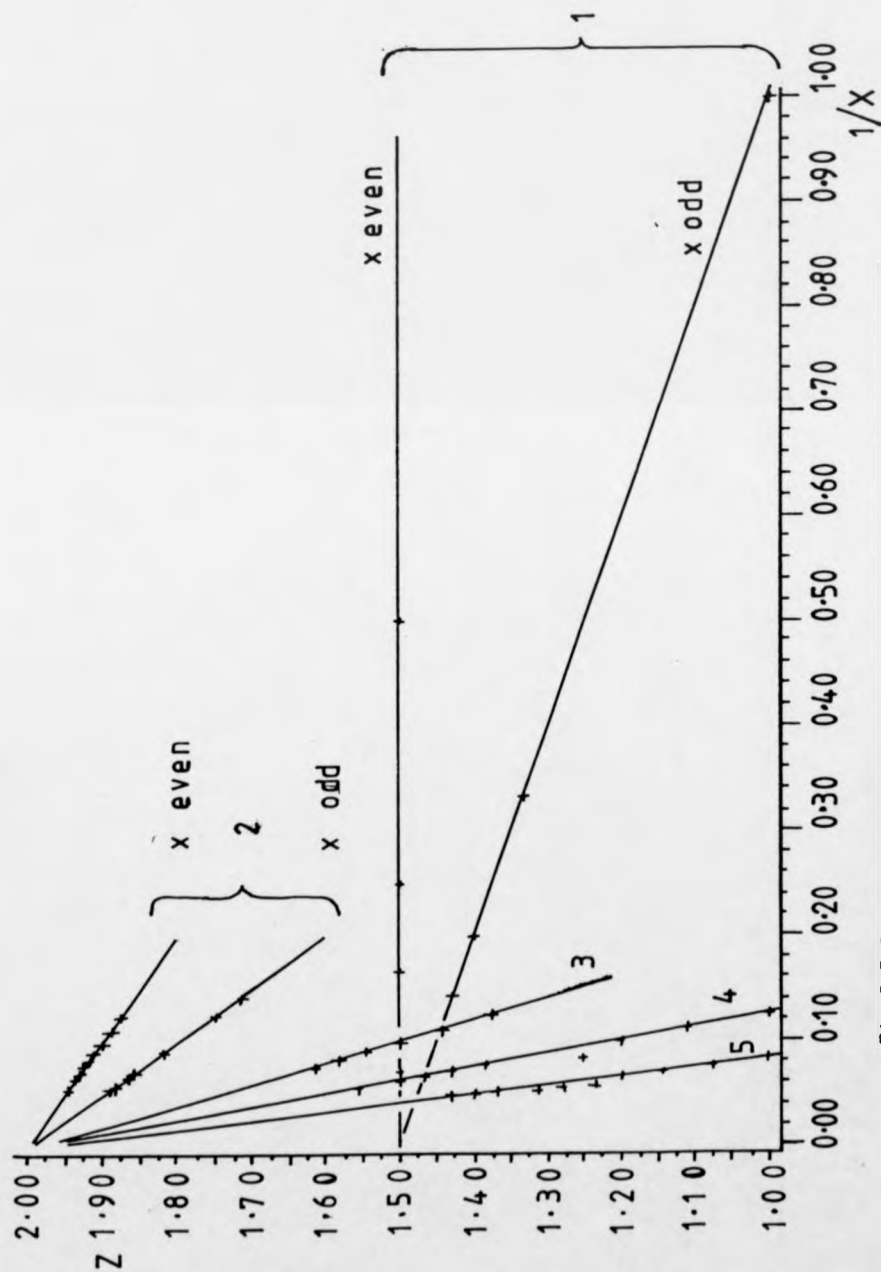


Fig 3.5.9 The Variation in Cerium : Oxygen Atom Ratio, z , with Cluster Size, x .

cerium : oxygen atom ratios and cluster size being expressed by the equations

| | | | | | | |
|--------|---|---|---------|---|------|-----------|
| Line 2 | Z | = | -1/x | + | 2 | Eqn. 3.18 |
| Line 3 | Z | = | -5/x | + | 2 | Eqn. 3.19 |
| Line 4 | Z | = | -8.6/x | + | 2.04 | Eqn. 3.20 |
| Line 5 | Z | = | -11.2/x | + | 1.95 | Eqn. 3.21 |

This shows these cluster series to tend towards Ln_2O_3 stoichiometry, which suggests that these clusters are able to attain a number of structural configurations with increasing cluster size, $x \geq 8$, each tending ultimately to the same stoichiometry.

In the case of cerium, parallels can be drawn between each of these plots and the dominant cerium oxide phases described by Bevan (168). For the clusters $x \leq 7$, even clusters show stoichiometries described by $\text{Ce}_{32}\text{O}_{48}$ while odd clusters are described by $\text{Ce}_{32}\text{O}_{47.5}$. These correspond to the $\text{Ce}_{32}\text{O}_{48}$ phase reported by Bevan and others to have a lanthanide A-type, hexagonal structure. For clusters with $x \geq 8$, the z-ratio distribution for the various cluster series described above show close agreement with those of the four most stable higher oxide phases, (Fig. 3.5.10).

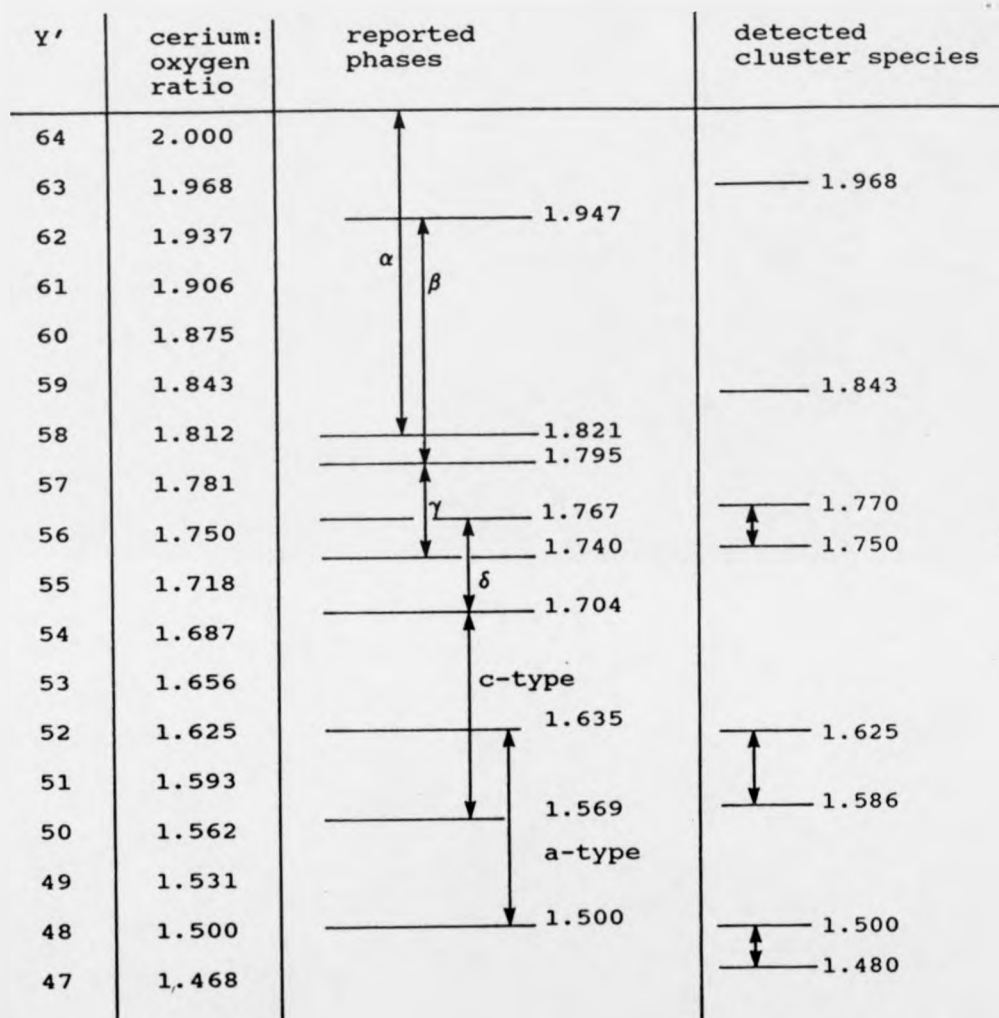


Fig 3.5.10 The Cerium : Oxygen System, $Ce_{22}O_{y'}$.

| | Cluster z ratio | Phase | Cerium : Oxygen ratio | Structure |
|--------|-----------------|----------|-----------------------|-----------|
| line 2 | 1.968 | α | 1.821 - 2 | FCC |
| line 3 | 1.843 | β | 1.792 - 1.947 | Rhomb. |
| line 4 | 1.75 - 1.77 | γ | 1.740 - 1.785 | Rhomb. |
| line 5 | 1.57 - 1.63 | C-Type | 1.569 - 1.704 | BCC |

This suggests that the cerium oxide clusters formed during fast atom bombardment are related to known oxide phases and hence assume the same structural arrangements, with the plots 2, 3, 4 and 5 representing the changeover between body-centred cubic and face-centred cubic structures.

3.5.5 EUROPIUM CLUSTERS

The data for europium clusters are very complex with no readily recognisable patterns being apparent. The distribution of the spectral intensities for the major cluster species in each cluster series decreases with increasing cluster size, with increased relative intensities being observed at $x = 3, 7, 10, 15$ and 20 followed by an abrupt drop in intensity, (Fig. 3.5.11a).

In a plot of the 'additional' oxygen atom content, y , against cluster size, x , an irregular increase in y with increasing x is found while approximate plateau regions are observed in the regions of $x = 3, 7, 11, 19$ and 23 . These points are related by the linear equation

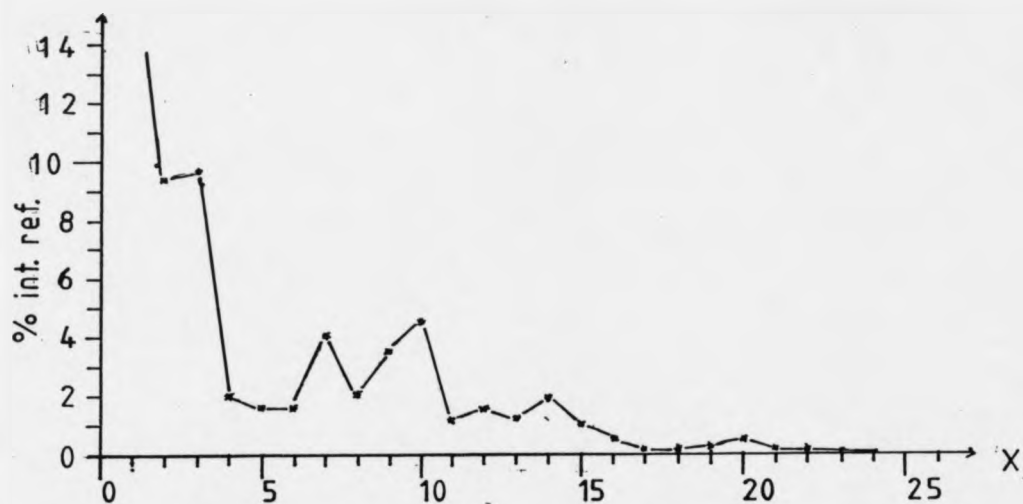
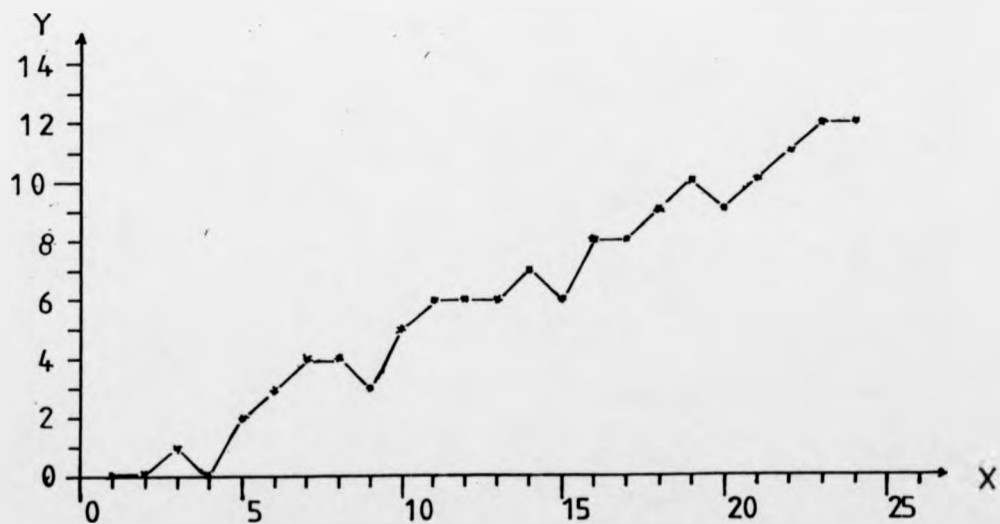


Fig 3.5.11 a) The Change in Relative Intensity with Cluster size.



b) The Change in Additional Oxygen Atom Content with Increasing Cluster Size.

$$Y = 0.5X + 0.5 \quad \text{Eqn. 3.22}$$

a subsidiary maximum was also observed at $x = 14$, (Fig. 3.5.11b).

These plateau regions align rather closely with the positions of the maxima in the relative intensities. This suggests that, as the cluster size increases, structural considerations strongly influence the value of y displayed and hence their relative intensities. Clusters exhibiting increased intensities, reflecting their more stable character, were found to involve the incorporation of larger numbers of additional oxygen atoms.

A plot of the europium : oxygen atom ratio, z , against $1/x$, (Fig. 3.5.12), features a complex relationship for odd clusters, while even clusters exhibit a constant value of $z = 1.5$. For the odd clusters with $x \leq 5$ a linear increase in z is observed as cluster size increases; this can be described by the equation

$$z = -0.5/x + 1.5 \quad \text{Eqn. 3.23}$$

However for larger odd clusters, $x > 7$, z is found to show a marked variation with increasing cluster size. This variation takes the form of an oscillation with the clusters corresponding to $x = 5 + 4n$ lying on the same line as $x = 5$, while the clusters $x = 7 + 4n$ lie on the line

$$z = 0.5/x + 1.5 \quad \text{Eqn. 3.24}$$

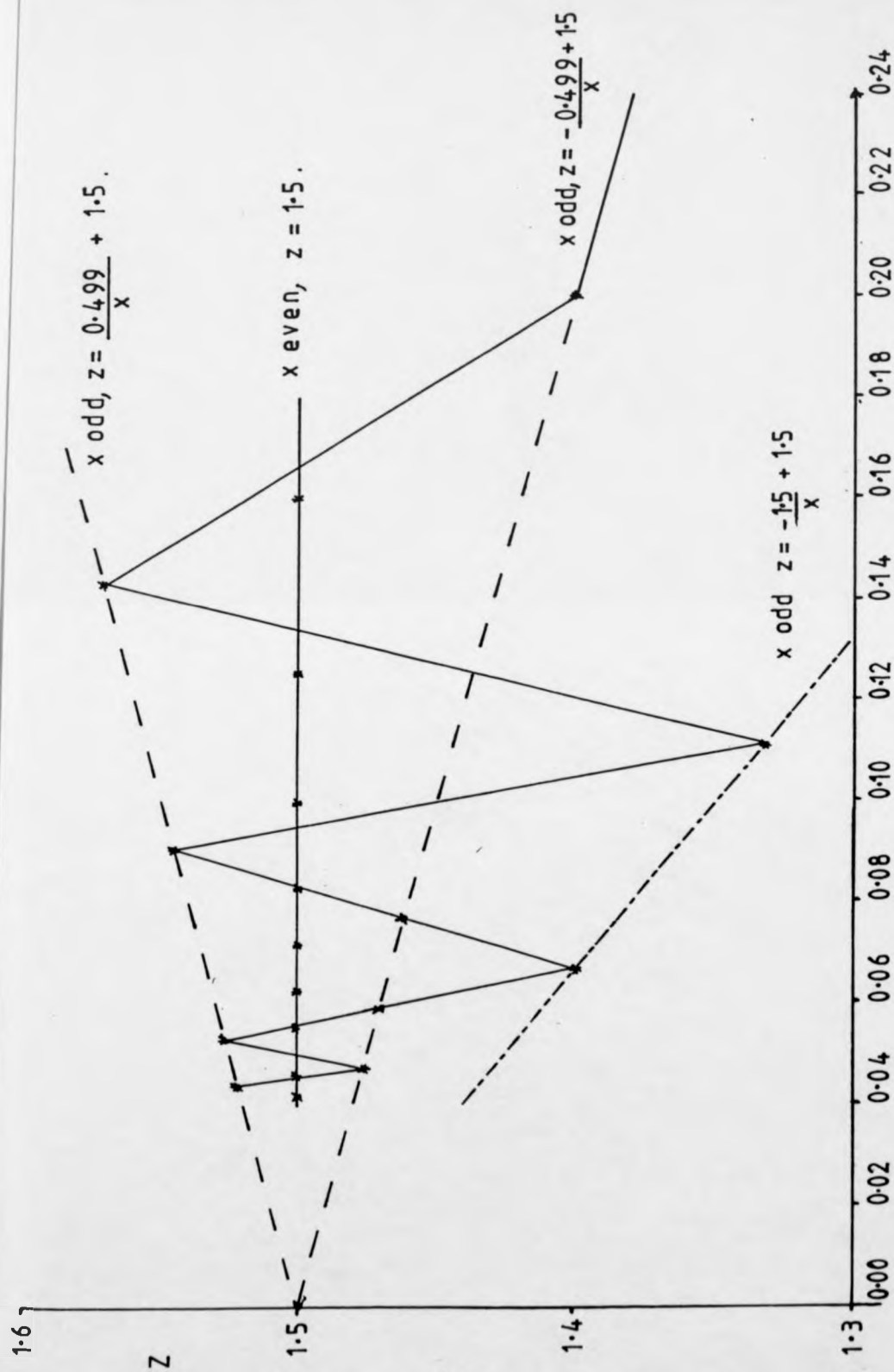


Fig 3.5.12 A Plot of the Metal : Oxygen Atom Ratio with Cluster Size

with the exception of $x = 9$ and 15 which correspond to

$$z = -1.5/x + 1.5 \quad \text{Eqn. 3.25}$$

The above three equations all show the europium : oxygen atom ratio to be equal to $z = 1.5$ for larger cluster sizes. This in turn suggests the ultimate formation of Ln_2O_3 stoichiometries when increasing numbers of cluster units associate. The most intense species corresponding to $x = 9$ and 15 have been found to contain fewer additional oxygen atoms and mark the positions of abnormalities in the intensity of the cluster spectrum of europium. This strongly suggests that these clusters mark the attainment of structural arrangements of enhanced stability.

3.5.6 SAMARIUM CLUSTERS

A plot of additional oxygen atom content, y , against cluster size, $x \leq 23$, for the more intense clusters of samarium gives rise to a number of distinct linear regions for both odd and even clusters, (Fig. 3.5.13). The odd clusters were found to follow a plot of

$$Y = 0.5X - 0.5 \quad \text{Eqn. 3.26}$$

over the whole range of x values recorded, with an additional plot also being observed for $5 \leq x \leq 15$ which corresponds to

$$Y = 0.5X - 1.5 \quad \text{Eqn. 3.27}$$

This suggests that odd clusters can exist in forms with a lower oxygen content up to $x = 15$, after which the former series is the more populated and hence of higher stability.

Even clusters however are found to show a number of distinct linear relationships which are dependent on cluster size. Clusters were initially observed to follow a

$$Y = 0.5X - 1 \quad \text{Eqn. 3.28}$$

relationship for $x \leq 10$, then an abrupt increase in additional oxygen atom content results in the detection of clusters with formulae consistent with the equation

$$Y = 0.5X \quad \text{Eqn. 3.29}$$

At $x = 15$ however, the even clusters are found to revert to the relationship for $x \leq 10$.

Evidence of even clusters of higher oxygen atom content for $4 \leq x \leq 12$ is also present, with the $x = 4$ and 6 clusters following the line

$$Y = 0.5x + 2 \quad \text{Eqn. 3.30}$$

while the clusters $6 \leq x \leq 12$ correspond to

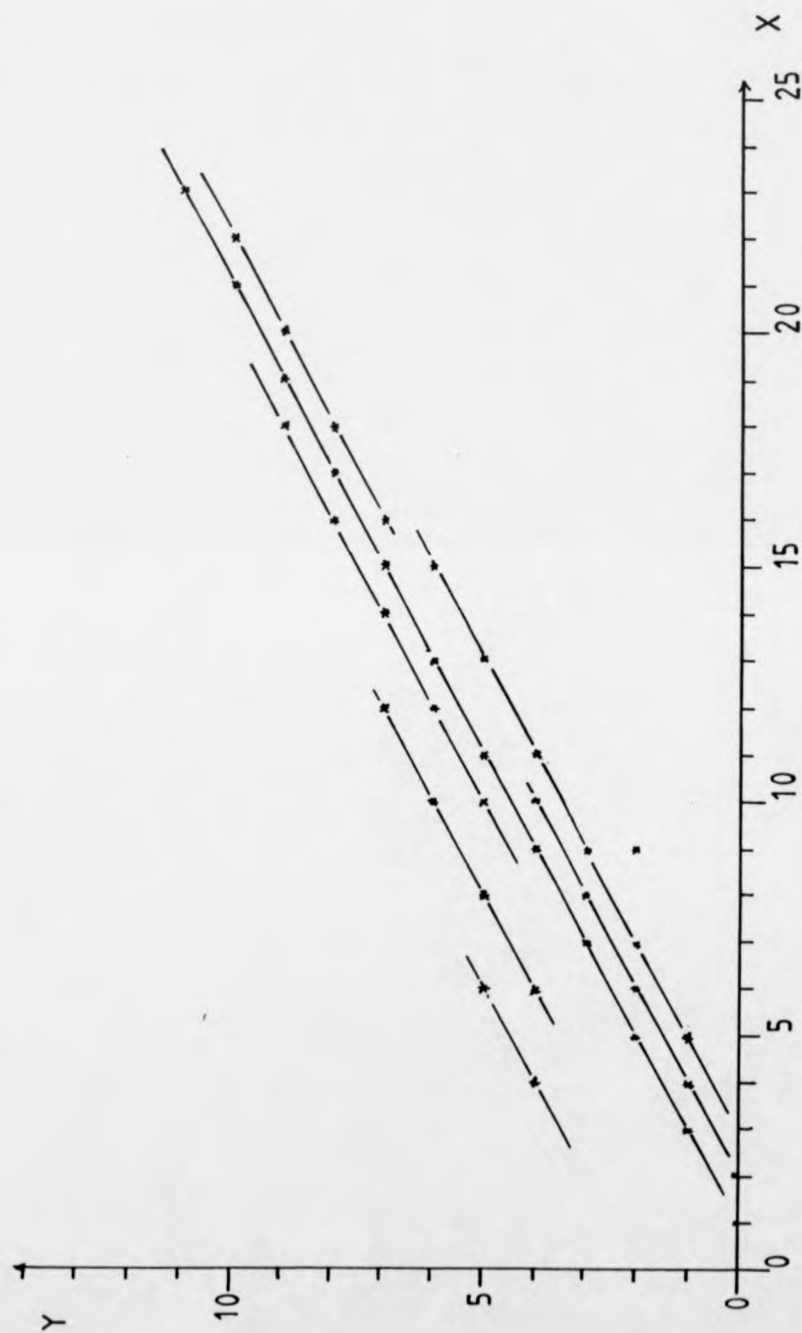


Fig 3.5.13 The Variation in the Number of Additional Oxygen Atoms with Cluster Size for Samarium Clusters

$$Y = 0.5x + 1$$

Eqn. 3.31

Hence even clusters can be seen to exist in several distinct size-dependent regions. These are $x \leq 6$, $6 \leq x \leq 12$, $10 \leq x \leq 18$ and $16 \leq x$ with the series of lower oxygen content observed for $x \leq 10$ being consistent with the $16 \leq x$ cluster series.

Similar trends can also be observed in a plot of the samarium : oxygen atom content, z , against $1/x$, (Fig. 3.5.14), in which all the clusters are seen to lie on lines radiating from $z = 1.5$ at $1/x = 0$, that is $x = \infty$. Thus clusters tend progressively towards the formation of Ln_2O_3 as cluster size increases. Various size-dependent abnormalities are present, centred approximately on the regions $x = 6$, 10, 15, and 19, at which abrupt changes in samarium : oxygen atom ratio occur between neighbouring x -values.

The above graphs show the most distinct ranges in cluster:oxygen content to occur in the region of $x = 10$ and 15 which correlates with the size-dependent intensity and the abnormalities in the metal : oxygen atom ratio observed in the cluster spectrum for europium. This suggests that structural changes occur at these cluster sizes for these closely related lanthanide metals, with the increased intensities of a number of cluster species reflecting their enhanced stabilities.

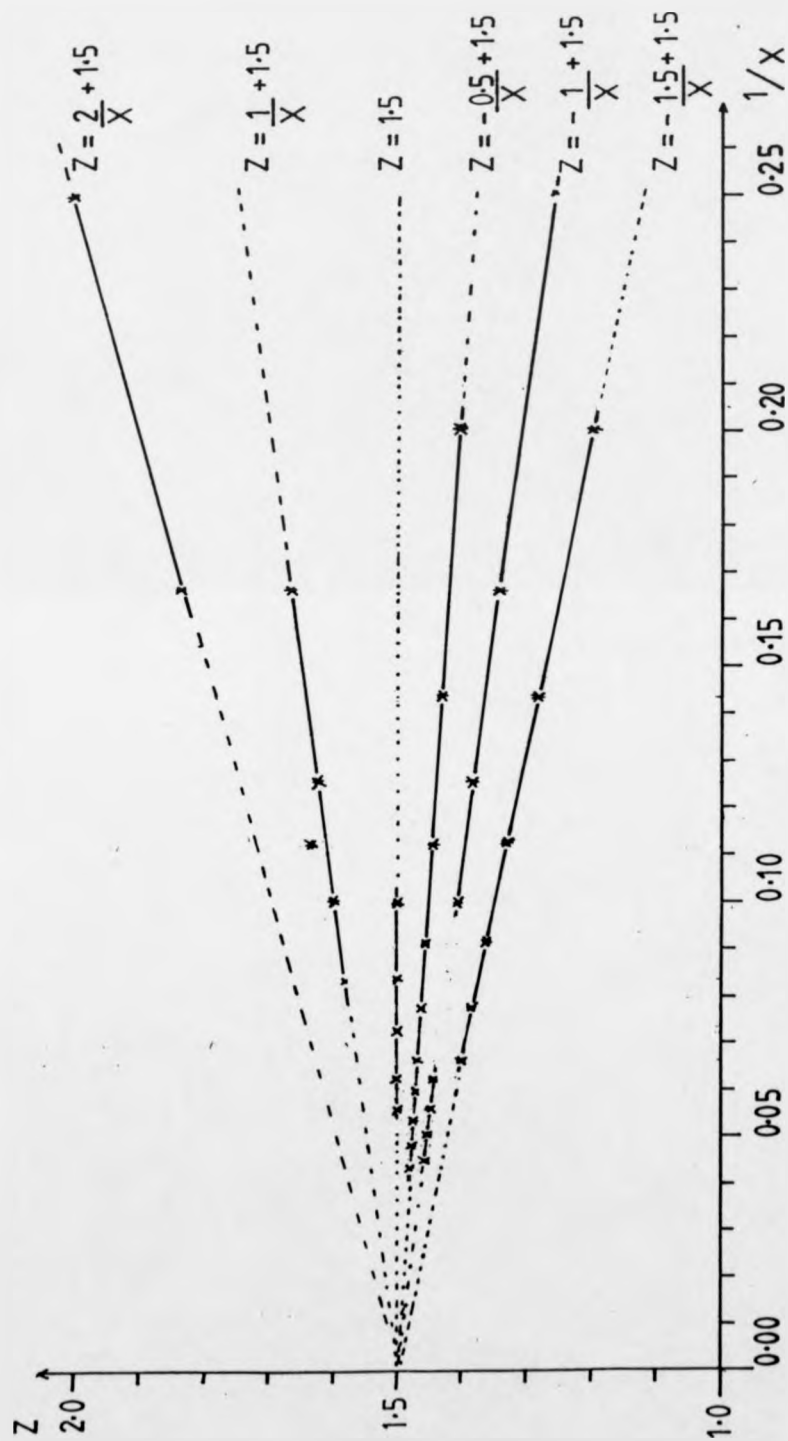


Fig 3.5.14 The Variation in Metal : Oxygen Atom Ratio with Cluster Size for Samarium Clusters.

3.6 CONCLUSIONS

The clusters observed for the lanthanide metals, although showing in some cases distinct behavioural influences, are found to display a number of similar trends over the range of cluster sizes studied. This is clearly demonstrated by the tendency of clusters to form atomic arrangements corresponding to Ln_2O_3 stoichiometries for all the lanthanide elements studied, over all or part of the cluster size range. This trend is consistent with the major lanthanide oxide found in the bulk phase and demonstrates the influence of bulk phase phenomena on small clusters. Other similarities between the clusters of the different lanthanide metals are found in the similar positions of some spectral abnormalities.

The cluster spectra obtained from most lanthanide metals display odd clusters which can be described by

$$z = \pm 0.5/x + 1.5 \quad \text{Eqn. 3.32}$$

with the negative gradient being predominant. This behaviour is clearly shown by clusters based on praseodymium and terbium, whose even clusters display a constant ratio of $z = 1.5$. However the odd clusters of these metals are observed to exhibit metal : oxygen atom ratios which are significantly lower than their neighbouring even clusters. The rate at which the z ratio for the odd clusters is found to increase to $z = 1.5$

is the same for both metals and the other lanthanide metals studied to at least $x = 9$.

Other similarities are also found to exist between various lanthanide metals and these generally occur in the region of $x = 10, 15$ and 20 . In the cluster spectrum of europium, intensity abnormalities in these regions are observed to coincide with the onset of plateau regions in the uptake of additional oxygen atoms and hence correspond to abrupt changes in the z ratios of these clusters. This behaviour is more abrupt for samarium clusters which show sudden changes in their z ratio over limited cluster size ranges. This is clearly demonstrated near $x = 15$, with both odd and even clusters showing marked changes in metal : oxygen atom ratios for $x > 15$. Both europium and samarium exhibit odd clusters corresponding to the relationship

$$z = -1.5/x + 1.5 \quad \text{Eqn. 3.33}$$

for selected x values for $x \leq 15$.

The clusters observed for lanthanum and holmium are also found to show abnormalities in intensity. In the case of the lanthanum-oxygen clusters a sudden increase in oxygen atom content for clusters in the region of $9 \leq x \leq 11$ is found. This peak is centred on the $x = 10$ cluster, which has the highest z ratio. The cluster spectrum for lanthanum is also observed to show an drop in intensity for the peak region and an increase in intensity for $x = 19$; however no abnormality in intensity is found at $x = 15$. Holmium clusters however show the

$x = 21$ cluster to be of enhanced stability and to coincide with a marked change in z ratio, with clusters of higher oxygen content being formed at $x \geq 21$. For cerium clusters, the initial sequence, 1, is found to intercept plots 2, 3, 4 and 5 in the regions of $x = 1, 9, 15$ and 20 respectively.

In addition to the relative positions of the various spectral abnormalities observed, the upper detection limit for many clusters was found to be $x \approx 23$, with few larger clusters being detected. This may also mark the position of a barrier to cluster stability.

The presence of intense clusters containing lower oxygen atom contents in the spectra of europium and samarium may reflect their ability to form divalent ions and thus relate to phases with $x < 1.5$ formed in the solid state. Hence the clusters corresponding to the line

$$z = -1.5/x + 1.5 \quad \text{Eqn. 3.34}$$

may be due to the known solid state phase In_2O_3 , $z = 1.333$.

In the case of cerium, which readily forms stable Ce^{4+} ions, close parallels can be drawn between the more intense clusters observed and a number of phases present in the solid state cerium-oxygen phase system described by Bevan (168). These similarities can be found over a range of cluster sizes and reflect the stoichiometries of the more stable phases formed in the region $z = 1.5$ to 2 . These limits in the cerium : oxygen atom ratio reflect the formation of Ce_2O_3 and CeO_2 respectively.

Although the oxide systems for praseodymium and terbium closely relate to that of cerium, the much reduced availability of the Ln^{4+} state for these metals is probably reflected in their lack of formation of higher-order oxide phases.

The various relationships described above between the metal : oxygen atom ratios, z , and the number of metal atoms present, x , in the corresponding clusters for the lanthanide metals investigated are all of a similar format and can be described by the general formula

$$z = 1.5 - [3x - 2(x + y)] 0.5/x \quad \text{Eqn. 3.35}$$

in which y is the number of additional oxygen atoms present in each cluster containing x metal atoms. This equation assumes the presence of Ln^{3+} metal ions and O^{2-} as the principal oxidation states exhibited. This is seen to be true in the case of praseodymium and terbium, with a perfect correlation being found to exist between experimental and calculated data. For the lanthanide metals in which additional oxidation states are available, however, relationships exist which

$$- [3x - 2(x + y)] > +1 \text{ or } < -1 \quad \text{Eqn. 3.36}$$

suggest that these clusters contain mixed oxidation states. This in turn fits the data for the cerium-oxygen clusters if allowances are made for the presence of Ce^{4+} , and Eu^{2+} and Sm^{2+} for europium and samarium respectively.

From Eqn. 3.35, an explanation for the presence of odd / even alternation can be deduced. For even clusters

$$[3x - 2(x + y)] = 0 \quad \text{Eqn. 3.37}$$

and consequently $z = 1.5$, hence neutral clusters should have no unpaired electrons. This in turn suggests that monopositively charged even clusters have a odd number of electrons, so are less stable due to the presence of the unpaired electron. In the case of clusters containing odd numbers of metal atoms, positively charged clusters would have even electron counts and hence enhanced stabilities. Similar behaviour is found for clusters of silver and related metals (106)(107).

In this investigation, the presence of various structural forms have been observed for a number of lanthanide metal oxide clusters. These are most clearly displayed by the different cluster relationships observed for cerium. This is a consequence of the availability of the +4 state and contrasts with the behaviour displayed by praseodymium and terbium oxide clusters despite the close similarities in their oxide phase systems. This can be viewed by considering the relative energies and interactions between the potential energy hypersurfaces for the various possible cluster geometries.

In the case of the less complex cluster sequences, for example those exhibited by praseodymium and terbium oxide clusters, the odd clusters are observed to be the dominant species over the size range studied. This infers that these clusters are energetically more stable

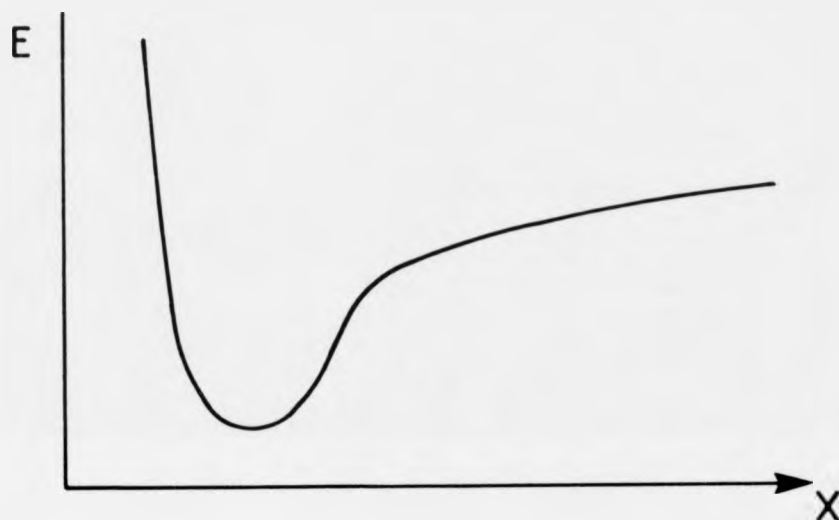


Fig 3.6.1 The Potential Energy Surface for Structure S_1 with Increasing Cluster Size

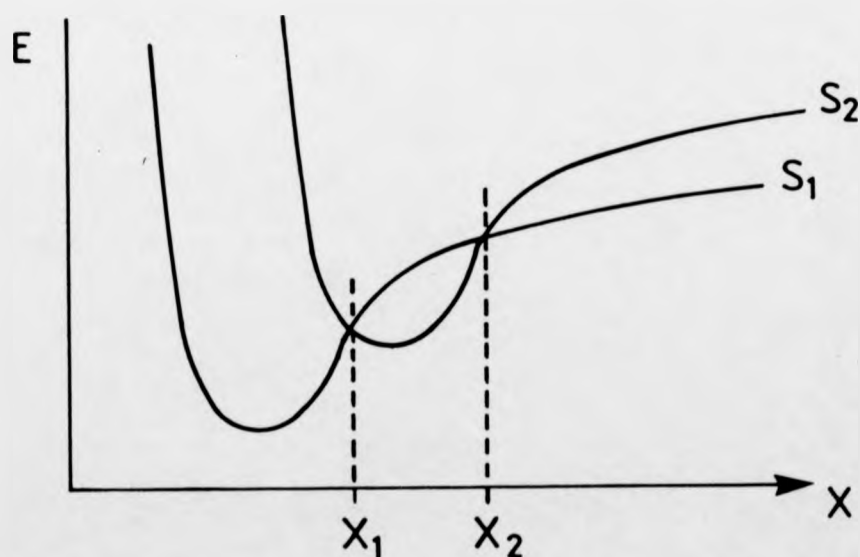


Fig 3.6.2 The Variation in the Potential Energy Surfaces for Structures S_1 and S_2 with Increasing Cluster Size, x .

than the even clusters in the same system; this however may be a consequence of their electronic structures. The structural arrangement adopted in both cases is the same and hence described by a single potential energy curve, (Fig. 3.6.1). The position of the energy minimum for this curve has been shown by laser excitation experiments conducted on other cluster systems to depend on the conditions of cluster formation.

As the cluster energy increases, the average binding energy of each constituent cluster unit decreases, while the number of degrees of freedom through which excess energy may be dissipated increases with cluster size. Hence at higher energies it becomes possible for clusters to undergo rearrangement to more energetically favourable structures, with the level to which higher energy forms are adopted being dependent on the differences in energy between the two possible forms ^a and the range of cluster sizes, x , for which these structures are more favourable, that is the extent of crossing of their relative potential energy hypersurfaces. In (Fig. 3.6.2) the variation in the potential energy surfaces for structures S_1 and S_2 with increasing x are described. Small clusters would be expected to exist in the more energetically favourable structure S_1 . As cluster size increases $x \rightarrow x_1$, the relative energies of successive clusters increase, so that at $x = x_1$ it becomes energetically favourable for the cluster to adopt structure S_2 as x increases. This may account for the sudden increase in metal : oxygen atom ratio of $x \approx 20$ observed for holmium.

However if at a higher x value, x_2 , structure S_1 may again occur at a lower energy, resulting in the clusters again assuming structure S_2 . This may be detected by the presence of a sharp discontinuity in the metal : oxygen atom ratio over a limited cluster size range, similar to that observed in the cluster spectrum of lanthanum in the region of $x = 10$.

This basic energy level model can be extended to describe the relative energies of the various phases found in the cerium-oxygen system, (Fig. 3.5.8). While cerium oxide clusters are observed to behave like those of praseodymium and terbium oxide at small values of x (1); the cerium oxide clusters are also seen to have another possible structural form (2) which is adopted only at $x > 7$. This suggests that although clusters $x < 7$ are able to exist in both these forms, form 1 is more energetically stable. These forms are considered to correspond to A-type and face centred cubic structures respectively. As the cluster size increases, i.e. $x > 7$, the presence of the potential energy hypersurfaces for other possible structural forms become significant, which in turn leads to the formation of clusters corresponding to the rhombohedral phases, while clusters corresponding to sequences 2 and 5 remain the most intense, hence stable, species which in turn reflects the stabilities of their face-centred cubic and body-centred cubic structures. This behaviour is not exhibited by praseodymium and terbium, suggesting that these additional phases are at sufficiently higher energies to make their formation energetically unfavourable. This is probably due to their less accessible Ln^{4+} state. A similar

explanation can also serve to describe the cluster distributions
observed for europium and samarium.

4.1 URANYL CLUSTERS

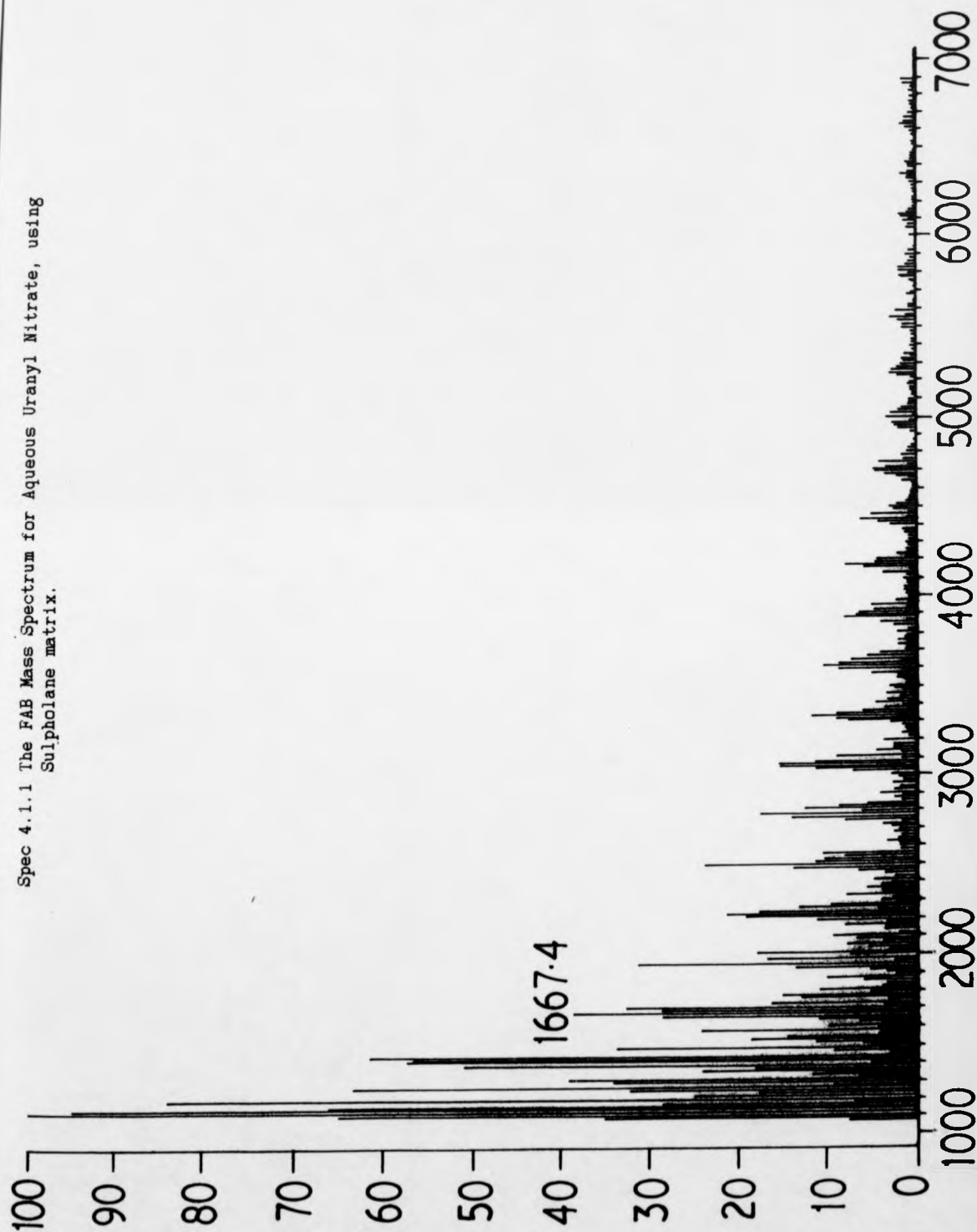
The FAB mass spectra obtained from uranyl nitrate hexahydrate solution, recorded using a number of matrices and co-solvents, show the presence of a number of distinct sequences of peaks the masses of which correspond to multiples of that of UO_2^+ , $m/z = 270$. These high mass species follow the general formulae $[(\text{UO}_2)_x \text{O}_y]^+$, with the number of additional oxygen atoms, y , present increasing with increasing cluster size, x . High mass spectra containing peaks of notable intensity corresponding to clusters with x up to 37 were recorded using the first two sectors of a Kratos Concept 4 sector mass spectrometer, although some clusters of larger sizes were observed.

The relative intensities of successive cluster series were found to show an exponential decrease with increasing cluster size, with abnormalities in intensity being observed in the region of

$$x = 9, 14 - 16, 19 - 22, 25, 27, \text{ and } 32$$

as well as possible odd/even alternation being observed at higher cluster sizes in most of the spectra studied. These intensity abnormalities in many cases are marked by the sudden onset of a decrease in intensity after a given cluster size or the presence of an anomalously high intensity of a particular cluster. As x increases the corresponding number of additional oxygen atoms, y , present in the most intense cluster of each successive series is observed to increase

Spec 4.1.1.1 The FAB Mass Spectrum for Aqueous Uranyl Nitrate, using Sulpholane matrix.



gradually. For a cluster with a given value of y [$(\text{UO}_2)_x \text{O}_y$] $^{+}$, increases in x results in the intensity undergoing a rapid increase before decreasing exponentially on further increases in cluster size.

The influence of matrix adduct formation on cluster size was also investigated for a number of matrices, with the presence of matrix adducts becoming more significant at larger cluster sizes.

A graphical plot of the variation in the number of additional oxygen atoms, y , present with increasing cluster size, x , gives rise to a number of distinct parallel linear lines. The first of these corresponds to clusters with odd values of x , which, with the exception of $x = 27$, can be described by the equation

$$Y = 0.5 X - 0.5 . \quad \text{Eqn. 4.1}$$

Clusters with even values of x show two size-dependent relationships corresponding to

$$Y = 0.5 X \quad \text{Eqn. 4.2}$$

at smaller cluster sizes ($x_1 = 2 - 16$, and also $20 - 22, 28$), and

$$Y = 0.5 X - 1 \quad \text{Eqn. 4.3}$$

for larger cluster sizes ($x_1 = 18, 24 - 26, 30 -$, and also 14).

These plots show uranyl clusters with even values of x initially to

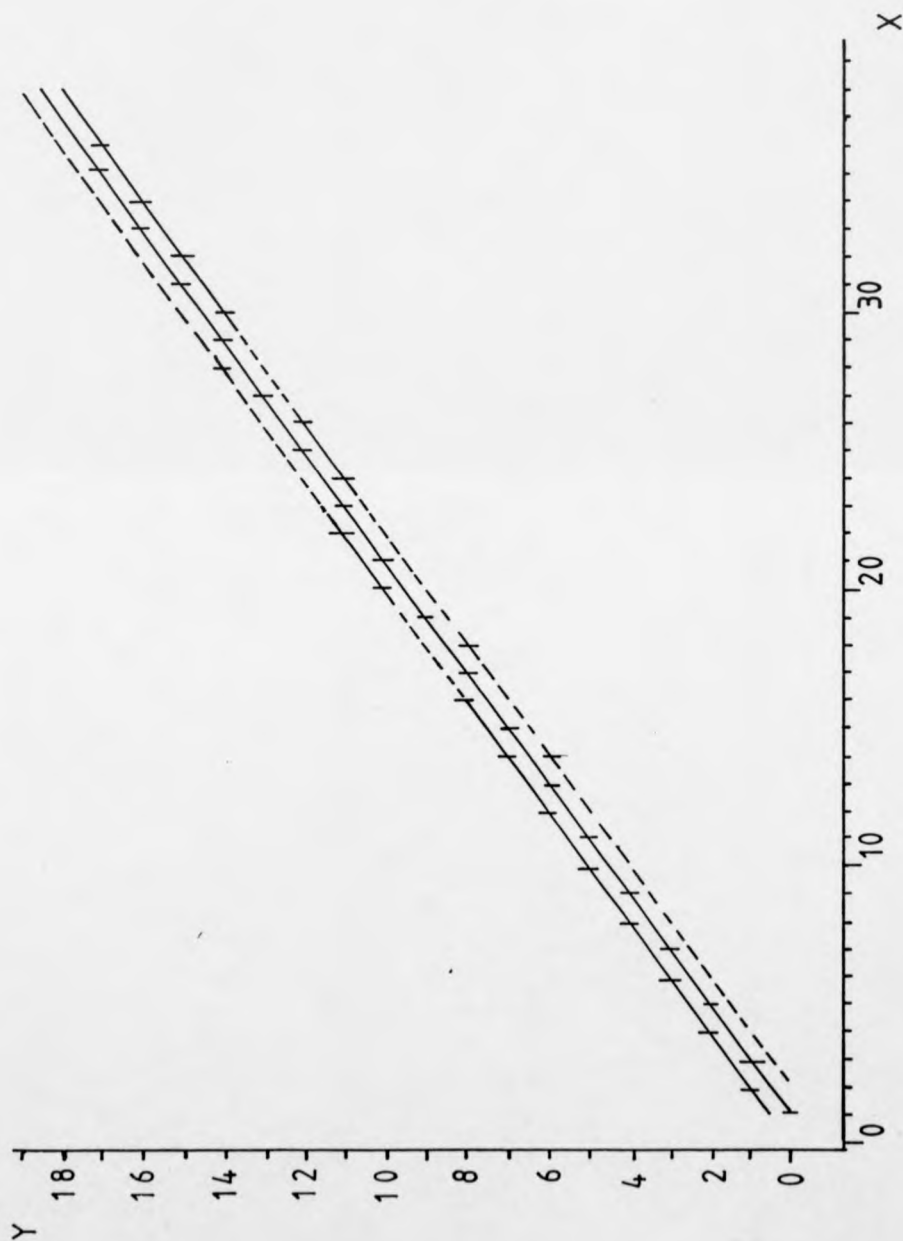


Fig 4.1.1 The Variation in Additional Oxygen Atom Content, y , with Increasing Cluster Size, x .

favour stoichiometries with uranium : oxygen atom ratios, $z = 2.5$, while larger clusters with even values of x preferentially form clusters with a reduced uranium : oxygen atom ratio. Clusters with odd values of x however adopt intermediate z ratios regardless of their cluster size. This suggests that clusters with even values of x undergo a gradual change in stoichiometry, with the more stable larger clusters having reduced numbers of additional oxygen atoms. This reduction on relative y with increasing cluster size, and the relationship between the uranium : oxygen atom ratio and cluster size for odd clusters shows clusters to adopt particular structural arrangements in which $z < 2.5$.

A plot of the variation in the uranium : oxygen atom ratio, z , with cluster size, x , gives rise to a single relationship for odd clusters in which the uranium : oxygen atom ratio approaches $z = 2.5$ as $x \rightarrow \infty$; at $x = 25$, however, a slight reduction in z is observed. A similar plot for even clusters gives rise to two distinct size-dependent relationships. The first of these, corresponding to clusters of size x_0 , is observed to show a constant value of z of 2.5 independent of cluster size. However as the cluster size increases a second relationship becomes dominant in which clusters of size x_1 display values of $z = 2.5$; with $z \rightarrow 2.5$ as $x \rightarrow \infty$.

A plot of the variation of the uranium : oxygen atom ratio, z , with the number of additional oxygen atoms, y , present gives rise to three plots. The first of these shows a constant value of $z = 2.5$ and corresponds to even clusters of the size range x_0 , while the other plots corresponding to even clusters of size x_1 and all odd clusters are

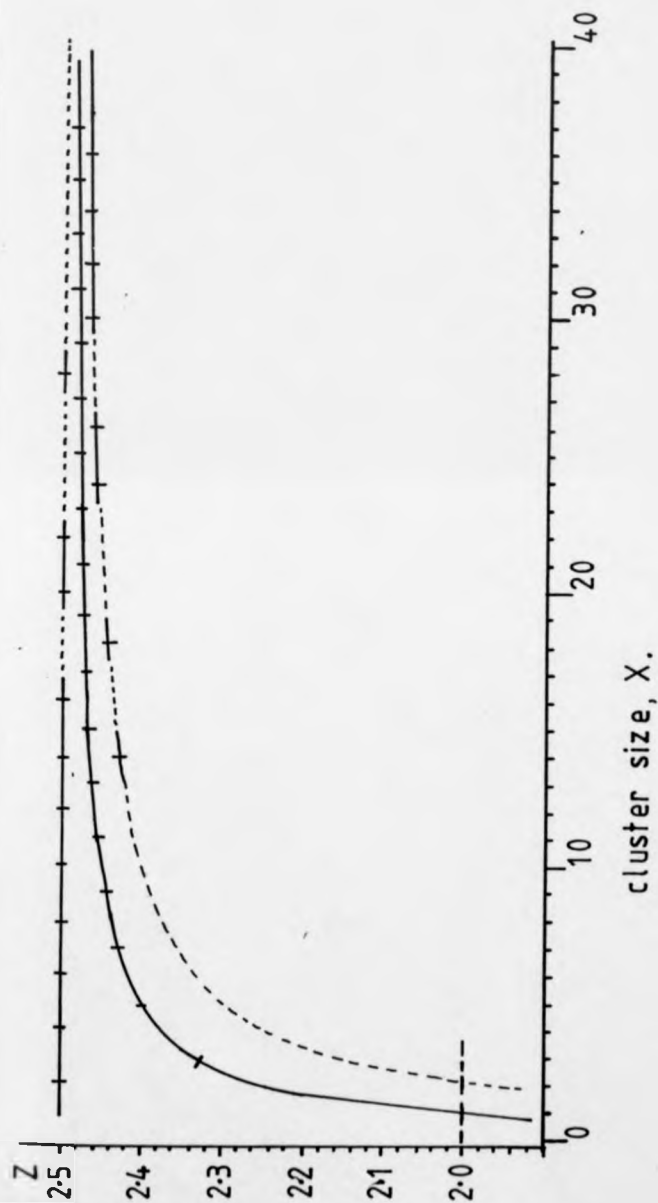


Fig 4.1.2 The Variation of Uranium : Oxygen Atom Ratio, z , with Cluster Size, x .

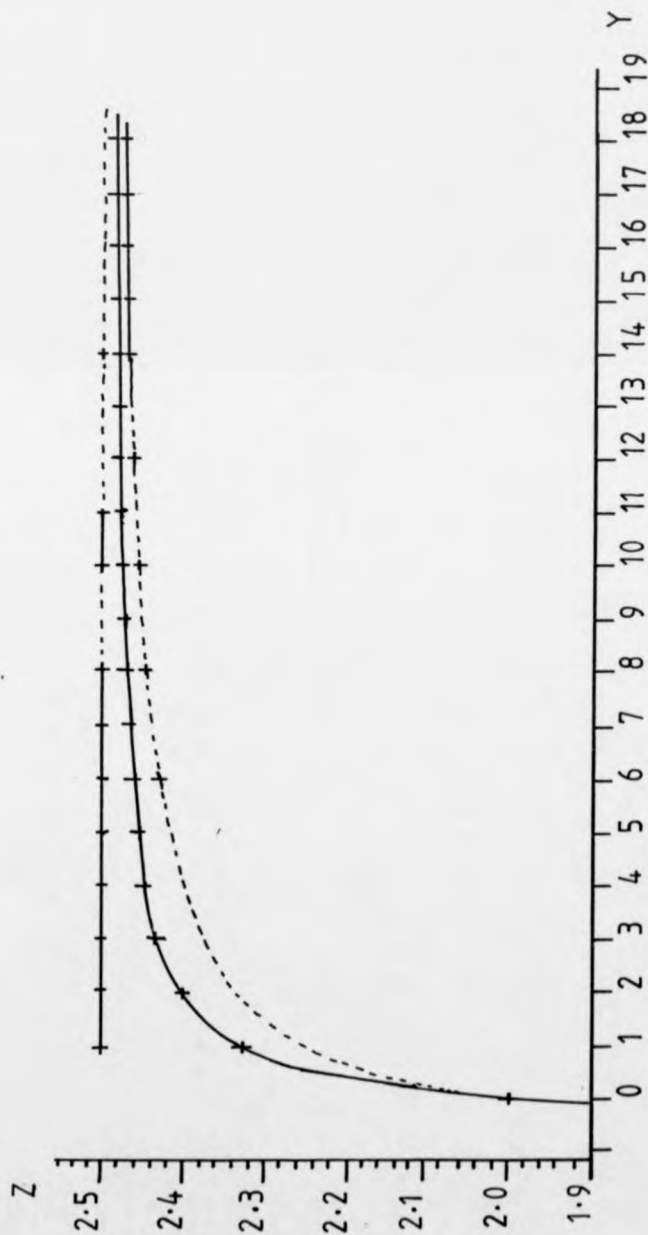


Fig 4.1.3 The Variation in Uranium : Oxygen Atom Ratio, z , with Increasing Numbers of Additional Oxygen Atoms, y .

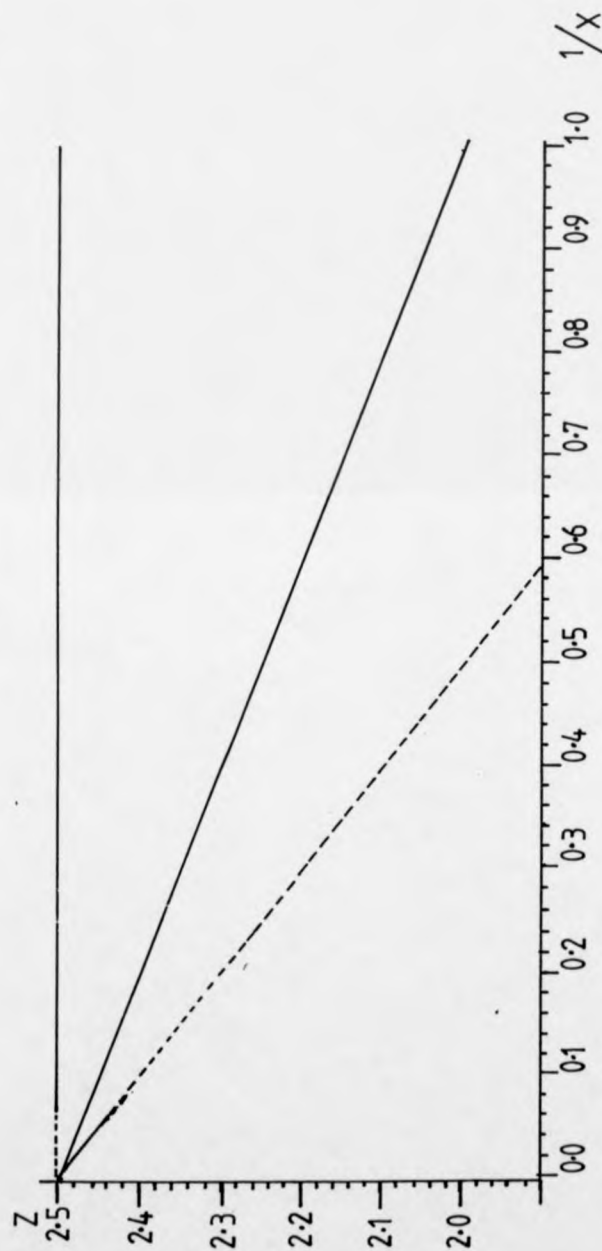


Fig 4.1.4 A Graphical Representation of the Variation of the Uranium : Oxygen Atom Ratio, Z , with $1/X$

observed to make intercepts at $y = 0$ and $y = \infty$ when $z = 2.0$ and $z = 2.5$ respectively. This suggests that these clusters have structures which are based on UO_2 units, i.e. $z = 2.0$.

The size-dependent behaviour of the uranium : oxygen atom ratio, z , can be expressed clearly by examining the variation in the cluster z ratio with $1/x$. The resulting graph yields three linear plots, with the relationship due to the odd clusters being expressed by the equation

$$Z = -0.49 / x + 2.49. \quad \text{Eqn. 4.4}$$

This shows the uranium : oxygen atom ratio to increase with the size of odd clusters size until $z = 2.5$ for very large clusters. Small even clusters, corresponding to those of size x_2 , display a constant value of $z = 2.5$, independent of cluster size, while the variation in z values for cluster of size x_1 can be expressed by the equation

$$Z = -1 / x + 2.49. \quad \text{Eqn. 4.5}$$

Hence small and very large even clusters are found to exhibit uranium : oxygen atom ratios of $z = 2.5$, while intermediate-sized clusters, still in the class x_1 , show values of $z < 2.5$. Thus when $y = 0$ the corresponding clusters show values of the uranium : oxygen atom ratio of

| | | |
|------------|------------|------------------------|
| $X = X_2,$ | $Z = 2.5,$ | U_2O_5 |
| $X = X_1,$ | $z = 2.0,$ | UO_2 |
| $X = X_1,$ | $Z = 2.5,$ | U_2O_5 |

Similarly clusters with odd values of x , while featuring $z < 2.5$ for small clusters, exhibit $z \approx 2.5$ for very large clusters.

$$\begin{array}{llll} X & = & 1, & Z = 2.0, & \text{UO}_2 \\ X & = & \infty, & Z \approx 2.5, & \text{U}_2\text{O}_5 \end{array}$$

This dependance of cluster stoichiometry on cluster size, most notably for even clusters, suggests that the clusters may adopt differing structural arrangements over different size ranges. If so even clusters are initially observed to adopt U_2O_5 stoichiometries independent of cluster size, with their neighbouring odd clusters exhibiting stoichiometries between UO_2 and U_2O_5 . However for intermediate-sized clusters the presence of even clusters with reduced uranium : oxygen atom ratios gradually become more significant before becoming the dominant even cluster stoichiometries in the region of $x = x_1 \approx 24$. Even clusters from this region in many cases are observed to show slightly lower relative intensities than neighbouring odd clusters.

If for the above uranium-oxygen clusters the uranium is assumed to be present as only U^{4+} and U^{6+} ions and oxygen as O^{2-} then the above relationship between the uranium : oxygen atom ratio and cluster size can be described by the equation

$$Z = 2.5 - 0.5 / X [6X_1 + 4X_2 - 2Y'], \text{Eqn. 4.6}$$

where $x_1 + x_2 = x$ and y' is the total number of oxygen atoms present in a cluster of size x . So for even clusters of size x_2 , described by equation Eqn. 4.2

$$Z = 2.5 - 0.5 / X [6X_1 + 4X_2 - 2Y'], \text{Eqn. 4.7}$$

if $x_1 = x_2$ then $z = 2.5$. For even clusters of size x_1 , described by equation Eqn. 4.3, if $x_1 = x_2$ then

$$Z = 2.5 - 0.5 / X [+2]$$

that is

$$Z = 2.5 - 1 / X \quad \text{Eqn. 4.8}$$

and for odd clusters, described by equation Eqn. 4.1, if $x_1 = x_2$ then

$$Z = 2.5 - 0.5 / X [+1] \quad \text{Eqn. 4.9}$$

Hence if clusters have equal numbers of U^{4+} and U^{5+} ions, $x_1 = x_2$, the resulting equations are identical to those obtained graphically. The above equations for even clusters, x_2 and x_1 , also show neutral even clusters to have even electron counts and hence singly-charged clusters contain unpaired electrons. However if $x_1 = x_2$ is substituted for odd clusters the resulting expression is in agreement with equation Eqn. 4.4 and show monopositive odd clusters to contain no unpaired electrons, but if $x_1 = x_2 + 1$ or $x_2 = x_1 + 1$ is substituted into the above equation,

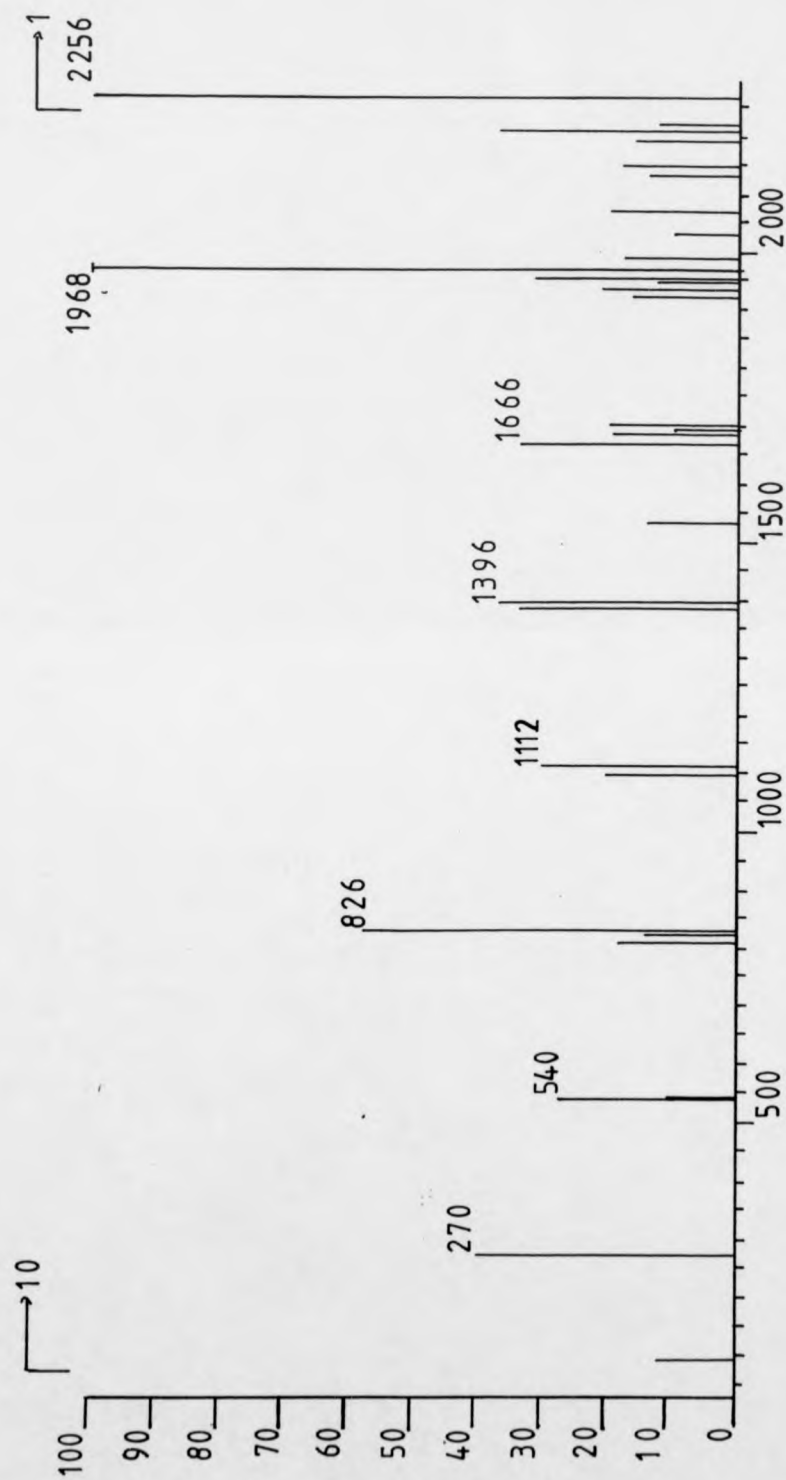
Eqn. 4.6, the resulting expression shows singly-charged odd clusters to contain an unpaired electron.

According to the above equation both odd and even clusters are found to contain unpaired electrons when singly charged so neither group of clusters initially exhibit higher stability electronic configurations resulting in no marked odd/even alternation. However the slight odd/even alternation has been observed for a limited range of x_1 values, this however may be due to relative instability of x_1 clusters at low mass or reduced intensities due to the equilibrium position between x_0 and x_1 structures for these cluster sizes.

The tendency for both odd and even uranyl clusters to approach a value of $z = 2.5$ at very large cluster sizes suggests that these clusters have structures and stoichiometries related to the various U_2O_5 phases. These phases have been shown by Hoekstra et al. (1975) to mark the changeover between fluorite-type structures and the lower density uranyl-bonded uranium-oxygen phase system at $2.4 < z < 2.5$. In which U_2O_5 exists in three major phases; α - U_2O_5 which is dominated by uranyl-type bonding and is stable at lower temperatures and pressures, β - U_2O_5 which has a hexagonal fluorite structure and the monoclinic γ - U_2O_5 phase. The latter two phases become increasingly stable at higher temperatures. Thus similarities can be found to exist between the cluster stoichiometries detected and the uranyl-fluorite phase boundary for the uranium-oxygen system which is marked by a sudden decrease in density for the uranyl-bonded phases.

4.2 THE COLLISION INDUCED DECOMPOSITION OF URANYL CLUSTERS

The collision induced dissociation, CID, spectra for members of the octa-uranyl, $x = 8$, cluster series were studied at various pressures using argon as collision gas. The CID spectrum for $[(UO_2)_8 O_8]^+$ was observed to follow a single limited fragmentation pathway under single collision conditions, i.e. $> 70\%$ parent beam transmission, this showed the formation of daughter clusters consistent with the loss of neutral UO_3 units. On increasing the collision gas pressure so as to reduce the parent ion beam to 50% transmission the fragmentation was observed to result in the formation of daughter clusters for $x = 8$ to 1. The daughter clusters formed are consistent with a fragmentation pathway that involves the initial loss of neutral UO_3 units followed by the loss of UO_2 units when the uranium : oxygen atom ratio, z , is equal to $z = 2.0$. On increasing the collision gas pressure further, the clusters of lower x value were observed to undergo a number of possible fragmentations, again due to the loss of various combinations of neutral UO_3 and UO_2 moieties, with $z > 2.0$ for the daughter clusters formed. This behaviour was found to occur in the fragmentation pathways of higher mass clusters as the collision gas pressure was further increased, with at approximately 30 % transmission the loss of neutral UO_4 units being observed in addition to UO_3 and UO_2 , with the $[(UO_2)_8 O_8]^+$ parent cluster being seen to undergo the loss of both UO_3 and UO_4 moieties at $< 10\%$ transmission conditions. The most intense fragments, daughter clusters, and hence the dominant fragmentation pathway was found to be that shown at low collision gas pressures. This suggests that the initial sequential loss of UO_3 units



Spec 4.2.1 The CID Spectrum for $(\text{UO}_2)^+ \text{O}_2^+$, $m/z = 2256$, Argon Collision Gas, Flexicell at 2KV and 30% Transmittance

until $z = 2.0$, followed by the loss of UO_2 units, to be the lowest energy fragmentation pathway available.

The cluster ion $[(\text{UO}_2)_5 \text{O}_4]^+$, $m/z = 2224$, was also observed to follow the above fragmentation pattern during collision induced dissociation.

For all hexa-uranyl parent clusters studied the daughter clusters formed showed increased relative intensities for the odd clusters $x = 1, 3, 5$ and 7 , this observation being independent of the collision gas pressure used.

The CID spectra for a number of hepta-uranyl, $x = 7$, clusters were studied over a range of collision gas pressures. In these spectra the extent of fragmentation was found to increase with increasing collision gas pressure, as also were the presence of additional fragmentation pathways developing. This is demonstrated by the large number of daughter clusters observed at low parent cluster transmittances. The dominant fragmentation pathway observed for most parent clusters in this series ($x = 7$, $y = 0$ to 6) involved the initial loss of neutral UO_3 units followed by the loss of UO_2 units when $z = 2.0$.

However a number of exceptions were observed as follows.

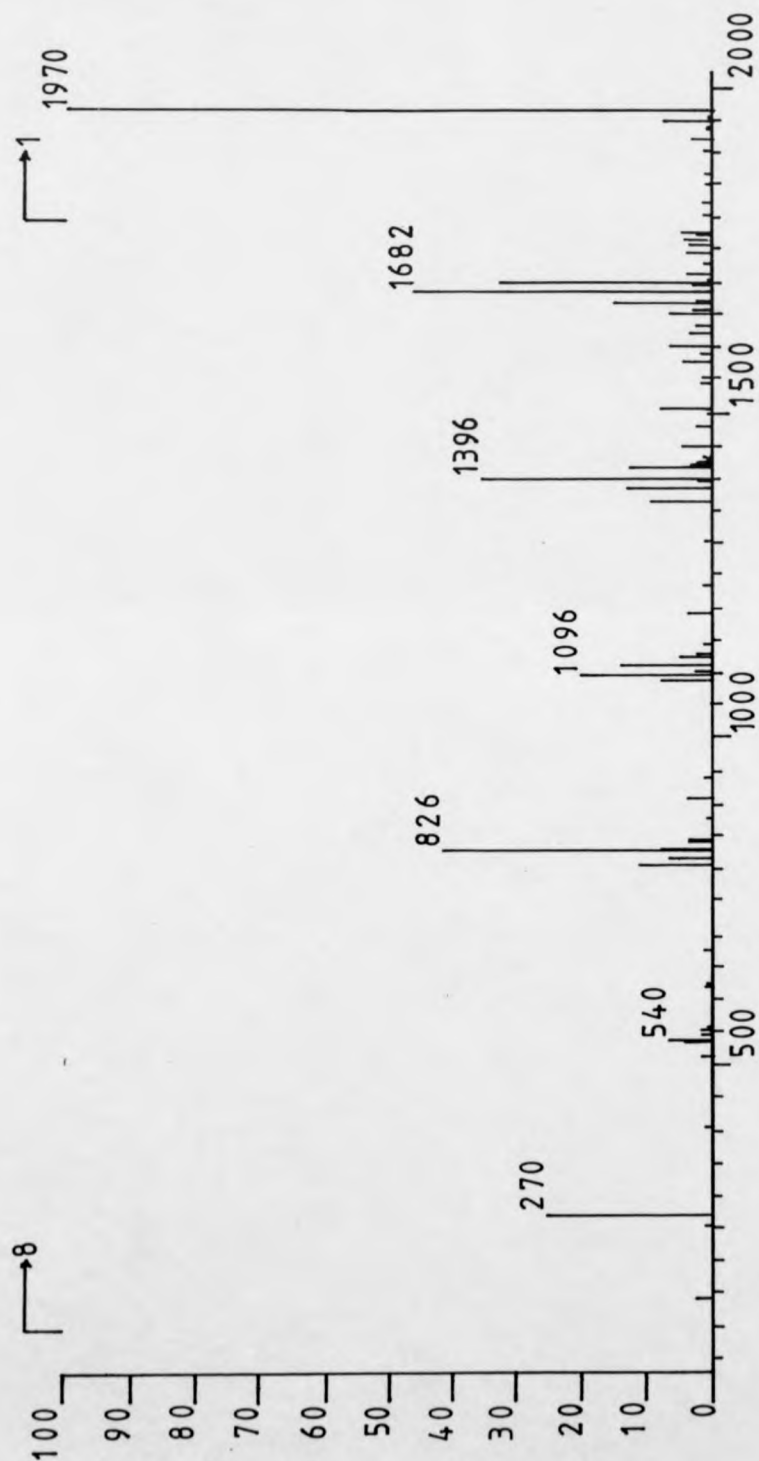
For $[(\text{UO}_2)_7 \text{O}_6]^+$, the $x = 5$ daughter fragments were observed to dissociate by the loss of UO_4 neutral units to form $[(\text{UO}_2)_4 \text{O}_2]^+$ over a range of collision gas pressures. This may be a result of the

$x = 5$ fragment cluster having an enhanced stability. The relative intensities of the $x = 1, 3, 5$ clusters were also found to be enhanced over the range of collision gas pressures used.

The CID spectra for $[(UO_2)_7 O_6]^+$ initially showed only limited fragmentation, with daughter clusters corresponding to $x \geq 3$ being observed at approximately 70% transmittance. The relative intensities of these species showed an exponential decrease with decreasing cluster size. For 50% transmittance the daughter clusters, $x = 1$ to 6, were present, although their relative intensities showed sharp decreases following the fragmentation of the $x = 3$ and 5 daughter clusters. This is consistent with the spectra obtained at higher collision gas pressures, at which these odd cluster species are observed to have increased relative intensities, with the $x = 3$ daughter cluster being dominant.

For the ion $[(UO_2)_7 O_4]^+$, the fragmentation spectra shows the $x = 3$ and 5 daughter clusters to have increased relative intensities. The daughter clusters corresponding to $x < 3$ only become significant when the parent ion beam attenuation exceeds 50%.

For $[(UO_2)_7 O_6]^+$ the CID spectra at high parent cluster beam transmittances, i.e. which therefore experience only a few collisions, show only low daughter cluster intensities, which decrease exponentially with decreasing cluster size. On increasing the collision gas pressure however, the relative intensities of the low mass fragment clusters were observed to increase. The increasing intensities of these low mass



Spec 4.2.2 The CID Spectrum for $(\text{UO}_2)_2\text{O}_2^+$, $m/z = 1970$, Argon Collision Gas, Flexicell at 2KV and 30% Transmittance

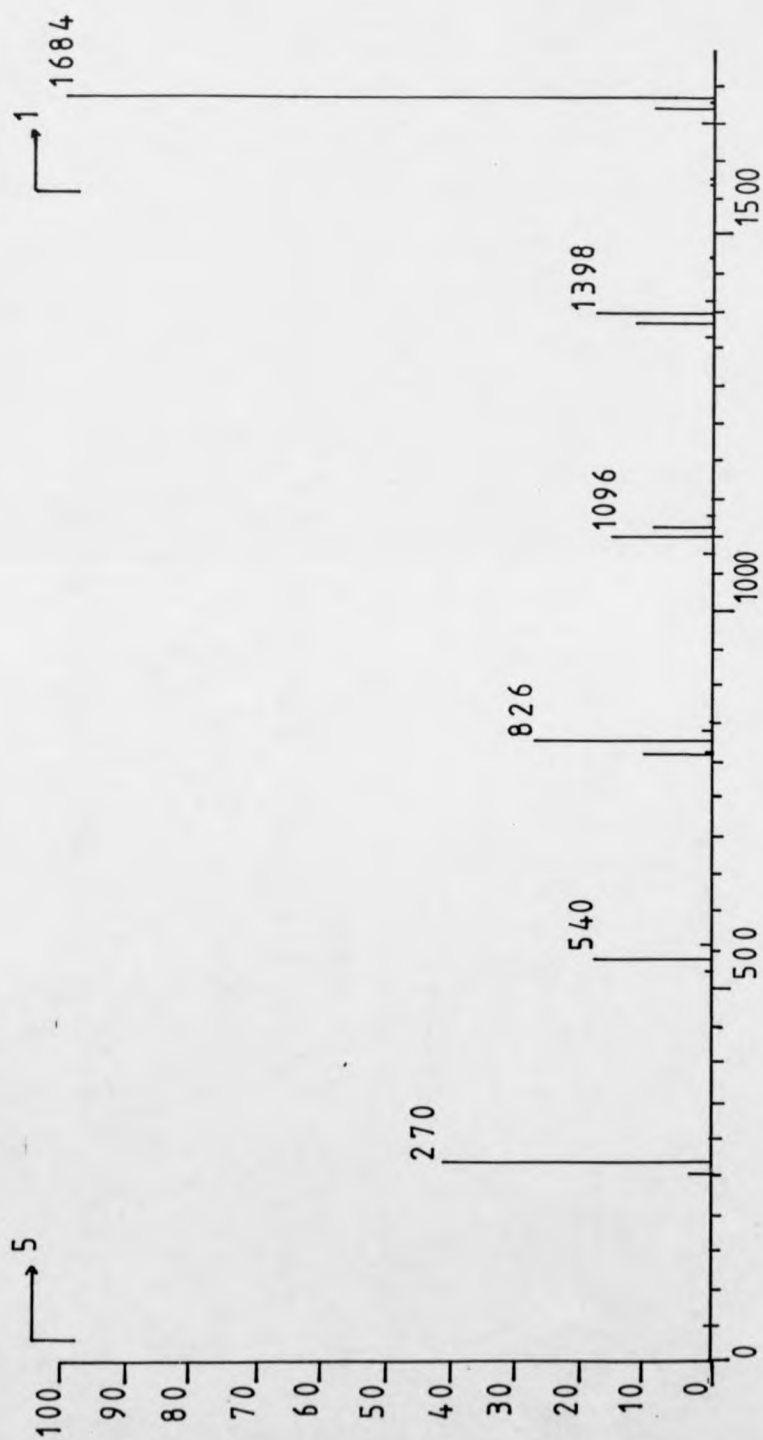
fragments becomes more evident as the parent cluster beam transmittance drops below 30%. As the transmittances decrease further, the relative intensities of the daughter clusters are found to be influenced by their structural stabilities. They also show the presence of additional fragmentation pathways. This occurs to such an extent that, when the transmittance approaches 10%, the odd clusters exhibit greatly enhanced intensities relative to neighbouring even clusters. This odd/even alternation may reflect increased electronic or structural stabilities for odd clusters.

The fragmentations observed for $[(\text{UO}_2)_7 \text{O}_2]^+$ and $[(\text{UO}_2)_7 \text{O}]^+$ ions displayed a similar character to that shown by $[(\text{UO}_2)_7 \text{O}_3]^+$, with the parent cluster undergoing the stepwise loss of neutral UO_3 and UO_2 units. The resulting daughter clusters exhibited odd/even alternation at high collision gas pressures. However the CID spectra recorded for $[(\text{UO}_2)_7]^+$ were found to be significantly different at higher collision gas pressures. As transmittances of parent clusters approached 10% the intensity of the $x = 6$ fragment cluster was observed to decrease relative to the other clusters, while the intensities of the daughter clusters corresponding to $[(\text{UO}_2)_x \text{O}_2]^+$ become more significant for $x = 3, 4, 5$. This indicates the presence of an additional fragmentation pathway being adopted at high collision gas pressures, hence energies, for $[(\text{UO}_2)_7]^+$ clusters.

The fragments observed in all the CID spectra for $[(\text{UO}_2)_7 \text{O}_y]^+$ were the same and corresponded to the general formula $[(\text{UO}_2)_x \text{O}_y]^+$, with x and y being reduced on each successive fragmentation. For higher

mass species the neutral unit lost was UO_3 , with this moiety being lost sequentially until the resulting daughter cluster had a formula that corresponded to $y = 0$, i.e. $z = 2.0$. Then the successive loss of UO_2 units occurred until a residual UO_2^+ species was formed. The character of the sequential loss of single neutral moieties, with the extent of fragmentation being directly proportional to the collision gas pressure, also gives a clear indication that the charge is retained on the larger dissociative fragment, namely the daughter cluster.

For the hexa-uranyl cluster series, $[(\text{UO}_2)_6\text{O}]^+$, the collision induced dissociation is observed to follow a similar sequence of events to those displayed by the hepta- and octa-uranyl clusters. In which parent clusters fragment by the sequential loss of single neutral units, resulting in mono-positively charged daughter clusters the y values of which are dependent on that of their parent cluster. The extent to which this fragmentation takes place is directly related to the collision gas pressure present. The dominant fragmentation pattern involves the parent cluster, $y \geq 1$, undergoing the initial loss of UO_3 units until the uranium : oxygen atom ratio is equal to $z = 2.0$; the resulting daughter clusters then undergo the loss of neutral UO_2 units ultimately resulting in the formation of the UO_2^+ ion. As the collision gas pressure increases the number of available fragmentation pathways increases, although that outlined above remains preferential. This behaviour is clearly demonstrated by comparing the numbers of additional oxygen atoms present in the daughter clusters formed on the collision-induced decomposition of the various hexa-uranyl parent clusters studied.



Spec 4.2.3 The CID Spectrum for $[(UO_2)_2O_4]^+$, $m/z = 1684$, Argon Collision Gas, Flexicell at 2KV and 30% Transmittance

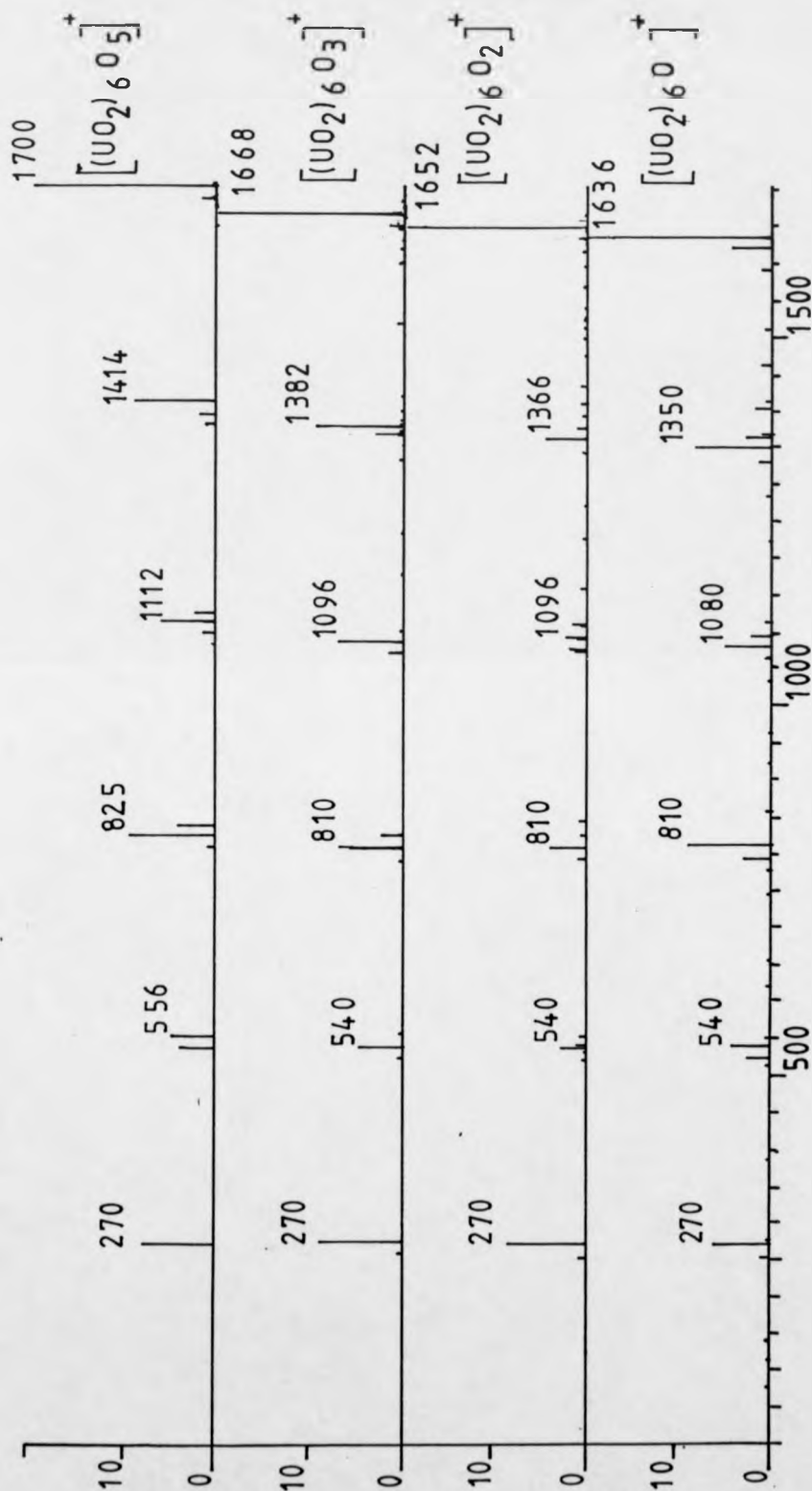


Fig 4.2.1 The CID Spectrum for $(\text{UO}_2)_6\text{O}_5^+$, Argon Collision Gas, Flexicell at 2KV and 30% Transmittance. These Clearly Display the Fragmentation Pattern and daughter Clusters formed and their Relative intensities.

Fig. 4.2.2 The variation in % internal reference for the daughter clusters of $[(\text{UO}_2)_x \text{O}_y]^+$ at 30%, 20% and 10% transmittance

| Species | M/Z | % Internal reference | | |
|----------------------------------|------|----------------------|-------|-------|
| | | 30% | 20% | 10% |
| $[(\text{UO}_2)_6 \text{O}_6]^+$ | 1700 | 100.0 | 100.0 | 70.2 |
| $[(\text{UO}_2)_5 \text{O}_4]^+$ | 1414 | 7.4 | 15.2 | 19.6 |
| $[(\text{UO}_2)_5 \text{O}_3]^+$ | 1398 | 1.5 | 8.5 | 8.2 |
| $[(\text{UO}_2)_4 \text{O}_3]^+$ | 1128 | 2.5 | 10.7 | 21.8 |
| $[(\text{UO}_2)_4 \text{O}_2]^+$ | 1112 | 4.3 | 6.3 | 11.9 |
| $[(\text{UO}_2)_3 \text{O}_2]^+$ | 842 | 3.7 | 13.8 | 20.9 |
| $[(\text{UO}_2)_3 \text{O}]^+$ | 826 | 7.6 | 21.3 | 33.3 |
| $[(\text{UO}_2)_2 \text{O}]^+$ | 556 | 3.8 | 13.0 | 25.1 |
| $[(\text{UO}_2)_2]^+$ | 540 | 3.2 | 19.5 | 14.0 |
| $[(\text{UO}_2)]^+$ | 270 | 7.0 | 55.6 | 100.0 |

The relative intensities also show odd clusters to be of notably higher intensity for parent clusters independent of the collision gas pressure used the exception to this being the $[(\text{UO}_2)_6 \text{O}_6]^+$ cluster, the dominant species of the $x = 6$ series in the uranyl cluster spectrum. The daughter clusters of this species show a decreasing intensity with decreasing cluster size, x . $[(\text{UO}_2)_5 \text{O}_4]^+$ however was found to undergo readily extensive fragmentation at low collision gas pressures, while the fragmentation of $[(\text{UO}_2)_5 \text{O}_2]^+$ is subdued relative to the other $x = 6$ species over a range of collision gas pressures. The enhanced and reduced fragmentation of the species with $y = 4$ and 2

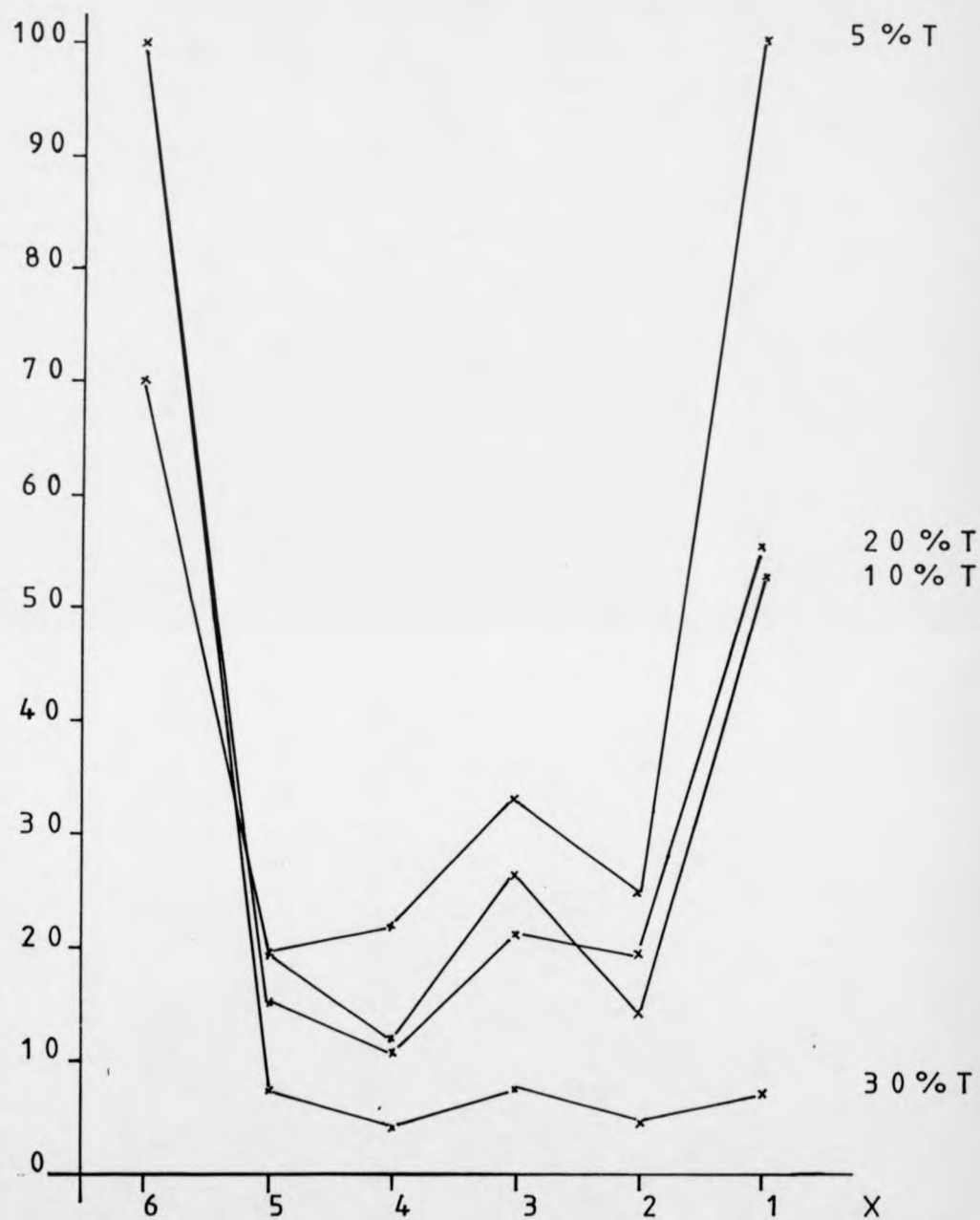


Fig 4.2.2 The Variation in Daughter Cluster Intensities with Decreasing Cluster size, x , for a Range of collision Gas Pressures

respectively may reflect their relative stabilities, being influenced by the high stability of the $y = 3$ species.

The odd/even alternation displayed by the daughter clusters becomes more prominent as the attenuation of the parent cluster beam increases; this can be observed for the CID of $[(UO_2)_x O_3]^+$ with the intensities of daughter clusters being approximately twice that of neighbouring even daughter clusters at 30% transmittance. However at very high collision gas pressures the relative intensities of the even clusters increase gradually relative to their neighbouring odd clusters.

The CID spectra recorded for $[(UO_2)_x]^+$ over a range of collision gas pressures display a similar relationship between the extent of fragmentation and the collision gas pressure to that shown by the more oxygenated $x = 6$ clusters. The intensities of all peaks increase with increasing collision gas pressure, with the $x = 3$ fragment cluster exhibiting enhanced intensities compared with other fragment clusters. However the favoured fragmentation pattern initially showed significant variations from that of other $x = 6$ parent clusters studied. These include the $[(UO_2)_x]^+$ parent cluster undergoing the initial loss of neutral UO_2 or UO units to form $[(UO_2)_{x-1}]^+$ and $[(UO_2)_{x-1} O]^+$ respectively before adopting a fragmentation pattern similar to that displayed by the other uranyl clusters, involving the loss of UO_3 and UO_2 units. At higher collision gas pressures no $x = 5$ daughter clusters were detected, while the $x = 4$ daughter cluster displayed significantly increased relative intensities.

The fragmentation patterns displayed by members of the tetra- and penta-uranyl cluster series are similar to that shown by the parent clusters of higher mass described above. The CID spectra also show the tri-uranyl fragments to exhibit enhanced intensities at higher collision gas pressures, while the relative intensity of the bi-uranyl clusters decreases. In many cases a number of possible $[(\text{UO}_2)_3 \text{O}_\gamma]^+$ clusters are formed, which shows the tetra-uranyl parent/daughter cluster to be able to undergo a number of different fragmentation pathways to form tri-uranyl daughter clusters of significant stability.

4.3 DISCUSSION OF RESULTS

From the above discussion of the CID spectra for the uranyl clusters at various collision gas pressures, a dominant fragmentation pattern for all the parent clusters studied becomes apparent. This involves parent clusters, $[(\text{UO}_2)_x \text{O}_y]^+$, initially undergoing the loss of neutral UO_2 units to form $[(\text{UO}_2)_{x-1} \text{O}_{y-1}]^+$ daughter clusters. This single fragmentation is dominant at low collision gas pressures. On increasing this pressure the number of collisions undergone by each parent cluster increases and hence a larger number occur in which sufficient excitation energy is acquired by the parent cluster to result in reaction; this results in increased daughter cluster formation. The daughter clusters so formed may subsequently undergo the loss of a number of additional UO_2 units until the uranium : oxygen atom ratio, z , of the product daughter clusters $[(\text{UO}_2)_{x-n} \text{O}_{y-n}]^+$, (where n is the number of dissociative collisions undergone by a given cluster ion from its parent cluster stoichiometry), nears $z = 2.0$. Then the daughter clusters, $[(\text{UO}_2)_{x-n} \text{O}_{y-n}]^+$ fragment by the stepwise loss of neutral UO_2 units, the extent to which fragmentation takes place being dependent on the collision gas pressure employed. At very high collision gas pressures collisions occur of sufficient energy for additional modes of fragmentation to become energetically accessible. This is demonstrated by the occurrence of UO_2 loss at increasingly larger daughter cluster sizes, $z < 2.0$. In many cases the loss of neutral UO_2 moieties takes place from the $x - 1$ cluster under these conditions. The extent to which fragmentation

occurs for a fixed collision gas pressure showed larger clusters, higher x value, to undergo fragmentation more readily. This suggests that as the cluster size increases, there is a corresponding decrease in the relative binding energies of the constituent units.

As the collision gas pressure increases odd/even alternation becomes increasingly evident for all clusters studied, with the series of daughter clusters with $x = 3$ displaying significantly enhanced relative intensities. This may reflect a greater stability of the 'odd' cluster, with the $x = 3$ daughter clusters being of notably higher relative stability. Similarly the extent of fragmentation and ease by which it occurs are found to be related to the y value of the parent clusters. This is demonstrated by the relative intensities of the daughter clusters formed from hexa-uranyl parent clusters, with parent clusters containing larger numbers of additional oxygen atoms displaying more extensive fragmentation at moderate collision gas pressures than clusters of low additional oxygen atom contents. Thus the level of oxygenation has a direct influence on the relative fragmentation rates of clusters of a given x -value, which suggests that the additional oxygen atoms may distort the cluster structure, reducing the relative binding energies of its constituent units.

The above results suggest that the structures and stoichiometries adopted by these clusters are controlled by energy relations between adjacent members of a series.

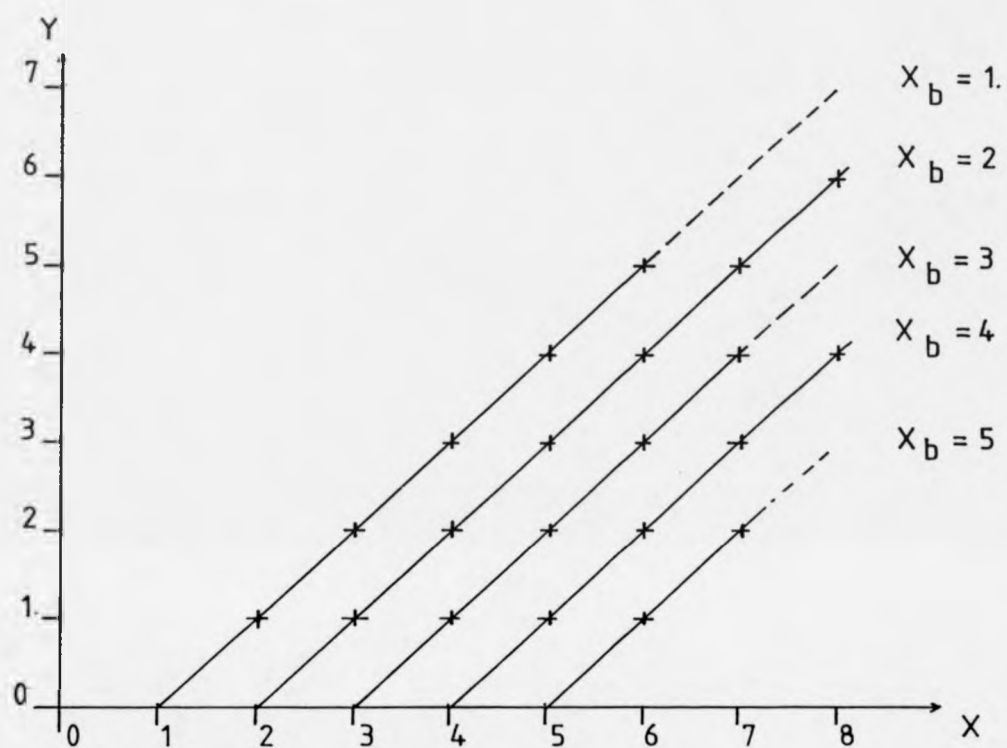


Fig 4.3.1 A Graphical Representation of the Different fragment Cluster Sequences, x_b , and Their Size Relationship to the Number of additional Oxygen Atoms Present, y .

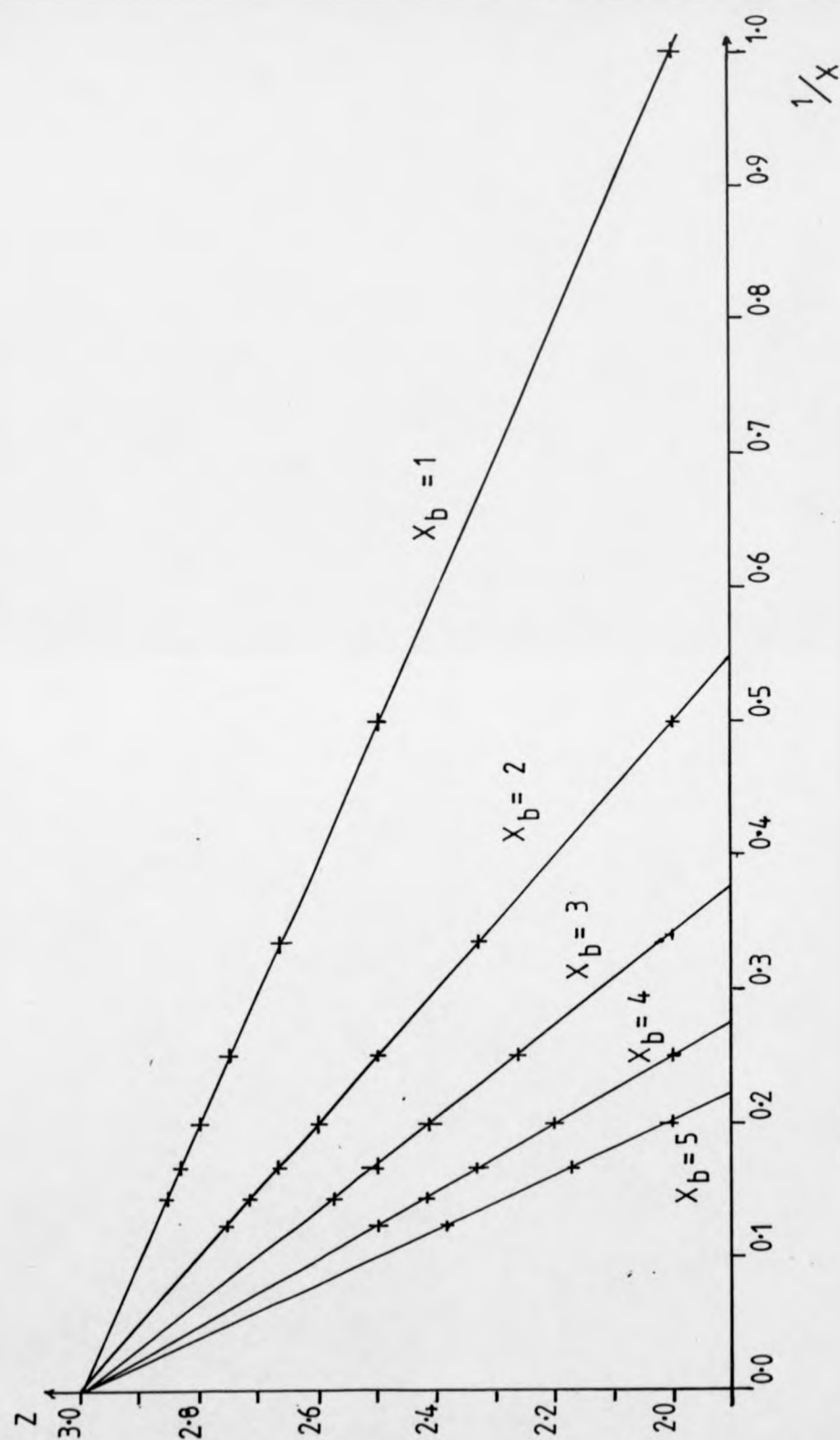


Fig 4.3.2 The Variation in the Uranium : oxygen Atom ratio, z , with $1/x$, for the Fragment Clusters Formed During CID

Graphical analysis of the preferred fragmentation pathways observed gives rise to a number of linear relationships, each denoting a given fragmentation series. These plots can be described by the general equation

$$Y = X - X_b, \quad \text{Eqn. 4.10}$$

where x_b denotes the respective daughter cluster size when no additional oxygen atoms are present, i.e. $z = 2.0$, with $x_b = 1, 2, 3, 4$ and 5 for the parent clusters studied. The variation in the uranium : oxygen atom ratio down these fragmentation pathways also gives rise to a number of linear relationships which can be characterised by the equation,

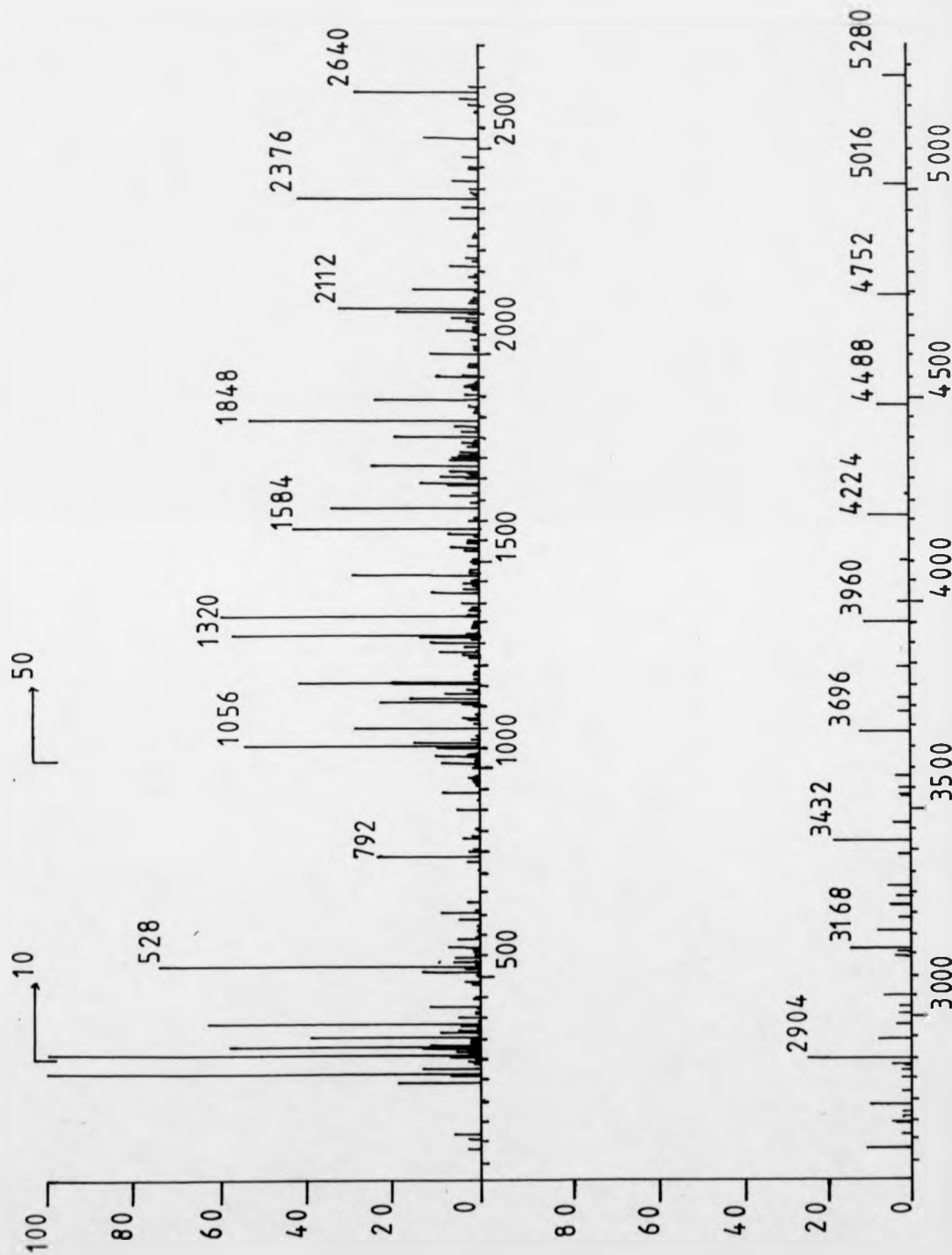
$$Z = -X_b/X - 3.0, \quad \text{Eqn. 4.11}$$

when $z > 2.0$. From this equation, the fragmentation patterns are found to show a uranium : oxygen atom ratio of $z = 3.0$ at very large parent cluster sizes. Such a ratio may indicate that the daughter clusters, resulting from the fragmentation processes, and their respective parent clusters, have structures based on uranyl-type bonding with $z = 3.0$ reflecting the stability of the uranium trioxide phases.

4.4 THORIUM CLUSTERS

The fast atom bombardment mass spectra of various thorium salts show the presence of cluster ions of notable intensity. These clusters have the general formula $[(ThO_2)_x]^+$ and have been recorded for $x \leq 20$, and show distinct odd/even alternation for $x \leq 14$. These clusters also show the presence of matrix adduct formation and incorporation of small numbers of additional oxygen atoms into lower mass clusters. These matrix adducts often dominate the resulting spectra.

Such dioxothorium clusters relate directly to the dominant phase of the thorium-oxygen phase system, ThO_2 , which has a fluorite structure.



Spec 4.4.1 The Cluster Spectrum for Thorium

4.5 CONCLUSIONS

The uranium-oxygen based clusters are found to follow the general formula $[(\text{UO}_2)_x \text{O}_y]^+$ and exhibit a tendency to adopt U_2O_5 , $z = 2.5$, stoichiometries at larger cluster sizes. However the stoichiometries for even clusters are observed to show size-dependent behaviour with the smaller clusters, x_n , showing $z = 2.5$ independent of cluster size, while clusters of size x , display reduced levels of oxygenation. This behaviour is clearly demonstrated by the variation in the uranium : oxygen atom ratio, z , with $1/x$, which shows intermediate sized 'even' clusters, $10 \leq x \leq 26$, to mark the change between these two uranium-oxygen regimes. This tendency of clusters to adopt stoichiometries corresponding to $z = 2.5$ may mark the boundary between the fluorite and uranyl-bonded oxide phases which occur in the solid state at $z = 2.4$. In the solid state this boundary is also marked by a sudden decrease in density as uranyl bonding becomes dominant. The above data obtained from the mass spectral analysis suggests that the uranium-oxygen clusters predominantly contain uranyl-type bonding, with the discontinuity in the uranium : oxygen atom ratio for intermediate-sized 'even' clusters denoting the onset of a phase change between the various U_2O_5 phases.

The CID spectra show marked odd/even alternation, inferring that 'odd' cluster ions have enhanced stabilities relative to neighbouring 'even' clusters. This may be due to odd clusters having more stable structural arrangements. The CID spectra also show fragmentation to

occur via regular sequences of loss of neutral units so as to cause a reduction in the uranium : oxygen atom ratio for each successive fragmentation step. A graphical plot of the resulting fragmentation pathways, z against $1/x$, gives rise to a series of linear plots that intercept at $z = 3.0$ for larger cluster sizes while displaying an abrupt termination at $z = 2.0$ irrespective of the initial parent cluster. The range in values of z observed for these fragmentation pathways may relate to uranyl-bonded units, and solid state uranium-oxygen phases reported, since $z = 3.0$ correlates directly with the uranyl bonded uranium trioxide phases, while $z = 2.0$ may represent the UO_2 moiety which is known to have significant stability in its various forms. Hence the relationships found for these clusters in both their mass spectral and CID studies strongly suggest that the uranium-oxygen clusters are constructed from uranyl-based cluster units with the resulting clusters showing a notable correlation to the solid state uranium-oxygen system, especially the stable U_2O_6 phases.

5.1 THE FAB SPECTRA OF THE LANTHANIDE ACETATES

The FAB spectra for uranyl acetate dihydrate has been shown to feature two distinct families of clusters; the first of these being the previously described uranium-oxygen clusters while the second family of clusters were consistent with the association of one or more neutral UO_2 units around a central monopositively charged uranyl acetate moiety. These central uranyl acetate species were found to be structurally significant (176).

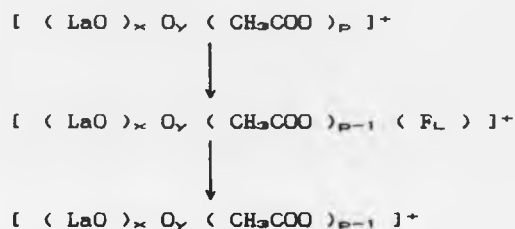
The lanthanide acetate complexes have similar structures to that of uranyl acetate, with the central oxo-lanthanide ion being directly coordinated to two acetate ligands, which act as a bidentate species, and four monodentate ligand bridges.

The FAB mass spectra for various lanthanide acetates were recorded in order to investigate the possible formation of structurally significant spectral species. These spectra were recorded using a variety of matrices

5.1.1 LANTHANUM ACETATE

The mass spectra for lanthanum acetate, $\text{LaO}(\text{CH}_3\text{COO})_3 \cdot 6\text{H}_2\text{O}$, shows, in addition to the previously described lanthanum-oxygen clusters, the presence of a number of related lanthanum acetate clusters. These clusters were found to have the general formula

$[(LaO)_x O_y (CH_3COO)_p]^+$, with clusters corresponding to $x \leq 18$ being recorded. The uranyl acetate species exhibited maximum values of $p \leq 2$, when no acetate fragments were present. When $p \leq 1$, acetate fragments were observed; these are consistent with a fragmentation pathway involving the sequential fragmentation of a single acetate ligand before its complete dissociation.



The relative intensities for clusters containing coordinated ligand fragments suggests that ligand fragmentation takes place by the pathway:



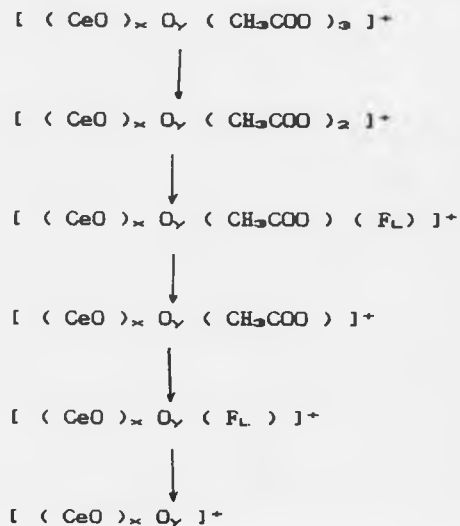
In higher order clusters, $x < 1$, the most intense ligated species contains a single unfragmented ligand, $p = 1$

The above spectral species suggest that the two bidentately coordinated acetate ligands are located at the central lanthanum-oxygen ion, which has a structure that is consistent with the crystal structure reported for lanthanum acetate.

5.1.2 CERIUM ACETATE

The crystal structure for cerium triacetate features ligand coordination similar in character to that described for lanthanum acetate, with two bidentate and four monodentate acetate ligands being involved (7).

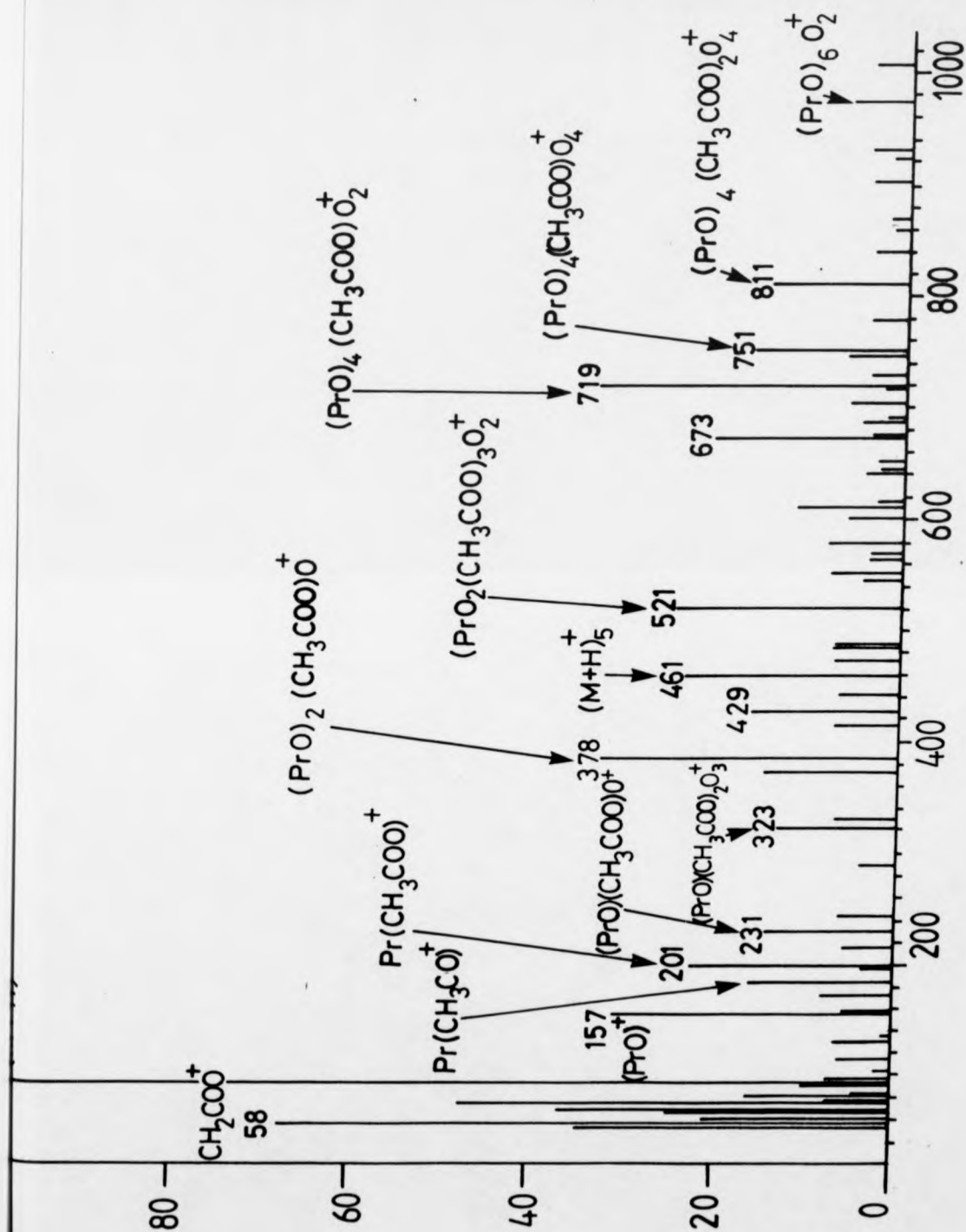
In the FAB spectra, the species observed adhere to the general formula $[(\text{CeO})_x \text{O}_y (\text{CH}_3\text{COO})_p]^+$, with the monoacetate clusters, $p = 1$, being the most intense ligated clusters over the range of cluster sizes studied. However unlike the lanthanum clusters, cerium clusters were found corresponding to the coordination of up to three acetate ligands, $p \leq 3$, although associated ligand fragments consistent with only $p \leq 2$ were observed. This suggests that the third acetate ligand may undergo complete dissociation without undergoing fragmentation. Hence the tris-acetate cluster may follow the fragmentation pathway



with the individual acetate ligands fragmenting in a similar manner to that observed in lanthanum acetate.

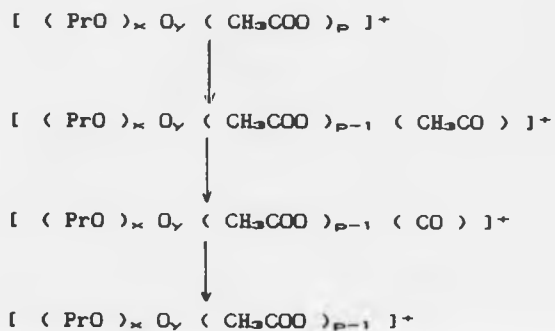
5.1.3 PRAESEDYMIUM ACETATE

The mass spectra for praeesodymium acetate displays the presence of several series of peaks above that for elemental praeesodymium. These were found to correspond to species of general formula $[(\text{PrO})_x \text{O}_y (\text{CH}_3\text{COO})_p]^+$, where the relationship between the cluster size, x , and the number of additional oxygen atoms present, y , is as previously described, although a small number of lower intensity species with increased y values were also observed. The former of these clusters shows the presence of up to two ligands, $p \leq 2$, with $p \leq 1$ being present for clusters containing ligand fragments. The fragmentation pattern by which these are formed involves the initial



Spec 5.1.1.2 FAB Spectrum of Praseodymium Acetate in Glycerol/water

loss of oxygen to form $[CH_3COO]$, which in turn give rise to the most intense clusters containing ligand fragments. These then undergo the subsequent loss of a methyl group before complete ligand dissociation.



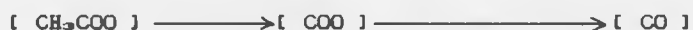
5.1.4 TERBIUM ACETATE

The FAB spectra for terbium acetate show a number of ligated terbium oxide clusters that follow the general formula $[(TbO)_x O_y (CH_3COO)_p]^+$. The ligated clusters observed show the presence of up to two unfragmented acetate ligands, $p \leq 2$, or the coordination of ligand fragments, F_L , when $p < 2$. These fragments correspond to a ligand fragmentation pathway similar to that exhibited by lanthanum acetate clusters for small values of x ; however at larger x values, an additional fragmentation pathway becomes increasingly significant. This additional pathway involves the loss of a methyl group from the acetate to yield a coordinated CO_2 group.

For small clusters



For larger clusters the pattern is:



For all values of x however clusters corresponding to $p = 1$, and containing no fragmented ligands were found to be the most intense.

5.1.5 HOLMIUM ACETATE

The spectrum for holmium acetate shows the presence of numerous ligated holmium oxide clusters of the general formula $[(\text{HoO})_x \text{O}_y (\text{CH}_3\text{COO})_p (\text{FL})]^+$, with with ligated clusters corresponding to $x \leq 5$ being detected. These clusters show the dominant ligated clusters to correspond to $y = 1$, $p = 1$ for the range of cluster sizes studied.

At smaller cluster sizes, $1 \leq x \leq 3$, clusters were observed to contain up to two acetate ligands or associated ligand fragments, with their relative intensities being found to decrease with increasing cluster size. However for $x = 4$ and 5 only mono-ligated clusters were observed. The coordinated acetate ligands were found to fragment in a similar manner to that shown by the lanthanum acetate clusters.

5.2 DISCUSSION OF RESULTS

In the spectra described above, the spectral species observed for several different lanthanide metals show the general formula $[(\text{LnO})_x \text{O}_y (\text{CH}_3\text{COO})_p (\text{FL})]^+$, over a range of cluster sizes, x .

For these clusters, the maximum ligand coordination was observed at $p = 2$, except for cerium with $p = 3$, in keeping with the lanthanide acetate crystal structures which show two acetate ligands to undergo bidentate coordination to the central oxometal cation. In the case of cerium, however, the availability of the Ce^{4+} state may lead to more extensive ligand coordination, although this additional ligand is dissociated without fragmentation to yield the more stable bis(acetate) species.

For the lanthanide acetate clusters, $p \leq 2$, ligands were found to undergo fragmentation before complete dissociation, with the coordinated ligand fragments suggesting that two possible size-dependent fragmentation pathways may exist. The commonest of these, observed for all metals either at smaller (or , in some cases, at all values of x detected, involves the initial decarboxylation of the fragmenting acetate ligand, followed by the loss of a methyl group before complete dissociation.



However, at higher x values, for certain lanthanide acetates, ligands were observed to undergo fragmentation by an additional pathway involving the initial loss of a methyl group.



This behaviour is most apparent for terbium acetate clusters.

The dependence on cluster size observed for these two possible ligand fragmentation patterns may reflect changes in ligand binding energies, with increasing cluster size making the additional fragmentation pathways more energetically favourable. Similarly the presence of up to one ligand fragment, F_L , at all cluster sizes studied, further suggests the importance of energetic/structural considerations in ligand fragmentation.

The above trends suggest that lanthanide acetate clusters, over the range of cluster sizes studied, have shell type structures in which the central, singly-charged, ligated oxo-lanthanide ion is surrounded by a shell containing $x - 1$ neutral oxo-lanthanide moieties

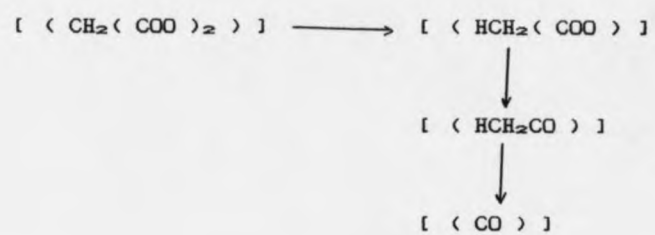
5.3 LANTHANIDE MALONATES

The FAB mass spectral analysis of a number of lanthanide malonate complexes of the form $[(LnO)_x (Mal)_y \cdot 8H_2O]^+$ were recorded, with a variety of matrices and co-solvents. The resulting spectra displayed the presence of several series of peaks corresponding to the general formula $[(LnO)_x O_y (Mal)_p (M)]^+$, where M represents the presence of a matrix adduct.

For these species, the mono-ligated clusters, $p = 1$, are always found to be the most abundant for the range of lanthanide metals studied, although larger praseodymium clusters containing up to three intact malonate ligands have been detected, reflecting the tris-ligated aqueous complex. Lanthanum malonate complexes gave rise to a limited

range of ligated clusters with the presence of only a single malonate ligand or its associated fragments being observed, over the range of cluster sizes investigated. However the presence of this ligand was observed to stabilize the $y = 4$ clusters for $x \leq 2$, as reflected in its increased relative intensity. Similar behaviour was also observed for the spectral species formed by the europium and holmium malonates. Cerium was observed to display mono- and bis-ligated clusters, although the second ligand was dissociated without fragmentation. The praseodymium malonate complex was however found to contain up to $p = 3$ intact malonate ligands at higher cluster sizes, $x \geq 4$, with the mono-ligated clusters being the most intense. However the presence of coordinated ligand fragments was observed only for $p \leq 1$, thereby suggesting that the third ligand is dissociated as a neutral intact malonate species.

Ligand fragmentation was found to occur in a similar manner for the various lanthanide metals studied, with the associated ligand fragmentation pattern suggesting that the malonate ligands are coordinated strongly via one of their carboxylic acid groups. In addition, the presence of only one ligand fragment on each cluster also infers that fragmentation occurs in a stepwise manner. The ligand fragments observed correspond to the fragmentation pattern.



5.4 AMINO ACID COMPLEXES OF THE URANYL ION

The biological significance of transition metals is largely based on their ability to assume a number of different oxidation states and hence participate in a variety of redox reactions. In the case of heavy metals and the late transition metals, however, this ability to interact with biomolecules and thus influence a range of biological processes, can pose an environmental problem, and accordingly this type of interaction has undergone many studies (177).

The importance of the reactions of uranyl ion with amino acids has meant that this system has been subjected to many investigations, with particular interest being directed towards the mode and extent of coordination (178)(179). For simple amino acids, coordination has been shown to occur via the carboxylate group, as opposed to the amino group, with the coordination being either mono- or bidentate in character. Such complexes containing 1, 2, 3 and 4 amino acids have been reported, with the uranyl ion exhibiting hexagonal bipyramidal coordination. This is also supported by crystal structure analysis, which reveals that six oxygen atoms coordinate in the equatorial plane. The mass spectra of simple amino acid and hydroxamate complexes of uranyl ion have also been described (54)(55) the former paper being based in the present author's M.Sc. thesis.

5.4.1 URANYL-(GLYCINE) COMPLEX

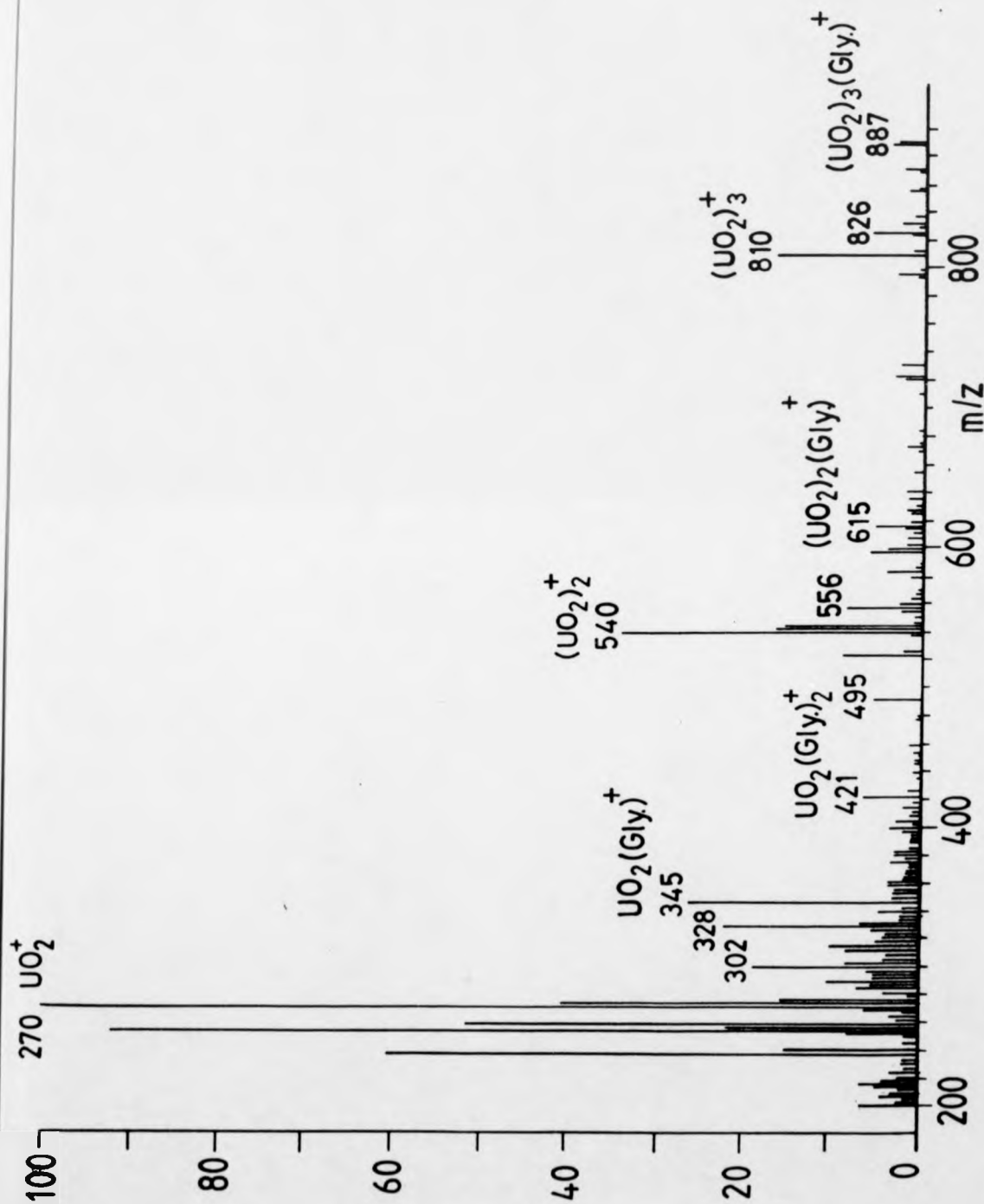
Alcock et al. have reported the crystal structure for the complex formed between the uranyl ion and glycine, in which glycine was found to coordinate in two distinct ways, with the carboxylate groups of two glycine ligands acting as a bidentate, while the remaining glycine ligands coordinate monodentately (180).

The FAB spectra for the uranyl-glycine complex exhibit several series of peaks, each following the general formula $[(\text{UO}_2)_x \text{O}_y (\text{Gly})_p]^+$, with $p \leq 4$ coordinated amino acid ligands being observed. Hence there are two major processes occurring, the first of these involves the dissociation and fragmentation of ligands, while the second involves the formation of ligated cluster ions, $x < 1$.

These uranyl glycine complexes were found initially to eliminate intact neutral glycine ligands before undergoing the sequential loss of neutral ligand fragments followed by the complete dissociation of the resulting carboxylic acid residue. This ligand fragmentation involved glycine losing a amino-methane moiety, resulting in a coordinated CO_2 group,



This is clearly demonstrated by the ligated mono-uranyl species which follow the general formula $[(\text{UO}_2)_x (\text{Gly})_p (\text{FL})]^+$, where $x = 1$. These correspond to species containing up to four glycine ligands, which



Spec 5.4.1 Spectrum of Uranyl-Tetraglycine Complex.

directly eliminate up to two neutral glycine ligands without any fragmentation being detected. However, species with $p \leq 2$ are observed to undergo ligand fragmentation before dissociation via the fragmentation pathway given above.

The $[(UO_2)_2 (Gly)]^+$ cluster, however, was found to undergo ligand fragmentation involving the initial loss of the amino group followed by the subsequent loss of the methyl group to yield a coordinated CO_2 group. For larger clusters, $x \geq 2$, the mono-glycine clusters, $p = 1$, are found to be the most abundant, with slight evidence for the tris-glycine cluster being observed for $x = 2$. This glycine ligand is found to fragment by the loss of a neutral aminomethane moiety to yield bare uranium-oxygen clusters.

The FAB spectra recorded using a twin sector probe tip (see section 2.2.3) were recorded, with one sector being loaded with uranyl nitrate solution and the other with glycine solution. The resulting spectra showed the presence of species similar to those described above, but at lower intensity. However more extensive fragmentation was found to have occurred, resulting in clusters containing $p \geq 2$ ligand fragments.

5.4.2 URANYL-(α -, β -ALANINE) COMPLEXES

For α -alanine, similar spectral trends to those for glycine are observed, with the tris(α -alanine) species showing increased intensities relative to the bis- and tetrakis- species, while the

mono(α -alanine) coordinated species remained the most abundant ligated uranyl cluster. However, unlike the uranyl-glycine species observed, α -alanine was found to undergo the formation of a pentakis(α -alanine) uranyl complex. In this, α -alanine would be expected to act using 4 monodentate ligands and a single bidentate ligand, resulting in the central uranyl ion attaining a maximum coordination number of six in its equatorial plane. Clusters of higher x-value were also observed; these showed the presence of several prominent species of the form $[(\text{UO}_2)_x (\alpha\text{-alanine})]^+$.

Coordinated α -alanine was observed to fragment via loss of a methyl group to yield an amino acid residue before undergoing further fragmentation resulting in a coordinated CO_2 group before dissociation.

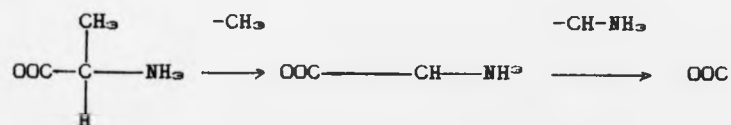
The mass spectra for the uranyl-(β -alanine) complex showed many similarities to those exhibited by the α -alanine complex. The mono-ligated species were observed to be the most abundant, while the tris(β -alanine) species were found to show enhanced relative intensities compared to neighbouring bis- and tetrakis- species. The penta-(β -alanine) complex was again observed, but at a reduced intensity relative to that for the corresponding penta-(α -alanine) species.

P- FAB spectra obtained using a twin sector probe tip for the β -alanine complex also showed the mono- and tris- ligated species to be of considerable intensity, however no pentakis species was observed.

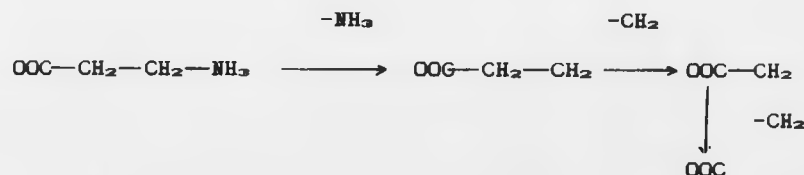
The spectral intensities were approximately 1/12 of those obtained using a standard FAB probe tip for otherwise identical reaction conditions.

From the coordinated fragments observed in both the above mass spectral investigations on β -alanine, the same pattern of events is evident, that is in which β -alanine initially undergoes fragmentation by the loss of its amino group before the successive loss of two methyl groups resulting in coordinated CO_2 group which subsequently dissociates.

α -Alanine



β -Alanine



The fragmentation patterns observed for α - and β -alanine ligands shows the carboxylic acid residue to be powerfully bonded to the uranyl centre.

5.5 URANYL-(α -, β -, γ -AMINOBUTANOIC ACID) COMPLEXES

The mass spectra for the series of uranyl-(α , β , γ -aminobutanoic acid) complexes were recorded to investigate the effect of the position of the amino group on its coordinating ability and the resulting fragmentation pattern.

The uranyl-(α , β , γ -aminobutanoic acid) complexes were all bright yellow in colour and showed increasing levels of crystallinity as the distance between the functional groups increased. That is,

| | |
|------------------------------|---------------------|
| α -aminobutanoic acid | mid. viscosity oil. |
| β -aminobutanoic acid | high viscosity oil. |
| γ -aminobutanoic acid | crystalline solid. |

This shows the position of the amino group to significantly influence the level of crystallinity of the complex formed. Bombieri et al. reported the uranyl-(γ -aminobutanoic acid) complex to be tris(γ -aminobutanato) dioxouranium (VI) dinitrate and to have a crystal structure in which three bidentate γ -aminobutanoic acid ligands coordinate in the equatorial plane of the uranyl ion, rendering the latter hexacoordinate in character (181).

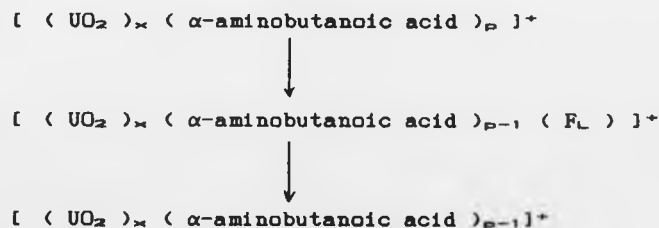
The resulting mass spectra for the α - and β -aminobutanoic acid complexes were dominated by the UO_2^+ peak, $m/z = 270$, and showed the presence of several uranyl-based cluster series, while the spectrum for the γ -aminobutanoic acid complex was dominated by the $m/z = 387$ peak.

5.5.1 URANYL-(α -AMINO BUTANOIC ACID) COMPLEXES

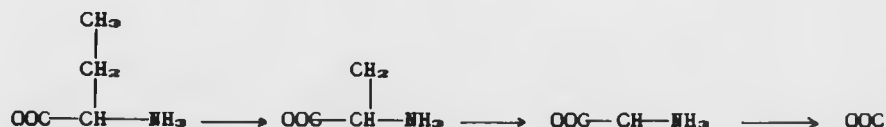
The mass spectra for the complex formed between α -aminobutanoic acid and the uranyl ion showed the presence of monopositive species which can be described by the general formula

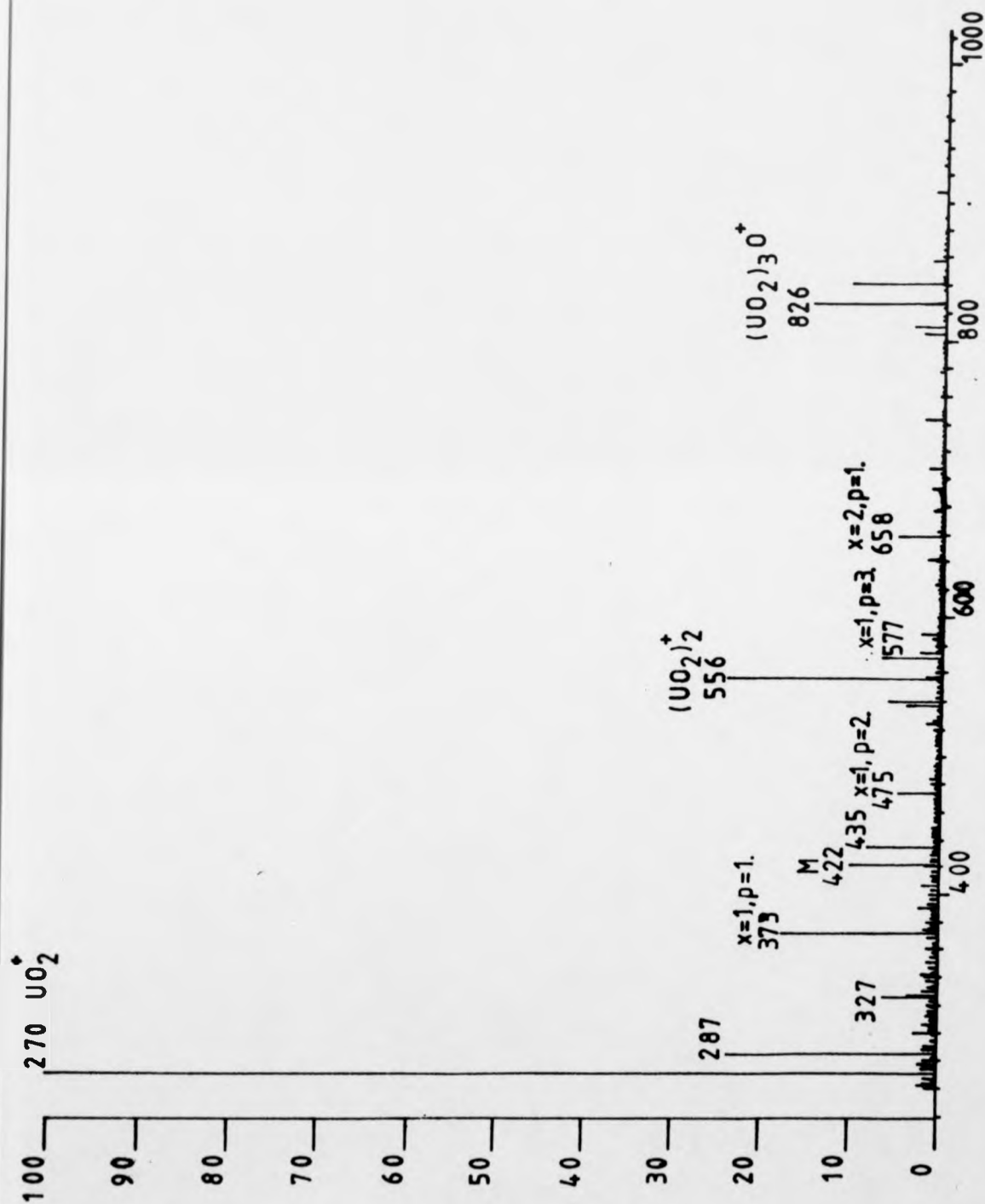
$[(\text{UO}_2)_x (\alpha\text{-aminobutanoic acid})_p (\text{F}_L)]^+$, with clusters corresponding to $x \leq 4$ being recorded. These species displayed a maximum ligand content of $p = 3$, when $p < 3$ coordinated ligand fragments, F_L , were also observed. The spectral intensities showed clusters with $p = 1$ to be the most abundant species, while the $p = 3$ species also exhibited high relative intensities.

The spectral data shows each ligand to undergo fragmentation by the sequential loss of neutral fragments before dissociation.



In which the coordinated ligand fragments, F_L , are consistent with α -aminobutanoic acid undergoing fragmentation by the pathway,





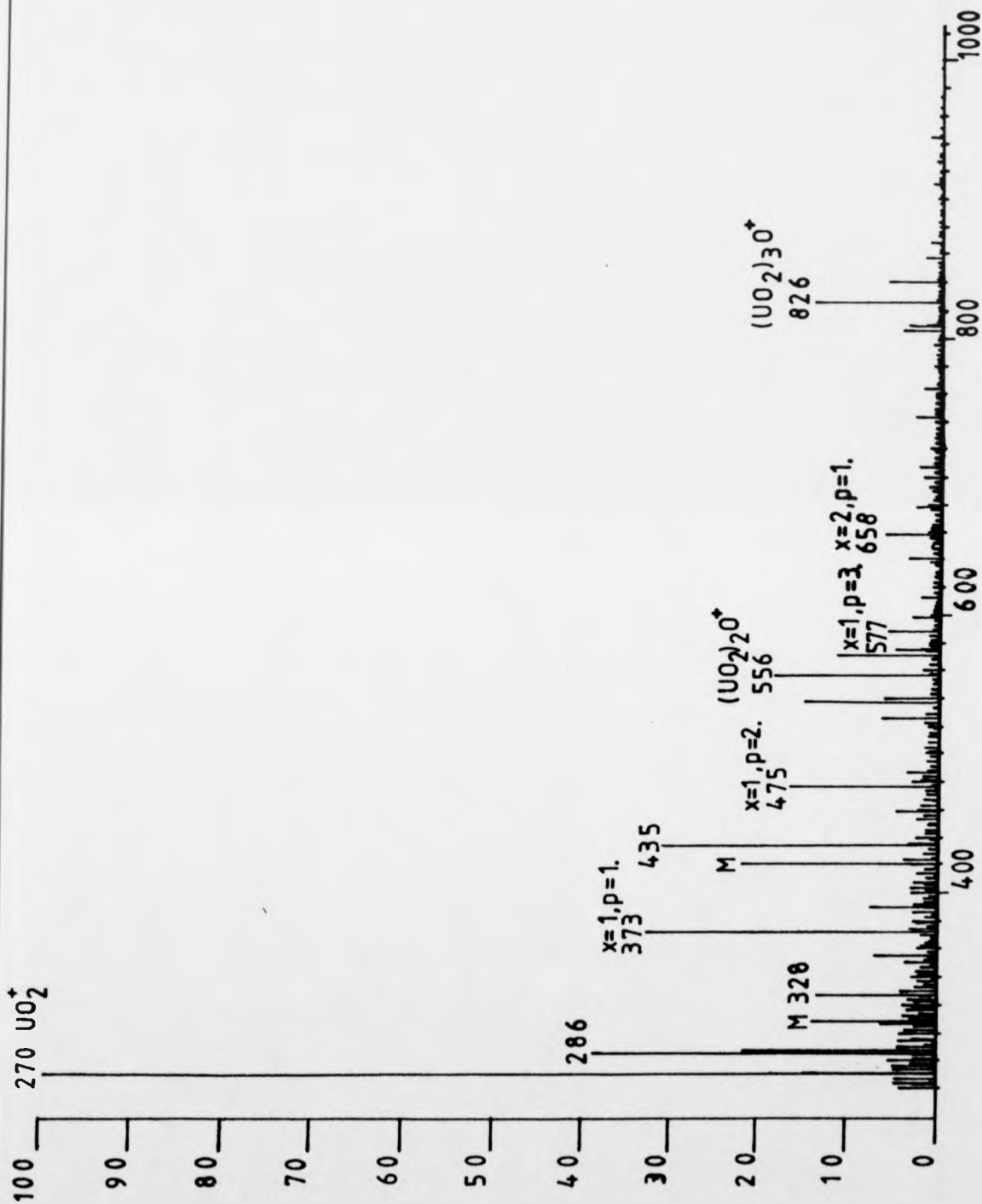
Spec 5.5.1 Mass Spectrum of Uranyl-(α -Aminobutanoic Acid) Complex

with clusters containing associated ligand fragments being detected over the size range $1 \leq x \leq 3$. The most intense clusters containing ligand fragments were found to contain the amino acid residue, $[OOC-CH-NH_3]$ with the $[OOC]$ fragment being more significant for clusters with smaller x values. The presence of an additional ligand fragment involving the loss of the amino group from the amino acid residue was observed at reduced relative intensity for the monouranyl cluster, $x = 1$.

5.5.2 URANYL-(β -AMINO BUTANOIC ACID) COMPLEXES

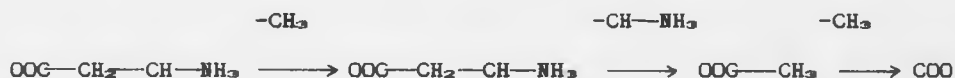
The mass spectrum showed the presence of several series of monopositive cluster series of general formulae $[(UO_2)_x (\beta\text{-aminobutanoic acid})_p (F_L)]^+$, with $x \leq 4$ being observed. The monouranyl species, $x = 1$, shows the presence of species containing up to $p \leq 4$ coordinated ligands, with the tetrakis- species being of low intensity compared with the other ligated species. The spectral intensities for ligated species corresponding to $x = 1$ show an exponential decrease in intensity with increasing p value for $p \leq 3$.

The higher order clusters, $2 \leq x \leq 4$, showed the bis- and mono- β -aminobutanoic acid coordinated species to be formed, with the mono- β -aminobutanoic acid clusters to be of higher intensity. The relative intensities of those clusters containing coordinated ligand fragments, $x \leq 4$, showed ligand fragmentation to occur predominantly by one of two



Spec 5.5.2 Mass Spectrum of Uranyl-(β Aminobutanoic Acid) Complex

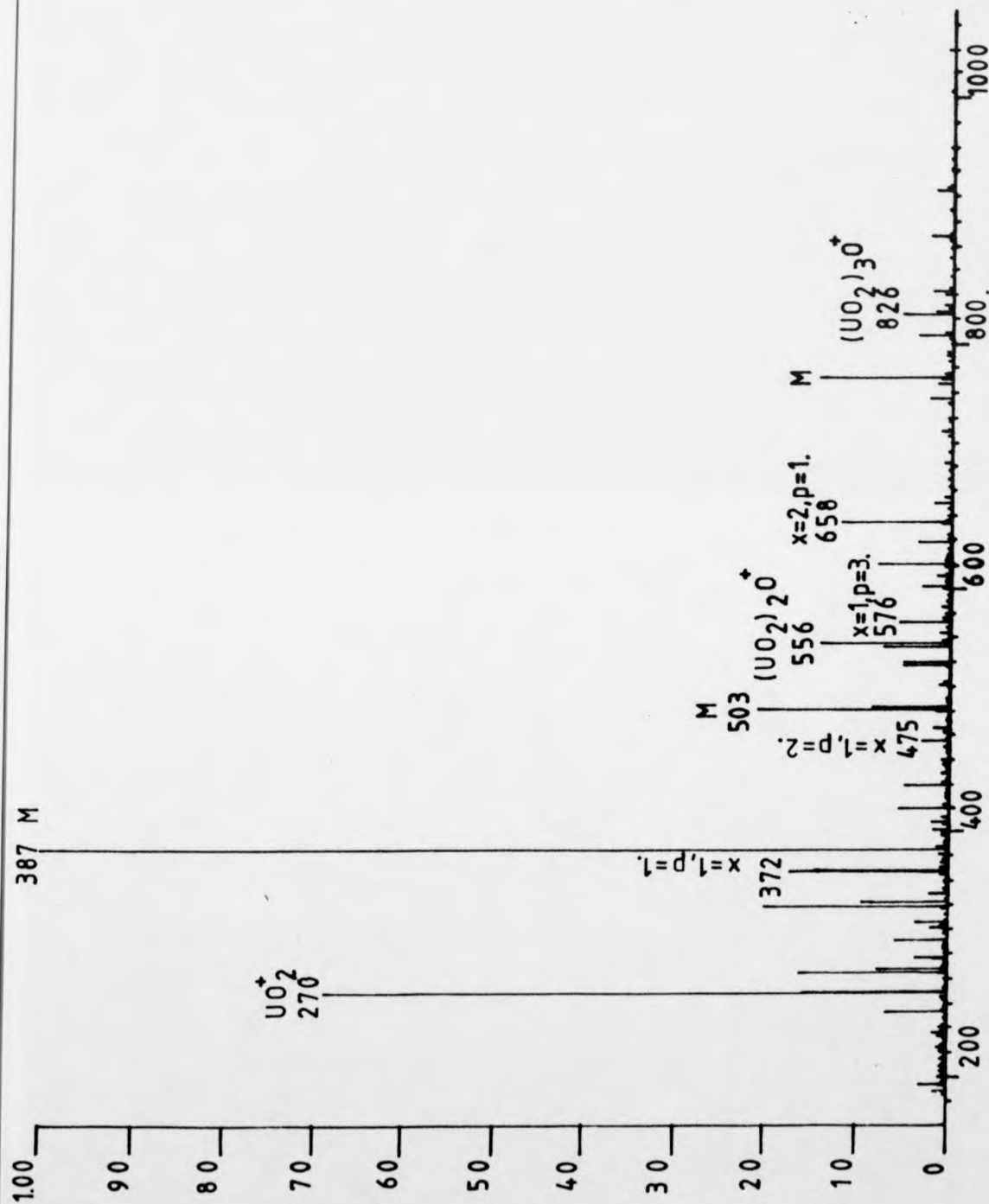
possible pathways depending on the influence of the position of the amino groups on ligand binding. The dominant fragmentation pathway involves the sequential fragmentation of a given ligand before its complete dissociation, with ligands being found to fragment via the following sequence



in which the amino group loses methylamine moiety for low p value clusters, with the most intense coordinated ligand fragment observed being the [OOC-CH₃] fragment. However as p increases, the presence of additional fragments of comparable intensity are found, suggesting that fragmentation by both possible pathways are of near equal probability.

5.5.3 URANYL-(γ-AMINO BUTANOIC ACID) COMPLEXES

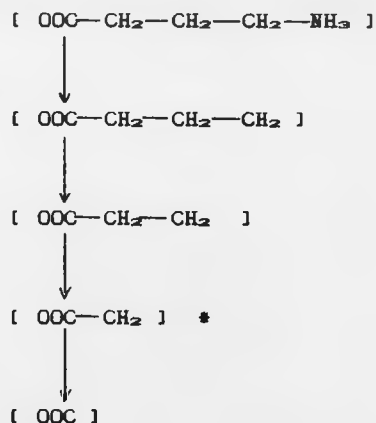
The uranyl-based species observed in the mass spectrum of the tris(γ-aminobutanato) dioxouranium(VI) complex are expressed by the general formula [(UO₂)_x (γ-aminobutanoic acid)_p (F_L)]⁺, with clusters consistent with x ≤ 4 being observed. The most abundant of these ligated clusters is the mono-γ-aminobutanato species, while clusters containing three γ-aminobutanoic acid ligands were observed to be of next highest intensity. In addition, although at much lower intensity, the tetrakis-(γ-aminobutanoic acid) was also recorded.



234 a

Spec 5.5.3 Mass Spectrum of Uranyl-(γ Aminobutanoic Acid) Complex

The clusters observed showed the presence of no coordinated ligand fragments for $p \geq 3$, which suggests only weak binding for the fourth adducted fourth γ -aminobutanoic acid ligand. For clusters containing $p < 3$ ligands, however, coordinated ligand fragments were observed which suggests that the ligands undergo sequential fragmentation via a pathway involving the initial loss of the amino group followed by the stepwise loss of methyl units to yield a coordinated CO_2 group. The lower mass fragments were found to be of high relative intensity, with the ethanoic fragment, *, being the most intense.



5.5.4 TRENDS OBSERVED IN THE URANYL-(α, β, γ -AMINO BUTANOIC ACID) CLUSTERS FORMED.

The mass spectral data for the uranyl-(α, β, γ -aminobutanoic acid) complexes studied exhibit a number of discernible trends involving ligand coordination and fragmentation.

1) The mass spectra show the mono-(α, β, γ)-aminobutanoic acid clusters to be the most abundant ligated cluster in each x series, with the tris-n-aminobutanoic acid species also being formed preferentially. The enhanced relative intensities for the latter of these being consistent with the central uranyl ion exhibiting hexa-coordination in its equatorial plane, with the (α, β, γ)-aminobutanoic acid acting in a bidentate manner.

ii) The relative intensities of the species observed are found to increase with increasing separation of the NH_2 and CO_2H groups in the ligand.

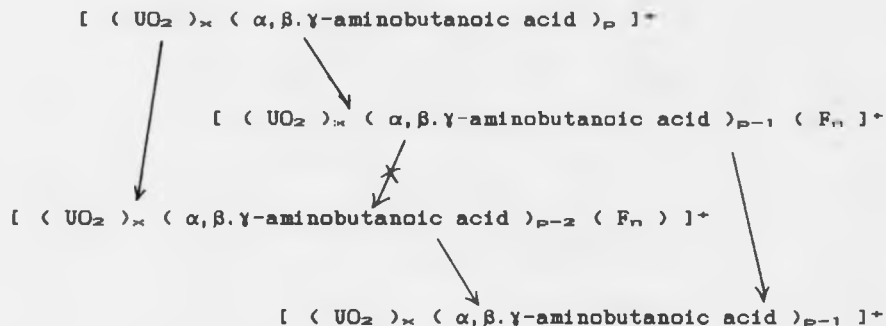
(α -aminobutanoic acid) < (β -aminobutanoic acid) < (γ -aminobutanoic acid)

This parallels the changes observed in the crystallinity of the complexes formed, suggesting that a six-membered ring confers both special stability and ease of packing in the lattice.

iii) For higher order clusters, $x > 1$, up to three coordinated n-aminobutanoic acid ligands or associated ligand fragments were observed. This supports a model of the cluster structure whereby a singly charged, ligated, core is surrounded by a number of neutral UO_2 groups.

iv) Similar ligand dissociation and fragmentation pathways are observed, involving the sequential fragmentation of an individual ligand

rather than the consecutive stepwise fragmentation of all the ligands present.



v) The fragmentation patterns observed show the amino group to predominantly lose a methylamine moiety, although this behaviour is less distinct for (γ -aminobutanoic acid).

5.6 URANYL-(SERINE) AND (THREONINE) COMPLEXES

Serine and threonine are closely related, water-soluble amino acids, both containing hydroxyl groups in their γ -positions.

The FAB spectra for the uranyl-serine complex feature a number of peaks of high relative intensity which correspond to the mono-, bis- and tris-ligated species as well as a low intensity peak due to the formation of the pentakis-serine complex. No evidence for the tetrakis complex or its fragments were observed. The pattern of fragmentation ions observed suggests that the pentakis ligated species experienced the sequential loss of two neutral intact serine ligands, resulting in the

formation of the more stable tris-ligated species. This subsequently undergoes ligand fragmentation, involving the sequential loss of hydroxide and methyl groups or a single methanol molecule, resulting in a coordinated amino acid residue which dissociates following the loss of an amino or methylamine species.

The FAB spectrum for the uranyl-threonine complex shows the presence of species containing up to three threonine ligands, with the mono-threonine ligated clusters being of highest intensity. The ligand fragmentation pattern observed is consistent with threonine undergoing the sequential loss of methyl and methanol groups, resulting in coordinated amino acid residues, which fragment to yield CO_2 groups at lower values of x , before complete dissociation.

5.7 SUMMARY OF THE FAB SPECTRA FOR URANYL-(AMINO ACID) COMPLEXES.

The FAB mass spectra for the uranyl-amino acid complexes studied feature a number of similarities and display marked trends in their ligand dissociation and fragmentation patterns.

The observed species are observed to follow the general formula $[(\text{UO}_2)_x (\text{amino acid})_p (\text{F}_L)]^+$, over a cluster size range $x \leq 4$. The ligated clusters contain up to five coordinated amino acid ligands, $p \leq 5$, with their relative intensities being observed to vary with the number of ligands present. The mono-ligated clusters, $p = 1$, exhibited the highest intensities with the bis-clusters being at a slightly lower relative intensity than that of the tris-ligated species. The tetrakis-species are observed to display notably weaker intensities, that is, approximately equal to those of the pentakis- amino acid species.

The higher relative intensities displayed by the tris-amino acid species are consistent with the expected increased stability of the hexa-coordinate uranyl ion. This in turn shows the ligands to function as a bidentate species.

Higher mass cluster species, $x > 1$, containing up to three amino acid ligands, $p \leq 3$, or associated fragments, were detected, with the mono-ligated clusters being of notably higher relative intensity. The presence of $p \leq 3$ amino acids in higher order clusters suggests that the

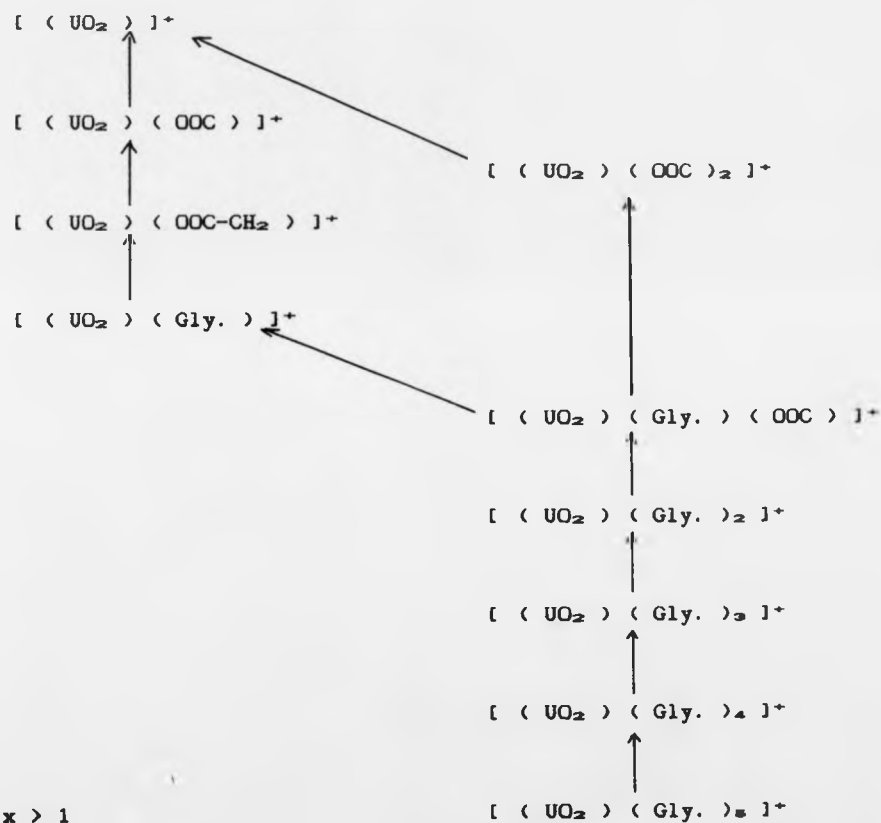
cluster structures consist of a single central coordinated uranyl ion, with a number of additional dioxouranium moieties forming a shell-like structure around this central ion.

The degree of ligation is also found to be dependent on the character of the amino acid present. Our results indicate that the simpler amino acids show a decrease in relative intensity as the aliphatic side chain increases in length; this behaviour is demonstrated by comparison of the relative intensities for glycine, α -alanine and α -aminobutanoic acid. However species with more complex side chains, capable of forming more stable carbonium ions, are found to show higher intensities, which may be a consequence of their larger inductive effect. Other influences affecting the relative intensities of the ligated species formed are observed to be related to the position of the amino group in the amino acid. The data for the α, β, γ -aminobutanoic acid complexes shows the relative intensities of a given species to increase as the separation between the carboxylic acid and amino groups increases. This behaviour is most obvious for the tris-ligated species; this pattern of behaviour is reflected in the increased crystallinity of the γ -aminobutanoic acid complex, possibly pointing to a common origin. Similarly, the intensities of the more ligated clusters containing β -alanine are increased relative to those incorporating α -alanine although the effect is less marked. This influence is a consequence of the reduced acid strengths, with the pKa values for the ligands involved increasing as the separation between the carboxylic acid and the amino group increases. Similarly, the results obtained for serine and cysteine indicate that serine complexes are of

notably higher intensity at lower coordination. However, similar spectral species are observed for both ligands, with the tris-aminoacid species being of increased relative intensity and the presence of a pentakis-ligated species being observed. For threonine, which contains one more methyl group than serine, and which is slightly more acidic in character, similar trends are also seen, although only species containing up to three ligands or associated fragments, $p \leq 3$, are observed.

Fig. 5.7.1 The fragmentation pattern observed for the uranyl-glycine species observed in the mass spectra of tetrakis-(glycine) uranyl nitrate.

For $x = 1$



For $x > 1$

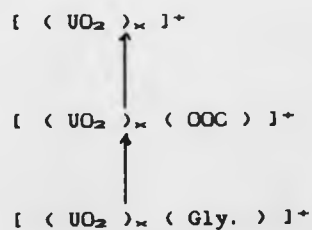


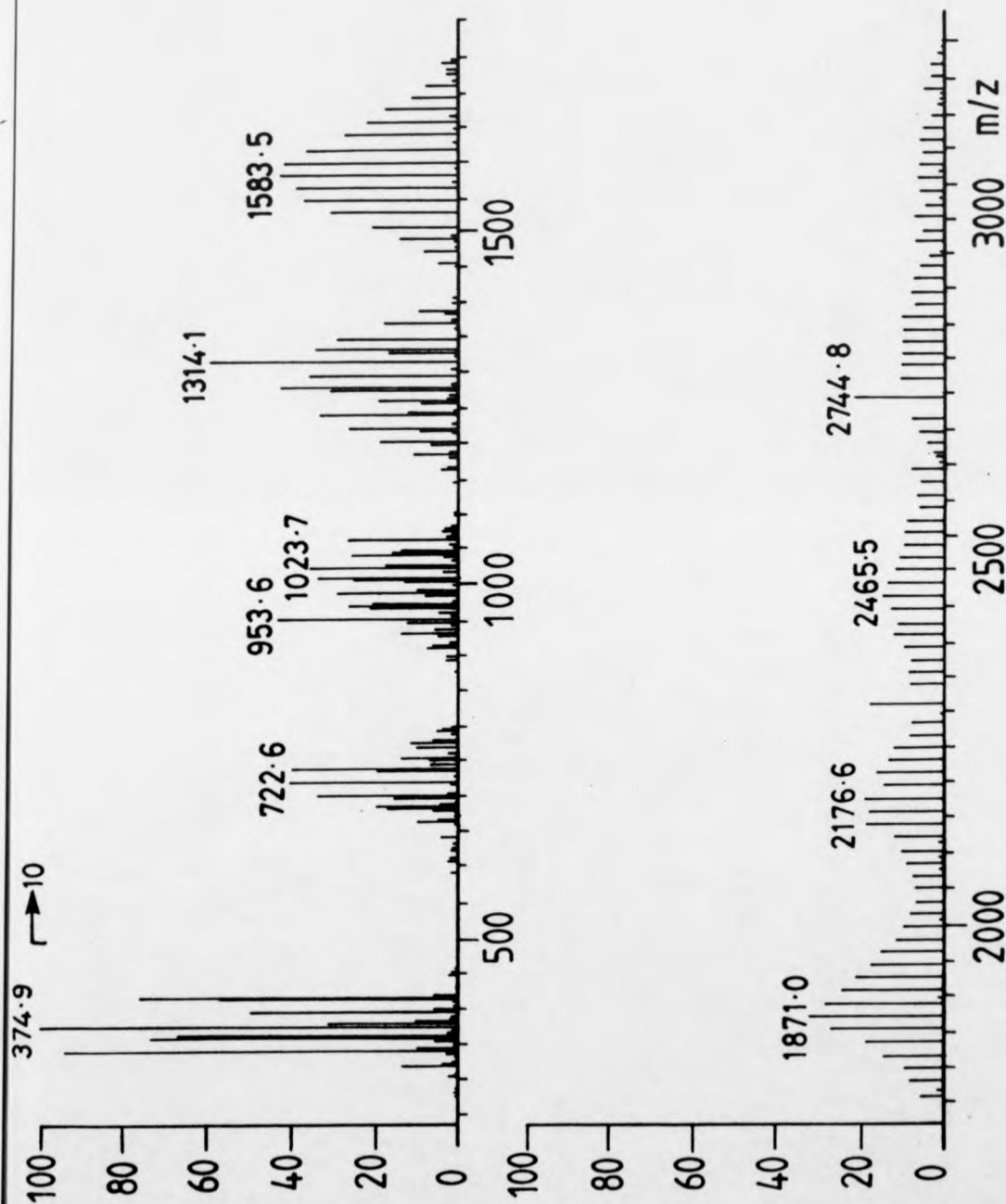
Fig. 5.7.2 The relative intensities, with respect to $[\text{UO}_2]^+$
 ($m/z = 270$), for the various uranyl-(amino acid) clusters
 studied

| | | no. of amino acids, p. | | | | |
|------------|------|------------------------|------|------|-----|-----|
| Amino acid | | 1 | 2 | 3 | 4 | 5 |
| | Gly. | 25.6 | 4.5 | 5.8 | 3.2 | |
| α | Ala. | 21.5 | 3.8 | 4.9 | 0.9 | 1.0 |
| β | Ala. | 16.8 | 2.9 | 5.2 | 1.2 | 0.5 |
| | Val. | 32.8 | 14.8 | 14.1 | 5.7 | 4.7 |
| α | ABA. | 17.5 | 5.0 | 1.9 | | |
| β | ABA. | 32.3 | 16.2 | 2.6 | 1.6 | |
| γ | ABA. | 20.9 | 7.7 | 3.8 | 0.9 | |
| | Ser. | 10.2 | 0.9 | 1.2 | | 0.9 |
| | The. | 4.3 | 1.2 | 1.9 | | |
| | Cys. | 1.6 | 0.7 | 1.0 | | 0.2 |

5.8 THE FAB MASS SPECTRUM OF URANIUM(IV) CHLORIDE

The mass spectrum for UCl_4 was recorded by FAB-MS using negative ion detection, for masses upto 3500 daltons with a number of matrix compounds and co-solvents. The resulting spectra are very rich in species and show the presence of a number of sequences of clusters of general formula $[\text{U}_x\text{Cl}_n]^-$ as well as related species containing characteristic matrix adducts. Adduct species were found to be least significant for sulfolane when cooled, while dimethyl sulphoxide gave rise to clusters containing methyl sulphoxide moieties.

These $[\text{U}_x\text{Cl}_n]^-$ cluster series were observed to decrease in relative intensity with increasing cluster size, x , with each cluster series containing species corresponding to a number of n values. The most intense cluster species in a series was found to increase with increasing x value, with the range of n values observed also exhibiting a corresponding shift to higher values. For the $x = 1$ series, values of n consistent with between one and six chlorine atoms being present were observed, $1 \leq n \leq 6$, with the most intense species being $[\text{UCl}_3]^-$. The $x = 2$ series showed values of $n = 3$ to 8, with the $n = 5$ species being most intense. This gradual increase in the chlorine atom content with increasing cluster size is observed to continue until the species with $x = 5$, which exhibits a slightly increased relative intensity, after which the increase becomes more gradual.



Spec 5.8.1 Negative ion FAB Spectrum of UCl₄ in DMSO Matrix

This behaviour can be clearly demonstrated in a plot of the chlorine content, n , against cluster size, x , for the most abundant species observed for a given value of x . The resulting plot gives rise to two different size-dependent relationships, which are seen to intersect at $x = 5$. These relationships correspond to

$$n = 2x + 1 \quad \text{Eqn. 5.1}$$

for lower mass clusters, $x \leq 5$, and for higher mass clusters, $x \geq 5$,

$$n = 1.5x + 3.5 \quad \text{Eqn. 5.2}$$

This behaviour can also be represented graphically by a plot of the uranium : chlorine ratio, z , against cluster size, x . The resulting graph shows the presence of two distinct curves that intersect at $x = 5$. In addition, when the ranges of z are also plotted they are found to give rise to two distinct regions for the compositions of uranium-chlorine clusters. In the first of these regions, $x \leq 6$, the lower and upper compositions are found to tend towards the plot observed for the most intense clusters at $x \geq 5$. While in the second region, $x \geq 6$, the limits of the composition range tend towards the curve due to the most intense cluster present for clusters of size $x < 6$.

This suggests that the range of values of n observed for each x value is strongly related to a stable stoichiometry compound and hence the stoichiometry of the more stable uranium-chlorine species present, although these may not always correspond to the most intense clusters.

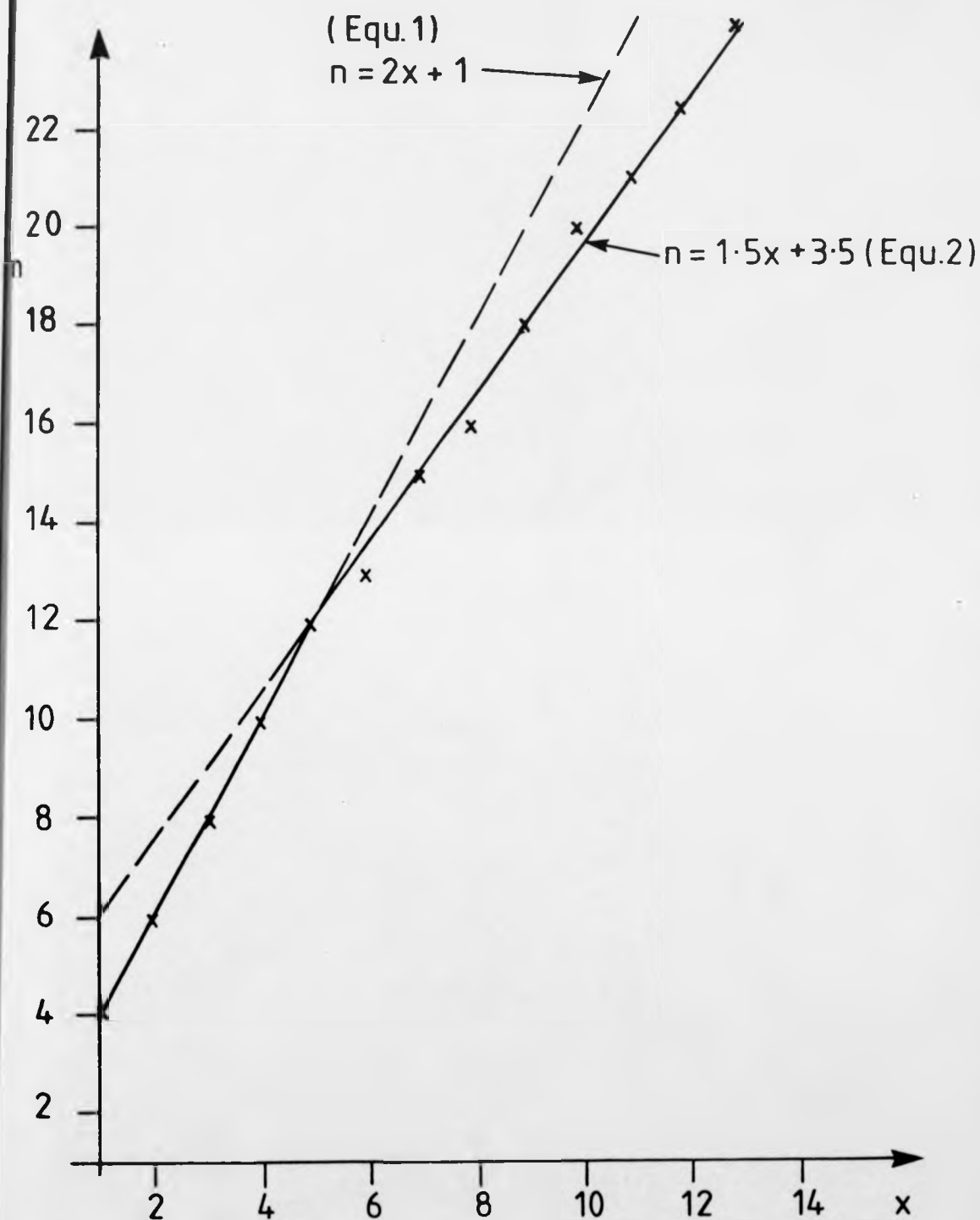
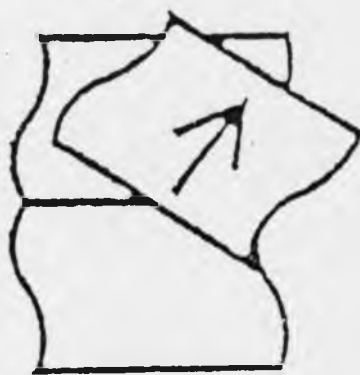


Fig 5.8.1 Graphical Representation of the Variation in Chlorine Atom Content, n , with Cluster Size, x , for the Most Abundant Clusters in Each Series

PAGE(S) MISSING
NOT AVAILABLE

247



A plot of the uranium : chlorine atom ratio, z , against $1/x$ is found to illustrate the above clearly by giving rise to a number of size-dependent linear relationships centring on $z = 1.5$ and 2.0 at very high cluster sizes. For clusters of small x values, $x < 5$, the relationship can be described by the equation.

$$z = 1/x + 2.0 \quad \text{Eqn. 5.3}$$

While the composition range boundaries for this cluster size range centre on $z = 1.5$, the upper composition range is described by the equation.

$$z = 5.5/x + 1.5 \quad \text{Eqn. 5.4}$$

While the lower boundary is found to show odd/even alternation, with $x = 2, 4, 6$ and 8 showing a constant z value of $z = 1.5$, the lower boundary for $x = 1, 3, 5$ and 7 is described by the equation.

$$z = -0.5/x + 1.5 \quad \text{Eqn. 5.5}$$

For clusters $x > 5$ the linear relationship exhibited by the most intense clusters corresponds to the equation.

$$z = 3.5/x + 1.5 \quad \text{Eqn. 5.6}$$

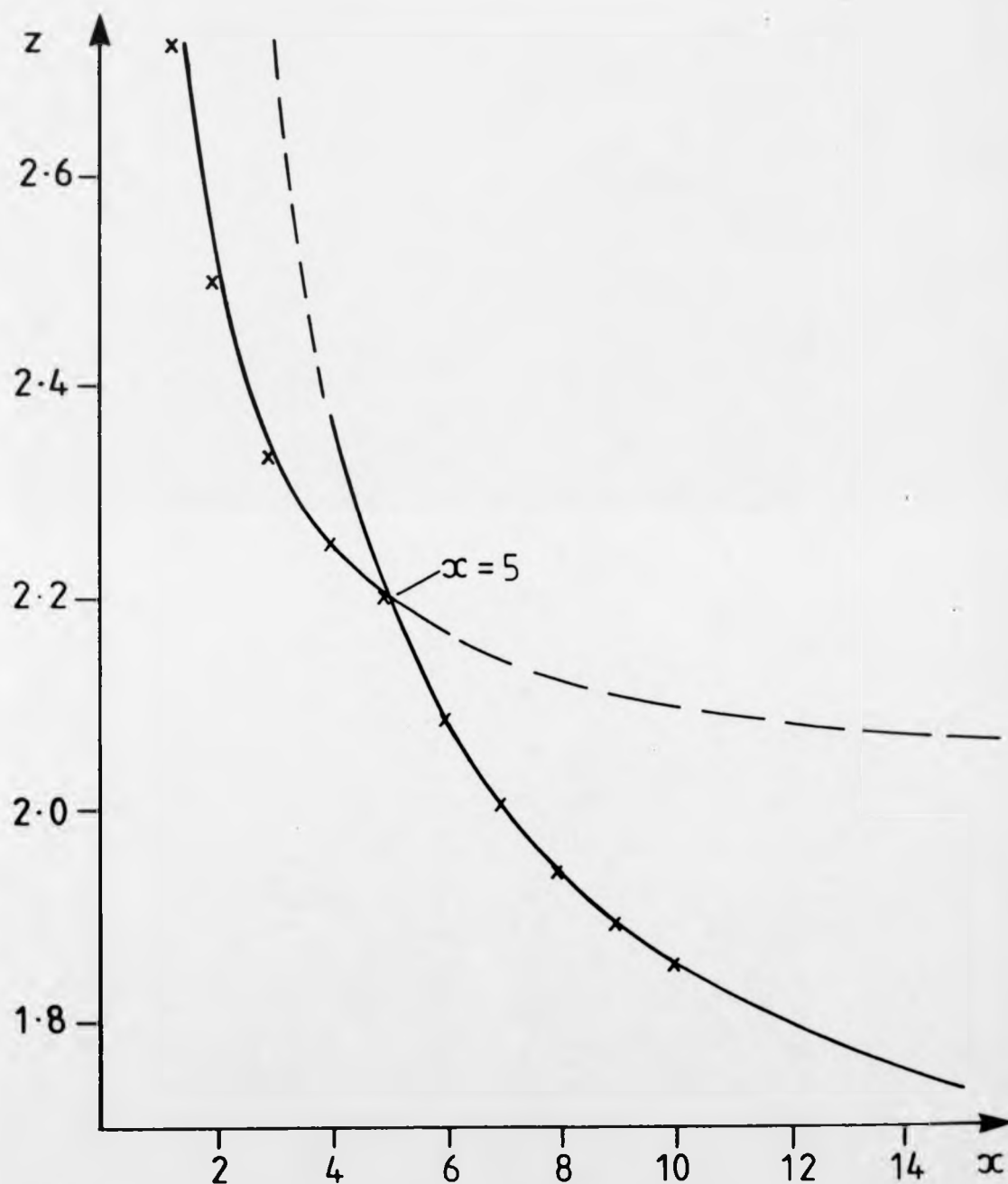


Fig 5.8.2 Graphical Representation of the Variation of Uranium : Chlorine Atom Ratio, z , with Cluster Size, x , for the Most Abundant Clusters in Each Series

However the composition boundaries for this size range are observed to be centred around $z = 2.0$, with no odd/even alternation being observed. The upper composition boundary is found to correspond to the equation

$$z = 2.0/x + 2.0 \quad \text{Eqn. 5.7}$$

and the lower limit by

$$z = -0.5/x + 2.0 \quad \text{Eqn. 5.8}$$

The upper and lower limits for the range of chlorine atom contents are found to be related to the ultimate stoichiometries formed by the most intense clusters observed. This tendency to attain equivalent compositions at high x values suggests the formation of particular crystal lattices or structural arrangements, with the preferred structure being dependant on cluster size. Since the relative cluster binding energies decrease with increasing cluster size, the dominant structural form exhibited is governed by energetic considerations. Hence the changes in the linear relationships observed between z and $1/x$ at $x \approx 5$ may denote a change in structural arrangement of the cluster units to a structure that is more energetically favourable at larger cluster sizes, with the transition point between these structures being isoenergetic.

Prior to this point, $x < 5$, the composition boundaries are influenced by structural considerations for both possible structural arrangements, while at $x > 5$ the composition boundaries are strongly

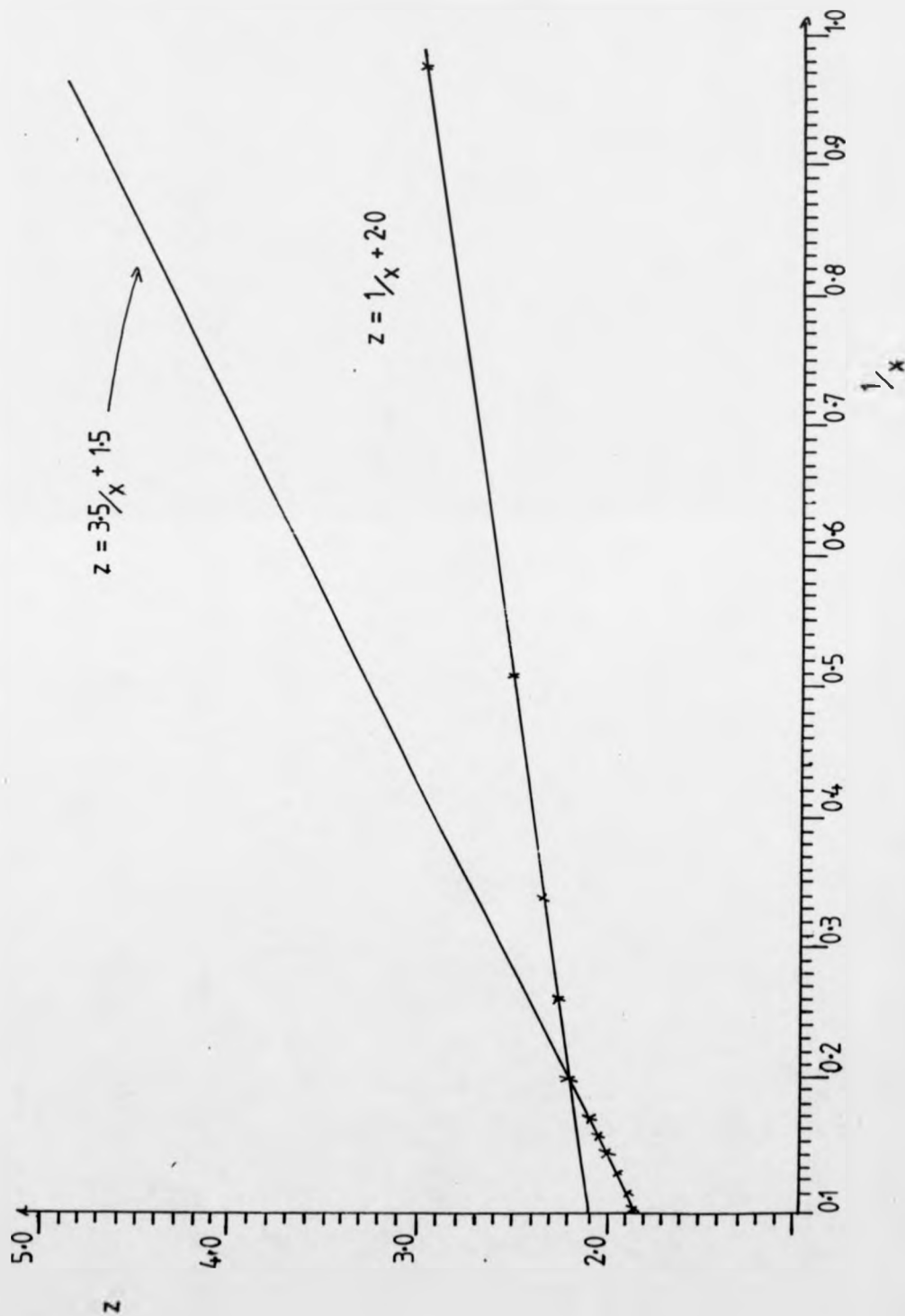
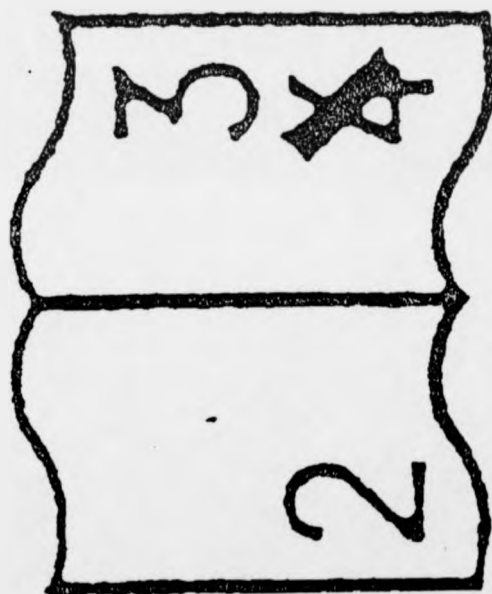


Fig 5.8.3 Graphical Representation of the Variation of z with $1/x$, Showing the Crossover Between the two Cluster Structures at $z = 5$

related to the dominant structure prior to rearrangement at $x = 5$. The level of this influence, $x \leq 5 \leq x$, suggests that these structural arrangements are of similar energies over the cluster size range studied, although the differences between them is large enough to cause a marked structural rearrangement at $x = 5$.

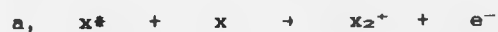
PAGINATION ERROR

251



6.1 CLUSTER CHEMISTRY

There are various means by which cluster formation can take place; these association reactions can generally be divided into two major groups. The first of these involves the formation of a charged species upon the association of a charged species with a number of neutral units. Examples of these associative ionization processes are,



Homonuclear associative ionization



Heteronuclear associative ionization



Rearrangement ionization



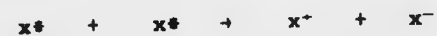
Penning ionization



Dissociative Penning ionization



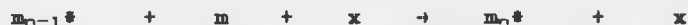
Collisional electron release



Excited pair ionization

The second type of cluster formation reaction involves the association of neutral units. The reactions resulting in cluster formation during fast atom bombardment are generally considered to belong to the second group.

Evidence suggests that during their initial growth, clusters are formed by a series of third-body-assisted energetic association reactions of the type



with the third party removing the excess exothermic energy and hence its role becomes less important as the cluster size increases, i.e. as the cluster itself is progressively more able to provide pathways for the dissipation of the energy released via its increased number of degrees of vibrational freedom. Similarly third-body reactions may also occur involving charged species. Excess cluster energy may also be lost via one or more fragmentation reactions, involving the dissociative loss of cluster units. This type of evaporative dissociation has been reported for a wide range of cluster systems, with several studies suggesting that structural magic numbers originate solely from the dynamic processes of unimolecular dissociation, with unstable clusters undergoing fragmentation to form more stable combinations of atoms (85). Examples of this are the 21-mer of water and the model of Echt et al. for gaseous clusters, which attributes magic numbers to the completion of icosahedral structures (182).

The ionization of neutral clusters, even at low energies, may also induce extensive fragmentation or rearrangement reactions concurrent with the ionization event. Hence the observed distributions of charged clusters may not accurately represent the situation of their neutral counterparts. This has been clearly demonstrated by the observation that the formation of a dimer ion within a rare gas cluster should release sufficient energy to evaporate dissociatively a number of atoms from the newly formed cluster ion (84)(184). Similar behaviour has also been observed for ammonia clusters. These studies have shown the average kinetic energy release, and hence the binding energy, of cluster ions to decrease with increasing cluster size, and the dissociation rates of the clusters to be dependent on the time lapse after the ionization/cluster formation event. Chen et al. have suggested that clusters with metastable lifetimes too long for the fragmentation process to be described by statistical vibrational predissociation, may dissociate by tunnelling through a rotational barrier (186). This is likely even in clusters of heavy atoms or molecules, since such tunnelling is relatively insensitive to the mass of the escaping species (185).

Hence in addition to cluster formation reactions, the size distribution and the relative intensities of the resulting clusters are dependent on an array of factors, both thermodynamic, kinetic and structural, which influence the position and rate at which the equilibrium for cluster formation reaction is reached. The major factors affecting the rate at which equilibrium is reached following ionization can be summarised;

i, Ion-molecule reactions may proceed between the newly ionized entity and a neighbouring species. This reaction may result in various third-body reactions.

ii, The energy content of a cluster increases as the neutral species rearranges to accommodate a newly-formed charge; this may lead to extensive evaporative dissociation as the cluster cools.

iii, Kinetic energy release measurements have shown that clusters of neighbouring x-values have comparable vibrational energies.

iv, The rates of unimolecular dissociation decrease with time after the ionization event and hence the relative binding energies increase. This is because of the energy distribution of a cluster population, with the number of clusters having energies in excess of their dissociation threshold decreasing on cooling.

6.2 CONCLUDING SUMMARY

The variety of FAB-induced species detected during this research are found to follow a number of similar general trends, with the sequences of clusters formed showing a direct relationship to many bulk state phenomena. These singly-charged clusters are formed by gas phase association reactions and show the strong influence of the energetics and patterns established for the bulk metal salts at small cluster sizes. The cluster sizes at which these influences begin to emerge affect significantly the structures and reactions of a given class of clusters; indeed these are observed to depend strongly on the metal component, reflecting changes in the availability of energy states.

Monometallic species ($x = 1$) are also found to exhibit coordination phenomena that are directly related to stabilities in the bulk state. The occurrence of many bulk state phenomena are best interpreted by consideration of the energetic influences present during cluster formation and subsequent decomposition. This work has shown cluster formation to take place in the gas phase, via a number of third-body-assisted associative reactions;



where X acts as a third body.

During cluster formation in the presence of a matrix compound or co-solvent, the formation of matrix adducts can also take place to an extent depending on the relative ionization energy of the matrix present.

The presence of certain matrix compounds is also found to influence the relative intensities and distributions of differently sized clusters. However the use of sulpholane as a matrix compound is found to yield cluster spectra comparable with those formed from pure compounds, although the presence of impurities is observed to influence cluster formation. The effects of temperature and pressure on cluster formation are observed to be similar to those observed during chemical ionization, which supports the proposal of their essentially gas phase origin.

The clusters formed by one or more of these associative reactions are thought to undergo a number of possible energy-loss processes before dynamic equilibrium is established between cluster formation and fragmentation reactions. Additional reactions, including collisional de-excitation and stabilization reactions, as well as cluster rearrangements, enable the dissipation of excess energy. The resulting clusters have been shown to adopt preferentially to energetically-stable structural arrangements which are consistent with the metal salt phases in the bulk state. This behaviour is clearly demonstrated by considering the uranium-oxygen clusters reported above, where the clusters adopt stoichiometries that coincide with the sharp change in bulk density marking the transition between the fluorite and uranyl-

bonded phases of U_2O_5 . Similarly the clusters observed for a number of oxides of lanthanide metals are also found to display trends consistent with changes in their available oxidation states (and the resulting complexity of their oxide phases) as well as the influence of the lanthanide contraction. These include similarities in the positions of several spectral abnormalities and size-dependent phenomena, including the adoption of $z = 1.5$, $z = \text{metal : oxygen atom ratio}$, at large values of x . However the availability of the M^{4+} oxidation state for cerium results in the achievement of $z = 2.0$, while the clusters based on europium and samarium tend towards the formation of oxygen-deficient clusters at $x \leq 15$, reflecting the availability of their M^{2+} states.

The stoichiometries displayed by these clusters can be expressed by the equation

$$z = 1.5 - 0.5/x [3x - 2(x + y)] \quad \text{Eqn3.35}$$

This expression can be used to explain several spectral phenomena and the formation of clusters containing lanthanide ions of mixed oxidation state. In addition it allows insight to be gained into the relative stabilities of the clusters formed by interpreting possible electronic structures, as well as enabling direct parallels to be drawn between the clusters observed and the bulk-state lanthanide-oxide phases reported.

Similarly the uranium-oxygen atom clusters formed by the FAB of various uranyl salts can be described by the equation

$$Z = 2.5 - 0.5/x [6x_1 + 4x_2 - 2y']$$

Eqn4.7

Where x_1 and x_2 respectively are taken as denoting the numbers of U^{6+} and U^{4+} ions in a given cluster, while y' refers to the total number of oxygen atoms present. This equation can be used to explain why no odd/even alternation is observed for uranyl clusters since both odd and even clusters are found to contain unpaired electrons, unlike the lanthanide-oxygen clusters. From the z values obtained, the uranium-oxygen atom clusters are found to coincide with the sharp change in density reported for the bulk state uranium-oxygen phases, which marks the change between fluorite and uranyl type bonding in the U_2O_5 phases. Similar results are also obtained for thorium-oxygen atom clusters as well as those observed for uranium-chlorine atom clusters.

In addition to the metal-oxygen and -chlorine clusters described, various clusters containing coordinated ligands and ligand fragments are also detected. These clusters displayed a number of similar trends, especially between clusters containing related ligands and often reflecting coordination stabilities in the bulk state. The ligated clusters formed by the FAB of a number of Uranyl-(amino acid) complexes all showed the tris-(amino acid) clusters to exhibit enhanced relative intensities, corresponding to the preferred hexa-coordination of the uranyl ion in its equatorial plane. This also shows the amino-acid ligands to function with a bidentate character. At larger cluster sizes, $x > 1$, species containing up to three amino-acid ligands or associated fragments were detected, with the mono-ligated clusters being of highest relative intensity. The extent and strength

of ligand association has also been found to be dependent on the character of the amino acid ligands; this in many cases is found to be related to the stabilities of the carbonium ions derived from the respective ligands. While the presence of $p \leq 3$ ligated clusters in higher-mass species suggests that these species consist of a singly-charged ligated uranyl ion surrounded by a shell like structure of neutral dioxouranium moieties.

The spectra for the lanthanide acetates studied are found to display the presence of related species of general formula $[(LnO)_x O_y (CH_3COO)_p F_L]^+$, with values of $p \leq 2$ being observed for all lanthanides, except cerium which exhibits $p \leq 3$. These ligand coordinations and their relative intensities reflect the reported crystal structures. In addition the dominant fragmentation pattern displayed by the acetate ligands is observed to be dependent on both the lanthanide metal present and the cluster size. This observation points to a dependence of the preferred ligand fragmentation pattern on the size, and hence stability, of the cluster. Similar results are also obtained for the lanthanide malonates and uranyl acetate clusters.

6.3 FUTURE WORK

Future research into the nature, formation and decomposition mechanisms, and structures and stabilities of metal-oxygen and metal-halide clusters should aim to establish the energy differences between the different series of stoichiometries arising for each metal. This study could include the use of mass analysed ion kinetic energy scan, MIKES, to investigate the energy relationship between the regions of intersection in the relative ion abundances of these series, and related size-dependant structural changes. Similar studies could be extended to related metal-oxide and metal-halide systems.

In addition, investigations into the structural influences of cluster size could also be carried out using a high pressure FAB source. In these studies, the admittance of reactive buffer gases into the source during bombardment may result in spectral species showing changes in their relative intensities and reveal information about adduct formation. Also by using reactive buffer gases of known ionization potentials, information regarding the relative energies of the resulting species and their formation pathways may be obtained.

Similarly, investigations into the formation of ligated clusters may be carried out with the high pressure source. These studies will enable the interpretation of trends occurring as regards the extent of ligand coordination with respect to differing reagent gases and cluster sizes. These investigations may in turn give information

concerning the number and type of available sites for ligand coordination and their relative energies. These investigations could be usefully extended to related metals.

Other means of vapourising metal salts could be utilised, such as laser desorption or field desorption. Such approaches, which involve 'softer' energising of the sample, may lead to greater retention of ligand moieties in the resulting cluster.

- 1 BARBER M., BORDOLI R. S., SEDGWICK R. D., TYLER A. N.,
J. Chem. Soc., Chem. Commun. 1981 325
- 2 SURMAN D. J., VICKERMAN J. C.,
J. Chem. Soc., Chem. Commun. 1981 324
- 3 BRUCE M. I., LIDDEL M. J.,
Applied Organomet. Chem. 1987 1 191
- 4 BARBER M., BORDOLI R. S., SEDGWICK R. D., TYLER A. N.,
Nature 1981 293 270
- 5 FENSELAU C., COTTER R. J.,
Chem. Rev. 1987 87 501
- 6 BARBER M., BORDOLI R. S., SEDGWICK R. D., TYLER A. N., ELLIOT G. J.,
Anal. Chem. 1982 54 645A
- 7 Mc NEAL C. J.,
Anal. Chem. 1982 54 43A
- 8 BEUHLER R. J., FRIEDMAN L.,
Int. J. Mass Spectrom. Ion Phys. 1988 78 1
- 9 CONNELLY M. J., ORTH R. G.,
Anal. Chem. 1987 59 903
- 10 MAGEE C. W.,
Int. J. Mass Spectrom. Ion Phys. 1983 49 211
- 11 WILLIAMS D. H., FINDERS A. F., MAYLOR S., GIBSON B. W.,
J. Am. Chem. Soc. 1987 109 1980
- 12 a) SUNNER J. A., KULATINGA R., KABARLR P.,
Anal. Chem. 1987 58 2009
- b) MICHL J.,
Int. J. Mass Spectrom. Ion Phys. 1983 53 255

- 13 ADAMS F., GIJBELS R., VAN GRIEKEN R.,
Chemical Analysis 1988 95
- 14 KING B. V., TSONG I. S. T., LIN S. H.,
Int. J. Mass Spectrom. Ion Proc. 1987 78 341
- 15 SUNNER J., IKONOMOU M. G., KEBARLE P.,
Int. J. Mass Spectrom. Ion Proc. 1988 82 221
- 16 ABERTH W. H., BURLINGAME A. H.,
Anal. Chem. 1988 60 1426
- 17 JENNINGS K. R., KEMP T. J., SIEKLUCKA B.,
Inorg. Chim. Acta. 1988 141 163
- 18 JENNINGS K. R., KEMP T. J., SIEKLUCKA B.,
J. Chem. Soc., Dalton Trans. 1988 2905
- 19 ASHTON P. R., FENTON D. E., PRASAD R. N., JINDAL M., JAIN M.,
Inorg. Chim. Acta. 1988 146 99
- 20 GREGORY B., JABLONSKI C. R., WANG Y. P.,
J. Organomet. Chem. 1984 269 75
- 21 BRISDON B. J., FLOYD A. J.,
J. Organomet. Chem. 1985 288 305
- 22 DOLNIKOWSKI G. G., WATSON J. T., ALLISON J.,
Anal. Chem. 1984 56 197
- 23 ROMANOWSKI G., WANLZEK K. P.,
Spectros. Int. J. 1987 5 101
- 24 ILLIES A. J.,
J. Chem. Phys. 1988 92 2889
- 25 GUBSIC M. B., MORSE M. D., SMALLEY R. B.,
J. Chem. Phys. 1985 82 590

- 26 CAMPANA J. E., GREEN B. N.,
J. Am. Chem. Soc. 1984 106 531
- 27 a) BEST S. P., CLARK R. J. H., COONEY R. P.,
Inorg. Chim. Acta 1988 145 141
- b) EKSTROM A.,
Inorg. Chem. 1974 13 2237
- 28 PYYKKO P., LAAKKONEN L. J., TATSUMI K.,
Inorg. Chem. 1989 28 1801
- 29 TATSUMI K., HOFFMANN R.,
Inorg. Chem. 1980 19 1656
- 30 GORLLER-WALRAND C., COLEN R. P.,
Inorg. Chim. Acta. 1988 142 151
- 31 BURROWS H. D., FORMOSINHO S. J., DA-GRACA MIGUEL.
Inorg. Chim. Acta. 1987 139 301
- 32 HOEKSTRA H. R., SIEGEL S., GALLAGHER F. X.,
J. Inorg. Nucl. Chem. 1970 32 3237
- 33 MATIN A., EDWARDS R. K.,
J. Phys. Chem. 1965 69 1788
- 34 LATTA R. E., FRYELL R. E.,
J. Nucl. Mater. 1970 35 195
- 35 WILLIS B. T. M.,
Nature 1963 197 755
- 36 ROUSE K. D., WILLIS B. T. M., PRYOR A. W.,
Acta. Crystallogr. B. 1968 22 117
- 37 ROBERTS L. E. J., WALTER A. J.,
J. Inorg. Chem. 1961 22 213

- 38 WILSON W. B.,
J. Inorg. Nucl. Chem. 1961 19 212
- 39 ZACHARIASEN W. H.,
Acta. Crystallogr. 1948 1 265
- 40 GREAVES C., FENDER B. E. F.,
Acta. Crystallogr. B. 1972 28 3609
- 41 ENGMANN R., DE WOLFF P. M.,
Acta. Crystallogr. 1963 16 993
- 42 DEBETS P. C.,
Acta. Crystallogr. 1966 21 589
- 43 WAIT E.,
J. Inorg. Nucl. Chem. 1955 1 309
- 44 SIEGEL S., HOEKSTRA H. R., SHERRY E.,
Acta. Crystallogr. 1966 20 292
- 45 HOEKSTRA H. R., SIEGEL S.,
J. Inorg. Nucl. Chem. 1973 35 761
- 46 MORSS L. R.,
Actinides in prospective, Ed. EDELSTEIN N. M.,
Pergamon press, oxford, 1982. ISBN
- 47 ARMENTROUT P. B., BEAUCHAMP J. L.,
Chem. Phys. 1980 50 27
- 48 JOHNSEN R., BIONDI M. A.,
J. Chem. Phys. 1972 57 1975
- 49 MORELAND P. L., ROKOP D. J., STEVENS C. M.,
Int. J. Mass Spectrom. Ion Proc. 1970 5 127
- 50 ARMENTROUT P. B., HODGES R. V., BEAUCHAMP J. L.,
J. Chem. Phys. 1977 66 4683

- 51 DEVIENNE F. M., COMBARIEU R., TEISSEIRE M.,
Surf. Sci. 1981 106 204
- 52 ARMENTROUT P.B., BEAUCHAMP J. L.,
Chem. Phys. 1980 50 21
- 53 READ P. A.,
M. Sc. Thesis, University of Warwick, 1989
- 54 BROWN D. A., BUGÉ H., COOGAN R., DOOCEY D., KEMP T. J.,
MULLER A., SHIELDS L.,
J. Inorg. Biochem. 1991 43 589
- 55 KNIGHT W. D., CLEMENGER K., de HEER W. A., SAUNDERS W. A.,
CHOU M. Y., COHEN M. L.,
Phys. Rev. Letts. 1984 52 2141
- 56 BALADRON C., AIONSO J.,
Physica B 1988 154 73
- 57 UPTON T. H.,
J. Chem. Phys. 1987 86 7054
- 58 a) EKARDT W.,
Phys. Rev. B. 1984 52 1925
- b) EKARDT W.,
Phys. Rev. B. 1984 29 1558
- 59 CLEMENGER K.,
Phys. Rev. B. 1985 32 1359
- 60 MINGOS D. M. P., WALES D. J.,
Introduction to cluster chemistry
Prentice Hall Int., 1990 ISBN 0-13-474305-9

- 61 ASHCROFT N. W., MERMIN N. D.,
Solid state physics
Holt-Saunders Int. Editions, 1981 ISBN 0-03-049346-3
- 62 HUTCHINGS M. T.,
Solid State Phys. 1964 16 227
- 63 MINGOS D. M. P., SLEE T., ZHENYANG L.,
Chem. Rev., 1990 90 383
- 64 STONE A. J.,
Inorg. Chem. 1981 20 563
- 65 MINGOS D. M. P., ZHENYANG L.,
Chem. Phys. 1989 137 15
- 66 a) KATAKUSE I., ICHIHARA T., FUJITA Y., MATSUI T., SAKURAI T.,
MATSUDA H.,
Int. J. Mass Spectrom. Ion Proc. 1985 69 229
b) KATAKUSE I., ICHIHARA T., FUJITA Y., MATSUI T., SAKURAI T.,
MATSUDA H.,
Int. J. Mass Spectrom. Ion Proc. 1986 74 33
- 67 LINDSAY D. M., WANG Y., GEORGE T. F.,
J. Chem. Phys. 1987 87 1685
- 68 GREENWOOD N. N., EARNSHAW A.,
Chemistry of the elements
Pregamon Press, 1984, ISBN 0-08-022057-6,
- 69 HUHEEY J. E.,
Inorganic chemistry
Harper and Row Press, 1983, ISBN 0-06-350352-2,

- 70 COTTON F. A., WILKINSON G.,
Advanced inorganic chemistry, 4th Edition
John Wiley & Sons, Inc., 1980, ISBN 0-471-02775-8,
- 71 STONE A. J.,
J. Mol. Phys. 1980 41 1339
- 72 STONE A. J.,
Inorg. Chem. 1981 20 563
- 73 MORSE M. D.,
Chem. Rev. 1986 86 1049
- 74 SALAHUB D. R.,
Adv. Chem. Phys. 1987 69 447
- 75 FAYET M., M^cGLINCHEY M. J., WOSTE L. H.,
J. Am. Chem. Soc. 1987 109 1733
- 76 FAYET M., M^cGLINCHEY M. J., WOSTE L. H.,
J. Am. Chem. Soc. 1987 109 5305
- 77 WALES D. J., STONE A. J.,
Inorg. Chem. 1989 28 3120
- 78 HARRIS T. A., KIDWELL R. S., NORTHBY J. A.,
Phys. Rev. Letts. 1984 53 2390
- 79 LEVINGER M. F., RAY D., MURRAY K. K., MULLIN S. A., SCHULZ C. P.,
LINEBERGER W. C.,
J. Chem. Phys. 1988 89 71
- 80 BOCK U., MEYER H.,
J. Chem. Phys. 1986 84 4854
- 81 ECHT O., SATTLER K., RECKNAGEL E.,
Phys. Rev. Letts. 1981 47 1121
- 82 ECHT O., KANDLER O., LEISNER T., MIEHLE W., RECKNAGEL E.,

- J. Chem. Soc. Faraday Trans. 1990 86 2411
- 83 STACE A. J., MOORE C.,
Chem. Phys. Letts. 1983 96 90
- 84 MARK T. D., SCHEIER P., LEITER K., RITTER W., STEPHAN K.,
STAMATOVIC A.,
Int. J. Mass Spectrom. Ion Proc. 1986 74 281
- 85 STACE A. J., LETHBRIDGE P. G., UPHAM J. E., WOODWARD C. A.,
J. Chem. Soc. Faraday Trans. 1990 86 2405
- 86 UPPEBRINK J., VALES D. J.,
J. Chem. Soc. Faraday Trans. 1991 87 215
- 87 LEITNER D. M., DOLL J. D., WHITNELL R. M.,
J. Chem. Phys. 1991 94 6644
- 88 ECHT O., MORGAN S., DAO P. D., STANLEY R. J., CASTLEMAN A. W. (Jr),
Ber. Bunsen. Phys. Chem. 1984 88 217
- 89 ECHT O., DAO P. D., MORGAN S., CASTLEMAN A. W. (Jr),
J. Chem. Phys. 1985 82 4076
- 90 WEI S., TZENG W. B., CASTLEMAN A. W. (Jr),
J. Chem. Phys. 1990 93 2506
- 91 LIFSHITZ C., LOUAGE F.,
J. Phys. Chem. 1989 93 5633
- 92 BASS L. M., CATES R. D., JARROLD M. F., KIRCHNER N. J., BOWERS M. T.,
J. Am. Chem. Soc. 1988 105 7024
- 93 CASTLEMAN A. W. (Jr), TZENG W. B., WEI S., MORGAN S.,
J. Chem. Soc. Faraday Trans. 1990 86 2417
- 94 MUNSON M. S. B.,
J. Am. Chem. Soc. 1965 87 5313

- 95 BASS L. M., CATES R. D., JARROLD M. F., KIRCHNER N. J., BOWERS M. T.,
J. Am. Chem. Soc. 1983 105 7024
- 96 MORGAN S., KEESEE R. G., CASTLEMAN A. W. (Jr)
J. Am. Chem. Soc. 1989 111 3841
- 97 MORTON T. H.,
Tetrahedron 1982 38 3195
- 98 BEAUCHAMP J. L., CASERIO M. C., Mc MAHON T. B.,
J. Am. Chem. Soc. 1974 96 6243
- 99 TZENG W. B., WEI S., CASTLEMAN A. W. (Jr),
J. Am. Chem. Soc. 1989 111 6035
- 100 STACE A. J., SHUKLA A. K.,
J. Phys. Chem. 1972 76 409
- 101 LUCSYNSKI Z., WINCEL H.,
Int. J. Mass Spectrom. Ion Phys. 1977 23 37
- 102 HABERLAND H., KORNMEIER H., LANGOSCH H., OSCHWALD M., TANNER G.,
J. Chem. Soc. Faraday Trans. 1990 86
- 103 BRECHNIGNAC C., CAHUZAC PH., LEYGNIER J., WEINER J.,
J. Chem. Phys. 1989 90 1492
- 104 BRECHNIGNAC C., CAHUZAC PH., CARLIER F., DE FRUTOS M., LEYGNIER J.,
J. Chem. Soc. Faraday Trans. 1990 86
- 105 DEVIENNE F. M., ROUSTON J. C.,
Org. Mass Spectrom. 1982 17 173
- 106 KATAKUSE I., ICHIHARA T., FUJITA Y., MATSUO T., SAKURAI T.,
MASSUDA H.,
Int. J. Mass Spectrom. Ion Proc. 1986 74 33

- 107 KATAKUSE I., ICHIHARA T., FUJITA Y., MATSUO T., SAKURAI T.,
MASSUDA H.,
Int. J. Mass Spectrom. Ion Proc. 1986 67 229
- 108 GANTEFOR G., GAUSA M., MEIVES-BROER K. H., LUTZ H. D.,
J. Chem. Soc. Faraday Trans. 1990 86
- 109 ZHENG L. S., KARNER C. M., BRUCAT P. J., YANG S. H., PETTIETTE C.
L., CRAYCROFT M. J., SMALLEY R. E.,
J. Chem. Phys. 1986 85 1681
- 110 FAYET P., WOSTE L.,
Surf. Sci. 1985 156 134
- 111 ANDREON J. A., MARTINS J. L.,
Surf. Sci. 1985 156 635
- 112 SETTLER K., MUHIBACH J., ECHT O., PFAU P., RECKNAGEL E.,
Phys. Rev. Letts. 1981 47 160
- 113 HOAREAU A., MELINON P., CABAUB B.,
J. Phys. D. 1985 18 1731
- 114 BUCKNER S. W., GORD J. R., FREISER B.S.,
J. Chem. Phys. 1988 88 3678
- 115 DEAN L. K. L., BUSCH K. L.,
Org. Mass Spectrom. 1989 24 733
- 116 CALLAHAN J. H., ROSS M. M., BARONAUSKI A. P.,
37 American Society Mass Spectrom. 1989 may
- 117 BERGEMANN W., MEIVES-BROER K. H., LUTZ H. D.,
Phys. Rev. Letts. 1986 56 2248
- 118 JARROLD M. F., BOWER J. E., KRAUS J. S.,
J. Chem. Phys. 1987 86 3876

- 119 a) UPTON T. H.,
 Phys. Rev. Letts. 1986 56 2168
- b) UPTON T. H.,
 J. Chem. Phys. 1987 86 7054
- 120 JARROLD M. F., BOWER J. E.,
 J. Chem. Phys. 1987 87 1610
- 121 PACCHIONI G., FANTUCCI P.,
 The physics and chemistry of small clusters, Editor JENA.
 New York Press, 1987,
- 122 RUATTA S. A., HANLEY L., ANDERSON S. L.,
 Chem. Phys. Letts. 1987 137 5
- 123 JARROLD M. F., BOWER J. E.,
 J. Chem. Phys. 1987 87 5728
- 124 JARROLD M. F., BOWER J. E.,
 J. Am. Chem. Soc. 1988 110 70
- 125 WEN Y., ARROWSMITH J., FREAS R. B.,
 38 American Society Mass Spectrom. 1990 589
- 126 HANLEY L., ANDERSON S. L.,
 Chem. Phys. Letts. 1985 122 410
- 127 HETTICH R. L., FREISER B. S.,
 J. Am. Chem. Soc. 1985 107 6222
- 128 ZAKIN M. R., COX D. M., KALDOR A.,
 J. Chem. Phys. 1989 87 5046
- 129 ZAKIN M. R., BRICKMAN R. D., COX D.M., KALDOR A.,
 J. Chem. Phys. 1988 88 3555
- 130 RILEY S. J., PARKS E. K., WEIMAN G. C., POBO L. G., WEIXLER S. J.,
 J. Chem. Phys. 1984 80 1360

- 131 WHETTEN R. L., COX D. M., TREVOR D. J., KALDOR A.,
J. Phys. Chem. 1985 89 566
- 132 ZAKIN M. R., BRICKMAN R. D., COX D. M., KALDOR A.,
J. Chem. Phys. 1988 88 6605
- 133 HANLEY L., ANDERSON S. L.,
Chem. Phys. Letts. 1985 122 410
- 134 WHETTEN R. L., COX D. M., TREVOR D. J., KALDOR A.,
Phys. Rev. Letts. 1985 107 518
- 135 GEUSIC M. E., MORSE M. D., O'BRIEN S. E., SMALLEY R. E.,
Rev. Sci. Instrum. 1985 56 2123
- 136 FREAS R. B., CAMPANA J. E.,
J. Am. Chem. Soc. 1986 106 1659
- 137 JACOBSON D. B., FREISER B. S.,
J. Am. Chem. Soc. 1986 106 27
- 138 FREAS R. B., DUNLAP B. I., WAITE B. A., CAMPANA J. E.,
J. Chem. Phys. 1987 86 1276
- 139 JACOBSON D. B., FREISER B. S.,
J. Am. Chem. Soc. 1984 106 462
- 140 JACOBSON D. B., FREISER B. S.,
J. Am. Chem. Soc. 1984 106 5351
- 141 FREAS R. B., CAMPANA J. E.,
J. Am. Chem. Soc. 1985 107 6202
- 142 FREAS R. B., CAMPANA J. E.,
J. Am. Chem. Soc. 1986 108 4659
- 143 FREAS R. B., RIDGE D. P.,
J. Am. Chem. Soc. 1984 106 825

- 131 WHETTEM R. L., COX D. M., TREVOR D. J., KALDOR A.,
J. Phys. Chem. 1985 89 566
- 132 ZAKIN M. R., BRICKMAN R. D., COX D. M., KALDOR A.,
J. Chem. Phys. 1988 88 6605
- 133 HANLEY L., ANDERSON S. L.,
Chem. Phys. Letts. 1985 122 410
- 134 WHETTEM R. L., COX D. M., TREVOR D. J., KALDOR A.,
Phys. Rev. Letts. 1985 107 518
- 135 GEUSIC M. E., MORSE M. D., O'BRIEN S. E., SMALLEY R. E.,
Rev. Sci. Instrum. 1985 56 2123
- 136 FREAS R. B., CAMPANA J. E.,
J. Am. Chem. Soc. 1986 106 1659
- 137 JACOBSON D. B., FREISER B. S.,
J. Am. Chem. Soc. 1986 106 27
- 138 FREAS R. B., DUNLAP B. I., WAITE B. A., CAMPANA J. E.,
J. Chem. Phys. 1987 86 1276
- 139 JACOBSON D. B., FREISER B. S.,
J. Am. Chem. Soc. 1984 106 462
- 140 JACOBSON D. B., FREISER B. S.,
J. Am. Chem. Soc. 1984 106 5351
- 141 FREAS R. B., CAMPANA J. E.,
J. Am. Chem. Soc. 1985 107 6202
- 142 FREAS R. B., CAMPANA J. E.,
J. Am. Chem. Soc. 1986 108 4659
- 143 FREAS R. B., RIDGE D. P.,
J. Am. Chem. Soc. 1984 106 825

- 144 FAYET P., WOSTE L.,
Surf. Sci. 1985 156 134
- 145 BRUCAT P. J., ZHENG L.-S., PETTIETTE C. L., YANG S., SMALLEY R. E.,
J. Chem. Phys. 1986 84 3078
- 146 MORSE M. D., GEUSIC M. E., HEATH J. R., SMALLEY R. E.,
J. Chem. Phys. 1985 83 2293
- 147 MAGNERA T. F., DAVID D. E., MICHL J.,
J. Am. Chem. Soc. 1987 109 936
- 148 PARKS E. K., WINTER B. J., KLOTS T. D., RILEY S. J.,
J. Chem. Phys. 1991 94 1882
- 149 SEABURG C. W., RHODIN T. N., MERRILL R. P.,
Surf. Sci. 1980 93 117
- 150 MARTIN T. P., BERGMANN T., MALINOWSKI N.,
J. Chem. Soc. Faraday Trans. 1990 86
- 151 MURRELL J. N.,
Comment from J. Chem. Soc. Faraday Trans. 1990 86 2468
- 152 PASTOR G. M., STAMFLI P., BENNEMANN K. H.,
Phys. Sci. 1988 38 623
- 153 D'EVELYN M. P., RICE S. A.,
J. Chem. Phys. 1983 78 5081
- 154 BROCKNER S. W., GORD J. R., FREISER B. S.,
J. Chem. Phys. 1988 88 5678
- 155 ERVIN K., LOU S. K., ARISTON N., ARMENTROUT P. B.,
J. Phys. Chem. 1987 86 1715
- 156 HAMRICK Y. M., MORSE M. D.,
J. Phys. Chem. 1989 93 6494

- 157 DEMUYNCK J., ROHMER M-M., STRICH A., VELLIARD A.,
J. Chem. Phys. 1981 75 3443
- 158 a) TOLBERT M., BEAUCHAMP J. L.,
J. Am. Chem. Soc. 1984 106 8117
- b) BYRD G. D., BURNIER R. C., FREISER B. S.,
J. Am. Chem. Soc. 1982 104 3565
- c) ELKIND J. L., ARMENTROUT P. B.,
J. Phys. Chem. 1985 87 5626
- d) ELKIND J. L., ARMENTROUT P. B.,
J. Am. Chem. Soc. 1986 108 2765
- 159 FREAS R. B., RIDGE D. P.,
J. Am. Chem. Soc. 1980 102 7129
- 160 BRODBELT-LUSTIG J., VAN KOPPEN P., BOWERS M., DEARDEN P.,
BEAUCHAMP J.,
37 American Society Mass Spectrom. 1989 830
- 161 KING F. L., ROSS M. M., WYSOLKI V. H.,
37 American Society Mass Spectrom. 1989 1512
- 162 RAYANE D., MELINON P., TRIBOLLET B., CABAULD B., HOAREAU A.,
BROYER M.,
J. Chem. Phys. 1989 91 3100
- 163 a) GEUSIC M. E., FREEMAN R. R., DUNCAN M. A.,
J. Chem. Phys. 1988 88 163
- b) GEUSIC M. E., FREEMAN R. R., DUNCAN M. A.,
J. Chem. Phys. 1988 89 223
- 164 WADE K.,
Adv. Inorg. Chem. Radiochem. 1976 18 11

- 165 SUNNER J., KEBARLE P.,
J. Phys. Chem. 1981 85 327
- 166 a) KAHWA I. A., SELBIN J., HSIEH T., LAINE R. A.,
Inorg. Chim. Acta. 1988 141 131
- b) KAHWA I. A., SELBIN J., HSIEH T., EVENS D. W.,
PAMIDIMUKKALA K. M., LAINE R. A.,
Inorg. Chim. Acta. 1988 145 275
- 167 DAOLIO S., FACCHIN B., PAGURA C., GUERRIERO P., SITRAW S.,
VIGATO P. A.,
Inorg. Chim. Acta. 1990 178 131
- 168 BEVAN D. J. M.,
J. Inorg. Nucl. Chem. 1955 1 49
- 169 VON BRAUER G., GRADINGER H.,
Z. Anorg. Allg. Chem. 1954 277 89
- 170 HYDE B.G., BEVAN D. J. M., EYRING L.,
Phil. Trans. A 1966 259 583
- 171 BURNHAM D. A., EYRING L.,
J. Phys. chem. 1968 72 4415
- 172 a) FERGUSON R. E., GUTH E. D., EYRING L.,
J. Am. Chem. Soc. 1954 76 3890
- b) GUTH E. D., HOLDEN J. R., BAENZIGER M.G., EYRING L.,
J. Am. Chem. Soc. 1954 76 5239
- 173 BAENZIGER M. G., FICK. H. A., SCHULDT H. S., EYRING L.,
J. Am. Chem. Soc. 1961 83 2219
- 174 GUTH E. D., EYRING L.,
J. Am. Chem. Soc. 1954 76 5242

- 175 HOEKSTRA H. R., SIEGEL S., GALLAGHER F. X.,
J. Inorg. Nucl. Chem. 1970 32 3237
- 176 JENNINGS K. R., KEMP T. J., READ P. A.,
J. Inorg. Chim. 1989 157 157
- 177 a) NEELY W. C., ELLIS S. P., CODY R. M.,
Photochem. Photobiol. 1971 13 505
- b) GATTANI M. L.,
Science 1952 116 596
- c) JORGENSEN C. K.,
Revue de Chemie Minerale 1977 14 127
- 178 a) FELDMAN I., KOVAL L.,
Inorg Chem. 1963 2 145
- b) CHEL'TSON P. A., SITNIKOV V. I., PODNEBESOVA G. V., OLOVA I. M.,
Russ. J. Inorg. Chem. 1984 29 1770
- 179 a) RUMANUJAM V. V., RENGARAJ K., SIVASANKAR B.,
Bulletin Chem. Soc. Japan 1979 52 2713
- b) GUSTEN H.,
Gmelin Handbuch 1983, supplement VA6, 80
- 180 ALCOCK M. W., FLANDERS D. J., KEMP T. J., SHAND M. A.,
J. Chem. Soc., Dalton Trans. 1985 517
- 181 BOMBIERI G., BENETOLLO F., DELPRA A., ROJAS R.,
J. Inorg. Nucl. Chem. 1979 41 201
- 182 ECHT O., SATTLER K., RECKNAGEL E.,
Phys. Rev. Letts. 1982 47 1121
- 183 LEUTWYLER S., BOSIGER J.,
Chem. Rev. 1990 90 489

- 184 a) STACE A. J., MOORE C.,
Chem. Phys. Letts. 1983 96 80
- b) ECHT O., COOK M. C., CASTLEMAN A. W. (jr),
Chem. Phys. Letts. 1987 135 229
- c) KREISLE D., ECHT O., KNAPP M., RECHNAGEL E.,
Phys. Rev. A 1986 33 768
- 185 CASTLEMAN A. W. (jr), TZENG W. B., WEI S., MORGAN S.,
J. Chem. Soc., Faraday Trans. 1990 86 2417
- 186 CHENG M. H., GISLASON M., MAHAN B. H., TSAO C. W., WERNER A. S.,
J. Chem. Phys. 1970 52 518

- 184 a) STACE A. J., MOORE C.,
Chem. Phys. Letts. 1983 96 80
- b) ECHT O., COOK M. C., CASTLEMAN A. W. (jr),
Chem. Phys. Letts. 1987 135 229
- c) KREISLE D., ECHT O., KNAPP M., RECHNAGEL E.,
Phys. Rev. A 1986 33 768
- 185 CASTLEMAN A. W. (jr), TZENG W. B., WEI S., MORGAN S.,
J. Chem. Soc., Faraday Trans. 1990 86 2417
- 186 CHENG M. H., GISLASON M., MAHAN B. H., TSAO C. W., WERNER A. S.,
J. Chem. Phys. 1970 52 518